Università degli Studi di Ferrara

DOTTORATO DI RICERCA IN
"SCIENZE CHIMICHE"

CICLO XXIX

COORDINATORE Prof. Bignozzi Carlo Alberto

Development of new molecular systems and innovative materials for regenerative photoelectrochemical cells

Settore Scientifico Disciplinare CHIM/03

Dottorando
Dott. Casarin Laura

Tutore
Prof. Bignozzi Carlo Alberto

Cotutore
Prof. Caramori Stefano

Anni 2014/2016

Contents

Chapter 1: DSSC principles

Chapter 2: Experimental methods

Chapter 1: DSSC principles

1.1 Solar energy prospects

In the last decades attention to the renewable energies domain has expanded, due to a worldwide increased sensitivity to environmental issues. In particular photovoltaic technologies have gained a considerable relevance in the market, in fact a growing number of companies have been recently entering the silicon based solar panels business, an already consolidated technology yielding high solar conversion efficiencies (~20%), whose costs have decreased and whose performances have been perfected over the years.

But also other photovoltaic technologies have emerged, including dye-sensitized solar cells, organic photovoltaics, perovskite photovoltaics, and inorganic quantum dot solar cells, with the promise to be less expensive, thinner, more flexible, and amenable to a wide range of lighting conditions, all of which make them suitable for a host of applications beyond rooftop and solar-farm panels [1]. In figure 1.1 a picture of the available photovoltaic technologies is given, together with their certified efficiencies.

According to a recent market analysis report by Grand View Research Inc., dye-sensitized solar cells (DSSC) are currently the most efficient and stable third-generation thin film solar technology available [2]. DSSC efficiencies range around 12%, so they may not be as attractive for large-scale deployments where higher-efficiency cells are more viable. Nonetheless their easier manufacturing, the fact they can be fabricated on flexible supports via inexpensive solution-phase techniques such as high-speed roll-to-roll printing, makes them appealing for "low density" applications where the mechanical robustness and light weight of the glass-less collector is a major advantage. As a result of their kinetic characteristics, DSSC work even in low-light conditions, becoming able to work under cloudy skies and non-direct sunlight, whereas traditional designs would suffer a "cut-out" at some lower limit of illumination, when charge carrier mobility is low and recombination becomes a major issue. The cut-off is so low they are even being proposed for indoor use, collecting energy for small devices from the lights in the house. Finally, their transparency and color characteristics confer them a big potential in architecture and design applications, like the integration in windows and façades.

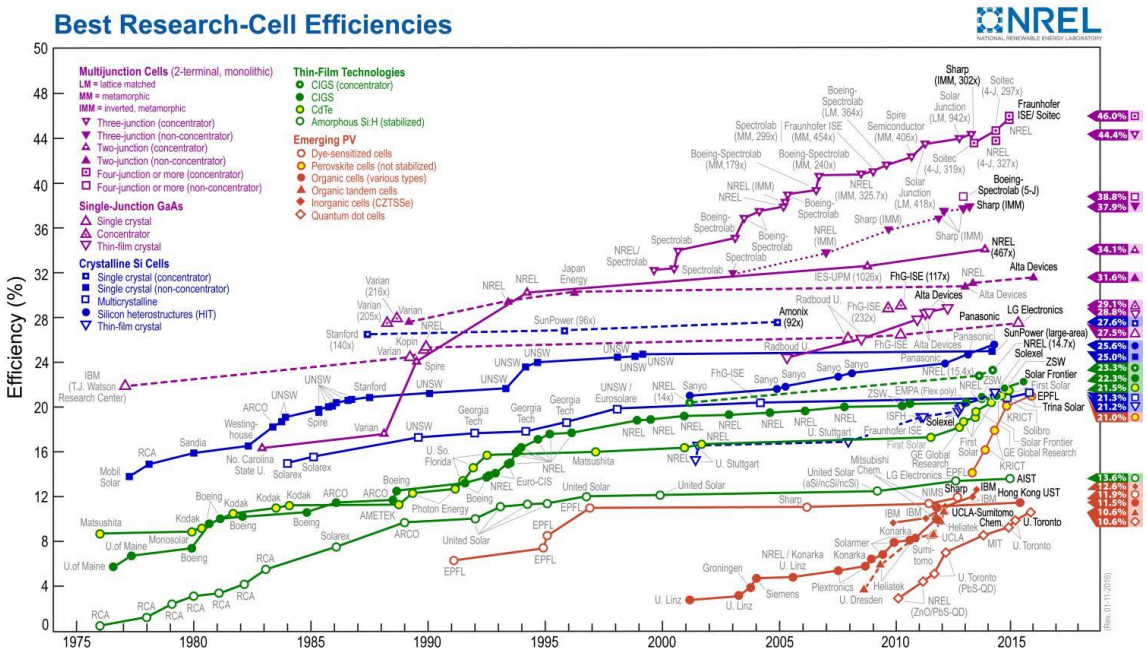

Figure 1.1 Best solar cells efficiencies chart (2016) as recorded by NREL (National Renewable Energy Lab)

1.2 Semiconductors

The interest in semiconductor materials is led by their special conductive characteristics, which make them suitable for energy conversion applications. In particular our focus will be on the photoelectrochemical properties of the semiconductor/electrolyte interface, in particular on the generation of an electrical current following the exposure to electromagnetic radiation of proper frequency.

A semiconductor is a solid phase material whose conductivity is intermediate between conductors (metals) and insulators, with values ranging from about 10^{-9} to 10^{3} $Ohm^{-1}cm^{-1}$, and whose properties can be understood by examining their electronic structure [3].

To treat electronic levels in solids, one approach is to consider the levels for the isolated atoms, and to evaluate what happens as an assembly of isolated atoms is brought together to form a big crystal, that is an association of valence electrons ranging over the whole solid. Due to the essentially infinite number of atoms that must be considered, the electronic structure of solids is typically discussed in terms of *energy bands*, made up of atomic orbitals of the individual atoms. As a result of the large number of interacting orbitals, the spacing between electronic energies within a band, arising from a given quantum state, becomes so small that the band can be effectively considered a continuum of energy levels. However the energy gap between the groups of levels, corresponding to different atomic quantum states, is preserved. Thus we see that the allowed electronic energies fall into energy bands of closely spaced levels, with forbidden gaps between these bands. As with

molecular orbitals, often the energy levels of interest are the highest occupied (called the *valence band, VB*) and the lowest unoccupied (called the *conduction band CB*) bands. It is the energy gap between these bands (*band gap*, i.e. the difference in energy between the upper edge of the valence band and the lower edge of the conduction band) that determines the properties of the material.

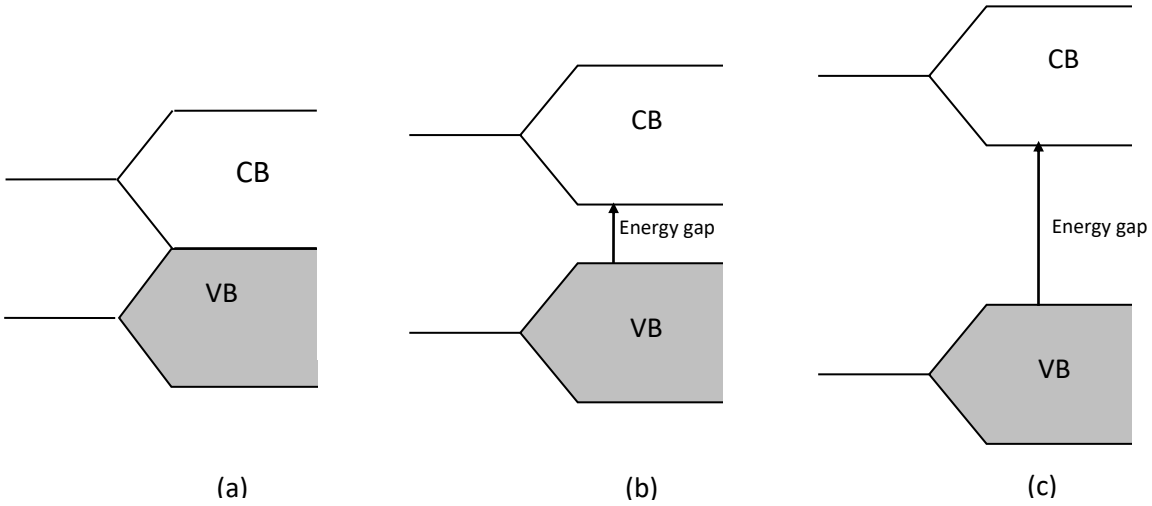

Figure 1.2: Representation of conduction band (CB) and valence band (VB) in terms of band theory for a metal (a), a semiconductor (b), and an insulator (c).

In *insulators* the valence band is full, the conduction band is empty and no net motion of charge results from application of an electric field. In *metals* the uppermost energy band containing electrons is only partially filled, or a filled band overlaps an empty band. These electrons are free to move in a field, and, since they are present in large numbers, this results in very high conductivities (10^4–10^6 $Ohm^{-1}cm^{-1}$). In *semiconductors* the situation is similar to that of insulators, except that the band gap is smaller and electrons can be thermally or optically promoted to the conduction band, resulting in an electrical conductivity that is smaller than that of metals, because of the smaller number of current carriers. The promotion of electrons from the VB to the CB leaves a positively charged vacancy in the VB, which is referred to as a *hole*. Holes can be moved through space by transfer of one electron to the vacancy, therefore they are assumed to be mobile.

There is another method to generate charge carriers within a semiconductor, referred to as *doping.* Doping involves the addition of a different element to the semiconductor structure: the simplest example of this involves the introduction of a group V (e.g. P) or a group III (e.g. B) element to a group IV element like Si. Doping Silicon with Phosphorus introduces occupied energy levels into the band gap which are close in energy to the lower edge of the CB, allowing facile promotion of electron into the CB (fig. 1.3 a). The addition of an electron deficient element like Boron to the

semiconductor lattice results in the formation of vacant energy levels close to the upper edge of the valence band, which allows facile promotion of electrons from the VB (fig. 1.3 b).

Doped semiconductors, referred to as extrinsic semiconductors, in which the majority charge carriers are electrons are referred as *n-type* semiconductors, while those in which holes are the dominant charge carriers are indicated as *p-type* semiconductors.

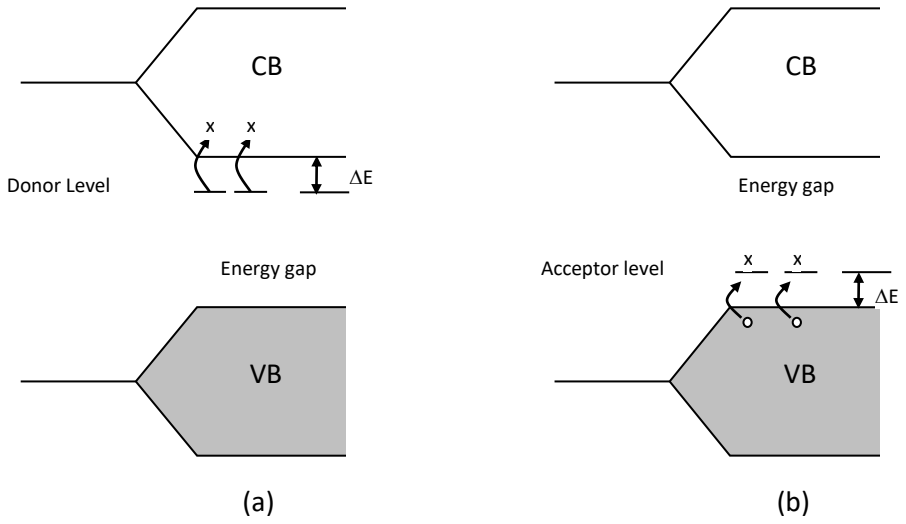

Figure 1.3: Energy levels diagram of an n-type semiconductor (a) and of a p-type semiconductor (b)

Another important concept in the discussion of solid state materials is the ***Fermi Level***. The *Fermi-Dirac distribution* is given by

$$f(E) = \frac{1}{1 + e^{\frac{(E - E_F)}{kT}}} \qquad \text{(Eq. 1.1)}$$

where $f(E)$ is the probability that a state of energy E is occupied, E_F is a parameter called the Fermi energy, k is the Boltzmann's constant and T is the absolute temperature.

It can be easily seen from equation1.1 that E_F is the energy for which $f(E) = \frac{1}{2}$, in other words it is a virtual energy level which has the 50% of probability to be occupied by electrons.

We have considered the system from a statistical point of view, while thermodynamically it can be demonstrated that the Fermi energy is nothing but the *electrochemical potential of electrons in a solid* (equation 1.2), since the definition of electrochemical potential $\bar{\mu}$ is expressed by equation 1.3:

$$\left(\frac{\partial S}{\partial N}\right)_{E,V} = \frac{E_F}{T} \qquad \text{(Eq. 1.2)}$$

$$\bar{\mu} = \left(\frac{\partial G}{\partial N}\right)_{p,T} = -T\left(\frac{\partial S}{\partial N}\right)_{E,V} \qquad \text{(Eq. 1.3)}$$

(where dN represents the electrons that are added to the energy state E). This result is physically understandable considering two systems in equilibrium: thermodynamically we expect them to exchange particles (electrons in this case) until their electrochemical potentials are equal. From the Fermi statistics point of view, transfer of particles from one system to another, which fills states of lower energy in one system while emptying higher lying filled states in the other, will proceed until the distributions over energy in the two systems match, i.e., the Fermi levels are equal.

For an intrinsic semiconductor the Fermi level lies at the midpoint of the band gap (fig.1.4 a). Doping changes the distribution of electrons within the solid and consequently changes the Fermi energy: for an n-type semiconductor the Fermi level lies just below the conduction band, whereas for a p-type it lies just above the valence band (fig. 1.4 b,c).

In addition, the Fermi energy of semiconductor electrodes varies with the applied potential, for example by applying a positive potential the Fermi level will be lowered, and vice versa.

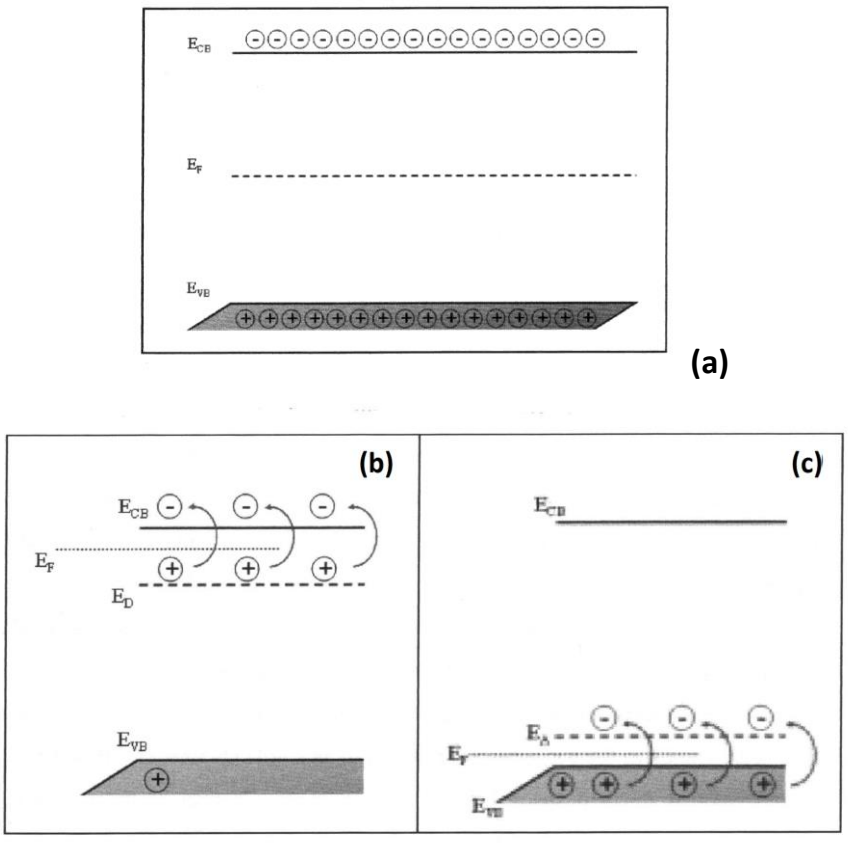

Figure 1.4 Fermi level in an intrinsic (a), in an n-type (b), and in a p-type semiconductor (c)

The ***interface between a semiconductor electrode and an electrolytic solution*** is also of great interest for our studies and needs to be described. As in the previous considerations, in order for the two phases to be in equilibrium, their electrochemical potentials must be the same.

As we just said, the electrochemical potential of electrons in a semiconductor is determined by its Fermi level, which can be expressed also by equation 1.4, whereas the electrochemical potential of electrons in solution is determined by the redox potential of the electrolyte, expressed by means of the Nernst equation (equation 1.5):

$$E_F = E_C + kTln\left(\frac{n_C}{N_C}\right) \qquad \text{(Eq. 1.4)}$$

where E_c is the energy at the conduction band edge, kT is the thermal energy, n_c is the density of conduction band electrons, and N_c is the effective density of conduction band states. With respect to vacuum, E_c is given by the electronic affinity E_A.

$$E_{redox} = E^0_{redox} - kTln\left(\frac{c_{red}}{c_{ox}}\right) \qquad \text{(Eq. 1.5)}$$

where E^0_{redox} is the formal redox potential, c_{ox} and c_{red} are the concentrations of the oxidized and reduced species of the one-electron redox system.

If the redox potential of the solution and the Fermi level of the semiconductor do not lie at the same energy, a movement of charge between the semiconductor and the solution is required in order to equilibrate the two phases. The excess of charge that is then located on the semiconductor, due to the relatively low density of charge carriers, extends into the electrode for a significant distance (10-100 nm) forming the so called *space charge region.*

For an n-type semiconductor at open circuit the Fermi level is typically higher than the redox potential of the electrolyte, hence electrons will be transferred from the electrode to the solution. Therefore there is a positive charge associated with the space charge region, which is reflected in an upward bending of the band edges (figure 1.5 a). Since the majority of charge carriers are removed from this region, this is also called *depletion layer*. On the contrary, a p-type semiconductor has a Fermi level that is generally lower than the redox potential of the electrolyte, so that an electron flow from the solution to the electrode occurs. This generates a negative space charge which causes a downward bending of the bands (figure 1.5 b). Since the majority of carriers (holes) are removed from this region the term depletion layer is used also in this case.

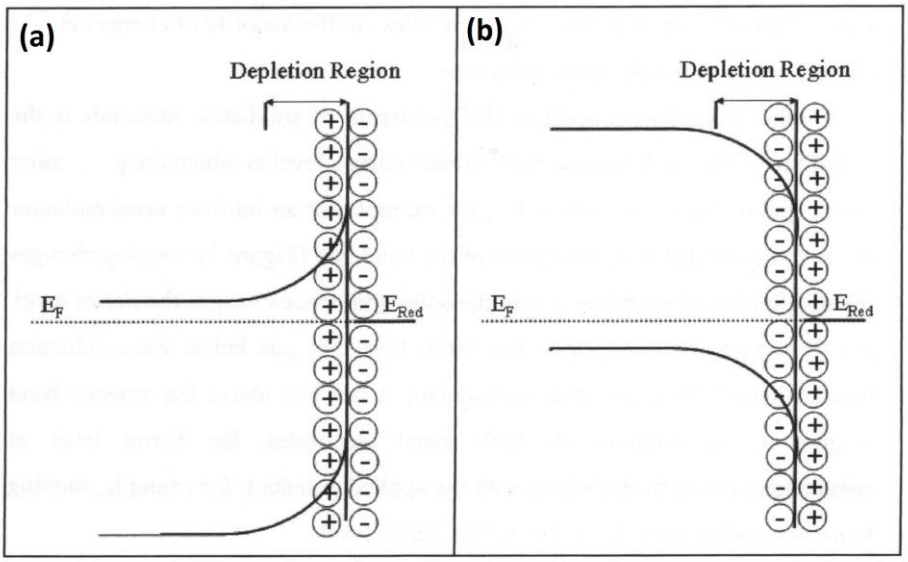

Figure 1.5 Band bending for an n-type semiconductor **(a)** and a p-type semiconductor **(b)** in equilibrium with an electrolyte.

The formation of a space charge region and the consequent *band bending* is an important feature in the photovoltaic effect description: if the semiconductor electrode is exposed to radiations of sufficient energy, electrons can be promoted to the conduction band. If this process occurs in the interior of the semiconductor, recombination of the promoted electron and the resulting hole typically occurs, together with the production of heat. However, if it occurs in the space charge region, the electrical field existing here will favour the spatial charge separation. For example, for an n-type semiconductor the band edges curve upwards, the photoproduced electron moves to the interior of the semiconductor, while the hole moves towards the interface. The hole is usually a high energy species able to extract an electron from a redox couple present in solution, that is, the n-type semiconductor electrode acts as a photoanode.

1.3 Photoelectrochemical solar cells

Silicon is the most popular solar cell material for commercial applications because of its great abundance and an energy band gap (1.1eV at room temperature) which allows to absorb large part of the visible and NIR solar radiation. Silicon solar cells are made of two layers of this semiconductor material, which are doped in order to polarize the junction (p-n junction). When a photon having enough energy is absorbed, an electron is excited from the valence into the conduction band, leaving a positively charged hole. This effect creates a potential difference across

the junction of the two differently doped silicon layers, which acts separating the carriers and inducing a current flow through the external circuit.

In contrast to these types of systems, where the semiconductor assumes both the tasks of light absorption and charge carrier transport, the two functions are separated in *dye sensitized solar cells* (DSSC). Light is absorbed by a sensitizer molecule anchored to the surface of a wide band-gap semiconductor. Charge separation takes place via photoinduced electron injection from the dye into the conduction band of the solid. Carriers are transported through the conduction band of the semiconductor to the charge collector, a transparent conductive oxide substrate (usually FTO, fluorine doped tin oxide), while the original state of the dye is restored by an electron donor species usually dissolved in an organic solvent.

The semiconductor oxide of choice in DSSC is ***titanium dioxide***, used in the anatase crystalline form. TiO_2 is a chemically inert, nontoxic and cheap material which has given the highest efficiencies in DSSC, although alternative metal oxide systems such as ZnO, SnO_2 and Nb_2O_5 also gave promising results. Ternary oxides, such as $SrTiO_3$ and Zn_2SnO_4, have been investigated as well, together with core-shell structures, such as ZnO-coated SnO_2 [4-8].

TiO_2 is an n-type semiconductor with a wide energy band-gap of 3.2 eV, that makes it transparent to visible light. However, due to its high affinity toward carboxylates, salicylates, phosphonates and boronates it can be sensitized by a large variety of dyes. Mesoporous films can be easily produced from nanocrystalline (10-20 nm particles diameter [9]) TiO_2 via a sol-gel type process involving an hydrothermal step, yielding a colloidal paste that can be deposited on the FTO substrates by screen-printing or doctor-blading [10]. Successively, the nanocrystalline oxide particles are sintered together by heating at high temperature (up to 500°C), improving electronic conduction through the film. The aspect of mesoporous TiO_2 electrodes is reported in the SEM picture of figure 1.6.

The so produced mesoporous TiO_2 electrodes can reach, depending on film thickness (usually ca. 10 μm), an effective surface area that is 100-1000 times larger than the apparent one, which makes them the perfect base for absorbing a monolayer of sensitizer. In fact high roughness is necessary to adsorb a high number of dye molecules, in order to have quantitative light harvesting thus producing a respectable photovoltaic effect, since only the first adsorbed dye monolayer is capable of photoinduced charge injection.

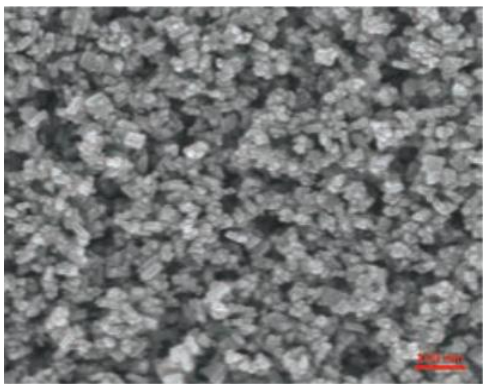

Figure 1.6 SEM image of the surface of a mesoporous TiO_2 film prepared from 18NR-T colloidal paste, after sintering (Aldrich)

1.4 Excited states and electron transfer theory

Theory of excited states and their deactivation pathways needs to be briefly described, since dye sensitized solar cells operation is based on a series of electron transfer processes that follow the sensitizer excitation by light.

The redox properties of excited states are noticeably different from those of the fundamental state. An electronically excited molecule can be considered a new chemical entity with new thermodynamic properties, as can be seen from the following diagram (figure 1.7).

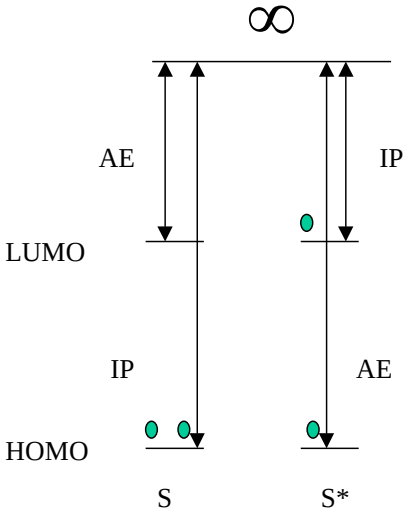

Figure 1.7 Electronic configuration of a sensitizer in the fundamental state (S) and in the excited state (S*)

The excited species possesses a lower ionization potential (IP) and a higher electronic affinity if compared with the ground state as a consequence it is both a better reducing and oxidizing agent. If entropy differences between the excited and the fundamental state are negligible it is possible to calculate, with good approximation, the excited states redox potentials, starting from the ground state redox potential and knowing the spectroscopic excitation energy, indicated as E^{00}, according to equations 1.6 and 1.7:

$$E\ (S^{+}/S^{*}) = E(S^{+}/S) - E^{00} \qquad \text{(Eq. 1.6)}$$

$$E\ (S^{*}/S^{-}) = E(S/\ S^{-}) + E^{00} \qquad \text{(Eq. 1.7)}$$

where $E(S^{+}/S)$ and $E(S/S^{-})$ are, respectively, the oxidation and reduction potentials of the ground state. E^{00} corresponds to the energy difference between the fundamental vibrational levels of the electronically excited state and the electronic ground state, and can be measured considering the first vibrational component of the emission spectrum, or roughly, in case of no observable emission, from the onset of the absorption spectrum.

A molecule in an electronically excited state *A can go through different decay processes to return to the ground state, that are schematized in figure 1.8. For example A* can undergo radiative or non-radiative unimolecular decay processes, involving, respectively, the emission of the excitation energy in the form of light radiation or the transformation of electronic energy into vibrational, which is dissipated in the form of heat. A* can eventually deactivate by chemical reactions. Otherwise, bimolecular processes can take place in the presence of a second molecule B, to whom the excitation can be transferred in the form of energy or electrons, following equations 1.8 and 1.9:

$$A^{*} + B \rightarrow A + B^{*} \qquad \text{energy transfer} \qquad \text{(Eq. 1.8)}$$

$$A^{*} + B \rightarrow A^{+} + B^{-} \qquad \text{electron transfer} \qquad \text{(Eq. 1.9)}$$

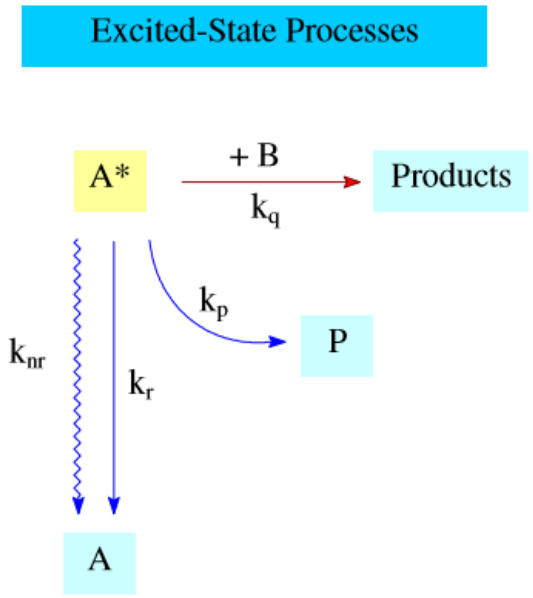

Figure 1.8. Deactivation pathways for the excited molecule A*, where the indicated kinetic constants are k_r and k_{nr} for the radiative and radiationless unimolecular decays, k_p for the unimolecular chemical deactivation, k_q for the excited state quenching by energy or electron transfer.

Equation 1.9 reports the case of oxidative quenching of the excited state of molecule A, while the reductive quenching, where A* is quenched by the acquisition of an electron from the donor B which is correspondingly oxidized, is also a possibility, based on the thermodynamics of the systems involved.

In the case of DSSC system, an oxidative quenching like that of equation 1.9 takes place, that is the photoexcited sensitizer is deactivated by the transfer of one electron to the TiO_2 conduction band. The rate constant of this electron transfer can be expressed by the Marcus equation [11]:

$$k_{et} = \nu_N \kappa_e \exp\left(\frac{-\Delta G^*}{kT}\right) \qquad \text{(eq 1.10)}$$

where k and T are the Boltzmann constant and the absolute temperature, respectively. ν_N is the *nuclear frequency factor*, and κ_e is the *transmission coefficient*, a parameter expressing the probability of the system to evolve from the reagent to the product configuration, once the crossing of the potential energy curves along the reaction coordinate has been reached.

ΔG^* is the *activation energy* for the process, and is expressed by equation 1.11:

$$\Delta G^* = \frac{(\Delta G^0 + \lambda)^2}{4\lambda} \qquad \text{(Eq. 1.11)}$$

where $\Delta G°$ is the *free energy variation* accompanying the process, while λ is the *reorganization energy* and represents the energy necessary to transform the nuclear configurations of the reactant

and of the solvent to those of the product state. λ is usually separated into inner λ_i and outer λ_o components: λ_i is due to the vibrational rearrangement consequent to the electron transfer, while λ_o is comprehensive of the repolarization of the solvation sphere.

Treating electron transfer reactions also from the quantum mechanical point of view, the rate constant is represented by the following equation [12]:

$$k_{et} = \frac{2\pi}{\hbar}\left(H_{if}^{el}\right)^2 FCWD \qquad \text{(Eq. 1.12)}$$

where FCWD is the Franck-Condon factor weighted for the Boltzmann population of the energy levels and H^{el}_{if} is the *electronic coupling factor* between the two electronic states involved in the process, which turns out to be very important in determining the electron transfer rate.

Therefore, based on the Marcus theory it is possible to distinguish three distinct kinetic regimes, which are represented by the potential energy curves diagram of figure 1.9:

1) a *normal region* when $-\lambda < \Delta G^0 < 0$, in which an increase in driving force is favorable to the electron transfer kinetics reducing the activation energy required for the process,
2) an *activationless* situation when $\Delta G^0 = -\lambda$, point at which the electron transfer rate is maximum and no activation energy is required,
3) an *inverted region* when $-\lambda < \Delta G^0$, where an increase in driving force decreases the electron transfer rate.

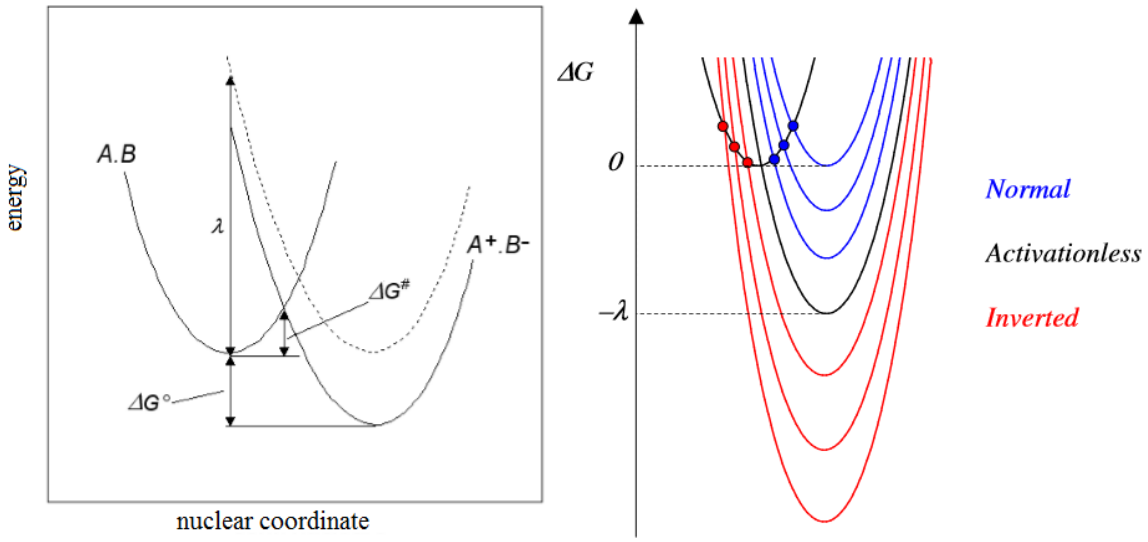

Figure 1.9 Left: potential energy curves for the case $\Delta G^0 \neq 0$, reporting the significant parameters of the Marcus equations. Right: potential energy curves relative to the electron transfer reactions taking place in the normal region (blue), activationless (black), in the inverted region (red).

1.5 Electron transfer dynamics in DSSC

As explained above, a DSSC is based on a nanocrystalline structured wide band gap semiconductor layer (TiO_2), sintered on a transparent conductive oxide (FTO) covered glass based electrode, through which the cell is illuminated. The TiO_2 film is covered by a monolayer of sensitizer molecules, and its mesoporous structure is filled with an electrolytic solution containing a redox couple (commonly I^-/I_3^- or $Co^{II/III}$) that acts as electron mediator. The basic operational principles of DSSC are depicted in figure 1.10, where the main electron transfer processes are indicated by numbers 1-7 [13]. Upon illumination electrons are injected from the photoexcited sensitizer into the semiconductor and move toward the FTO substrate, while the electronic mediator restores the oxidized dye in its reduced form and transports the positive charges to the counter electrode, where the regenerative cycle is completed by electron transfer to reduce the oxidized mediator.

The *open circuit voltage* generated under illumination, measured between the FTO and the counter electrode, corresponding to the difference between the electrochemical potential of the electron at the two contacts, is the difference between the Fermi level of the mesoporous TiO_2 layer and the redox potential of the electrolyte ($V_{OC} = E_F - E_{redox}$).

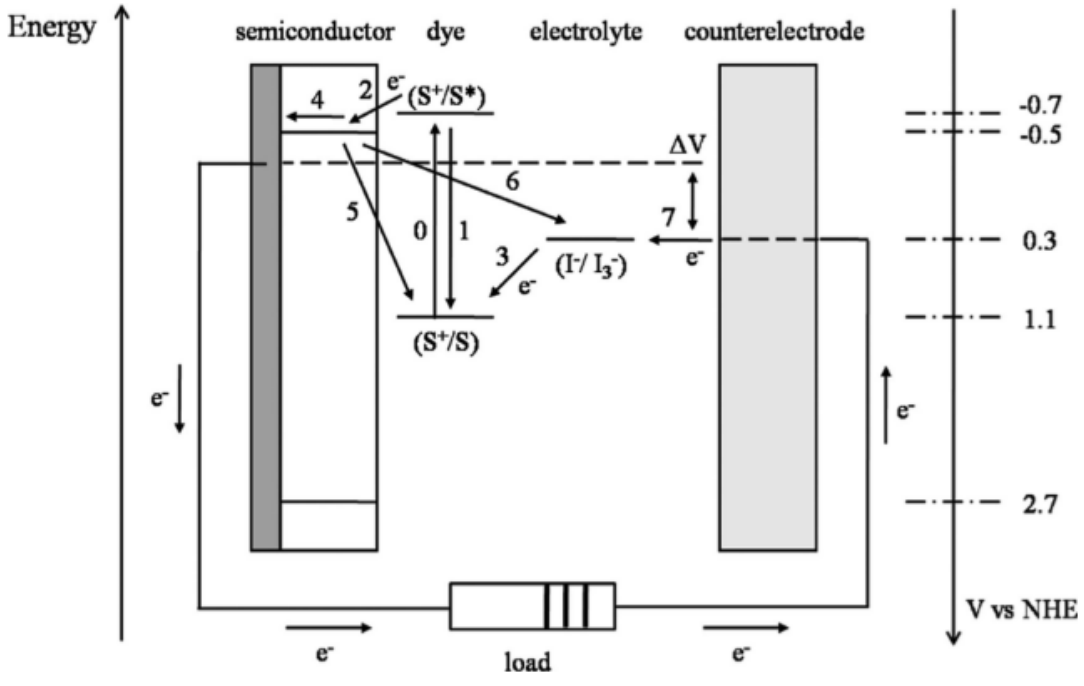

Figure 1.10 Energy levels diagram for DSSC. The primary electron transfer processes are indicated by numbers (1-7) [13]. The potentials for a DSSC based on a ruthenium dye on TiO_2 and the I^-/I_3^- redox couple are shown.

Besides the desired pathway of the electron transfer processes (2, 3, 4, and 7) described above, some loss reactions, 1, 5, and 6 can unfortunately take place. Reaction 1 is the direct deactivation of the excited dye, related to the dye's excited state lifetime. Recombination of injected electrons in TiO_2 with the oxidized dyes (5) was found to be much slower than dye regeneration by an efficient electron donor like iodide, at least at the concentrations commonly employed for this kind of cells [14,15]. Hence the main electron recombination pathway, really affecting DSSC performances, is that occurring between the injected electrons and the oxidized mediator (6), present in the electrolyte solution permeating the mesoporous photoanode surface. This electron transfer process can occur either at the interface between the nanocrystalline oxide and the electrolyte or at areas of the anodic contact (FTO) that are exposed to the electrolyte. In practice, the second route can be suppressed by using a compact TiO_2 blocking layer deposited on the anode, strategy which is necessary for DSSC employing one-electron redox systems such as cobalt complexes [16-18]. Summing up, for a successful operation of DSSC it is important that the electron transfer mediator reacts rapidly with the oxidized sensitizer, reducing it and preventing it from recombining with the photoinjected electrons. In addition the oxidized mediator must not recombine with the electrons in the TiO_2 conduction band, a process that if very efficient would heavily limit the power output of the cell.

All of these electron transfer processes taking place at the oxide/dye/electrolyte interface need to be understood and mastered to improve our ability to identify predictive materials and optimized structure/function relationships. To have an idea of their kinetics, the typical processes time constants under working conditions (1 sun), in a ruthenium dye sensitized solar cell with iodide/triiodide electrolyte, are summarized in figure 1.11 [13, 19].

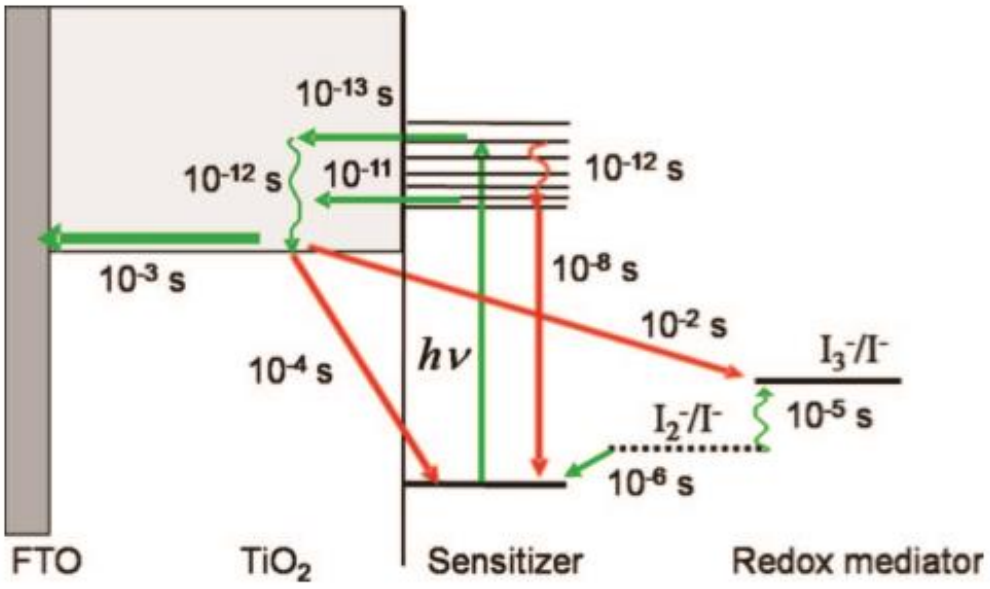

Figure 1.11. DSSC processes and their typical time constants under working conditions (1 sun) in a Ru dye-sensitized solar cell based on iodide/triiodide electrolyte [13]. Red arrows indicate the recombination processes.

- Reactions 1 and 2: electron injection and excited state decay

Although the detailed mechanism of the injection process is still under debate, it is generally accepted that an ultrafast electron transfer process, with time scales of the femtosecond order, takes place from the excited dye into the TiO_2 conduction band (reaction 2) [13, 20-23]. More specifically, it was found that besides a dominant ultrafast (<100 fs) injection there is a slower minor component occurring on a picosecond timescale, which has been ascribed to an injection mechanism proceeding via the lower (compared with the singlet) energy triplet excited state [24].

Hence a kinetic competition is possible between electron injection and excited state decay of the dye (reaction 1), given by the dye excited state lifetime, which for typical ruthenium complexes used in DSSC is of 20-60 ns.

The *quantum efficiency for injection*, which is influenced by the electronic properties of both the dye and the semiconductor, as well as by the distance between them, is defined as follows:

$$\Phi_{inj} = \frac{k_{inj}}{k_{inj}+k_1} \qquad \text{(Eq. 1.13)}$$

where k_{inj} and k_1 are the rate constants for electron injection and the excited dye decay (radiative and non-radiative), respectively. For high quantum yield of injection, k_{inj} should be about 100 times larger than k_1.

- Reaction 3: Regeneration of the Oxidized Dye

After photoinduced electron injection from the dye into the conduction band of TiO_2, the dye is in its oxidized state and must be reduced by an electron donor in the electrolyte [13]. The interception of the oxidized dye by the electron donor, usually I^-, occurs in the microsecond time domain.

The *regeneration efficiency,* Φ_{reg}, is defined as:

$$\Phi_{reg} = \frac{k_{reg}}{k_{reg}+k_{rec}} \qquad \text{(Eq. 1.14)}$$

where k_{reg} is the rate constant for regeneration, and k_{rec} is the (pseudo-) first-order rate constant for electron-oxidized dye recombination. Regeneration efficiency expresses the probability for the oxidized dye to be regenerated by the electron donor in the electrolyte, rather than by recombination with an electron in the TiO_2. For various sensitizers, very high Φ_{reg} values, approaching unity, were found with iodide (regeneration halftimes of 100 to 10 μs) [25-29], but fast regeneration kinetics were also found for one-electron redox mediators like cobalt complexes [30, 31]. Regeneration kinetics are affected by the specific electrolyte composition (ions, additives) and viscosity, which limits the donor species diffusion rate: in nonviscous electrolytes, the diffusion rate constant, k_{diff}, is in the range 10^9-10^{10} M^{-1} s^{-1}.

- Reaction 4: electron transport through the mesoporous oxide film

Electrons photoinjected in TiO_2 from the dye molecules have to cover a path in the mesoporous structure up to the FTO anodic contact. Charge transport is highly efficient (ms timescale) in such an electrolyte-infiltrated nanocrystalline layer. Electrons can percolate the interconnected nanocrystals by hopping from one crystallite to the next, while surrounded by the electrolyte ions compensating their charge.

Charge transport mechanisms are still under debate, but the gradient in electron concentration appears to be the main driving force for transport in the mesoporous TiO_2 film, that is, electron transport occurs by diffusion [32-34]. Another theory that is currently very accredited is that ascribing electron transport through TiO_2 to a *multiple trapping (MT) model* [35-39]. According to it, electrons are mostly trapped in localized states below the conduction band, from which they can escape by thermal activation, arriving to the CB. Electron traps can be located either in the bulk, at grain boundaries, or at the TiO_2/electrolyte interface. Their origin could correspond to trapping of electrons at defects in the bulk or surface regions of the mesoporous oxide, or to Coulombic trapping due to local field effects through interaction of electrons with the polar TiO_2 crystal or with cations of the electrolyte [40-42].

- Reactions 5 and 6: recombination of the photoinjected electrons with the oxidized dye molecules or the electrolyte species

The kinetics of the back-electron-transfer reaction from the conduction band to the oxidized sensitizer (reaction 5) follows a multiexponential time law and occurs on a microsecond to millisecond time scale [13]. This recombination mechanism, which has been studied in detail using nanosecond laser spectroscopy [25, 26, 28, 43-48], depends on the electrons concentration in the semiconductor, thus on the light intensity. Also application of a potential to the mesoporous TiO_2 electrode has a strong effect on the recombination rates [26, 28, 32, 49], since it induces an increase of electrons concentration in the TiO_2 particles which produces a considerable enhancement of the recombination kinetics. Under actual working conditions, electron concentration in the TiO_2 particles is rather high, and recombination kinetics may compete with the dye regeneration process.

Recombination of electrons in TiO_2 with acceptors in the electrolyte (reaction 6) is normally referred to as the *electron lifetime*. This parameter has been mainly studied in actual devices by measuring the transient response of the open circuit potential (V_{OC}) [50, 51], while the steady-state value of Voc also provides information on the recombination: under illumination at open circuit, the net rate of electron injection from dyes into the mesoporous oxide is balanced by the net rate of electron transfer to electron acceptors, assuming that only recombination of electrons with acceptors in the electrolyte occurs, as oxidized molecules are very rapidly regenerated. Electron

lifetime values observed with the I^-/I_3^- are very long (1-20 ms under one sun light intensity), if compared with other redox systems used in DSSC, explaining the success of this redox couple.

- Reaction 7: reduction of electron acceptors in the electrolyte at the counter electrode

Transport of the redox mediator between the electrodes is mainly driven by diffusion [13]. Typical redox electrolytes have a high conductivity and ionic strength so that the influence of the electric field and transport by migration is negligible. In viscous electrolytes, such as ionic liquids, diffusion coefficients would be too low to maintain a sufficiently large flux of redox components, which can limit the photocurrent of the device [52], giving rise to a high diffusion impedance, which acts as a series resistance in the solar cell. Fortunately, in the case of the iodide/triiodide electrolyte, an alternative type of charge transport occurs, called the Grotthus mechanism: when high mediator concentrations are used, charge transport takes place by the formation and cleavage of chemical bonds, which contributes significantly to charge transport in viscous electrolytes, such as ionic liquids [53].

At the counter electrode in standard DSSC, the oxidized mediator is restored in its reduced form, for example in the case of the iodide/triiodide redox couple:

$$I_3^- + 2e^- \rightarrow 3I^- \quad \text{(Eq. 1.15)}$$

The counter electrode must be catalytically active to ensure rapid reaction and low overpotential. Platinum is a suitable catalyst for the reaction in equation 1.15, as I_2 (I_3^-) dissociates to I atoms (I atoms and I^-) upon adsorption, enabling a rapid one-electron reduction.

The charge transfer reaction at the counter electrode leads to a series resistance in the cell, called charge transfer resistance R_{CT}. An overpotential η is needed to drive the I_3^- reduction at a certain current density J.

A poor counter electrode will affect the current-voltage (I-V) characteristics of the DSSC by lowering the fill factor. Ideally, R_{CT} should be $\leq 1\Omega/cm^2$ to avoid significant losses, and this has been reached using platinum based counter electrodes in iodide based devices, while other particular materials like nanocarbons and conductive polymers have revealed to be better with different electrolytes [54-57].

1.6 Molecular sensitizers

Since the TiO_2 band gap is too high (~3.2 eV) to absorb visible light, a sensitizing dye is anchored to the mesoporous semiconductor layer to capture sunlight. The light harvesting efficiency (LHE)

is a parameter which expresses the absorbing properties of the dye, determined from its absorption spectrum, and will be further discussed in chapter 2. LHE depends on the amount of dye attached to the semiconductor surface, its extinction coefficient and on the dye absorption width.

As one of the crucial parts in dye-sensitized solar cells, the photosensitizer should ideally fulfill some essential characteristics [13]:

1) An absorption spectrum covering the whole visible region and even the part of the near-infrared (NIR);

2) Appropriate anchoring groups (-COOH, $-H_2PO_3$, $-SO_3H$, etc.) to strongly bind the dye onto the semiconductor surface;

3) An excited state (S^+/S^*) that is higher in energy than the TiO_2 conduction band edge, so that an efficient electron transfer process between the excited dye and the semiconductor CB can take place;

4) An oxidized state level (S^+/S) which is more positive than the redox potential of electrolyte (I^-/I_3^-), to allow efficient dye regeneration;

5) Limited tendency to aggregate on the semiconductor surface, which can be achieved through the dye's molecular structure optimization, or by adding coadsorbers that prevent aggregation.

6) Photochemical, thermal and electrochemical stability are also required.

Based on these conditions, many different photosensitizers including metal complexes [58, 59], porphyrins [60], and metal-free organic dyes [61, 62, 63] have been designed and applied to DSSC.

The first reported efficient dyes, in terms of conversion efficiency and long-term stability, were **polypyridyl ruthenium complexes** [64, 65] based on the structure of N3 (Fig. 1.12), [66] in which the role of the carboxylic acid groups is to bind strongly to the semiconductor surface, facilitating electron injection, while the –NCS groups finely tune the oxidation potential of the complex in order to favour the regeneration by the redox shuttle and to increase the visible light absorption. Ancillary ligands like bipyridines or terpyridines, were also amply employed in the ruthenium dyes design, to tune their photophysical and electrochemical properties and thus improve photovoltaic performances, in particular by changing their substituents (alkyl, aryl, heterocycle, etc.). Optimized devices based on the N719 [67], Z907[68-70], and N749 [71] sensitizers reached over 11% efficiency .

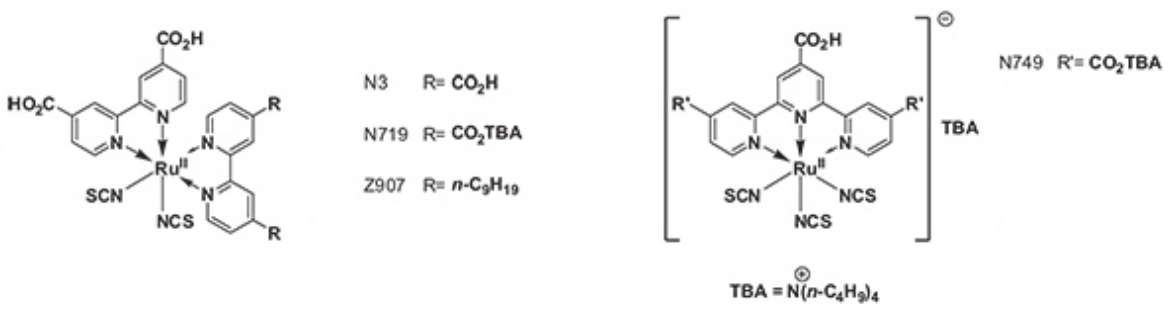

Figure 1.12 Structure of the most common polypyridyl ruthenium based sensitizers

There are multiple examples reported of dyes based on other transition metal complexes [13], in particular Osmium (II) complexes were found to be promising due to their prominent absorption characteristics, however slower dye regeneration by iodide was identified as the reason for lower photocurrent, with respect to ruthenium complexes [72, 73]. These latter can be thus considered as the best performing among the metal complexes thanks to their superior properties: a broad absorption spectrum, suitable excited and ground state energy levels, relatively long excited-state lifetime, and good (electro)chemical stability. One of their drawbacks is, however, the limited absorption in the near-infrared region of the solar spectrum, together with a low extinction coefficient, problems that were overcome by the introduction of porphirynic and organic dyes. **Porphyrins** exhibit intense spectral response bands in the near-IR region and possess good chemical, photochemical, and thermal stability [74]. Indeed, owing to appropriate LUMO and HOMO energy levels and very strong absorption of the Soret band in the 400-450 nm region, as well as the Q-band in the 500-700 nm region, porphyrin derivatives were successfully suited as panchromatic photosensitizers for DSSC showing efficient photoinduced electron injection into the conduction band of TiO_2 [75, 76]. The electrochemical [77, 78] and light-harvesting properties [79, 80] of such molecules are also easily tunable acting, with specific chemical functionalizations, either on four meso or eight β-pyrrolic positions. Some representative examples of these photosensitizers, which allowed to reach record efficiencies up to 13% [81-83], are collected in figure 1.13.

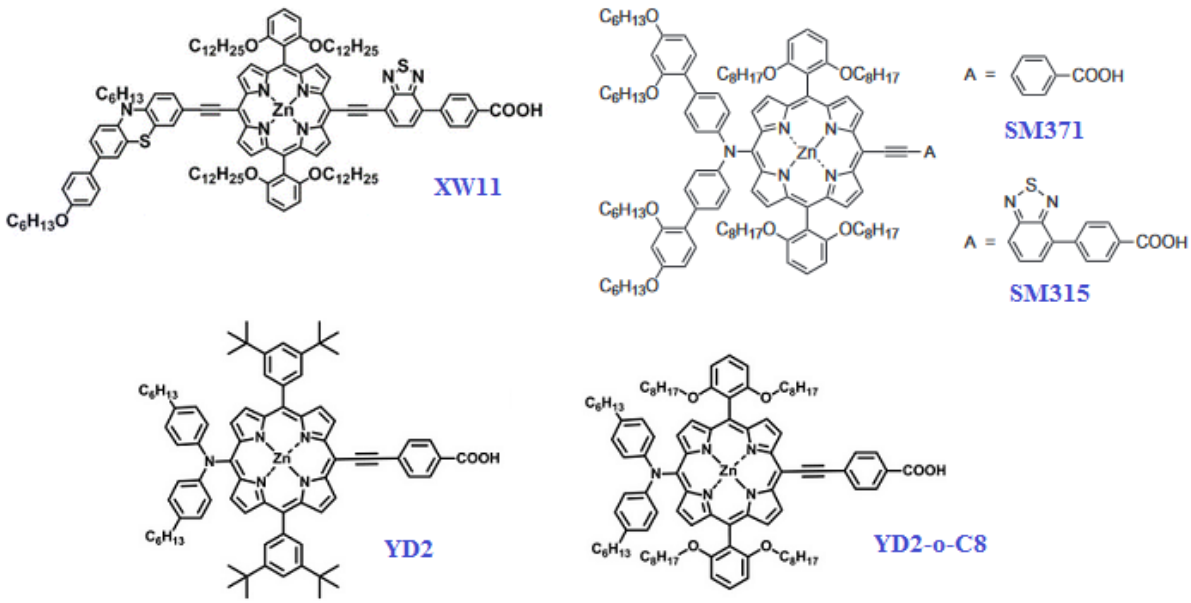

Figure 1.13: Structures of some known phorphyrin dyes which allowed to obtain record efficiencies [81-83]

On the other hand, **metal-free organic dyes,** as an alternative to the noble Ru complexes sensitizers, exhibit considerably higher molar extinction coefficients (31000 $M^{-1}cm^{-1}$ at 500 nm for D35[61], with respect to the 14000, at a 396 nm absorbance maximum, for N3[66]) and can be

designed with more freedom, since they can be in different forms and they are generally characterized by a donor–π-bridge–acceptor (D-π-A) structure, with whom it is easy to design new dye structures, extend the absorption spectra, adjust the HOMO and LUMO levels and complete the intramolecular charge separation. When a dye of this type absorbs light, intramolecular charge transfer occurs from subunit A to D through the π-bridge, then the excited dye injects the electron into the conduction band of the semiconductor via the electron acceptor group. To date, hundreds of n-type organic dyes have been adopted to act as sensitizers for DSSC and have obtained impressive efficiencies. The most employed organic dyes are collected in figure 1.14.

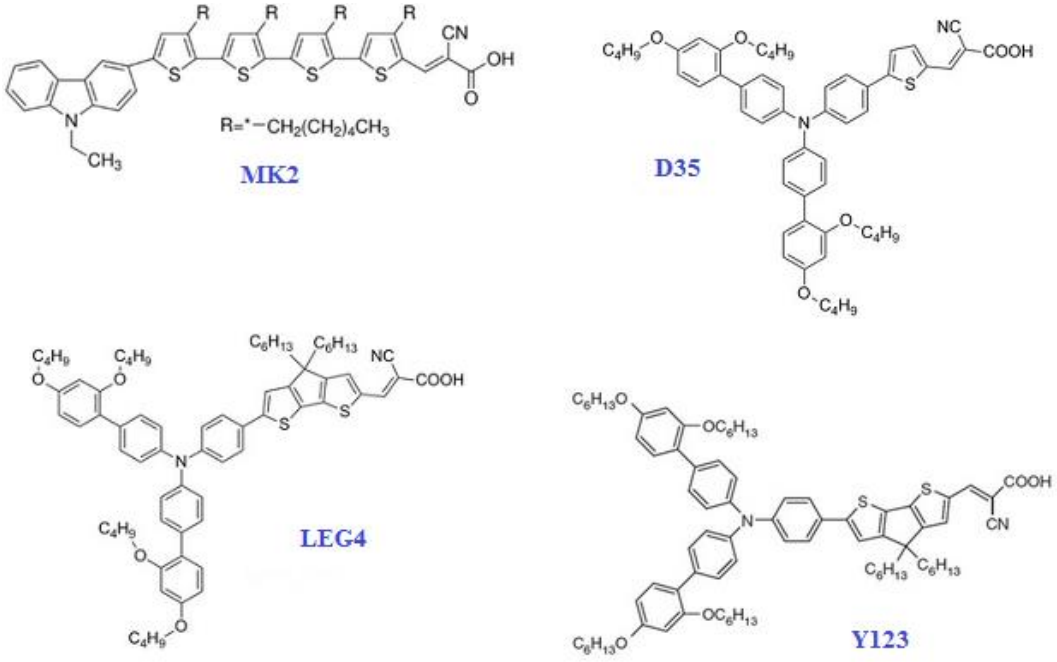

Figure 1.14: Structures of some metal-free organic dyes which allow to obtain high efficiencies [61-63, 84]

1.7 Counter electrode materials

Platinum is recognized as a benchmark material in the field of cathodic catalysts, due to its excellent conductivity and high catalytic activity. Pt based counter electrodes for dye-sensitized solar cells can be rather easily prepared by deposition of a thin catalytic layer of the noble metal onto a conducting FTO glass substrate, which is a very poor cathodic material itself, having a very high charge transfer resistance, more than 106 Ω cm^2, in a standard iodide/ triiodide electrolyte [85]. Spray pyrolysis technique allows to prepare transparent electrodes with charge transfer resistances of less than 1 Ω cm^2, while other methods such as electrodeposition [86] and vapor-deposition [87] on TCO substrates were found to dissolve in iodide/triiodide electrolytes.

Despite demonstrating to be the best cathodic material in DSSC based on the I^-/I_3^- redox mediator, Pt has obvious drawbacks like the high cost and limited availability, which restricts its application to the mass production of DSSC. Moreover, conventional Pt cathodes have shown poor catalytic activity towards iodine-free redox couples like the $Co^{II/III}$ based electrolytes, resulting in poor fill factors and relatively moderate power conversion efficiencies. Other interesting materials emerged as an alternative in this sense, mainly including inorganic transition metal compounds [88-91], organic conductive polymers [53-55] and carbonaceous materials (particularly carbon nanotubes [56] and graphene [57]).

In particular **PEDOT** (poly-3,4-ethylenedioxythiophene) is an intrinsically conductive polymer displaying high conductivity (up to 300 S cm^{-1}) and stability, which exhibits good catalytic properties in association with Co(II)/(III) redox couples, producing enhanced photocurrents with respect to Pt or Au counter electrodes, because of a decreased mass transport resistance arising from a larger electroactive area of the polymer-based material [92, 93]. In contrast, other conducting polymers (polyaniline, polypyrrole) were much less suited, especially in terms of chemical and electrochemical stability [94].

Carbon materials have been investigated, in particular in the last years much attention has been recently paid to nanocarbons like graphene and nanotubes which can be easily deposited on FTO coated glass by spray-coating, providing transparent electrodes whose performances are comparable to those obtained with platinum and PEDOT. Nanocarbons based counter electrodes are characterized by good electronic conductivity as well as high-surface area for increased catalytic effect [95, 96].

1.8 Electronic mediators

The role of electrolytes in most electrochemical devices like capacitors, electrolytic cells, fuel cells, or batteries is to serve as the medium for the transportation of charge carriers, which are in the form of ions, between a pair of electrodes [97, 98]. In DSSC the electrolyte is indeed responsible for the inner charge transport between the counter electrode, where it captures the electrons arriving through the external circuit, and the photosensitized anode, where it acts regenerating the oxidized dye. The electrolytes used in DSSC can be broadly classified into 3 categories: liquid electrolytes,[99, 100] quasi-solid electrolytes [101, 102], and solid-state conductors [103, 104]. In this thesis work we have been treating liquid electrolytes, in which case the chosen redox couple is dissolved in an organic solvent. Anyhow the electrolyte, its transport kinetics and the way it interacts with the electrode interfaces, plays a central role in determining both the light-to-electric conversion efficiency and long-term stability of the device [105, 106]. The efficiency of a DSSC device is determined by its photocurrent density (J_{SC}), photovoltage (V_{OC}), and fill factor (FF), as will be

explained in chapter 2. J_{SC} can be affected by the transport of the redox couple components in the electrolyte; the FF can be affected by the diffusion of charge carriers in the electrolyte and by the charge transfer resistance on the electrolyte/electrode interface. Finally the V_{OC} is significantly affected by the redox potential of the electrolyte.

As a consequence, a good electrolyte should be able to rapidly reduce the oxidized dye back to its ground state, after electron injection into the conduction band of TiO_2, guaranteeing fast diffusion of charge carriers (higher conductivity) and producing good interfacial contact with the mesoporous semiconductor layer and the counter electrode, limiting at the same time solvent leakage. The solvent used must have long-term stability, including chemical, thermal, optical, electrochemical characteristics, and not cause desorption or degradation of the sensitized dye. Finally, the electrolyte should not exhibit a significant absorption in the range of visible light.

Since their discovery in 1991 [107, 108], the redox mediator at the base of the DSSC operation has been the **iodide/triiodide couple (I^-/I_3^-),** displaying fast regeneration and slow recombination kinetics.

For typical I^-/I_3^- redox electrolytes, dye regeneration can be expressed as follows [97]:

$$D^+ + I^- \xrightarrow{dye\ regeneration} D + I_3^-$$

In fact, the reaction contains a series of successive reactions at the TiO_2/electrolyte interface [109-113]:

$$D^+ + I^- \rightarrow [D\cdots I] \xrightarrow{I^-} D^+ + I_2^{-\bullet} \xrightarrow{I_2^{-\bullet}} D + I_3^- + I^-$$

$$D^+ + I_2^{-\bullet} \rightarrow [D\cdots I_2] \xrightarrow{I^-} D + I_3^-$$

The regenerative cycle is completed by the conversion of I_3^- to I^- ions at the counter electrode.

However, the iodine-based redox shuttle possesses a number of unfavorable characteristics [114]. First, its redox potential (+0.35 V vs NHE) is not ideally positioned for many sensitizers [115-117], leading to a significant loss in the maximum open circuit potential (Voc) and a corresponding loss in the maximum overall power conversion efficiency (PCE) of the cells. Furthermore, I_3^- and other polyiodide intermediates absorb a good portion of visible light (300–450 nm), thus leading to lower short-circuit photocurrent density (Jsc) values, due to the subtraction of photons to the photoactive dye molecules. When upscaling of DSSC is conceived of, it must also be considered that the iodine-based redox couple corrodes silver lines used to collect the electrons in large-scale modules.

These limitations led to the search for alternative redox couples. In particular, a line of research was focused on the study of transition metals systems, such as ferrocene [118, 119], copper [120-122] and cobalt complexes [123, 124].

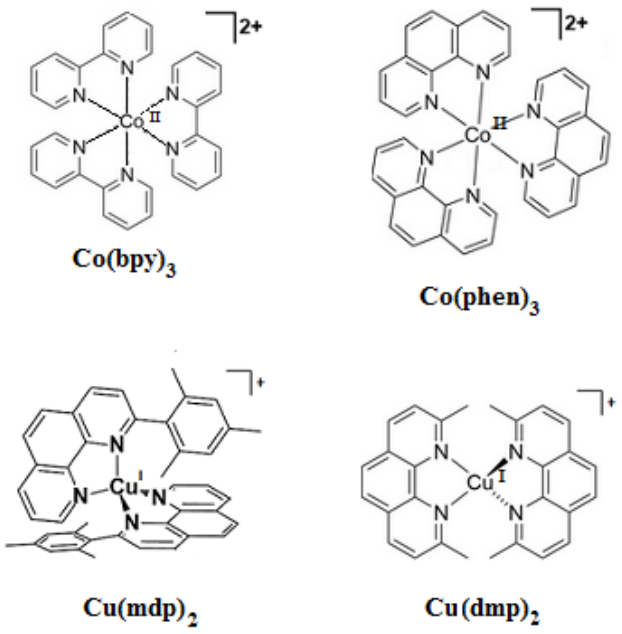

Figure 1.15: Structures of some cobalt and copper redox couples successfully used as electronic mediators alternative to iodide/triiodide [121-123] (bpy = 2,2'-bipirydine; phen = 1,10-phenanthroline; mdp= 2-mesityl-4,7-dimethyl-1,10-phenanthroline ; dmp = 2,9-dimethyl-1,10-phenantroline)

Among the different iodine-free electrolytes proposed in the last two decades, **polypyridine cobalt(II)/(III) complexes** have revealed to be the most promising alternative for several reasons: they are generally less colored than iodine based solutions (molar extinction coefficients $\varepsilon \sim 100\ M^{-1}\ cm^{-1}$), and therefore compete less with the dye in visible light absorption; they are less corrosive to metal cathodes and generally show more positive redox potentials than I^-/I_3^-, therefore increasing the potentially obtainable phtovoltage. Moreover cobalt complexes have synthetically-tunable redox potentials [123, 125-127], which can be adjusted as needed, in combination with specific dyes and semiconductors, by playing on the withdrawing properties of the ligands coordinated to the central metal.

The $Co^{2+/3+}$ one-electron redox system displays good electron transfer kinetics, but this also includes back-donation in recombination reactions. To solve the problem of *high recombination rates* from the TCO and semiconductor surface, the importance of a blocking underlayer has to be highlighted [128, 129]. Another concern about cobalt based electrolyte consists in *mass transport limitations*, due to the slow diffusion of the species between the electrodes and in especially inside the pores of dye-sensitized TiO_2. This effect is evident in particular in the case of highly sterically hindered complexes, like $Co(dtb)_3^{2+/3+}$ (dtb = 4,4′-di-tert-butyl-2,2′-bipyridine) [130, 131], while is less important for the model complex $Co(bpy)_3^{2+/3+}$ (bpy = 2,2′-bipyridine).

Redox mediators based on cobalt complexes allowed dye-sensitized solar cells to achieve record efficiencies exceeding 14% [132], which however haven't been certified. Unfortunately, these electrolytes demonstrate lower long-term stability trends if compared to the traditional

iodide/triiodide redox couple. In view of the large-scale commercialization of cobalt-based DSSC, the scientific community has recently proposed various approaches and materials to increase the stability of these devices, which comprise gelling agents, crosslinked polymeric matrices and mixtures of solvents. Also, playing on the denticity of the ligands coordinated to the cobalt center can help to increase their stability thanks to a reduced reorganization energy factor [133].

The cobalt complexes solubility in common organic solvents employed in liquid-state DSSC, like acetonitrile, is lower if compared to that of the iodide/triiodide case. The employment of high-boiling solvents like sulfolane, propylene carbonate and various nitriles can help the solubility decreasing at the same time the solvent volatility, but attention must be paid to the effect of an increased viscosity on the electrolyte diffusion rates.

Finally additives like **lithium** salts and **4-tert-butylpyridine (TBP)** have to be mentioned, since they were proven to be important for achieving high cell performance, both in the cases of iodine and cobalt based electrolytes. Indeed, Li^+ ions are expected to cause a lowering of the TiO_2 conduction band energy level, thus leading to an improvement in electron injection efficiency and electron lifetime [134]; on the contrary, TBP typically gives a negative shift of the TiO_2 conduction band, and reduced interfacial recombination losses are observed, resulting in a relatively higher Voc [135]

References

(1) ACS Chemical and engeneering news, **2016**, Volume 94, Issue 18, pp. 30-35

(2) "Dye sensitized solar cell market analysis by application and segment forecasts to 2022", **2016**, http://www.grandviewresearch.com/industry-analysis/dye-sensitized-solar-cell-market

(3) Hannay, N. B. "Semiconductors"; Reinhold Publishing Corporation: New York, **1959**.

(4) Tennakone, K.; Kumara, G..; Kottegoda, I.; Perera, V., *Chem.Comm.* **1999**,15, 15.

(5) Sayama, K.; Suguhara, H.; Arakawa, H. *Chem.Mater.* **1998**, 10, 3825.

(6) Hamann, T. W.; Jensen, R. A.; Martinson, A. B. F.; Van Ryswyk, H.; Hupp, J. T. *Energy EnViron. Sci.* **2008**, 1, 66.

(7) Pagliaro, M.; Palmisano, G.; Ciriminna, R.; Loddo, V. *Energy EnViron. Sci*. **2009**, 2, 838.

(8) Jose, R.; Thavasi, V.; Ramakrishna, S. *J. Am.Chem. Soc*. **2009**, 92, 289.

(9) Barbè, C. J.; Arendse, F.; Comte, P.; Jirousek, M.; Lenzmann, F.; Shklover, V.; Graetzel, M. *J.Am.Chem.Soc* **1997**, 80, 3157.

(10) Heglein, A. *Chem.Rev.* **1989**, 89, 1861.

(11) Bolton, J. R.; Archer, M. "Basic electron transfer theory"; *Advances in Chemistry*, **1991**, vol 228, chapter 2, pp 7-23

(12) Bignozzi, C. A.; Schoonover, J. R.; Scandola, F. "Molecular Level Artificial Photosynthetic Materials", **1997**, John Wiley & Sons: New York.

(13) Hagfeldt A., Boschloo G., Sun L., Kloo L., Pettersson H., *Chem. Rev*. **2010**, 110, 6595–6663

(14) Kuciauskas, D.; Freund, M. S.; Gray, H. B.; Winkler, J. R.; Lewis, N. S. J. *J.Phys.Chem.B.* **2001**, 105, 392-403.

(15) Kelly, C. A.; Farzad, F.; Thompson, D. W.; Stipkala, J. M.; Meyer, G. J. *Langmuir* **1999**, 15, 7047-7052.

(16) Sapp, S. A.; Elliott, C. M.; Contado, C.; Caramori, S.; Bignozzi, C. A. *J. Am. Chem. Soc.* **2002**, 124, 11215.

(17) Nusbaumer, H.; Zakeeruddin, S. M.; Moser, J. E.; Grätzel, M. *Chem.Eur. J.* **2003**, 9, 3756.

(18) Cameron, P. J.; Peter, L. M.; Zakeeruddin, S. M.; Grätzel, M. *Coord.Chem. Rev*. **2004**, 248, 1447.

(19) Ardo, S.; Meyer, G. J. *Chem. Soc. Rev.* **2009**, 38, 115.

(20) Asbury, J. B.; Ellingson, R. J.; Ghosh, H. N.; Ferrere, S.; Nozik, A. J.; Lian, T. Q. *J. Phys. Chem. B* **1999,** 103, 3110.

(21) Ramakrishna, G.; Jose, D. A.; Kumar, D. K.; Das, A.; Palit, D. K.; Ghosh, H. N. *J. Phys. Chem. B* **2005**, 109, 15445.

(22) Kuang, D.; Ito, S.; Wenger, B.; Klein, C.; Moser, J.-E.; HumphryBaker, R.; Zakeeruddin, S. M.; Gra¨tzel, M. *J. Am. Chem. Soc.* **2006,** 128, 4146.

(23) Benko, G.; Kallioinen, J.; Korppi-Tommola, J. E. I.; Yartsev, A. P.; Sundstrom, V. *J. Am. Chem. Soc.* **2002**, 124, 489.

(24) M. Borgwardt, M. Wilke, T. Kampen, S. Mähl, M. Xiao, L. Spiccia, K. M. Lange, I. Y. Kiyan & E.F. Aziz, *Nature Scientific Reports* 6, **2016,** Article number: 24422

(25) Clifford, J. N.; Palomares, E.; Nazeeruddin, M. K.; Gra¨tzel, M.; Durrant, J. R. *J. Phys. Chem. C* **2007,** 111, 6561.

(26) Haque, S. A.; Tachibana, Y.; Klug, D. R.; Durrant, J. R. *J. Phys. Chem. B* **1998**, 102, 1745.

(27) Pelet, S.; Moser, J.-E.; Gra¨tzel, M. *J. Phys. Chem. B* **2000**, 104, 1791.

(28) Kuciauskas, D.; Freund, M. S.; Gray, H. B.; Winkler, J. R.; Lewis, N. S. *J. Phys. Chem. B* **2001**, 105, 392.

(29) Mori, S. N.; Kubo, W.; Kanzaki, T.; Masaki, N.; Wada, Y.; Yanagida, S. *J. Phys. Chem. C* **2007**, 111, 3522.

(30) Nusbaumer, H.; Moser, J.E.; Zakeeruddin, S. M.; Nazeeruddin, M. K.; Grätzel, M., *J. Phys. Chem. B* **2001**, 105, 10461.

(31) Nusbaumer, H.; Zakeeruddin, S. M.; Moser, J.-E.; Gra¨tzel, M. *Chem.sEur. J.* **2003**, 9, 3756.

(32) O'Regan, B.; Moser, J.; Anderson, M.; Gra¨tzel, M. *J. Phys. Chem.* **1990**, 94, 8720.

(33) Sodergren,S.; Hagfeldt,A.; Olsson,J.; Lindquist,S.E. *J. Phys. Chem.* **1994,** 98, 5552.

(34) Solbrand, A.; Lindsträm, H.; Rensmo, H.; Hagfeldt, A.; Lindquist, S. E.; Sodergren, S. *J. Phys. Chem. B* **1997,** 101, 2514.

(35) Dloczik, L.; Ileperuma, O.; Lauermann, I.; Peter, L. M.; Ponomarev, E. A.; Redmond, G.; Shaw, N. J.; Uhlendorf, I. *J. Phys. Chem. B* **1997**, 101, 10281.

(36) Van de Lagemaat, J.; Frank, A. J. *J. Phys. Chem. B* **2000,** 104, 4292.

(37) Bisquert, J.; Vikhrenko, V. S. *J. Phys. Chem. B* **2004,** 108, 2313.

(38) Fisher, A. C.; Peter, L. M.; Ponomarev, E. A.; Walker, A. B.; Wijayantha, K. G. U. *J. Phys. Chem. B* **2000,** 104, 949.

(39) Bisquert, J. *J. Phys. Chem. B* **2004**, 108, 2323.

(40) Westermark, K.; Henningsson, A.; Rensmo, H.; So¨dergren, S.; Siegbahn, H.; Hagfeldt, A. *Chem. Phys. Lett.* **2002**, 285, 157.

(41) Peter, L. M. *Acc. Chem. Res*. **2009**, 42, 1839.

(42) Hendry, E.; Koeberg, M.; O'Regan, B. C.; Bonn, M. *Nano Lett.* **2006**, 6, 755.

(43) Kelly, C. A.; Farzad, F.; Thompson, D. W.; Stipkala, J. M.; Meyer, G. J. *Langmuir* **1999**, 15, 7047.

(44) Hasselmann, G. M.; Meyer, G. J. *J. Phys. Chem. B* **1999**, 103, 7671.

(45) Clifford, J. N.; Palomares, E.; Nazeeruddin, M. K.; Gra¨tzel, M.; Nelson, J.; Li, X.; Long, N. J.; Durrant, J. R. *J. Am. Chem. Soc.* **2004**, 126, 5225.

(46) Haque, S. A.; Tachibana, Y.; Willis, R. L.; Moser, J. E.; Gra¨tzel, M.; David, R. Klug; Durrant, J. R. *J. Phys. Chem. B* **2000**, 104, 538.

(47) Tachibana, Y.; Moser, J. E.; Gra¨tzel, M.; Klug, D. R.; Durrant, J. R. *J. Phys. Chem*. **1996**, 100, 20056.

(48) Tachibana, Y.; Haque, S. A.; Mercer, I. P.; Durrant, J. R.; Klug, D. R. *J. Phys. Chem. B* **2000**, 104, 1198.

(49) Yan, S. G.; Hupp, J. T. *J. Phys. Chem.* **1996**, 100, 6867.

(50) Schlichthorl, G.; Huang, S. Y.; Sprague, J.; Frank, A. J. *J. Phys. Chem. B* **1997**, 101, 8139.

(51) Zaban, A.; Greenshtein, M.; Bisquert, J. *ChemPhysChem* **2003**, 4, 859.

(52) Papageorgiou, N.; Athanassov, Y.; Armand, M.; Bonhote, P.; Pettersson, H.; Azam, A.; Gra¨tzel, M. J. *Electrochem. Soc.* **1996**, 143, 3099.

(53) Matsui H., Okada K., Kitamura T., Tanabe N., Sol. *Energy Mater.Sol.Cells* **2009**, 93, 1110-1115

(54) Wenger, B.; Grätzel, M.; Moser, J. E. *J. Am. Chem. Soc.* **2005**, 127, 12150.

(55) Tachibana, Y.; Haque, S. A.; Mercer, I. P.; Moser, J. E.; Klug, D. R.; Durrant, J. R. *J. Phys. Chem. B* **2001**, 105, 7424.

(56) Jose, R.; Thavasi, V.; Ramakrishna, S. *J. Am. Chem. Soc.* **2009**, 92, 289.

(57) Ito, S.; Miura, H.; Uchida, S.; Takata, M.; Sumioka, K.; Liska, P.; Comte, P.; Pechy, P.; Graetzel, M. *Chem. Commun.* **2008**, 5194.

(58) Bignozzi, C. A.; Schoonover, J. R.; Scandola, F. Progr.*Inorg.Chem* **1997**, 44, 345.

(59) Hafgeldt, A.; Graetzel, M. *Chem.Rev.* **1995**, 95, 49.

(60) Kay, A.; Graetzel, M. *J.Phys.Chem.* **1993**, 97, 6277.

(61) S. M. Feldt, E. A. Gibson, E. Gabrielsson, L. Sun, G. Boschloo, A. Hagfedlt, *J. Am. Chem. Soc.,* **2010,** 132, 16714.

(62) H.N. Tsao , C. Yi , T. Moehl, J. H. Yum, S.M. Zakeeruddin, M.K. Nazeeruddin, M. Graetzel , *ChemSusChem* **2011,** 4, 591.

(63) Kashif, M. K.; Axelson, J. C.; Duffy, N. W.; Forsyth, C. M.; Chang, C. J.; Long, J. R.; Spiccia, L.; Bach, U. , *J. Am. Chem. Soc.* **2012**, 134 16646.

(64) Y. Qin and Q. Peng, *International Journal of Photoenergy*, **2012**, vol. 2012, Article ID 291579

(65) W.Y. Wong, "Organometallics and Related Molecules for Energy Conversion" *Springer* **2015**, Chapt.4

(66) M. K. Nazeeruddin, A. Kay, 1. Rodicio, R. Humpbry-Baker,E. Miiller, P. Liska, N. Vlachopoulos, and M. Gratzel, *J.Am. Chem. Soc*., Vol. 115,No. 14, **1993**

(67) Nazeeruddin, M. K.; Zakeeruddin, S. M.; Humphry-Baker, R.; Jirousek, M.; Liska, P.; Vlachopoulos, N.; Shklover, V.; Fischer, C. H.; Gra¨tzel, M. *Inorg. Chem***. 1999,** 38, 6298.

(68) Wang, P.; Zakeeruddin, S. M.; Exnar, I.; Gra¨tzel, M. *Chem. Commun*. **2002**, 2972.

(69) Wang, P.; Zakeeruddin, S. M.; Humphry-baker, R.; Moser, J. E.; Gra¨tzel, M. *AdV. Mater.* (Weinheim, Ger**.) 2003**, 15, 2101.

(70) Wang, P.; Zakeeruddin, S. M.; Moser, J. E.; Nazeeruddin, M. K.; Sekiguchi, T.; Gra¨tzel, M. *Nat. Mater.* **2003**, 2, 498.

(71) Nazeeruddin, M. K.; Pechy, P.; Gra¨tzel, M. *Chem. Commun.* **1997**, 1705.

(72) Altobello, S.; Argazzi, R.; Caramori, S.; Contado, C.; Da Fre, S.; Rubino, P.; Chone, C.; Larramona, G.; Bignozzi, C. A. *J. Am. Chem. Soc*. **2005**, 127, 15342.

(73) Alebbi, M.; Bignozzi, C. A.; Heimer, T. A.; Hasselmann, G. M.; Meyer, G. J. *J. Phys. Chem. B* **1998**, 102, 7577.

(74) L.L.Li and E.W.G. Diau *Chem. Soc. Rev.,* **2013**, 42,291—304

(75) Lammi, R. K.; Wagner, R. W.; Ambroise, A.; Diers, J. R.; Bocian, D. F.; Holten, D.; Lindsey, J. S. *J. Phys. Chem. B* **2001**, 105, 5341.

(76) Cherian, S.; Wamser, C. C. *J. Phys. Chem. B* **2000**, 104, 3624.

(77) Mussini, P. R.; Orbelli Biroli, A.; Tessore, F.; Pizzotti, M.; Biaggi, C.; Di Carlo, G.; Lobello, M. G.; De Angelis, F. *Electrochim. Acta* **2012**, 85, 509−523.

(78) Lo, C.-F.; Hsu, S.-J.; Wang, C.-L.; Cheng, Y.-H.; Lu, H.-P.; Diau, E. W.-G.; Lin, C.-Y.. *J. Phys. Chem. C* **2010**, 114, 12018− 12023.

(79) Li, L.-L.; Diau, E. W.-G., *Chem. Soc. Rev.* 2013, 42, 291−304. (80) Bessho, T.; Zakeeruddin, S. M.; Yeh, C.-Y.; Diau, E. W.-G.; Grätzel, M. *Angew. Chem., Int. Ed.* **2010**, 49, 6646−6649.

(81) A.Yella, H.W.Lee, H.N. Tsao,C.Yi, A. K. Chandiran, Md.K.Nazeeruddin, E.Wei-Guang Diau,C.Y.Yeh,

S.M Zakeeruddin, M.Grätzel, *Science* , **2011**: Vol. 334, Issue 6056, pp. 629-634

(82) S. Mathew, A. Yella, P. Gao, R. Humphry-Baker, B.F. E. Curchod, N.Ashari-Astani, I. Tavernelli, U. Rothlisberger, Md. K. Nazeeruddin and M. Grätzel, *Nature Chemistry* **2014**, 6, 242-247

(83) Y. Xie, Y. Tang, W. Wu, Y. Wang, J. Liu, X.Li, H.Tian,and W.H. Zhu, *J.Am.Chem.Soc*. **2015**, 137, 14055−14058

(84) Yang W, Vlachopoulos N, Hao Y, Hagfeldt A, Boschloo G. *Phys Chem Chem Phys.* **2015,** 17(24):15868-75

(85) Hauch, A.; Georg, A. *Electrochim. Acta* **2001,** 46, 3457

(86) Papageorgiou, N.; Maier, W. F.; Grätzel, M. J. *Electrochem. Soc.* **1997**, 144, 876.

(87) Olsen, E.; Hagen, G.; Lindquist, S.-E. *Sol. Energy Mater. Sol. Cells* **2000**, 63, 267.

(88) Q. W. Jiang, G. R. Li and X. P. Gao,*Chem. Commun*., **2009**,6720–6722

(89) H. N. Tian, E. Gabrielsson, Z. Yu, A. Hagfeldt, L. Kloo andL. C. Sun,*Chem. Commun*., **2011**,47, 10124–10126.

(90) M. X. Wu, Y. D. Wang, X. Lin, N. S. Yu, L. Wang, L. L. Wang,A. Hagfeldt and T. L. Ma,*Phys. Chem. Chem. Phys*., **2011**,13,19298–19301.

(91) M. J. Ledoux and C. Phamhuu,*Catal.Today*,**1992**,15,263–284

(92) Carli S., Casarin L., Bergamini G., Caramori S., Bignozzi C.A., *J. Phys. Chem. C* **2014**, 118, 16782−16790

(93) Carli, S.; Busatto, E.; Caramori, S.; Boaretto, R.; Argazzi, R.; Timpson, C. J.; Bignozzi, C. A., *J. Phys. Chem. C* **2013**, 117, 5142−5153.

(94) Bay, L.; West, K.; Winther-Jensen, B.; Jacobsen, T. *Sol. Energy Mater. Sol. Cells* **2006**, 90, 341.

(95) F.Hao,P. Dong, Q. Luo, J. Li, J. Lou, H. Lin *Energy Environ. Sci.* **2013**, 6, 2003-2019

(96) L. Kavan, Liska P., Zakeeruddin S., Gretzel M., *Electroch. Acta* 195 **2016**, 34–42

(97) J. Wu, Z. Lan, J. Lin, M. Huang, Y. Huang, L. Fan, and G. Luo, *Chem. Rev*., **2015**, 115 (5), 2136–2173

(98) Xu, K. *Chem. Rev*. **2004**, 104, 4303.

(99) Yu, Z.; Vlachopoulos, N.; Gorlov, M.; Kloo, L. *Dalton Trans*. **2011**, 40, 10289.

(100) Gorlov, M.; Kloo, L. *Dalton Trans*. **2008**, 2655-2666.

(101) Wu, J.; Lan, Z.; Hao, S.; Li, P.; Lin, J.; Huang, M.; Fang, L.; Huang, Y. *Pure Appl. Chem*. **2008**, 80, 2241.

(102) Freitas, J.; Nogueira, A.; De Paoli, M. *J. Mater. Chem*. **2009**, 19, 5279.

(103) Li, B.; Wang, L.; Kang, B.; Wang, P.; Qiu, Y. *Sol. Energy Mater. Sol. Cells* **2006**, 90, 549.

(104) Zhang, W.; Cheng, Y.; Yin, X.; Liu, B. *Macromol. Chem. Phys.* **2011**, 212, 15.

(105) Yu,Z.;Vlachopoulos,N.;Gorlov,M.;Kloo,L. *DaltonTrans.* **2011**, 40, 10289–10303.

(106) Wang, M.; Grätzel, C.; Zakeeruddin, S.M.; Grätzel, M. *Energy Environ. Sci*. **2012**, 5, 9394–9405.

(107) O'Regan, B.; Grätzel, M. *Nature* **1991**, 353, 737–740.

(108) Grätzel, M.. J. *Photochem. Photobiol. C* **2003**, 4, 145–153.

(109) Boschloo, G.; Hagfeldt, A. *Acc. Chem. Res*. **2009**, 42, 1819.

(110) Clifford, J.; Palomares, E.; Nazeeruddin, M.; Gratzel, M.; Durrant, J. *J. Phys. Chem. C* **2007,** 111, 6561.

(111) Schiffmann, F.; Vondele, J.; Vande, J.; Urakawa, A.; Wirz, R.; Baiker, A. *Proc. Natl. Acad. Sci. U.S.A.* **2010**, 107, 4830

(112) Rowley, J.; Farnum, B.; Ardo, S.; Meyer, G. *J. Phys. Chem. Lett.* **2010**, 1, 3132.

(113) Privalov, G.; Timofei, B.; Hagfeldt, A.; Svensson, P.; Kloo, L. *J. Phys. Chem. C* **2009**, 113, 783.

114) Cong, J.; Yang, X.; Kloo, L.; Sun, L. *Energy Environ. Sci.* **2012**, 5, 9180–9194.

(115) Maza, W.A.; Haring, A.J.; Ahrenholtz, S.R.; Epley, C.C.; Lin, S.Y.; Morris, A.*J. Chem. Sci.* **2015**, 7, 719–727.

(116) Gao, H.H.; Qian, X.; Chang, W.Y.; Wang, S.S.; Zhu, Y.Z.; Zheng, J.Y. *J. Power Sources* **2016**, 307, 866–874.

(117) Su, H.C.; Wu, Y.Y.; Hou, J.L.; Zhang, G.L.; Zhu, Q.Y.; Dai, J.. *Chem. Commun.* **2016**, 52, 4072–4075.

(118) Cazzanti, S.; Caramori, S.; Argazzi, R.; Elliott, C. M.; Bignozzi, C. A. *J. Am. Chem. Soc.* **2006**, 128, 9996.

(119) Gregg, B. A. Coord. *Chem. ReV.* **2004**, 248, 1215.

(120) Hattori, S.; Wada, Y.; Yanagida, S.; Fukuzumi, S. *J. Am. Chem. Soc.* **2005**, 127, 9648.

(121) A. Colombo, C. Dragonetti, M. Magni, D. Roberto, F. Demartin, S. Caramori, and C.A. Bignozzi, *ACS Appl. Mater. Interfaces*, **2014**, 6 (16), 13945–13955

(122) Y. Saygili, M. Söderberg, N. Pellet, F.Giordano, Y.Cao, A. B.Muñoz-García, S. M. Zakeeruddin, N. Vlachopoulos, M. Pavone, G.Boschloo, L. Kavan, J.E. Moser, M. Grätzel, A. Hagfeldt, M. Freitag *J. Am. Chem. Soc*., **2016**, 138 (45), 15087–15096

(123) Sapp, S.A.; Elliott, C.M.; Contado, C.; Caramori, S.; Bignozzi, C.A.. *J. Am. Chem. Soc.* **2002**, 124, 11215–11222.

(124) Bella F., Galliano S., Gerbaldi C. and Viscardi G. *Energies* **2016**, 9, 384,

(125) Klahr, B.M.; Hamann, T.W., *J. Phys. Chem. C* **2009**, 113, 14040–14045.

(126) Tsao, H.N.; Yi, C.; Moehl, T.; Yum, J.H.; Zakeeruddin, S.M.; Nazeeruddin, M.K.; Grätzel, M., *ChemSusChem* **2011**, 4, 591–594.

(127) Feldt, S.M.; Gibson, E.A.; Gabrielsson, E.; Sun, L.; Boschloo, G.; Hagfeldt, A., *J. Am. Chem. Soc.* **2010**, 132, 16714–16724.

(128) Nusbaumer, H.; Zakeeruddin, S. M.; Moser, J. E.; Grätzel, M., *Chem.Eur. J.* **2003**, 9, 3756. (129) Cameron, P. J.; Peter, L. M.; Zakeeruddin, S. M.; Grätzel, M., *Coord. Chem. ReV.* **2004**, 248, 1447.

(130) Nelson, J. J.; Amick, T. J.; Elliott, C. M., *J. Phys. Chem. C* **2008**, 112, 18255.

(131) Klahr, B. M.; Hamann, T. W. *J. Phys. Chem. C* **2009**, 113, 14040.

(132) Kakiage, K.; Aoyama, Y.; Yano, T.; Oya, K.; Fujisawa, J.I.; Hanaya, M. *Chem. Commun*. **2015**, 51, 15894–15897

(133) Izatt, R.M.; Pawlak, K.; Bradshaw, J.S.; Bruening, R.L., *Chem. Rev.* **1991**, 91, 1721–2085

(134) Nakade, S.; Makimoto, Y.; Kubo, W.; Kitamura, T.; Wada, Y.; Yanagida, S., *J. Phys. Chem. B* **2005**, 109, 3488–3493.

(135) Koh, T.M.; Nonomura, K.; Mathews, N.; Hagfeldt, A.; Grätzel, M.; Mhaisalkar, S.G.; Grimsdale, A.C. *J. Phys. Chem. C* **2013**, 117, 15515–15522.

Chapter 2: Experimental techniques

In this chapter the electrochemical, photoelectrochemical and spectroscopic methods employed in this thesis work will be described, together with the solar cells fabrication, in all their components. The outlined techniques summarized below were essential in order to fully characterize the studied systems, like new electrode materials and molecular systems, in solution or attached to a surface, and especially to understand the functioning of solar devices developed during these studies, addressing the electron transfer and mass transport kinetics responsible for their power conversion efficiencies.

2.1 Electrochemical methods

Various electrochemical techniques were employed in this thesis work for various scopes, first of all for the DSSC characterization, which allows to obtain all the performance defining parameters of the cell. Moreover, electrochemical methods were useful to determine the redox potentials and diffusion coefficients of new electronic mediators, the resistive characteristics of interfaces, but also to produce special materials through electrodeposition techniques.

In Figure 2.1 a scheme of the basic experimental apparatus for electrochemical measurements is represented [1]. A three electrodes system is involved, including a working electrode, a counter electrode and a reference electrode. An electronic instrument known as *potentiostat* has control of a voltage difference between the working and reference electrodes, applied in accord with the program defined by a function generator. The response from the potentiostat, which constitutes the experimental observable, is a current flow between the working and counter electrode. An Autolab PGSTAT 302/N potentiostat, equipped with a FRA2 frequency response analyzer was used in this thesis work.

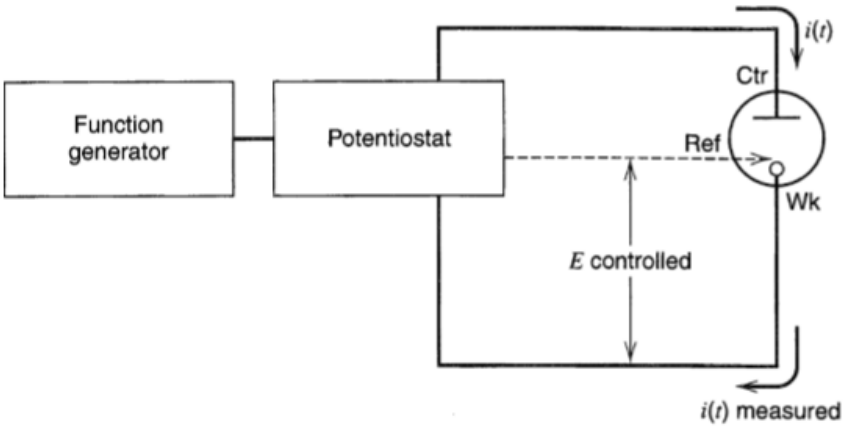

Figure 2.1 Experimental arrangement for controlled-potential experiments

2.1.1 Linear sweep voltammetry

Linear sweep voltammetry (LSV) is a potentiodynamic method where the potential is varied linearly with time (i.e., the applied signal is a voltage ramp), as it is represented in figure 2.2 a, with sweep rates usually ranging from 10 to 500 mV/s with conventional electrodes [2]. The resulting current change is recorded as a function of the applied voltage. For example, if an electrolytic solution containing the Co^{2+} ion is analyzed by LSV, its oxidation to Co^{3+} takes place at the working electrode surface, producing a voltammogram like that reported in figure 2.2 b, where the peak maximum represents the $Co^{2+/3+}$ process potential (E_p^a).

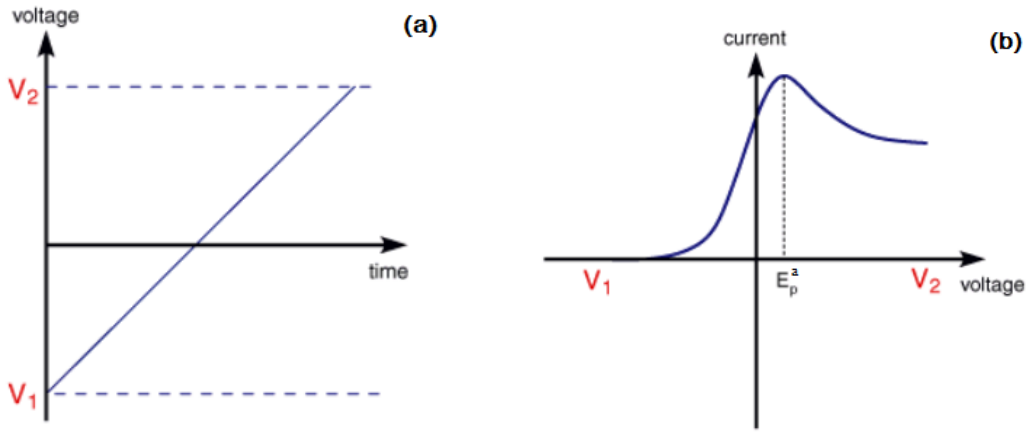

Figure 2.2 Linear voltage sweep applied in LSV (a) and voltammogram produced (for example, by the Co^{2+}oxidation)

The characteristics of the linear sweep voltammogram recorded depend on a number of factors including the rate of the electron transfer reaction(s) and the chemical reactivity of the electroactive species, but also the voltage scan rate: the total current increases with increasing scan rate, based on the diffusion layer size and on the time taken to record the scan.

2.1.2 Cyclic voltammetry

Cyclic voltammetry (CV) is very similar to LSV. In this case the voltage is swept between two values at a fixed rate, however now when the voltage reaches V_2 the scan is reversed and the voltage is swept back to the initial value V_1, following a triangular diagram, as represented in figure 2.3a. The current outcome is monitored respect to the applied potential, producing a voltammogram like the one reported in figure 2.3b.

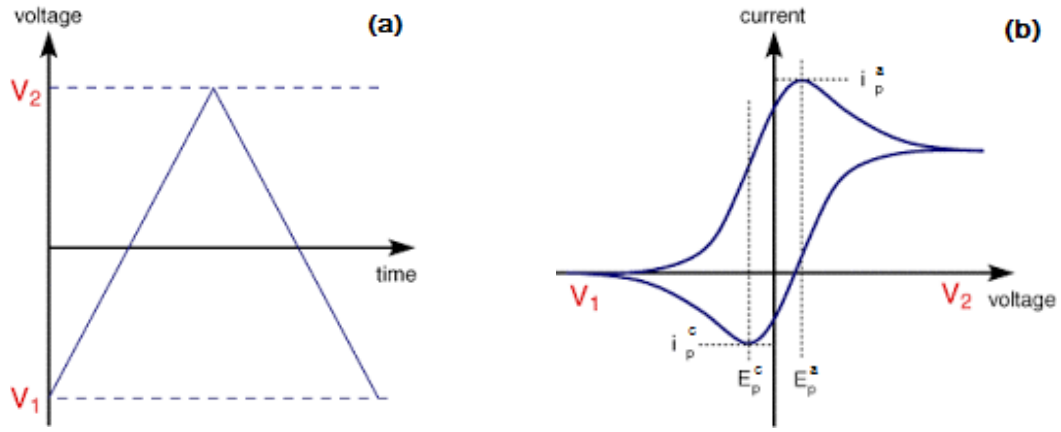

Figure 2.3 Cyclic voltage sweep applied in CV (a); typical cyclic voltammogram recorded for a reversible single electron transfer reaction (b)

The forward sweep produces an identical response to that seen for the LSV experiment. When the scan is reversed, the oxidation product (Co^{3+}) is simply gradually converted back to the reduced form (Co^{2+}), moving back through the equilibrium position.

For a perfectly reversible process, the voltage separation between the current peaks in the recorded CV is:

$$\Delta E = E_p^a - E_p^c = \frac{59}{n}\,\text{mV} \qquad \text{(Eq. 2.1)}$$

where E_p^a and E_p^c are the anodic and cathodic maximum peak potentials and n is the number of electrons involved in the electrochemical reaction. This value represents the reversibility of an electrochemical reaction, which decreases with increasing ΔE. Another parameter extractable from CV measurements is the *half-wave potential:*

$$E_{1/2} = \frac{E_p^a - E_p^c}{2} \qquad \text{(Eq. 2.2)}$$

which indicates an estimate of the formal potential E° of a redox couple involved in a reversible electron transfer process.

Cyclic voltammetry can be employed to obtain an estimate of the diffusion coefficient of an electroactive species in solution. The common procedure consists in performing a series of CV measurements in an electrolytic solution containing the investigated species, at a series of different scan rates. Subsequently, a linear plot of the current peak (i_p) vs. the square root of the scan rate ($v^{1/2}$) can be constructed, whose slope, in the case of a reversible process, is proportional to the square root of the diffusion coefficient (D), following the *Randles-Sevcik equation* [3] (equation 2.3). After appropriate substitution, the D value is yielded.

$$i_P = (2.69 \cdot 10^5)\, n^{3/2} A D^{1/2} C v^{1/2} \qquad \text{(Eq. 2.3)}$$

where *n* is the number of electrons transferred in the redox event (usually one), *A* is the working electrode area in cm^2, *C* is the species concentration in mol/cm^3.

2.1.3 Electronic impedance spectroscopy

Electronic impedance spectroscopy (EIS) is a powerful technique for the characterization of electrochemical systems, that can provide information about electrode processes and complex interfaces [4,5]. As shown in Figure 2.4, its fundamental approach is to apply a small amplitude sinusoidal excitation to a system under steady-state and measure the response, which is also a sinusoidal signal with the same frequency but different intensity and phase angle. The experiment is carried at a wide range of frequencies.

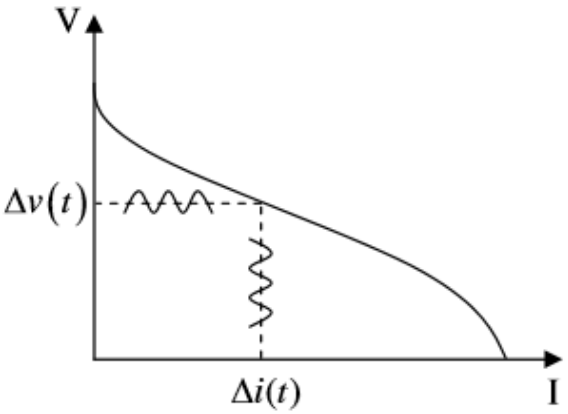

Figure 2.4 Principles of impedance spectroscopy

If an arbitrary potential E(t) is applied to a simple resistance R, the current i(t) is given as i(t) = E(t)/R. When the same potential is applied to the series connection of a resistance R and a capacitance C, the total potential difference is the sum of potential drops on each element. Taking into account that for a capacitance: E(t) = Q(t)/C, where Q is the charge stored in a capacitor, the following equation is obtained:

$$E(t)= i(t)R +Q(t)/C \qquad \text{(Eq. 2.3)}$$

Direct application of the Laplace transform to equation 2.3 gives:

$$i(s) = E(s) / (R +1/sC) \qquad \text{(Eq. 2.4)}$$

$$\frac{E(s)}{I(s)} = (R +1/sC) = Z(s) \qquad \text{(Eq. 2.5)}$$

where s = ν and Z(s) is called *impedance,* and is expressed in the units of resistance, Ω. The inverse of impedance is called admittance, Y(s) = 1/Z(s). They are *transfer functions,* which transform one signal, e.g. applied voltage, into another, e.g. current.

In EIS, we are interested in the system response to the application of an alternating voltage (av) input signal, expressed with the sinusoidal form: $E = E_0 \sin(\omega t)$, where E_0 is the signal amplitude, $\omega = 2\pi f$ is the angular frequency, and f is the av signal frequency.

Considering the application of an av signal to a series R-C connection, the derived steady-state equation is:

$$i(t) = \frac{E_0}{\sqrt{R^2 + \frac{1}{(\omega C)^2}}} \sin(\omega t + \varphi) = \frac{E_0}{|Z| \sin(\omega t + \varphi)} \qquad \text{(Eq. 2.6)}$$

where φ is the phase-angle between current and potential, $\varphi = \arctan\left(\frac{1}{\omega RC}\right)$. It is obvious that the current has the same frequency as the applied potential but is phase-shifted by the angle φ. The value |Z| has units of resistance. It is the length of a vector obtained by addition of two perpendicular vectors: R and $\frac{1}{\omega C}$.

In order to simplify the calculations of impedances, the result obtained for the periodic perturbation of an electrical circuit may be represented using complex notation. The impedance of the considered series R-C system, Z(ωj), may be represented as:

$$Z(\omega j) = Z' + jZ'' = R + \frac{1}{\omega C} = R - j\frac{1}{\omega C} \qquad \text{(Eq. 2.7)}$$

where the real and imaginary parts of the impedance are: $Z' = R$ and $Z'' = -\frac{1}{\omega C}$, respectively. It should be noted that the complex impedance Z(ωj), equation 2.7, may be obtained from Z(s), equation 2.5, by substitution: $s = j\omega$. In fact, this is the imaginary Laplace transform. In general, the complex impedance may be written for any circuit by taking R for a resistance, $1/j\omega C$ for a capacitance, and applying Ohm's and Kirchhoff's laws to the connection of the electrical system elements.

The complex impedance of an electrical system may be represented graphically using two types of plots: complex plane (*Nyquist plot*) and *Bode plots*. The complex plane is a plot of Z" versus Z', that is, the imaginary versus the real component, plotted for various frequencies, while the two Bode plots represent log |Z| (magnitude) and phase-angle, ϕ, versus log ω

The circuit shown in figure 2.5a could represent a physical system like the Helmholtz electrified interface, between an electrolytic solution and a polarized electrode, in which the diffusion impedance relative to the ionic species in solution is neglected. The equivalent circuit consists in a series connection of the resistance R_s with the parallel connection of R_{ct}-C_{dl}, where R_s is the serial resistance, R_{ct} is the charge transfer resistance at the electrodic interface, and C_{dl} is the electrified double layer capacity. The global impedance of the system is given as:

$$Z(\omega j) = R_s + \frac{1}{1/R_{ct} + j\omega C_{dl}} \qquad \text{(Eq. 2.8)}$$

The corresponding complex plane and Bode plots are also shown in Figure 2.5b,c,d (for Rct = 100 Ω, Rs = 10 Ω and C_{dl} = 20 μF). There are two limits of the impedance: at ω → ∞, Z → Rs and φ → 0, due to the presence of Rs; and, for ω → 0, Z → R_s + R_{ct}. The Nyquist plot shows a semicircle of radius R/2 with the center on the real axis, and the frequency at the semicircle maximum equal to: ω = $1/R_{ct}C_{dl}$ = 500 s^{-1}. The graph of log |Z| versus log ω, Figure 2.5c, contains two breakpoints or corner frequencies, that are simply frequencies at which the magnitude changes its slope, corresponding to the inverse of the characteristic time constant.

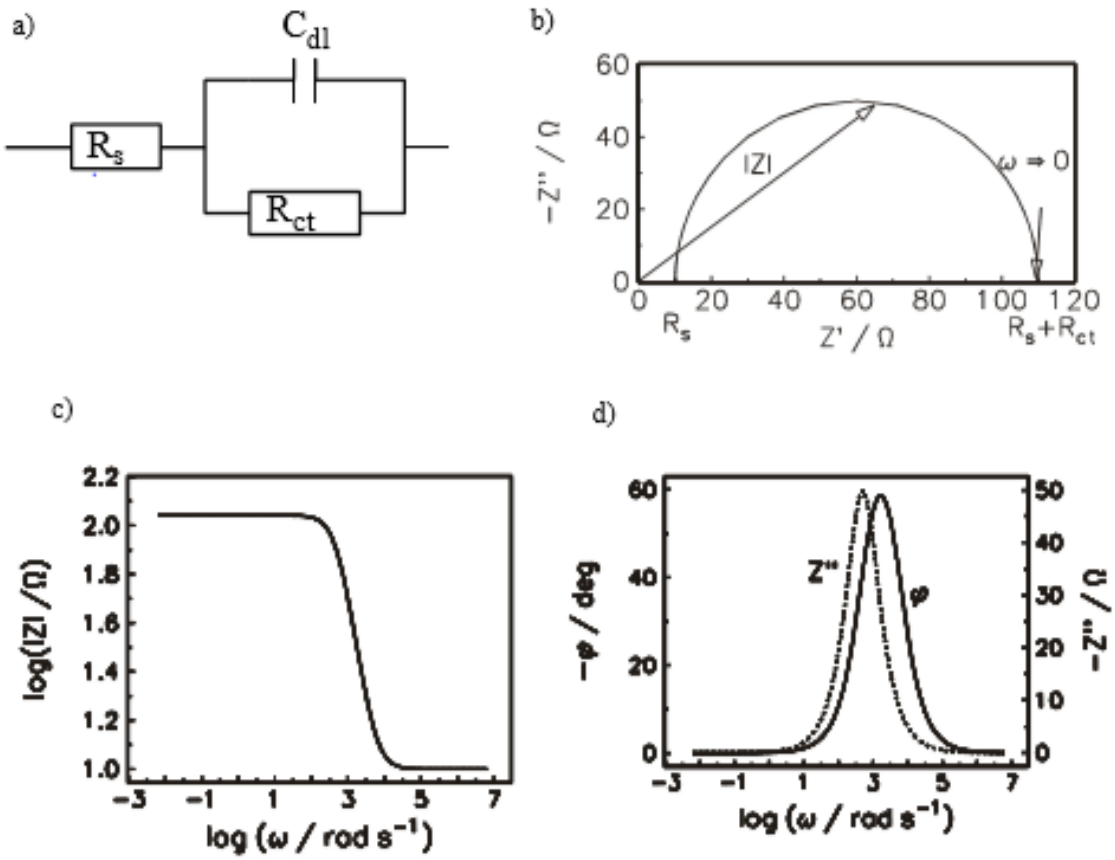

Figure 2.5 Complex plane (b) and Bode (c), (d), plots for the circuit (a), with R_s = 10Ω, R_{ct} = 100Ω, C_{dl} = 20μF

2.2 Photolectrochemical characterization

2.2.1 Photoelectrode preparation

The transparent conductive oxide (TCO) of choice in DSSC fabrication is a highly fluorine doped SnO_2 film (FTO, Pilkington) deposited on glass, with an average surface conductivity of about 10 Ω/sq. FTO allows effective light transmission while providing good conductivity for current collection, in addition it establishes a good mechanical and electrical contact with the dye sensitized oxide in order to obtain a satisfactory electronic percolation from the semiconductor to the electron collector.

To prepare the photoanodes, FTO glass plates were first washed in 2-propanol for 10 min using an ultrasonic bath, then heated at 450°C, in aerated oven, for 20 minutes. A blocking underlayer was applied in some cases, especially when using cobalt redox mediators, to limit recombination rates of the injected electrons with the electrolyte at the highly conductive FTO interface. The compact TiO_2 underlayer was deposited by spin-coating a 0,3 M titanium tetraisopropoxide solution in 1-butanol (1000 rpm for 10 s, 2000 rpm for 20 s). Then the substrates were heated at 500 °C for 15 min.

The substrate was then covered on two parallel edges with 3M adhesive tape (ca. 20 μm thick), to control the thickness and area of the TiO_2 film. A TiO_2 colloidal paste was then applied to one edge of the conducting glass and distributed with a glass rod sliding over the tape-covered edges (doctor-blade technique). Two different types of colloidal TiO_2 paste were used: transparent (18NR-T) or opaque (18NR- AO), both purchased by Dyesol. The second type was sometimes employed in order to reach higher efficiencies, thanks to increased light harvesting due to light scattering. After the TiO_2 deposition, the electrodes were heated up to 500°C, following a programmed temperature ramping: 25−120 °C (10 min), 120−450 °C (30 min), 450 °C (20 min), 450−500 °C (10 min), 500 °C (10 min). The resulting film thickness was ~7 μm. The sintering process regulates parameters such as the contact between interconnected nanoparticles and their coordination in the porous TiO_2 network, enhancing the film conductivity. After this, the electrodes were subjected to a $TiCl_4$ (0,4 M in water) overnight treatment, in order to improve the active area, owing to the $TiCl_4$ hydrolysis on the TiO_2 substrate. The electrodes were heated again at 450° for 30 minutes. Once cooled, they were immersed for 24 h in the sensitizer solution, usually a ~10^{-3} M solution in ethanol or in a 1:1 ACN/tert-butanol mixture. In the next chapters the specific dye absorption conditions will be reported.

2.2.2 Counter electrode preparation

Different kinds of counter electrodes were used in this thesis work: platinum, PEDOT and nanocarbons coated counter electrodes.

Platinum metal clusters were deposited on a FTO substrate by spraying a $5 \cdot 10^{-3}$ M solution of hexachloroplatinic acid in isopropanol. The procedure was repeated 5-7 times until a homogeneous distribution of hexachloroplatinic acid clusters on the surface was observable. The resulting electrodes were then dried in air for 5 minutes and heated at 380 C° for 15 minutes, during which the pyrolysis of the hexachloroplatinic acid occurs and metallic Pt clusters are formed. This procedure creates transparent counter electrodes.

The preparation of PEDOT and nanocarbons based counter electrodes used in this thesis work will be described in detail in the next chapters, especially in chapter 5.

2.2.3 Cell assembly

The most part of DSSC devices studied in this thesis work were assembled in open configuration, that is, the two electrodes were clipped together by small metallic clamps. Alternatively, to run stability tests and to enhance the performances, by reducing the spacing between the electrodes, closed cells were prepared, sealing them under a hot press (pressure applied at 100°C for 90 s). To separate the two electrodes and delimit the active area, which was either 0.2 or 0.25 cm^2, a thermoplastic polymer spacer was used (Surlyn, 25μm thick). Some drops of electrolyte were put on the marked area on the photoanode before closing it in the open configuration, while in the sealed cells the electrolyte was injected through a small hole using a vacuum pump. The hole was then sealed with epoxy resin.

The different electrolytic compositions employed in the works included in this thesis will be described in detail in each of the 3,4 and 5 chapters.

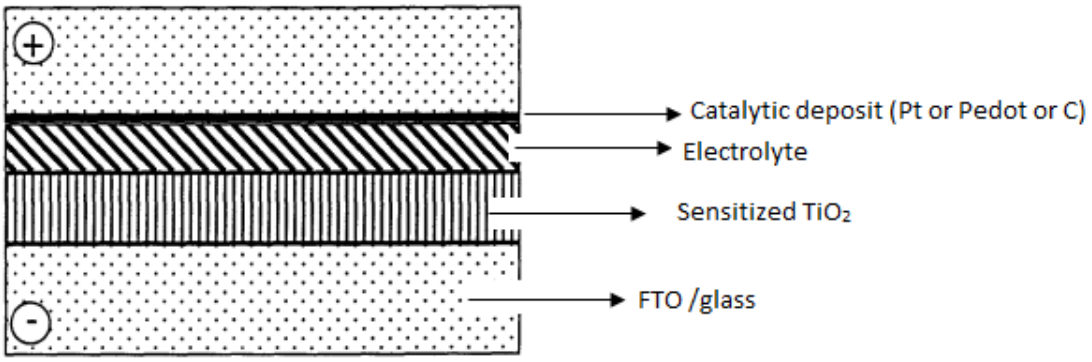

Figure 2.6 Schematic view of the DSSC sandwich strucure

2.2.4 Cell characterization

The general current-voltage characteristic of a solar cell may be approximated by the diode equation [6, 7] :

$$I = I_{ph} - I_S\left(e^{\frac{V_a}{V_t}} - 1\right) - \frac{V_a}{R_{sh}} \qquad \text{(Eq. 2.9)}$$

where I is the current, I_s is the saturation current of the diode, I_{ph} is the photocurrent which is assumed to be independent by the applied voltage V_a. R_{sh} is the shunt resistance of the circuit and is introduced to take into account the internal resistance and energy dissipation mechanisms of the cell. V_t is the thermal voltage given by: $V_t = nkT/e$.

Equation 2.9 can be obtained from the circuit represented in figure 2.7, which shows the equivalent circuit of the cell, where Rs is the series resistance, and R_L is the external load. Obviously it is only a simplified model of the DSSC which is actually thought to correspond to a multidiode model to take into account the different mechanisms of charge transport within the cell.

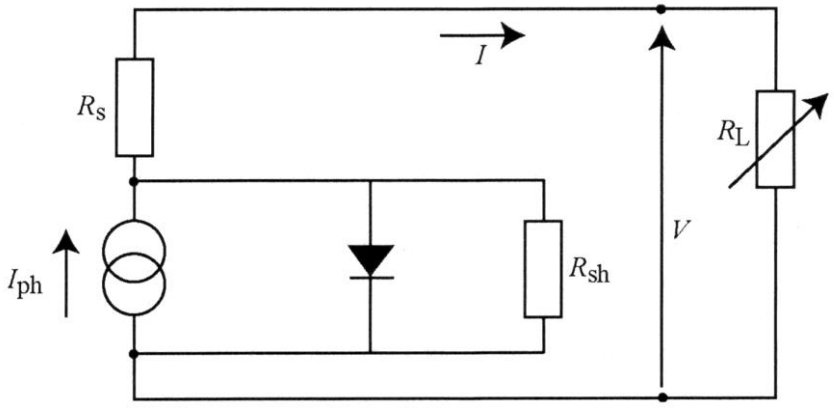

Figure 2.7 A DSSC under irradiation can be expressed as a non perfect current generator mounted in parallel to a non perfect diode

To experimentally characterize DSSC, **linear sweep voltammetry (LSV)** measurements were conducted (see chapter 2.1.1). The electrical terminals of the potentiostat were connected to the photoanodic and cathodic solar cell components, and an external potential ranging from 0 (short circuit, sc) up to the *open circuit voltage* (V_{oc}) was applied under illumination (for most cells measurements, "1 sun" power, corresponding to 100mW/cm^2, AM 1.5 G illumination). The current flow response was recorder as a function of the applied potential, generating profiles similar to that represented in figure 2.8 [8, 9].

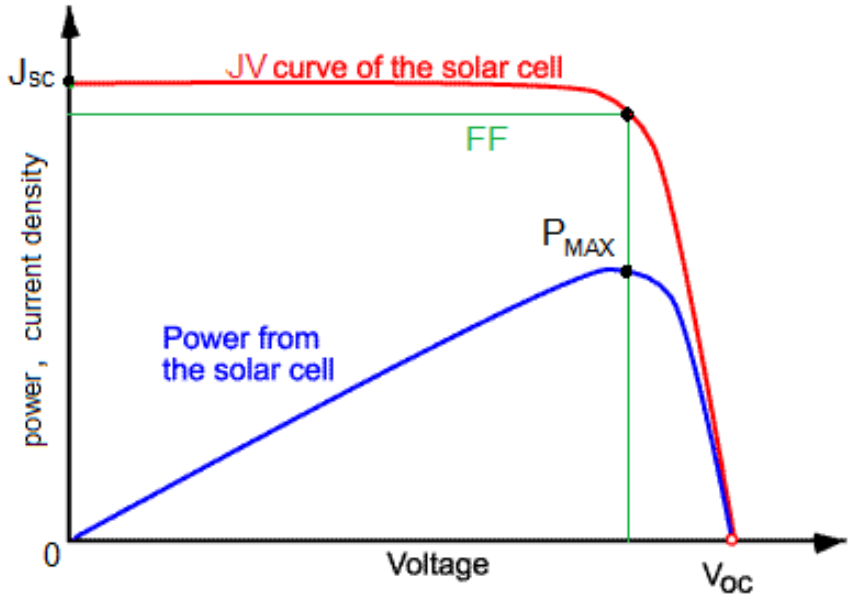

Figure 2.8 JV curve of a solar cell (red), showing the short-circuit current and open circuit voltage values; power curve as function of voltage (blue line); the area under the green square is the fill factor.

When the applied voltage is zero (i.e., when the solar cell is short circuited), the current across the solar cell is called *short circuit current (I_{SC})*, which is the largest current obtainable from the device. In the condition of zero voltage applied, the series resistance R_s is minimal, therefore V_a =0 and $I_{sc}=I_{ph}$.

To remove the dependence from the solar cell active area, it is more common to list the short-circuit current **density** (J_{sc} in A/cm^2) rather than the short-circuit current (A). The I_{SC} parameter also depends on the incident light intensity (number of photons) and spectrum (for most solar cell measurements, it is standardized to the AM1.5 spectrum), on the optical properties (absorption and reflection) and on the *electron collection efficiency* of the solar cell. This latter depends chiefly on the photoanode surface passivation and diffusion length. When the net current through the device reaches zero, the potential value detected corresponds to the maximum voltage available from a solar cell, which is is called *open circuit voltage (V_{oc})*. It can be obtained from equation 2.9 by setting I=0 and $V_a=V_{OC}$. Under these conditions:

$$V_{OC} \cong V_t \ln\left(\frac{I_{ph}}{I_S}\right) \qquad \text{(Eq. 2.10)}$$

Obviously both I_{sc} and V_{OC} are functions, through I_{ph}, of the irradiance.

The *fill factor (FF)* is a parameter whose value can range between 0 and less than 1 which, in conjunction with V_{OC} and J_{SC}, determines the maximum power extractable from a solar cell. The FF is defined as the ratio of the maximum power from the solar cell to the product of Voc and Jsc (where power P =J·V):

$$FF = \frac{(J \cdot V)_{MAX}}{J_{sc} \cdot V_{oc}} \qquad \text{(Eq. 2.11)}$$

Graphically, the FF is the area of the largest rectangle that could fit under the curve, and indicates the curve deflection from a square-like one.

The *overall solar-to-electrical energy conversion efficiency,* $\boldsymbol{\eta}$, for a solar cell is defined by the ratio of the maximum power generated by the cell ($P_{MAX} = V_{OC} \cdot J_{SC} \cdot FF$) and the incident light power (P_{in}, which usually equals 100 mW/cm^2):

$$\eta = \frac{J_{SC} \cdot V_{OC} \cdot FF}{P_{IN}} \qquad \text{(Eq. 2.12)}$$

Another fundamental measurement of the performance of a solar cell is the "external quantum efficiency", which is normally called the *incident photon to current conversion efficiency (IPCE)*. IPCE is defined as the number of electrons generated by the incident light divided by the number of incident photons. It is expressed as the product of the *quantum yield of charge injection* (Φ_{inj}), the *light harvesting efficiency* (LHE) and the *electron collection efficiency* (η_C):

$$IPCE = \Phi_{inj} \cdot LHE \cdot \eta_C \qquad \text{(Eq. 2.13)}$$

The *quantum yield of charge injection* is given by

$$\Phi_{inj} = \frac{k_{inj}}{\Sigma k_d + k_{inj}} \qquad \text{(Eq. 2.14)}$$

Where k_{inj} is the rate constant for electron injection and Σk_d is the sum of all rate constants for the excited state deactivation processes.

The *electron collection efficiency* η_C is basically determined by the efficiency of the photoinjected electrons recombination with the oxidized dye and with the oxidized form of the electronic mediator. Ideally these recombination processes can be minimized by a proper choice of sensitizers and electronic mediators, hence the injected electrons are free to reach the back contact without significant losses and η_C can be considered close to unity.

The *light harvesting efficiency* is given by:

$$LHE(\lambda) = 1\text{-}10^{-A(\lambda)} \qquad \text{(Eq. 2.15)}$$

where A is the absorbance of the sensitized semiconductor film at the wavelength λ. Obviously LHE depends on the absorption spectrum of the dye bound to TiO_2, and for this reason the photoaction spectrum usually matches the absorption spectrum of the sensitized nanocrystalline substrate.

Experimentally, the IPCE value corresponds to the photocurrent density produced in the external circuit under low intensity monochromatic illumination of the cell, divided by the photon flux that strikes the cell. From such an experiment the IPCE as a function of wavelength can be calculated from:

$$\mathrm{IPCE} = 1240 \cdot \frac{J_{SC}(\lambda)\ [\mathrm{A \cdot cm^{-2}}]}{\lambda[\mathrm{nm}] \cdot P_{IN}(\lambda)\ [\mathrm{W \cdot cm^{-2}}]} \qquad \text{(Eq. 2.16)}$$

Where J_{SC} is the photocurrent density collected under short circuit conditions expressed in A/cm^2, λ (nm) is the wavelength of the incident monochromatic light and P_{in} is the power of the incident photon flux in W/cm^2, usually measured by means of a calibrated photodiode.
IPCE spectra in this thesis work were collected with a custom built apparatus comprising an Applied Photophysics Monochromator, a 175 W Xe source (Luxtel) and various optical elements. Short circuit photocurrents were measured with an Agilent 34301 A multimeter while incident irradiance was provided by a calibrated silicon photodiode (OSD 100 7Q).

The current-voltage characteristics can also be measured in the dark, giving information about recombination to the oxidized redox species only, since no oxidized dye molecules are present in the dark. This is illustrated in figure 2.9.

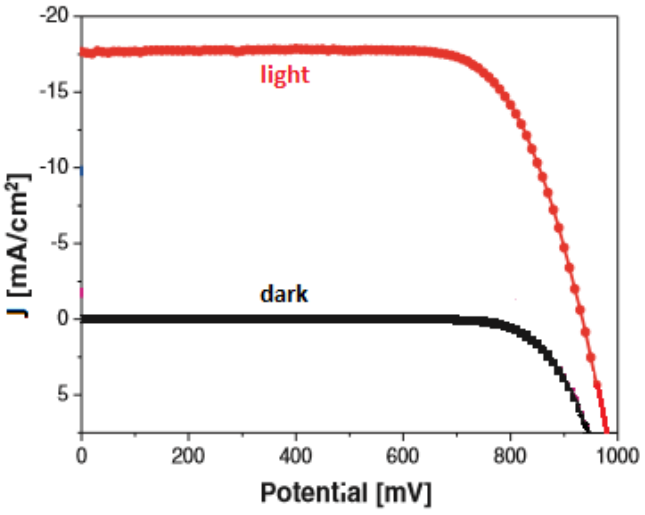

Figure 2.9 JV curve under 1 sun illumination (red), and under dark (black), in the case of a YD2-oC8/Y123 cosensitized DSSC with $Co(bpy)_3^{II/III}$ as redox mediator [10]

To investigate electronic and ionic processes occurring in DSSC, also **Electronic Impedance Spectroscopy (EIS)** was abundantly exploited [11-15]. Analysis of the EIS spectrum of a DSSC, which is fitted by means of an appropriate equivalent circuit representing the physical system under study, provides information about several important charge transport, transfer, and accumulation processes in the cell.

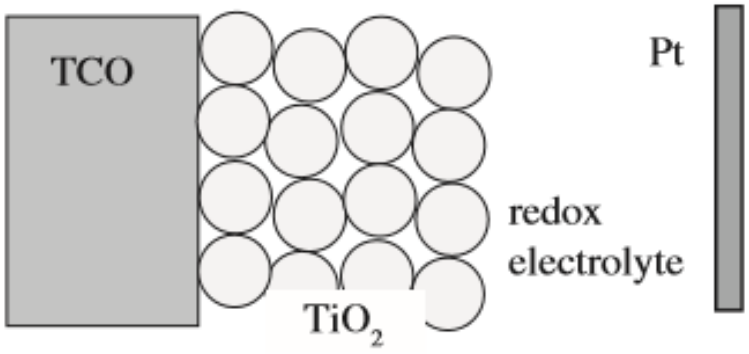

Figure 2.10 Schematic diagram of a DSSC.

The DSSC contains three spatially separated interfaces formed by FTO/TiO_2, TiO_2/electrolyte, and electrolyte/Pt-FTO, as can be observed in figure 2.10. In the dark under forward bias electrons are injected in the conduction band of the TiO_2 nanoparticles and their motion is coupled to that of the electron donor and acceptor ions in the electrolyte. Illumination gives rise to new redox processes at the TiO_2/dye/electrolyte interface, comprising electron injection from the photoexcited sensitizer, recombination with the parent dye, and regeneration of the sensitizer.

Electronic impedance spectroscopy, technique described in section 2.1.3, consists in measuring the current response to the application of an ac voltage as a function of the frequency. If a potential correspondent to the open circuit condition is applied to an operative DSSC under illumination, the measurement output has generally the aspect reported in figure 2.11. A charge-transfer resistance manifests itself as a semicircle in the Nyquist diagram and a peak in the Bode phase angle plot. Hence, the resulting Nyquist diagram typically features three semicircles that, in the order of increasing frequency, are attributed to the Nernst diffusion within the electrolyte (Z_D), the electron transfer at the oxide/electrolyte interface (Z_{TiO2}), and the redox reaction at the platinum counter electrode (Z_{CE}) [14]. Correspondently, the Bode phase plot shows three characteristic frequency peaks.

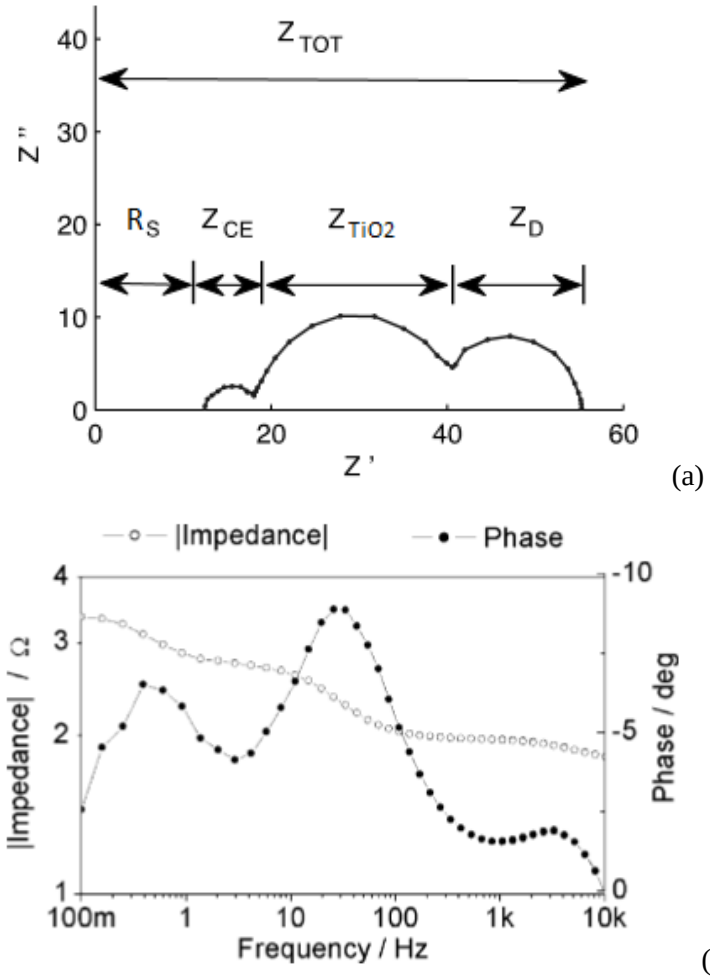

Figure 2.11 General electrical impedance spectrum of a dye-sensitized solar cell under open-circuit condition and 1000 W m^{-2} bias illumination, in the form of Nyquist (a) and Bode (b) plots.

If a low potential, closer to the short-circuit condition, is applied, the impedance of the TiO_2/dye/electrolyte interface becomes very high, since TiO_2 is rapidly depleted by electrons which are drawn to the back contact. To adequately fit the obtained measurement outcome, an **equivalent circuit** such as that reported in figure 2.12 is generally used, where R_S is the series resistance, representing the sum of the bulk electrolyte, substrate, and electric contacts resistances. The parallel combination of a charge transfer resistance (R_{CT}) and a costant phase element (CPE) represents the impedance Z of both the electrolyte/Pt-FTO interface (R_{CE}, CPE_{CE}) and the TiO_2/electrolyte one (R_{TiO2}, CPE_{TiO2}).

The interfacial double layer capacitance (C_{dl}) is replaced by a constant phase element (CPE) to account for the deviation from an ideal capacitor, arising from the non-homogeneity of the rough, porous electrodes surfaces involved, and causing a flattening of the Nyquist plot semicircles. In the Z_{TiO2} mesh a finite-length Warburg element is included (W_S), which represents the impedance due to redox species diffusion in the electrolyte, to and from the electrode surface. Since, the

impedance due to the electrolyte diffusion in the mesoporous TiO_2 layer is important with respect to that in the bulk solution, this term is frequently included in the Z_{TIO2} mesh of the circuit.

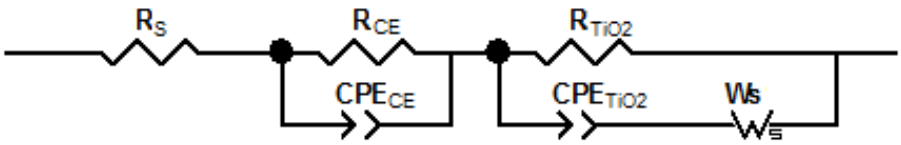

Figure 2.12 Electrical circuit model used to fit experimental EIS data of a DSSC under illumination.

Owing to the complexity of the DSSC system, and to the dependence of the interfacial processes kinetics on the specific cell composition, the assignment of equivalent circuits and the elucidation of processes occurring at the various device interfaces is never immediate and unambiguous. The observed spectra and the employed fitting circuit can undergo slight changes, depending on the TiO_2 layer structure, on the sensitizer and electrolyte nature, and each system should be singularly considered and analyzed.

For a deeper and more precise understanding of the electron transfer dynamics occurring at the electrolyte/counter electrode interface, useful in particular when new cathodic materials and electrolytes are investigated, a **symmetric (dummy) cell** made of two facing counter electrodes is prepared, and studied first by cyclic or linear sweep voltammetry in the dark. This measurement produces a voltammogram in which the slope of the linear interval, centered on the origin, is inversely proportional to the charge transfer resistance at the electrode surface, and the reached limiting current represents the highest current obtainable in the presence of the specific cathodic material and electrolyte combination employed, not accounting for the losses due to the anodic counter part (Figure 2.13).

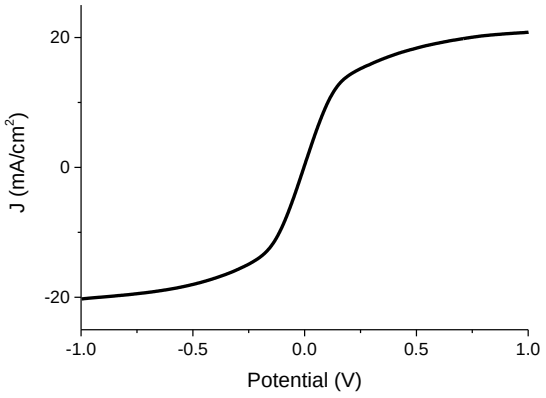

Figure 2.13 Voltammogram obtained by LSV for a dummy cell in the dark, made of PEDOT and $Co(bpy)_3$ electrolyte.

Secondly, EIS technique can be used, applying a V=0 potential in the dark, producing a Nyquist diagram consisting in two semicircles centered on the real axis. The smaller one at higher frequencies is ascribed to the charge transfer resistance at the counter electrode, whereas the largest at lower frequencies is attributed to the redox electrolyte diffusion resistance. This profile is reflected in the Bode phase diagram, where two frequency peaks arise in relation to the just mentioned processes.

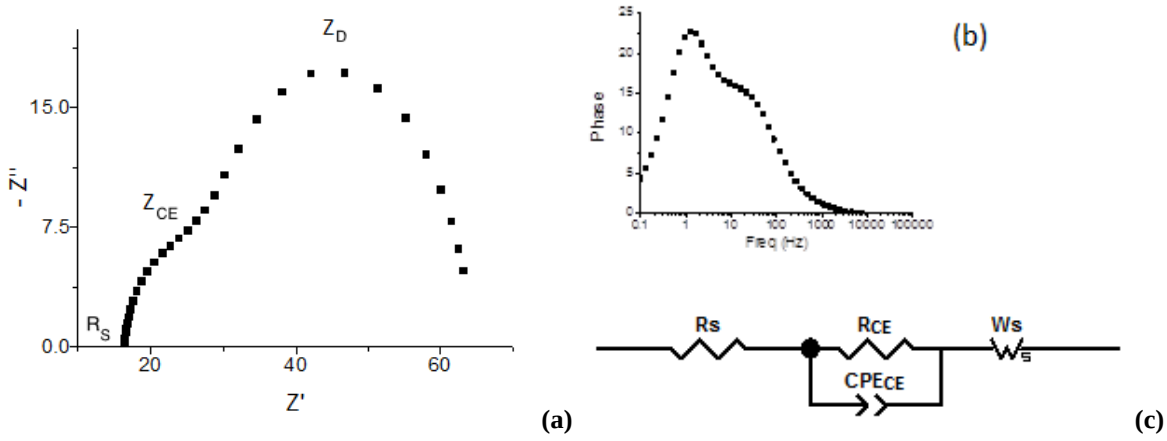

Figure 2.14 Experimental EIS data of a dummy cell made of PEDOT and $Co(dtb)_3$ electrolyte, measured at 0V under dark: Nyquist plot (a), Bode phase plot (b), electrical circuit model used to fit experimental data.

The equivalent circuit used to model this EIS spectrum is also reported in figure 2.14, where the counter electrode/electrolyte interface global impedance is represented by the parallel combination of a charge transfer resistance (R_{CE}) and a costant phase element (CPE_{CE}), in series with respect to a ohmic resistance Rs and a Warburg element identifying the electrolyte diffusion, element that can eventually be included in the CE mesh in the case of a highly porous electrodic material.
Due to the application of the Kirchhoff laws to the symmetric cell the equivalent resistance of the circuit is twice the resistance of each individual interface, while the equivalent capacitance is half the capacitance a single Helmholtz layer at the two symmetric electrodes.

2.3 Spectroscopic characterization

2.3.1 UV-visible spectroscopy

UV-visible spectroscopy measurements were performed in this thesis work to investigate the spectral profile of sensitizers, mediator complexes and electrodes, using a double beam JASCO V

570 spectrophotometer for the most part of the experiments, and an Agilent Cary 60 instrument for the measurements performed at University of North Carolina, regarding the work presented in Chapter 4. All experiments done were performed at room temperature.
The absorbance (A) of a sample at a specific wavelength is calculated from its transmittance (T) according to equation 2.17.

$$A(\lambda) = - \log T(\lambda) \qquad \text{(Eq. 2.17)}$$

where $T = I/I_0$, with I_0 and I being the incident and transmitted radiant intensity.

Thus, the recorded absorbance vs wavelength plots can give useful information for the DSSC application of certain materials and coloured molecules.
An important parameter that can be extracted is the molar extinction coefficient (ε), which is obtained by the Lambert-Beer's law:

$$A = \varepsilon \, l \, C \qquad \text{(Eq. 2.18)}$$

where C is the molar concentration of the species and l is the path length.

In the case of nontrasparent sensitized electrodes, found when the opaque TiO_2 paste (18NR-AO) was used, diffused reflectance spectra (R%) were recorded, by means of an integrating sphere (ISN-470 model, to enable R% measurements by the JASCO V 570 spectrophotometer), using a white $BaSO_4$ as 100% R% reference. In this operation mode, the spectrophotometer measures the back reflected light, diffusely scattered by the sample. The raw diffuse reflectance spectrum can then be corrected by means of the Kubelka-Munk transformation, which is comparable to the absorbance transformation in transmission spectroscopy. A transform of the measured spectroscopic observable is produced, which is approximately proportional to the absorption coefficient and hence to the sensitizer concentration, grafted on the opaque TiO_2 film. The Kubelka-Munk equation is expressed as follows:

$$F(R) = (1-R)^2 /2R = \varepsilon/s \qquad \text{(Eq. 2.19)}$$

Where R is the absolute reflectance of the sampled layer, ε is the molar absorption coefficient and s is the scattering coefficient.

Spectroelectrochemistry

This technique consists in the collection of absorption spectra while applying a potential to the studied system. For example it was employed in this thesis work to monitor the absorbance of

electrons in TiO_2, changing as their concentration changes under increasingly negative potential, in the context of a detailed dye regeneration study conducted at UNC.

Steady-state UV-vis absorption spectra were recorded on a Varian Cary 50 spectrophotometer, at room temperature, concomitant with bulk electrolysis of a standard three-electrodes cell. External biases were applied to a sensitized TiO_2 thin film, deposited on a FTO substrate working electrode, positioned diagonally in a 1 cm cuvette. A BAS CV-50W potentiostat was employed. Each potential step was held for around 2 to 3 minutes until the spectrum was invariant with time and the next potential was applied. A platinum disk counter electrode and an Ag/AgCl reference electrode (Bioanalytical Scientific Instruments, Inc.) in 0.5 M $LiClO_4$ acetonitrile solution were employed. The ferrocenium/ferrocene half-wave potential was measured at room temperature before and after each experiment and was used as an external standard to calibrate the reference electrode [1, 16].

2.3.2 Transient absorption spectroscopy

Electron transfer dynamics at the semiconductor/dye/electrolyte interface were studied mainly by time-resolved absorbance measurement in the ns-µs time domain. Following the excitation pulse, a population of excited dye molecules able to inject charge into the semiconductor is created. The electron injection is much faster (fs-ps) than the time resolution of the technique employed (ns), so that a population of oxidized dye molecules is instantaneously created. The decay of the oxidized dye absorption recorded in various conditions gives informations about the efficiency of charge transfer from the electron mediator and about the dynamics of electron recapture. Transient absorption spectroscopy (TAS) was used in particular to obtain the dye regeneration efficiencies in some of the studied dye/electrolyte systems.

Before the laser pulse (time zero), only dye molecules at the ground state, whose concentration and extinction coefficient are respectively $[A]_0$ and ε_A, are present in the sample. After excitation a population of oxidized dye is created, due to charge injection into TiO_2, with a certain concentration $[A^+]_t$ and extinction coefficient $\varepsilon_A{}^+$. For these reasons, absorption of the analysis light at a particular wavelength λ will be different before and after the laser pulse. The laser induced absorption variation is subjected to a temporal evolution, according to time evolution of the oxidized sensitizer population. The oscilloscope detects a time dependent tension which is proportional to the light intensity transmitted through the sample [7].

Before the excitation, the optical density of the sample is given by:

$$\log \frac{I_0}{I_t} = \varepsilon_A [A]_0 l = OD \qquad \text{(Eq. 2.20)}$$

where I_0 and I_t are light intensities transmitted at time 0 and t, and l is the optical path.

After excitation :

$$\log \frac{I_0}{I_t^+} = \varepsilon_A [A]_t l + \varepsilon_{A^+} [A^+]_t l = OD^+ \qquad \text{(Eq. 2.21)}$$

where $[A]_t = [A]_0 - [A^+]_t$

The resulting difference in optical density, detected by the oscilloscope, will be given by:

$$\Delta OD = \log \frac{I_0}{I_t} - \log \frac{I_0}{I_t^+} = (\varepsilon_{A^+} - \varepsilon_A)[A^+]_t \qquad \text{(Eq. 2.22)}$$

Usually the absorption coefficient of the oxidized dye (Ru(III)) is smaller than the absorption coefficient of Ru(II) (at least in large part of the visible region), thus ΔOD assumes negative values (bleaching). The considerations reported here are obviously of general validity and can be extended to every case in which the generation and evolution of a population of chemical species, with different absorption properties with respect to their initial state, is monitored spectroscopically. In many cases the excited state absorption can be stronger than the ground state, in this case ΔOD will be positive.

The *nanosecond transient absorption* apparatus is schematized in figure 2.15[17]:

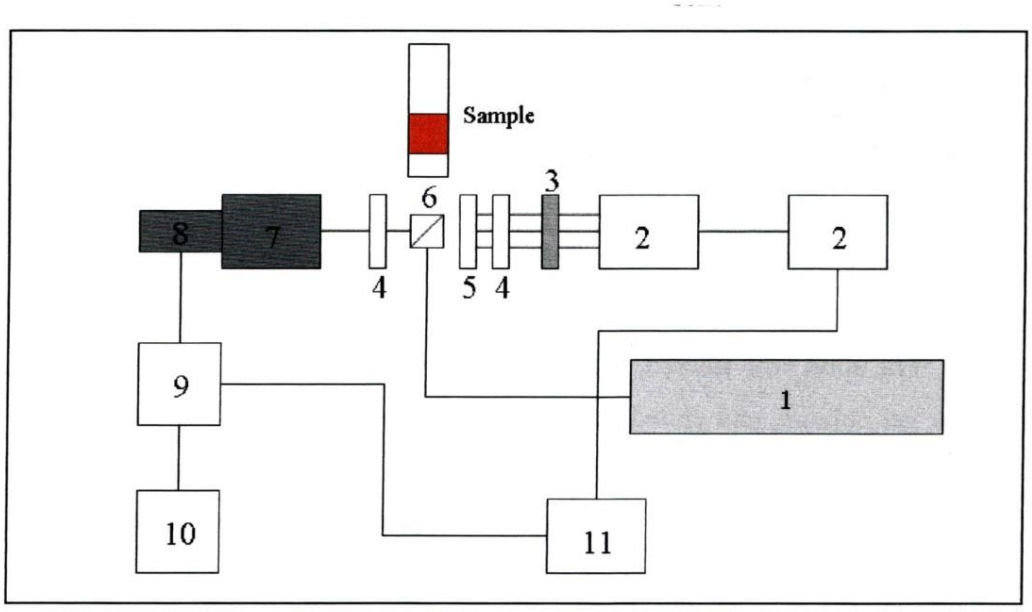

Figure 2.15 TAS apparatus: 1) Surelyte II Nd:YAG Laser; 2) Xe Lamp-Trigger; 3) Shutter; 4) Filter; 5) Diaphram; 6) Sample; 7) Monochromator; 8) Photomultiplier; 9) Oscilloscope; 10) Computer; 11) Switch.

The excitation source is a solid state Nd-Yag laser equipped with Q-switch and frequency multipliers in order to obtain 532, 355 and 266 nm excitation wavelengths, with a pulse amplitude

at half width of about 7 ns. Time resolved absorption studies were carried out using the 532 nm excitation. A typical pulse energy of ~2 $mJ \cdot cm^{-2}$ was employed, using a plano-concave lens and a combination of neutral filters. A continuous 150 Xe lamp generates the analysis light, which is oriented at 90° with respect to the excitation beam. A computer controlled external trigger sinchronizes all the components of the apparatus. The sample can be a solution or a solid sensitized TiO_2 film sintered on a microscope slide, that is oriented at 45° with respect to the excitation pulse. An interferential filter placed in front of the monochromator provided the elimination of the intense 532 nm light scattering. Appropriate cutoff and neutral filters can be added to avoid the TiO_2 electrons excitation and to eventually reduce the energy of the excitation or analysis light. Satisfactory signal to noise ratio were usually obtained by averaging from 10 to 30 shots. Signals from the photomultiplier (kinetic traces) were processed by means of a a Teledyne Lecroy Waverunner 604Zi (400 MHz, 10 GS/s) digital oscilloscope.

The just described setup was used in the part of the measurements performed at the University of Ferrara. Other measurements were conducted at the University of North Carolina (UNC), and a slightly different instrumental setup was involved [18]: samples were photo-excited by a frequency doubled, Q-switched, pulsed Nd:YAG laser (Quantel USA (BigSky) Brilliant B; 532 nm, 5-6 ns full width at half-maximum (fwhm), 1 Hz, ~10 mm in diameter) directed 45° to the film surface. A 150 W Xenon arc lamp coupled to a 1/4 m monochromator (Spectral Energy, Corp. GM 252) served as the probe beam (Applied Photophysics) that was aligned orthogonally to the excitation light. For detection at sub-100 μs time scales the lamp was pulsed with 80 V. Detection was achieved with a monochromator (Spex 1702/04) optically coupled to an R928 photomultiplier tube (Hamamatsu). Transient data were acquired on a computer-interfaced digital oscilloscope (LeCroy 9450, Dual 350 MHz). Typically 30 laser pulses were averaged at each observation wavelength over the range 380-800 nm for full spectra generation and 120-200 laser pulses were averaged for single wavelength measurements.

Transparent TiO_2 slides preparation

For what concerns the TAS measurements conducted on sensitized slides, immersed in the electrolytic solution, the transparent TiO_2 films were obtained, in Ferrara, by using the 18NR-T paste and applying the $TiCl_4$ post-treatment, as described in section 2.2.1. Alternatively, at UNC they were made with a transparent TiO_2 paste prepared by means of a literature reported procedure [19], based on $Ti(O\text{-}CH(CH_3)_2)_4$ (titanium tetraisopropoxide). The TiO_2 slides were then prepared by doctor blading the resulting paste, followed by sintering at 450 in air for 30 minutes.

Femtosecond transient absorption spectroscopy

To investigate ultrafast processes taking place in the sub-nanosecond timescale, like the electron injection driven by the dye photoexcitation, an investigation was conducted in Milan in collaboration with Prof. G.N.Cerullo [20]. The employed femtosecond transient absorption (TA) spectrometer is based on an amplified Ti:sapphire laser (Coherent Libra), generating 2-mJ, 100 fs pulses at 800 nm wavelength and 2-kHz repetition rate. A 300-μJ fraction of the pulse energy is used for the experiments, and is split into two beams. The first beam feeds an optical parametric amplifier, generating tunable pump pulses in the visible with ~70-fs duration; the second beam is focused in a CaF_2 crystal, generating a broadband white-light continuum (WLC) spanning the visible range (370-750 nm) and used as a probe. To avoid optical damage, the CaF_2 plate is slowly scanned in the beam focus. Pump and WLC probe pulses are non-collinearly focused on the sample and the transmitted probe, spatially selected by an iris, is sent to a silicon spectrometer capable of single-shot detection at the full 2-kHz repetition rate of the laser. The pump is modulated by a mechanical chopper at 1 kHz and the differential transmission spectra, defined as $\Delta T/T = (T_{pump\ on} - T_{pump\ off})/T_{pump\ off}$, are recorded as a function of probe wavelength and delay. Chirp-free ΔT/T maps by using a home-made dechirping algorithm.

2.3.3 Steady-state and time-resolved photoluminescence spectroscopy

Photoluminescence spectroscopy methods, at steady state and resolved in time, consist in recording the PL spectrum of an excited fluorophore at steady-state, and the PL decay with time after laser excitation, respectively.

These two techniques were employed in this thesis work to monitor PL quenching processes in solution of fluorescent ruthenium sensitizers, by specific redox mediators. Steady-state PL spectra were recorded using an ISS K2 fluorimeter while time-resolved PL single wavelength decays were acquired on a nitrogen dye laser with excitation centered at 455 nm [21] . Decays were monitored at the PL maximum and averaged over 180 scans.

To briefly describe the fluorescence quenching theory, the possible quenching mechanisms in a solution containing a fluorophore and a quencher species are depicted in figure 2.16 [22].

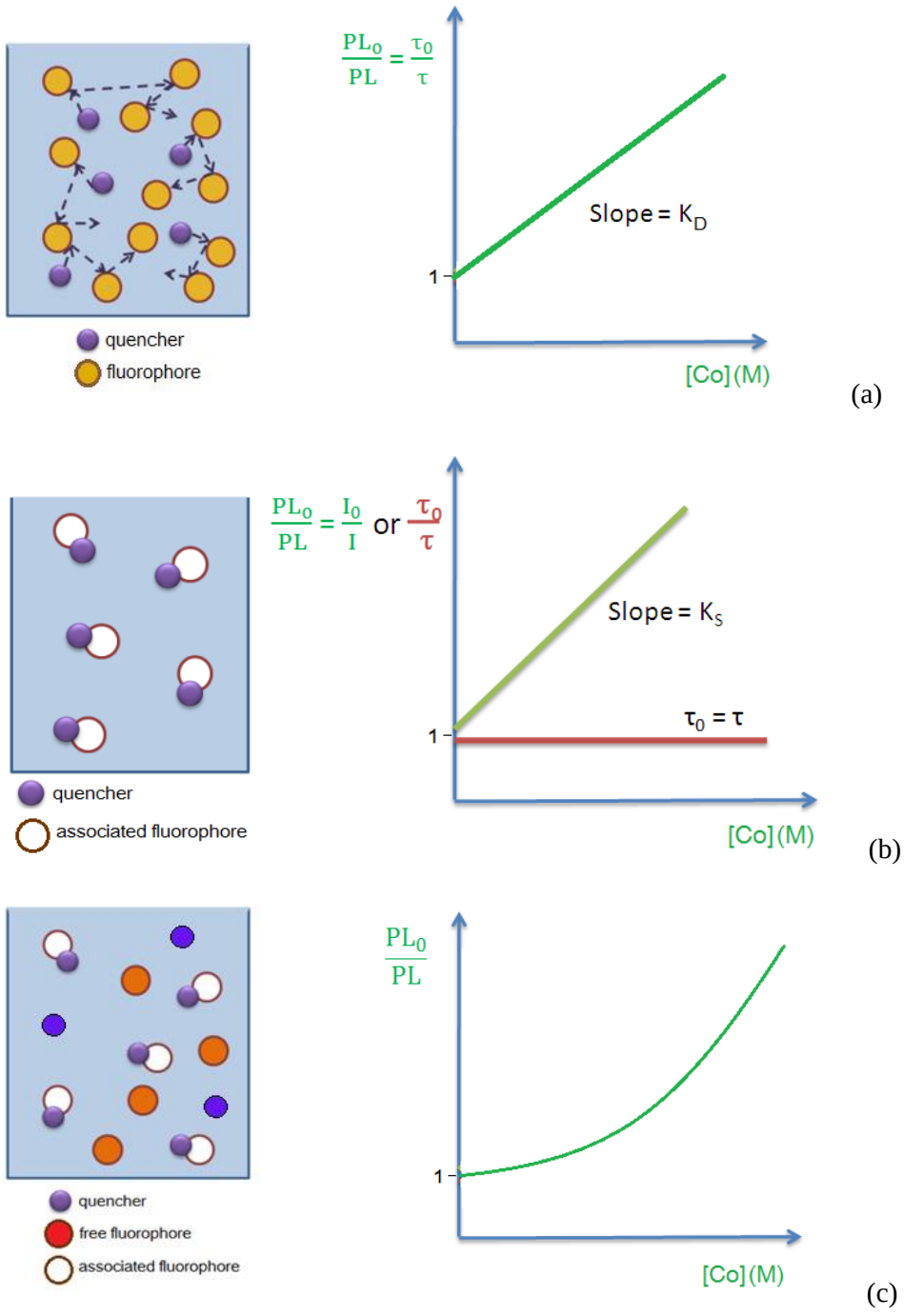

Figure 2.16 Possible mechanisms for PL quenching in solution: dynamic (a), static (b), and dynamic + static (c) quenching processes.

In the *diffusional (dynamic) mechanism*, represented in figure 2.16 a, the PL quenching is caused by the collision between fluorophore and quencher molecules in solution. Collisional quenching of fluorescence is described by the Stern-Volmer equation:

$$PL_0/PL = 1 + k_q\tau_0[Q] = 1 + K_D[Q] \qquad (2.23)$$

where PL_0 and PL are the photoluminescence intensities in the absence and presence of quencher, respectively; k_q is the bimolecular quenching constant; τ_0 is the lifetime of the fluorophore in the absence of quencher, and [Q] is the concentration of quencher. The Stern-Volmer quenching constant is given by $K_D = k_q\tau_0$. If the quenching is known to be dynamic, the Stern-Volmer constant will be represented by K_D. Otherwise this constant will be described as K_{SV}. Quenching data are usually presented as plots of PL_0/PL versus [Q]. This is because PL_0/PL is expected to be linearly dependent upon the concentration of quencher. A plot of PL_0/PL versus [Q] yields an intercept of one on the y-axis and a slope equal to K_D (Figure 2.16 a).

A linear Stern Volmer plot is generally indicative of a single class of fluorophores, all equally accessible to quencher. It is important to recognize that observation of a linear Stern-Volmer plot does not prove that collisional quenching of fluorescence has occurred, indeed we will see that static quenching also results in linear Stern-Volmer plots. Static and dynamic quenching can be distinguished by lifetime measurements. In fact collisional quenching, that results from diffusive encounters between the fluorophore and quencher during the lifetime of the excited state, is a time-dependent process, and it causes a decrease in the PL lifetime, or more precisely an equivalent decrease in fluorescence intensity and lifetime:

$$\tau_0/\tau = PL_0/PL = 1+ k_q\tau_0[Q] \qquad \text{(Eq. 2.24)}$$

The decrease in lifetime occurs because quenching is an additional rate process that depopulates the excited state. The decrease in yield occurs because quenching depopulates the excited state without fluorescence emission.

Quenching can also occur as a result of the formation of a nonfluorescent ground-state complex between the fluorophore and quencher (Figure 2.16 b).

$$F + Q \overset{K_S}{\leftrightarrow} [F\text{---}Q] \qquad \text{(Eq. 2.25)}$$

When this complex absorbs light it immediately returns to the ground state without emission of a photon. This is called *associational (static) mechanism*, which can also be described by the Stern-Volmer equation:

$$PL_0/PL = 1 + Ks[Q] \quad \text{(Eq. 2.26)}$$

Also in this equation the dependence of PL_0/PL on [Q] is linear, which is identical to that observed for dynamic quenching, except that the quenching constant is now the association constant, that is the equilibrium constant for the non-emitting complex formation. If the associated species is nonfluorescent, then the fraction of the fluorescence that remains (PL/PL_0) is given by the fraction of the total fluorophores that are not interacting with the quencher. This is why static quenching

does not decrease the lifetime because only the fluorescent molecules are observed, and the the non-associated fluorophores have the unquenched lifetime τ_0 ($\tau_0/\tau = 1$)

Besides the steady-state and time-resolved PL measurements, one additional method to distinguish static and dynamic quenching is by careful examination of the absorption spectra of the fluorophore. Collisional quenching only affects the excited states of the fluorophores, and thus no changes in the absorption spectra are expected. In contrast, ground-state complex formation will frequently result in perturbation of the absorption spectrum of the fluorophore.

Anyhow, in many instances the fluorophore can be quenched both by collisions and by complex formation with the same quencher. The characteristic feature of the Stern-Volmer plots in such circumstances is an upward curvature,concave towards the y-axis (Figure 2.16 c). Then the fractional fluorescence remaining (PL/PL_0) is given by the product of the fraction not complexed and the fraction not quenched by collisional encounters

$$PL_0/PL = (1 + K_D[Q])(1 + K_S[Q]) \qquad \text{(Eq. 2.27)}$$

This modified form of the Stern-Volmer equation is second order in [Q], which accounts for the upward curvature observed when both static and dynamic quenching occur for the same fluorophore.

References

(1) Allen J. Bard A.J., Faulkner L.R., "Electrochemical Methods, Fundamentals and Applications" 2nd Ed. *Wiley* (**2001**)

(2) University of Cambridge, Department of Chemical Engineering and Biotechnology website http://www.ceb.cam.ac.uk/research/groups/rg-eme/teaching-notes/linear-sweep-and-cyclic-voltametry-the-principles

(3) J.E.B.Randles, "Kinetics of rapid electrode reactions", *Discuss.Faraday Soc.*, **1947**, 1, 11-19

(4) A. Lasia, "Electrochemical Impedance Spectroscopy and Its Applications, Modern Aspects of Electrochemistry", B. E. Conway, J. Bockris, and R.E. White, Edts., Kluwer Academic/Plenum Publishers, New York, **1999**, Vol. 32, p. 143-248.

(5) Lai, W. (**2007**) "Impedance spectroscopy as a tool for electrochemical study of mixed conducting ceria". Dissertation (Ph.D.), California Institute of Technology.

(6) Nusbaumer, H. In Alternative Redox Systems for Dye Sensitized Solar Cell; EPFL: Lausanne, **2004**; pp 42-46

(7) Caramori S., Chemistry Ph.D thesis, "Electron transfer mediators for DSSC based on Co(II) coordination compounds", **2004,** University of Ferrara

(8) Christiana Honsberg and Stuart Bowden, Arizona State University's Solar Power Lab http://www.pveducation.org/

(9) Hagfeldt A., Boschloo G., Sun L., Kloo L., Pettersson H., , *Chem. Rev*. **2010**, 110, 6595–6663

(10) A. Yella, H.W. Lee, H. N. Tsao, C. Yi, A. K. Chandiran, Md.K. Nazeeruddin, E. W.G. Diau, C.Y. Yeh, S. M Zakeeruddin, M. Grätzel, *Science* **2011,** vol 334, pag 629

(11) Q.Wang, J.E. Moser, and M.Gratzel, *J. Phys. Chem. B* **2005**, 109, 14945-14953

(12) W.Qing, S. Ito, M. Grätzel, F. Fabregat-Santiago, I. Mora-Seró, J.Bisquert, T. Bessho, H. Imai. *J.Phys. Chem.B* **2006,** 110, 50, 25210-25221.

(13) M. Adachi,M.Sakamoto, J. Jiu, Y. Ogata, S. Isoda, *J. Phys. Chem. B* **2006**, 110, 13872-13880

(14) R. Kern, R. Sastrawan, J. Ferber, R. Stangl, J. Luther, *Electroch. Acta* **2002,** 47, 4213/4225

(15) Feldt, S. **2013**. Alternative Redox Couples for Dye-Sensitized Solar Cells. Acta Universitatis Upsaliensis. Digital Comprehensive Summaries of Uppsala Dissertations from the Faculty of Science and Technology 1017. 80 pp. Uppsala. ISBN 978-91-554-8595-5.

(16) K.C. D. Robson, K. Hu, G.J. Meyer, C.P. Berlinguette *J. Am. Chem. Soc.* **2013**, 135, 1961−1971

(17) M.Mba, M. D'Acunzo, P. Salice, T. Carofiglio, M.Maggini, S. Caramori, A. Campana, A. Aliprandi, R.Argazzi, S. Carli, and C.A. Bignozzi *J. Phys. Chem. C* **2013**, 117 (39), 19885- 19896

(18) Ke Hu Ph.D dissertation, **2014**, Johns Hopkins University "Fundamental insights into the charge transfer processes in dye-sensitized solar cells: hole transfer, regeneration, charge recombination, and electron injection"

(19) Heimer, T. A., D'Arcangelis, S. T., Farzad, F., Stipkala, J. M. & Meyer, G. J. *Inorg. Chem.* **1996,** 35, 5319–5324

(20) T. Virgili , G. Grancini , E. Molotokaite , I. Suarez-Lopez , S. K. Rajendran , A. Liscio , V. Palermo , G. Lanzani , D. Polli , and G. Cerullo *Nanoscale*, **2012**,4, 2219-2226

(21) Argazzi, R.; Bignozzi, C. A.; Heimer, T. A.; Castellano, F. N.; Meyer, G. J. *Inorg. Chem*. **1994**, 33, 5741−5749

(22) Lakowicz J. R. "Principles of Fluorescence Spectroscopy", *Springer* **2006,** Chapter 8, Third Edition

Chapter 3: Viable approaches for the sensitized photoelectrode improvement

To improve the overall cell efficiency by acting on the photoanodic component, the factors of light harvesting, charge injection and conversion into current have to be enhanced, while the recombination processes of the injected electrons with the oxidized dye and the redox mediator need to be reduced.

It has been previously mentioned how important passivation methods are in protecting the photoelectrode surface from recombination events occurring between the injected electrons and the oxidized redox mediator, which can take place either at the interface between the nanocrystalline oxide and the electrolyte, or at areas of the anodic contact (FTO) that are exposed to the electrolyte. In this sense, a new passivation method was developed, which consisted in treating the sensitized photoanode surface with a layer of commercially available short-chain silanes. The result was efficient suppression of electronic recombination, process which penalizes in particular solar cells based on cobalt mediators and common ruthenium sensitizers, so that higher cell efficiencies become available bypassing the necessity for highly engineered and expensive dye molecules.

Subsequently, a new category of β-monosubstituted zinc porphyrin dyes was characterized by the photophysical and photoelectrochemical point of view. Big efforts have been done over years in developing new sensitizers characterized by broad absorption in the visible spectrum, leading to high IPCE, and by bulky structures capable of sterically avoiding electronic recombination processes as well as surface aggregation. With such purposes, these porphyrinic sensitizers were designed, displaying a broad absorption in the visible range and high steric hindrance. The extensive study carried out on these dye molecules resulted in good spectroscopic properties and high cell performances, comparable to those obtained with the common meso push-pull structured porphyrin sensitizers, with the added advantage of a faster one-pot synthetic route that makes them cheaply available.

3.1 A surface passivation method to enhance efficiency in cobalt based DSSC

3.1.1 Introduction

The Iodine/Iodide redox couple is the most common choice for high performing electrolytes in liquid based DSSC [1-3], although polypyridine Cobalt complexes have emerged as one of the most promising classes of alternative redox mediators [4-7] which have scored absolute record efficiencies when used in conjunction to custom tailored dyes based on push-pull structures employed in optimized cell configurations. The use of unsubstituted kinetically fast redox couples like the simple $[Co(bpy)_3]^{2+}$ leads to high efficiencies, thanks to a relatively fast dye regeneration, good exchange currents at the catalytic counter electrodes and a reasonably efficient mass transport, at least in low viscosity electrolytes. One of the main drawbacks of fast Co(III)/(II) couples is their ability to recapture photoinjected electrons, which are mostly trapped in the TiO_2 surface states, yielding high recombination (dark) current. This drawback can be almost entirely eliminated by using bulky dyes having enough steric hindrance and assembling on the titania surface in such a way that the surface is completely screened from Co(III). Very successful examples of this approach have been provided first by Hagfeldt, with the D35 [8] dye, by Graetzel with the Y123 [9], YD2-O-C8[10] and SM315 [11] and by Koumura and Bach with the MK2 [12,13] sensitizers. Nevertheless, there is a limited choice of these types of highly engineered dyes, which are usually obtained through demanding and expensive multistep synthetic routes. Thus, it would be interesting for both fundamental and applicative reasons to devise general strategies for surface passivation, which can be applied to the widest numbers of already available dyes, including the existing ample variety of well known Ru (II) complexes, without requiring further chemical modification of the dyes themselves. Usually, with ruthenium (II) sensitizers [5, 6, 14-17], only limited performances have been achieved with cobalt electrolytes. The only notable example of a sterically hindered cyclometalated Ru(II) dye exhibiting comparable efficiencies (8.6%) under 1 sun illumination with both cobalt ($[Co(phen)_3^{3+/2+}]$) and I^-/I_3^- redox mediators, in the presence of chenodeoxycholic acid (CDCA), was described by Graetzel's group [18].

Besides achieving TiO_2 surface passivation by adopting either sterically hindered sensitizers or bulky redox mediators, the use of surface post-treatments based on molecular co-adsorbates can be a simple, reproducible and convenient route to protect exposed surface sites, left uncovered by the dye, from which recombination with the oxidized electrolyte would predominantly occur.

Functionalization of hydrophilic inorganic surfaces with silanes is a well-known procedure that yields very robust coupling between organic and inorganic materials [19-21]. Despite the large amount of literature about new sensitizers, alternative electrolytes and cathodic materials, the

employment of silane functionalization as a photoanode passivation tool has not been deeply investigated [22-24]. Some recently published results, concerning a family of multi-branched push-pull organic sensitizers, demonstrate that it is possible to improve charge collection efficiency in cobalt based DSSC by co-adsorbing long chain alkyl-silanes as surface passivating agents [25].

Here we extend and confirm the previous observation, showing that it is possible to achieve an even larger improvement in power conversion efficiency by the careful choice of short-chain silanes like aminopropyl-triethoxysilane (**APTS)** and trimethylammoniumpropyl-trimethoxysilane chloride (**TMAS**), featuring a positively charged end, which should help screening the TiO_2 surface from Co^{3+} species, by both steric and electrostatic repulsion. The $Co(bpy)_3^{2+/3+}$ redox couple was used, together with the rather common $[Ru^{II}(H_2DCB)(dnbpy)(NCS)_2]$ (**Z907**) sensitizer, in a comparative study conducted by means of photoelectrochemical techniques, which involved as a term of comparison the commonly used hexadecyl-(triethoxy)silane (**C16**).

Structures of the commercially available silanes employed in this study are reported in figure 3.1.

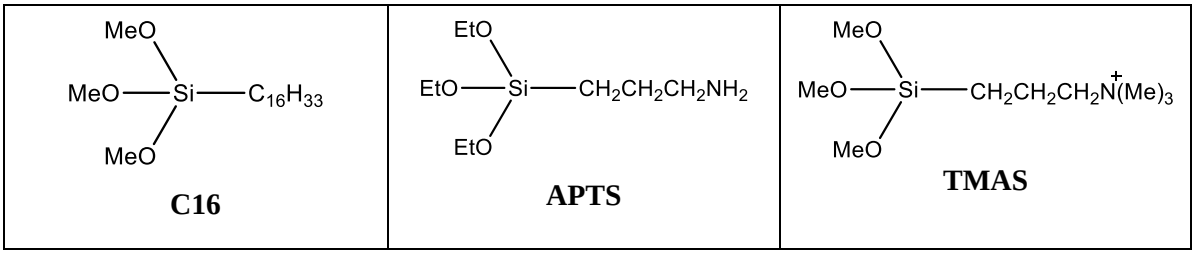

Figure 3.1 Structures of the silanes used in this study

3.1.2 Experimental

Materials

All chemicals and solvents were Sigma Aldrich products and were used as received, except for trimethylammoniumpropyl-trimethoxysilane chloride (50% solution in methanol), by ABCR-Gelest. Z907 dye and TiO_2 colloidal paste (18NR-T) were purchased by Dyesol, P25 TiO_2 from Degussa.

Platinized FTO counter electrodes were annealed at 400°C for 10 min in air immediately before use.

$[Co(bpy)_3](CF_3SO_3)_2$ and $[Co(bpy)_3](PF_6)_3$ complexes were prepared according to literature procedures [26].

Solar Cells Fabrication

We will use the terms **Z907**, **DCA**, **C16**, **TMAS** and **APTS** to indicate DSSC assembled with pure Z907 dye, Z907/20mM Deoxycholic acid, hexadecyl-(triethoxy)silane, trimethylammoniumpropyl-trimethoxysilane and aminopropyl-triethoxysilane respectively.

The TiO_2 blocking underlayer was obtained in this work by immersing the well cleaned FTO in 0.2 M $TiCl_4$ at room temperature overnight. The resulting slides were rinsed with deionized water and heated at 450 C° for 30 minutes. Mesoporous titania films were prepared according to the procedure described in chapter 2.2.1, with final $TiCl_4$ treatment. Subsequently, photoanodes were dipped for 24 hours in an ethanol solution of 0.1 mM Z907, or 0.1mM Z907 and 20mM DCA.

The silane post-treatment consisted in the immersion of the Z907 dyed photoanodes in a 0.1% v/v solution of the appropriate alcoxy-silane in toluene, for 1 hour at 55-60°C. Afterwards the electrodes were rinsed with toluene several times and dried under air before use.

Solar cells were equipped with transparent platinum counter electrodes and assembled in open configuration, as described in section 2.2.3. The active cell area was 0.25 cm^2.

The electrolyte formulation used for the DSSC characterization was based on $Co(bpy)_3^{3+/2+}$: 0.18M Co(II)/0.028M Co(III)/0.1M $Li(CF_3SO_3)$ in acetonitrile. In some cases 0.2 M 4-tert-butyl-pyridine (TBP) was also added.

Photoelectrochemical Characterization

Current−voltage measurements were performed at a scan rate of 20 $mV \cdot s^{-1}$. Cell performances were evaluated under AM 1.5 illumination (ABET sun simulator). Electrochemical Impedance Spectroscopy (EIS) potentiostatic measurements in DSSC were performed at open-circuit potential (Voc) by applying a sinusoidal perturbation of the amplitude of 10 mV in the 10^5-10^{-2} Hz frequency range. The electric equivalent of the cell at Voc is represented in figure 3.2, where the circuit elements modeling the TiO_2/electrolyte and the counter electrode (CE)/electrolyte interfaces are reported.

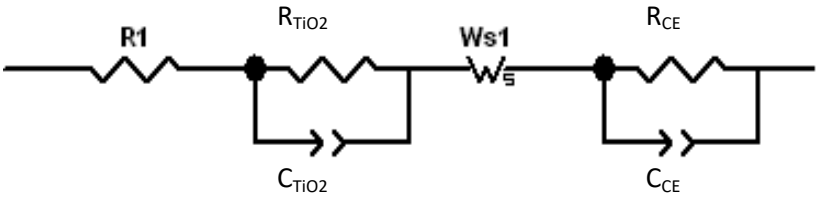

Figure 3.2 Electrical circuit model used to fit experimental EIS data at open circuit

IPCE spectra were collected with a custom built apparatus comprising an Applied Photophysics Monochromator, a 175 W Xe source (Luxtel) and various optical elements. Short circuit

photocurrents were measured with an Agilent 34301 A multimeter while incident irradiance was provided by a calibrated silicon photodiode (OSD 100 7Q).

Computational modeling

Computational studies were carried out by using Gaussian 09 C02 revision for windows. The geometry of a TiO_2 surface slab (101) ($Ti_{64}O_{128}$) was optimized at the Molecular Mechanics-Universal force Field (MM-UFF) level with charge embedding. Ground state equilibrium geometries of Z907, TMAS and $[Co(bpy)_3]^{3+}$ were optimized at the DFT-B3LYP level with a LANL2DZ basis set for the coordination complexes or with a 6-31G* set in the case of the organo-siloxane. In order to preserve the accurate ground state geometry of the molecular species, obtained by the DFT correlated method, the optimization of the molecular species bound to TiO_2 was accomplished by freezing the internal coordinates of the adsorbates with the exception of either the Ti-O-C or Ti-O-Si bond and of the first neighboring atoms of the TiO_2 slab, which were optimized at the MM-UFF level. All calculations were performed in vacuo.

3.1.3 Results and discussion

Photoelectrochemistry

The sensitized photoanodes absorption spectra are represented in figure 3.3, where the well defined 530 nm band, arising from the lowest MLCT transitions of Z907, can be observed.

While it is known that coadsorption of sensitizers and bile acids yields a lower dye surface coverage [27], in our case, where coadsorption was carried out by using 20 mM **DCA**, the absorption spectrum was not significantly modified with respect to the untreated sample, showing an almost perfect overlap at $\lambda > 550$ nm (figure 3.3, blue and black lines). On the other hand, a slight desorption was observed following silanization, with entirely analogous results regardless of the employed alkoxy silane specific structure. However this effect is minor, leading to a 3% order variation of the maximum optical density at 530 nm, along with a blue shift of ca. 5 nm (figure 3.3, purple line). Thus, the high LHE (Light Harvesting Efficiency) is substantially preserved with the silanized photoanodes, overcoming the 90 % in a wide region of the visible ranging from 550 to 400 nm.

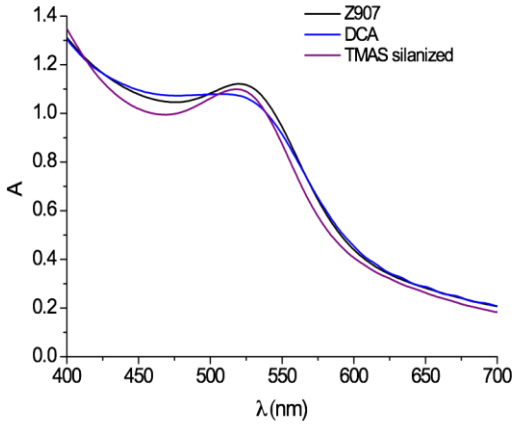

Figure 3.3 Visible spectra of Z907 sensitized photoanodes: untreated Z907 (black); Z907 coadsorbed in the presence of 20 mM DCA; Z907 after TMAS post-treatment (0.1 % v/v in toluene at 60 °C for 1h)

JV curves under light and dark are shown in figure 3.4 and the relative photovoltaic parameters are summarized in table 3.1. Initially, to point out more clearly the differences in the intrinsic passivation properties of the different photoanodes, an electrolytic mixture based on the $Co(bpy)_3^{2+/3+}$ redox couple, in the presence of 0.1 M Li^+ and in the absence of additional passivating additives, like 4-tert-butylpyirdine (TBP) [28,29], Gu-NCS [30] or N-alkyl-benzimidazoles [31,32], was used.

It can be observed that efficiencies vary in the order Z907 < Z907/**DCA** < **C16** < **TMAS** < **APTS.** This trend can be explained by differences in the recombination rate involving Co(III), as highlighted by the dark currents, whose threshold varies in the same order. It can be observed that the Z907 dye, despite the presence of long nonyl chains in the 4,4' position of the bipyridine, is not bulky enough to suppress the charge recombination arising from the kinetically fast Co(II)/(III) couple, as evidenced by both low open circuit photovoltage (Voc) and short circuit photocurrent density (Jsc), leading to poor efficiency values (0.6%). A modest improvement was achieved using **DCA** as coadsorbate, resulting in a significant increase of Voc (from 0.33 to 0.5 V) but in persistently modest Jsc (4.3 mA/cm^2) and FF (0.39). It appeared thus clear that, within the explored procedures, silanization was the best passivation strategy, leading, in the best cases, to either 5 or 6-fold improvements in cell efficiency. In particular, although the long chain hexadecyl-(triethoxy)-silane (**C16**) efficiently screened the TiO_2 surface against electron recapture, yielding an open circuit voltage of 0.6 V, the best performances were obtained with the comparatively shorter chain **APTS** and **TMAS** co-adsorbates, resulting in photocurrents in the range of 9-10 mA/cm^2 and in Voc > 0.6 V. In the case of **TMAS**, the highest photocurrent (10.7 mA/cm^2) was offset by a lower Voc and FF with respect to **APTS**, and the resulting efficiency was 18% lower.

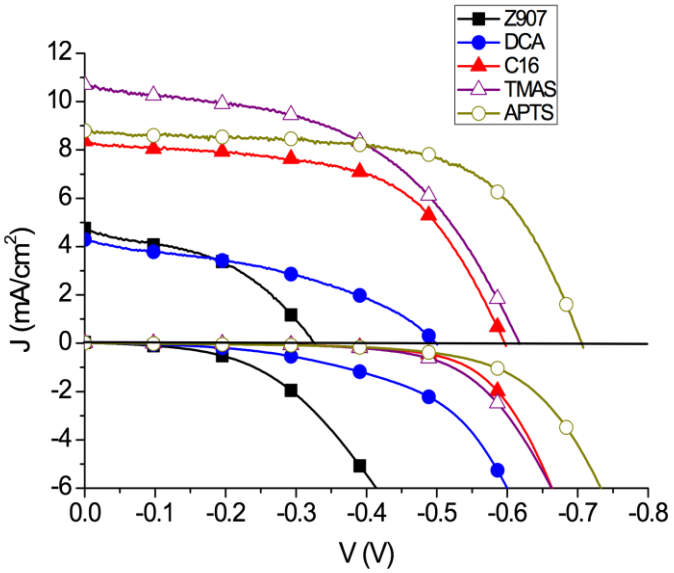

Figure 3.4 JVs of $Co(bpy)_3^{2+/3+}$ based DSSC equipped with transparent TiO_2 photoanodes, modified by different passivating agents: untreated electrodes (black); **DCA** (blue); **C16** (red); **TMAS** (purple); **APTS** (olive). 0.1 W/cm^2 A.M. 1.5 G illumination

	Voc (V)	**Jsc (mA/cm^2)**	**FF**	**η (%)**
Z907	0.33	4.75	0,42	0,66
DCA	0.5	4.30	0,39	0,84
C16	0.6	8.36	0,57	2,80
TMAS	0.62	10.70	0,50	3,30
APTS	0.7	8.81	0,64	3,94

Table 3.1 Efficiency parameters obtained in DSSC based on transparent TiO_2 photoanodes: open circuit voltage (Voc); short circuit photocurrent density (Jsc); fill factor (FF) and power conversion efficiency (η)

A trend similar to that observed on transparent TiO_2 electrodes was confirmed on semi-opaque photoanodes (figure 3.5 a), fabricated with an aqueous suspension of Degussa P25 TiO_2 in the presence of acetylacetone [33].

In this latter case the different particle size and the presence of larger light scattering aggregates may influence the density of surface trap states and hence the overall recombination kinetics. Although the photocurrent was generally improved, due to increased light scattering which enhanced LHE, a decreased Voc and FF were generally observed, resulting in the best η, observed also in this case with APTS, of the order of 3.4%. The photoaction spectra (IPCE vs λ), reported in figure 3.5 b, were qualitatively consistent with the JV curves, where, at short circuit, the top photocurrent, exceeding 10 mA/cm^2, was measured following the TMAS treatment, allowing to

reach IPCE values > 70%, nearly doubling the maximum monochromatic conversion obtained with the untreated photoanode.

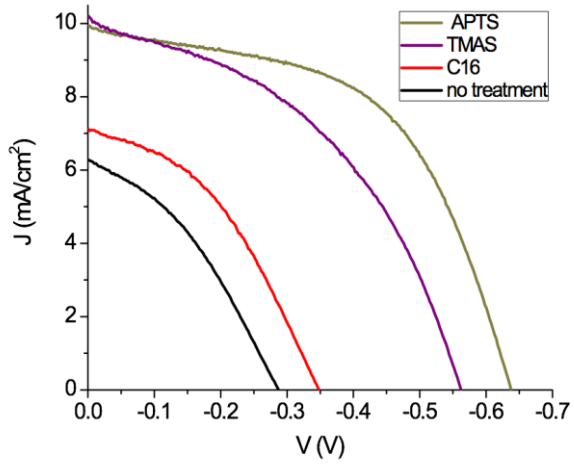

(a)

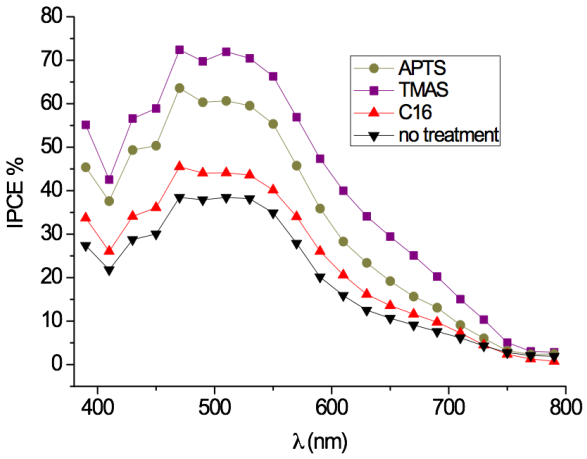

(b)

Figure 3.5 JV curves (0.1 W/cm^2 A.M. 1.5 G) (a) and IPCE spectra (b) recorded with semi-opaque TiO_2 photoanodes modified by different passivating agents: untreated electrodes (black); **C16** (red); **TMAS** (purple); **APTS** (olive)

The improved results can be clearly explained by reduced charge recombination, involving both TiO_2 and the exposed FTO collector, as evidenced by dark current-voltage curves in symmetric dummy cells based on sensitized TiO_2 electrodes where various combinations of passivating treatments, including the presence of compact TiO_2 underlayers at the FTO collector, were employed (figure 3.6). Interestingly the dark current varied in the order: (TiO_2 + Z907) > (TiO_2 + blocking underlayer + Z907) > (TiO_2 + Z907 + APTS) > (TiO_2 + blocking underlayer + Z907 + APTS), indicating that the APTS silane behaves as a barrier against charge recombination, by adsorbing on both the FTO and the TiO_2 surfaces. It is also evident that the presence of the compact TiO_2 blocking underlayer alone is not sufficient to achieve a complete suppression of the

back recombination involving Co(III); these results are consistent with previous observations made on a family of push-pull multi-branched dyes [25].

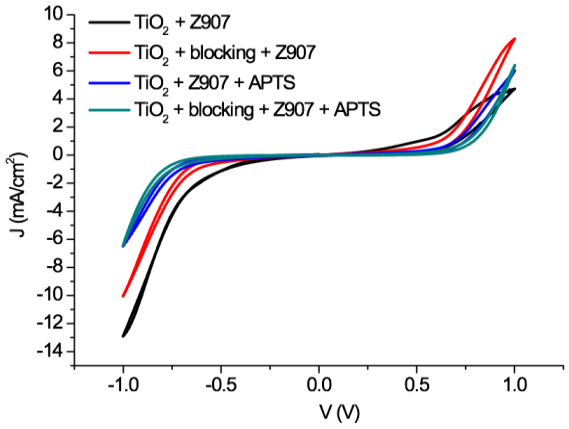

Figure 3.6 CVs on symmetric dummy cells (25 μm thick spacer) based on sensitized TiO_2 electrodes in the presence of various passivating treatments. Scan rate 5 mV/s

In order to develop a more quantitative understanding of the recombination kinetics related to the different passivation conditions, Electronic Impedance Spectroscopy (EIS) analysis was conducted on the cells whose performance is reported in figure 3.4. Measurements were performed at Voc under illumination (1 sun), comparing the basic cell, consisting of Z907 sensitized TiO_2 photoanodes, to the equivalent cells where the silane post-treatment was adopted.

In the complex plane plots (Nyquist plots, figure 3.7 A and B), a maximum of three depressed semicircles was individuated [34]: starting from the left, at high frequency a first small semicircle is present, ascribed to the charge transfer processes occurring at the counter electrode/electrolyte interface. Following, a wider loop can be found, originated by the charge transfer at the TiO_2/electrolyte interface [35]. Finally, at low frequency, a third loop is associated with the diffusional mass transport of the cobalt redox couple. In the Nyquist plots, high charge transfer resistance (large arcs) and low capacitance values are usually symptomatic of efficient recombination processes, resulting in a depletion of the stationary electron density in the TiO_2. This was observed for untreated **Z907** and **DCA** devices. Indeed, the chemical capacitance [36] is related to the occupied density of the states (DOS) in the TiO_2 by the formula:

$$DOS = (6.24 \times 10^{18}) \times C_{\mu}/[d(1-p)] \qquad \text{(Eq. 3.1)}$$

where C_{μ} is the capacitance per unit area, d is the thickness of the TiO_2 film, and p is the porosity [37].

In the correspondent imaginary (-Zi) vs frequency plot (figure 3.7 C), the middle-high ($10\text{-}10^3$ Hz) frequency peak corresponds to the charge transfer kinetics involving the recapture of photoinjected electrons by Co(III). The characteristic frequency f_{max}, corresponds to the effective rate constant for recombination k_{eff} ($f_{max} = k_{eff}$) [38], and becomes smaller for silanized DSSC, as can be appreciated

from the red, purple and olive curves in figure 3.7 C, where in the best cases (TMAS and APTS) the frequency of middle frequency peak decreases by at least one order of magnitude with respect to the untreated cell (table 3.2). As a result of the suppressed charge recombination, the electron lifetime τ_{el}, $[2\pi f_{max} = (R_{CT}C_{\mu})^{-1} = \tau_{el}^{-1}]$ undergoes a 10-20 fold increase when passing from the untreated cell (τ_{el} =0.14 ms) to the TMAS and APTS passivated cells (τ_{el} =15 ms and 26 ms respectively). It emerges that, in the case of **Z907** and **DCA** devices, recombination rate is so high that it is not possible to distinguish the typical three semicircles profile in the Nyquist plots (figure 3.7 A, blue and black lines), due to the overlap between the TiO_2/electrolyte frequency peak, shifted to high frequencies, and the fast charge transfer at the catalytic counter electrode, occurring in the 10^3-10^4 Hz frequency range. Clearly, the electron lifetime given in these conditions is only an approximate estimate of the comparative charge recombination kinetics, given that the different cells were providing different V_{OC}s and hence different chemical capacitances, affecting differently the charge recombination rate. Thus, EIS measurement were performed in a wider direct potential region, where the chemical capacitance of the TiO_2 is expected to prevailingly contribute to the overall capacitance of the photoanode.

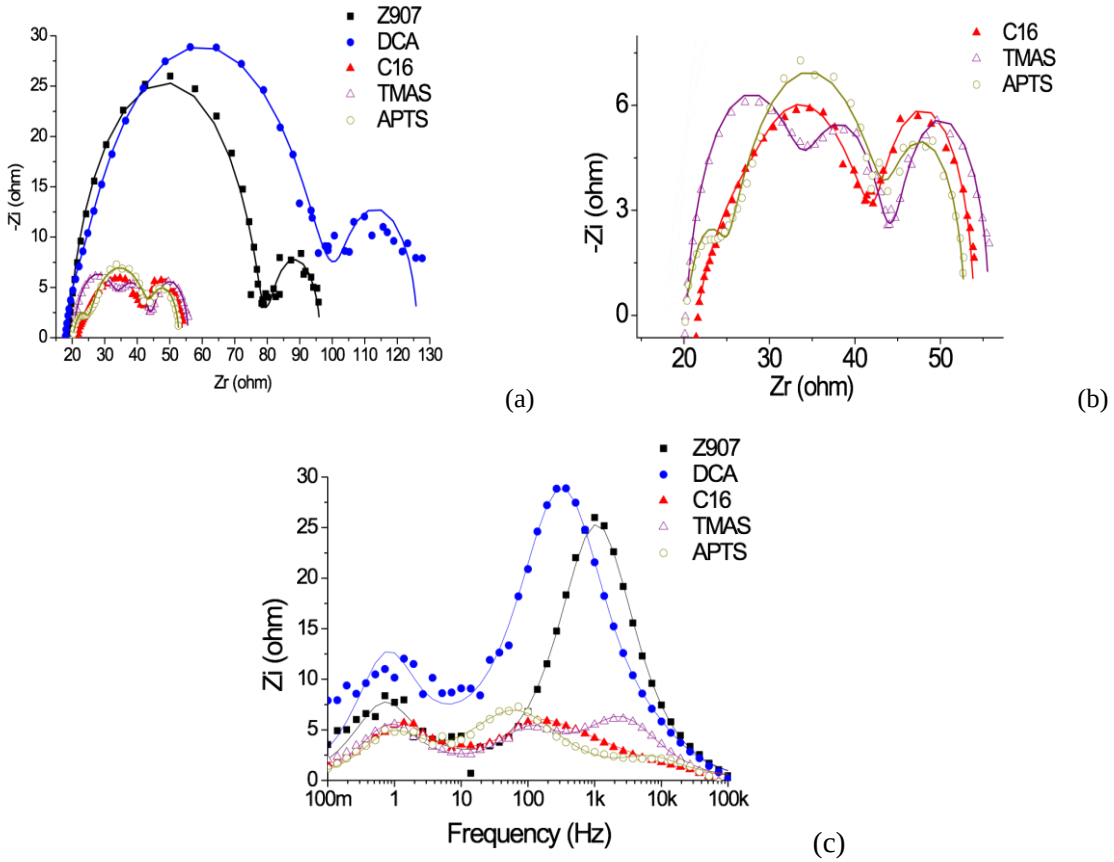

Figure 3.7 a) Nyquist plots of all cells under investigation; b) Magnified view of the Nyquist plots associated to cells passivated with silanes c) -Zi Vs Frequency plots. Solid lines represent the fitting curves obtained with the circuit reported in figure 3.2

	R_{ct} (Ω)	C_μ (μF)	k_{eff} (s^{-1})	τ_{el} (10^{-4}s)
Z907	60.2	2.4	1100	1.4
DCA	83.9	6.1	312	5.1
C16	17.5	41.3	220	7.2
TMAS	13.7	112.0	104	15.3
APTS	20.7	125.6	63	26.0

Table 3.2 Relevant parameters from EIS analysis at open circuit under illumination. R_{CT} is the charge transfer resistance at the TiO_2 electrolyte interface, C_μ is the chemical capacitance of the TiO_2, k_{eff} is the pseudo-first order recombination rate constant and τ_{el} is the electron lifetime calculated according to $\tau_{el} = R_{CT}C_\mu$. Data were extracted from the fitting to the equivalent circuit reported in figure 3.2

The comparison with respect to a cell incorporating the passivating compact TiO_2 underlayer, whose JVs are reported in figure 3.8, confirmed the substantial increase in the TiO_2 chemical capacitance (figure 3.9 a), paralleled by the augmented recombination resistance (figure 3.9 b) of the APTS treated cell, resulting in a longer electron lifetime (figure 3.9 c). However also in this case we were unable to identify a potential region where the chemical capacitance of both cells was fully comparable, resulting in the impossibility to obtain a pseudo-first order rate constant at the same TiO_2 states occupancy. Nevertheless, both the increased capacitance and recombination resistance of the silanized photoanode were consistent with a decrease in the charge recombination rate, owing to the blocking effect of the adsorbed silanes.

Finally, the effect of 0.2 M TBP addition to the cobalt electrolyte was tested (figure 3.8). In the presence of TBP a noticeable increase in photovoltage was comparatively observed in both cells equipped with the blocking underlayer, but, also in this case, efficiency of the APTS treated cell was greater, generating a photovoltage of 722 mV at the expense of a reduced Jsc, resulting in conversion efficiencies of the order of 3.4 %.

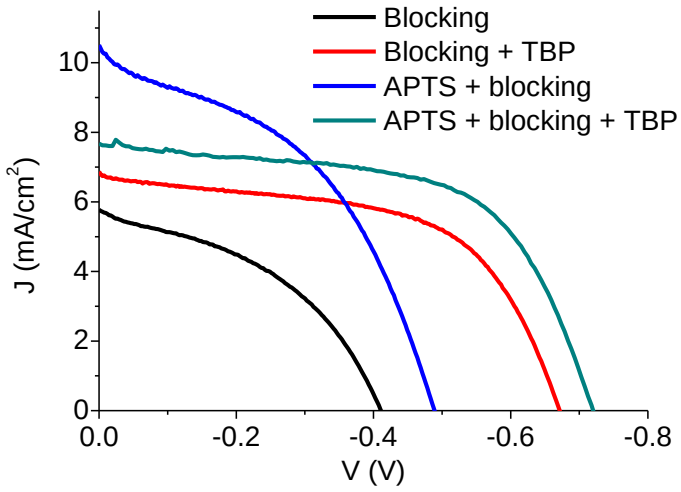

Figure 3.8 JV curves under illumination of DSSC in the presence and in the absence of 0.2 M TBP. Black and red lines: cells without the APTS treatment; Blue and green lines: APTS treatment

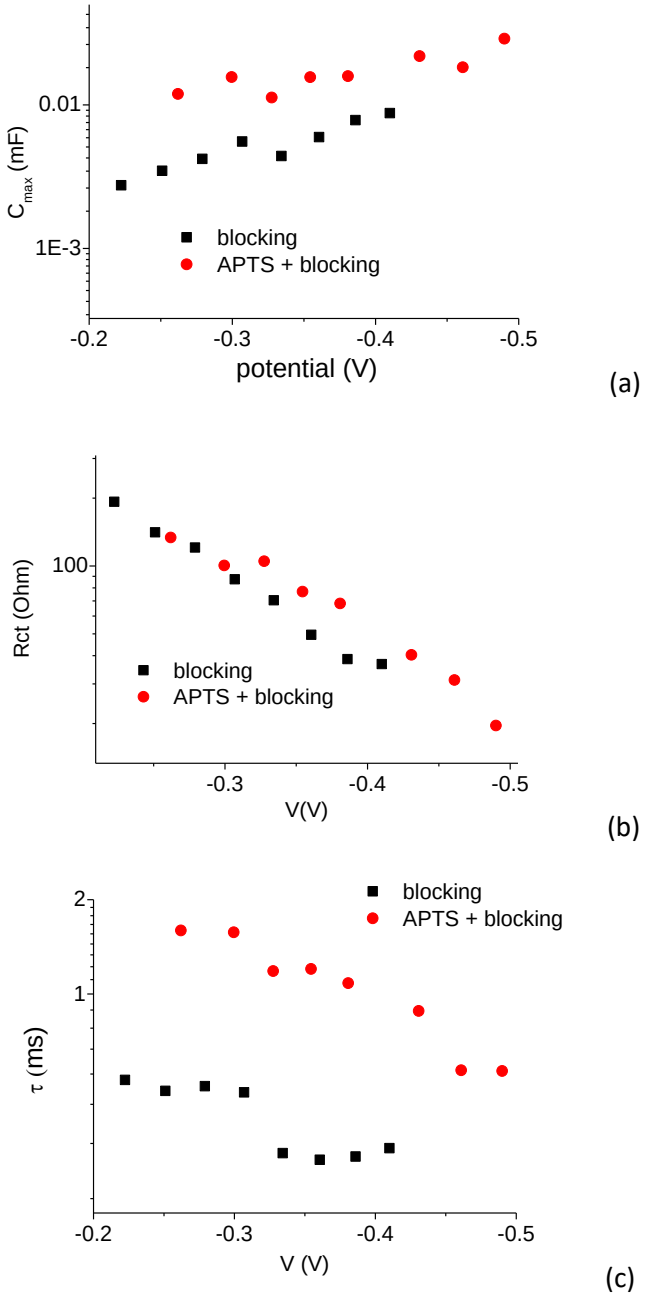

Figure 3.9 (a) Capacitance of the TiO_2 as a function of the applied voltage (corrected for IR drop) in cells equipped with the blocking underlayer with (red) and without (black) the APTS treatment; (b) charge transfer resistance of the TiO_2/electrolyte interface as a function of the applied voltage (corrected for IR drop) in cells equipped with the blocking underlayer with (red) and without (black) the APTS treatment; (c) apparent electron lifetime as a function of the applied voltage (corrected for IR drop) in cells equipped with blocking underlayer, with (red) and without (black) the APTS treatment. Data from cells reported in figure 3.8

Thus, the overall better efficiency obtained with TMAS and APTS finds a clear interpretation from EIS data, where the photoanode treatments with both **TMAS** and **APTS** result, within the explored series, in the highest chemical capacitance and electron lifetime observed. Interestingly, the APTS treated photoanode displays a superior recombination resistance maintaining at the same time a higher chemical capacitance, i.e. a higher stationary electron density in the TiO_2, with respect to the

TMAS treated ones. This is consistent with a superior screening against electron recapture, which results in the best Voc and FF.

The better passivation achieved with silanes characterized by a relatively short alkyl chain can be explained by their superior possibility of filling the surface sites left uncovered by the dye, resulting in a more complete and dense surface coverage. Further, the presence of cationic species may also represent an added benefit for repelling Co(III) from the surface through electrostatic interactions. Under this aspect, besides TMAS, which intrinsically bears a cationic charge, APTS can be equally successful since its tendency to form NH_3^+ groups, following acid-base equilibria on the surface of metal oxides like TiO_2, is known [39], since it bears acidic OH groups which undergo proton exchange. This possibility is even more substantial in the presence of the dye which, upon binding the surface, releases protons via its carboxylic groups.

Molecular Modeling

The morphological modeling of the surface and its interaction with the molecular adsorbates, comprising both Z907 and TMAPS is a useful tool to rationalize the screening effect induced by the presence of short chain silanes against electron recapture involving Co(III). The TiO_2 ($Ti_{64}O_{128}$) surface slab (101) having a projected 11x18 $Å^2$ area is modeled at the MM-UFF level. Although at this computational level the picture which is provided may be less accurate than that obtained by more sophisticated and computationally demanding QM/MM methods [40], usually finalized at the calculation of the electronic structure of the TiO_2, it represents a reasonable approximation for the bond distances and the equilibrium geometries of the molecules chemisorbed on the surface and a powerful tool to visualize their steric interactions. To this end, the equilibrium geometries of the adsorbates, previously computed at high level DFT, were frozen, and the only further optimization, after attaching the selected molecules to the tiania surface slab, involved the bond distances and angles of either the Ti-O-C bond (Z907) or Ti-O-Si bonds (TMAS) and of their first neighboring atoms in the TiO_2 slab. The silane was attached through just two Si-O-Ti bonds, in consideration of a previous study indicating that the complete substitution of OEt groups, leading to formation of the tripodal linkage is not thermodynamically probable, at least at moderate temperatures [41]. From Figure 3.10A it can be appreciated that the surface is large enough to comfortably accommodate one Z907 molecule, which binds the Ti atoms through the carboxylic groups almost normal (96°) to the surface, while, due to the cis-configuration, the bulky nonyl chains in the 4,4' position of the other bipyiridine point outwards, in two different directions. In principle, the slab is large enough to accommodate two Z907 dyes, but, for obvious steric reasons, the nonyl chains of the two molecules have to diverge, while the negatively charged NCS groups face each other (Figure 3.10b). Due to the relative dense packing on the surface, leading to electrostatic repulsion between the negative ends of the NCS groups, this situation will not probably represent the average condition of the

surface, where a lower surface concentration, like that represented in figure 3.10a will be more common. Nevertheless, even in the case of dense packing, which is favorable to the screening of most of the available surface, some sites are left exposed between the two dyes, as can be appreciated from the top view of Figure 3.10b, reported in Figure 3.10c. In principle, $[Co(bpy)_3]^{3+}$, having a relatively small diameter 11.8 Å of may infiltrate and reach the surface in correspondence of the exposed sites (Figure 3.11a).

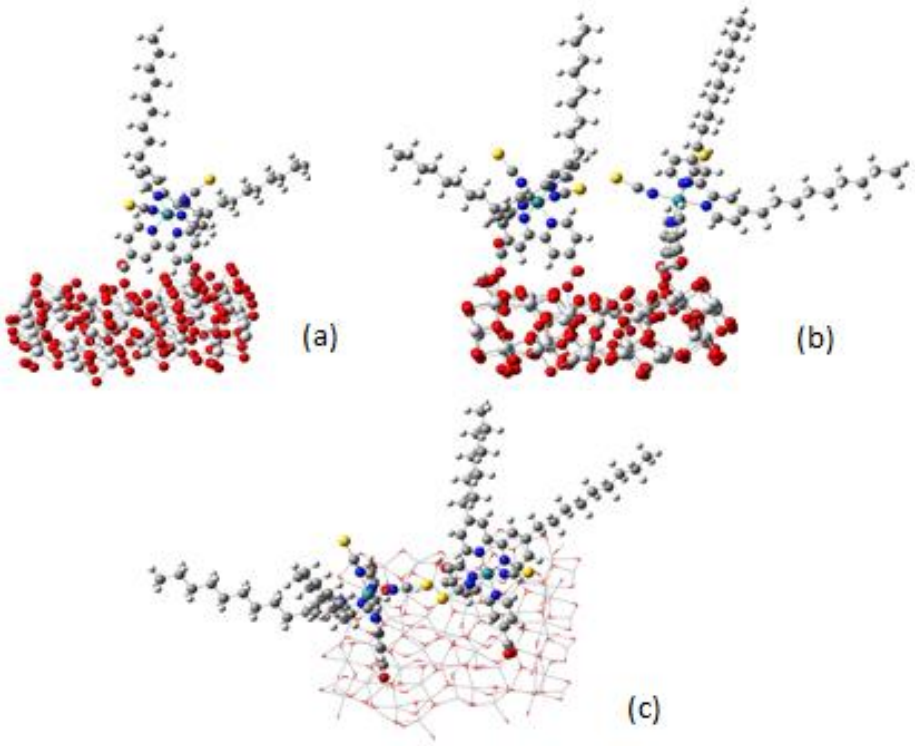

Figure 3.10 Z907 molecules interacting the 101 TiO_2 surface, showing the attachment of both a single molecule (a) and of two molecules (b) to the slab having a projected area of ca. 200 $Å^2$. Figure (c) is the top view of (b) where TiO_2 was represented with thin tubes, for sake of clarity.

In the presence of TMAS, which also orients approximately orthogonal to the surface, with a dihedral angle of ca 80°, the direct access of Co (III) to the exposed surface is precluded by the alkyl skeleton and by the positively charged quaternary head, having a tilt of about 30° with respect to the Ti-O-Si bonds. The length of the alkyl chain, 6.6 Å from the Si atom to the methyl termini, allows to decouple the cobalt mediator from the surface, slowing down electron recapture significantly. The same effect can be clearly exploited in the presence of more densely packed dye molecules (Figure 3.11C) where the relatively small TMAS molecules can saturate the exposed surface sites between adjacent dyes. Thus the benefit of using relatively short molecules, with enough steric bulk to protect the surface against approaching Co (III), but with the ability to fill the exposed pockets between bulky dye molecules, can be rationally explained on the basis of

relatively straightforward models. Clearly, the considerations that are valid for TMAS, can be safely extended to APTS, having an even smaller steric hindrance on the surface, but displaying a similarly long alkyl chain and a positively charged head, resulting form the quaternarization of the amino group due to acid-base equilibria on the protic surface of titania.

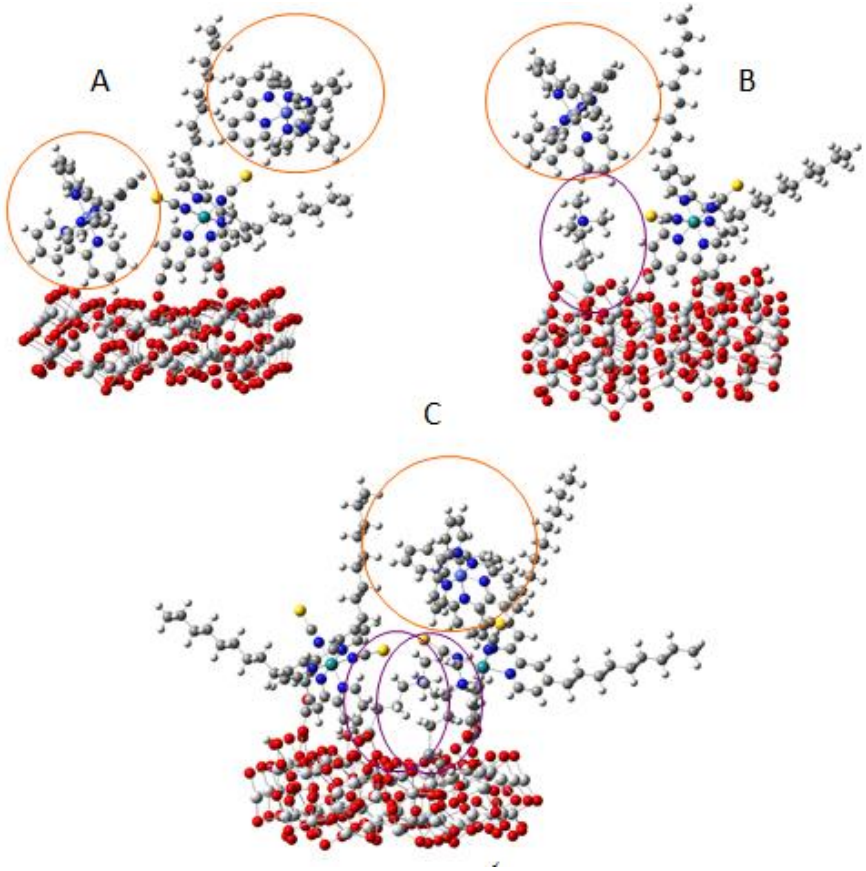

Figure 3.11. Suppression of recombination in the presence of TMAS: in (A) some of the Co(III) is blocked by the nonyl chains of Z907, but some is free to reach the exposed surface. In (B) the presence of TMAS repel Co(III) from the surface. In C the relatively short TMAS is able to saturate the exposed surface sites between adjacent dyes, preventing electron recapture. $[Co(bpy)_3]^{3+}$ is evidenced by orange circles and the TMAs by purple ovals.

3.1.4 Conclusion

A successful general strategy for improving the electron collection efficiency in dye sensitized solar cells based on common Ru(II) sensitizers, like Z907, and kinetically fast electronic mediators, like the $[Co(bpy)_3]^{2+/3+}$ redox couple employed in this study, was investigated [42].

The sensitized photoanode post-treatment with commercially available tri-alkoxy silanes was effective in screening the TiO_2 surface from the electron back recombination process involving the Co(III) metal centers, resulting in a 10-20 fold increase of the TiO_2 electrons lifetime under open

circuit conditions. Interestingly, silanes endowed with relatively short propyl chains like aminopropyl-triethoxysilane (**APTS)** and trimethylammoniumpropyl-trimethoxysilane (**TMAS**), bearing a cationic charge, proved to be more effective than longer and more sterically hindered C16 chains, in suppressing the dark current. In the best cases (**TMAS** and **APTS**), the silane treatment resulted in overall cell efficiency improvements of the order of 600 and 500 %, respectively, by comparison with the untreated photoanode based on the Z907 Ru(II) sensitizer.

The steric interactions between chemisorbed dyes, silanes, and Co(III) were rationalized through molecular modeling combining the MM description of the titania surface with the equilibrium geometries of the molecular entities computed at the DFT level. The modeling pointed out the benefit of using robust coadsorbates, displaying a strong and stable interaction with the TiO_2 surface and having enough steric bulk to protect the surface against approaching Co(III), but maintaining, at the same time, the ability to fill the exposed pockets between bulky dye molecules, where recombination may potentially occur.

References

(1) B. O'Regan, M. Graetzel, Nature 335 (**1991**) 737.

(2) IEA International Energy Agency. Potential for building integrated photovoltaics. Report IEA PVPS Task 7, NET Ltd., St. Ursen, Switzerland **2002**.

(3) C. Cornaro, S. Bartocci, D. Musella, C. Strati, A. Lanuti, S. Mastroianni, S. Penna, A. Guidobaldi, F. Giordano, E. Petrolati, T. M. Brown, A. Reale, A. Di Carlo, P*rog. Photovolt: Res. Appl.* (**2013**)

(4) H. Nusbaumer, J. E. Moser, S. M. Zakeeruddin, M. K. Nazeeruddin, M. Graetzel, *J. Phys. Chem. B* 105 (**2001**) 10461.

(5) H. Nusbaumer, S. M. Zakeeruddin, J. E. Moser, M. Graetzel, Chem. Eur. J. 9 (16) (**2003**) 3756.

(6) S. A. Sapp, C. M. Elliott, C. Contado, S. Caramori, C. A. Bignozzi, *J. Am. Chem. Soc*. 124 (**2002**) 11215.

(7) S. Cazzanti, S. Caramori, R. Argazzi, C. M. Elliott, Bignozzi C. A., *J. Am. Chem. Soc*. 128 (**2006**) 9996.

(8) S. M. Feldt, E. A. Gibson, E. Gabrielsson, L. Sun, G. Boschloo, A. Hagfedlt, *J. Am. Chem. Soc.* 132 (**2010**) 16714.

(9) H.N. Tsao , C. Yi , T. Moehl, J. H. Yum, S.M. Zakeeruddin, M.K. Nazeeruddin, M. Graetzel , *ChemSusChem* 4 (**2011**) 591.

(10) A. Yella, H. W. Lee, H. N. Tsao, C. Yi, A. K. Chandiran, M. K. Nazeeruddin, E. W. G. Diau, C. Y. Yeh, S. M. Zakeeruddin, M. Graetzel, *Science* 334 (**2011**) 629; DOI: 10.1126/science.1209688.

(11) S. Mathew, A. Yella, P. Gao, R. H. Baker, B. F. E. Curchod, N. A. Astani, I. Tavernelli, U. Rothlisberger, M. K. Nazeeruddin, M. Graetzel, *Nat. Chem.* 6 (**2014**) 242; DOI: 10.1038/NCHEM.1861.

(12) N. Koumura, Z. S. Wang, S. Mori, M. Miyashita, E. Suzuki, K. Hara, J. Am. Chem. Soc. 128 (**2006**) 14256.

(13) M.K. Kashif, J.C. Axelson, N.W. Duffy, C.M. Forsyth, C.J. Chang, J.R. Long, L. Spiccia, U. Bach, *J. Am. Chem. Soc.* 134 (**2012**) 16646.

(14) B. M. Klahr, T.W. Hamann, *J. Phys. Chem. C* 113 (**2009**) 14040.

(15) Y. Liu, J. R. Jennings, Y. Huang, Q.Wang, S. M. Zakeeruddin, M. Graetzel, *J. Phys. Chem. C* 115 (**2011**) 18847.

(16) P. G. Bomben, T. J. Gordon, E. Schott, C. P. Berlinguette , *Angew. Chem. Int. Ed*. 45 (**2011**) 10682.

(17) Y. Xie, T. W. Hamann, *J. Phys. Chem. Lett.* 4 (**2013**) 328.

(18) L. E. Polander, A. Yella, B. F. E. Curchod, N. A. Astani, J. Teuscher, R. Scopelliti, P. Gao, S. Mathew, J. E. Moser, I. Tavernelli, U. Rothlisberger, M. Graetzel, M. K. Nazeeruddin, J. Frey, *Angew. Chem. Int. Ed*. 52 (**2013**) 8731.

(19) C. Haensch, S. Hoeppener, U. S. Schubert, *Chem. Soc. Rev.* 39 (**2010**) 2323.

(20) A . Ulman, *Chem. Rev*. 96 (**1996**) 1533.

(21) B. Arkles, *CHEMTECH* 7 (**1977**) 766.

(22) B.A. Gregg, F. Pichot, S. Ferrere, C. L. Fields, *J. Phys. Chem. B* 105 (**2001**) 1422.

(23) S. M. Feldt, U. B. Cappel, E. M. J. Johansson, G. Boschloo, A. Hagfeldt, *J. Phys. Chem. C* 114 (**2010**) 10551.

(24) J. Spivack, O. Siclovan, S. Gasaway, E. Williams, A. Yakimov, J. Gui, *Sol. Energy Mater. Sol. Cells* 90 (**2006**) 1296.

(25) M. Mba, M. D'Acunzo, P. Salice, M. Maggini, S. Caramori, A. Campana, A. Aliprandi, R. Argazzi, S. Carli, C. A. Bignozzi, *J. Phys. Chem. C* 117 (**2013**) 19885.

(26) S.Carli, E. Busatto, S. Caramori, R. Boaretto, R. Argazzi, C. J. Timpson, C.A. Bignozzi, *J. Phys. Chem. C*, 117 (**2013**) 5142.

(27) Z. S. Wang, Y. Cui, Y. D. Oh, C. Kasada, A. Shinpo, K. Hara, J. Phys. Chem. C 111 (**2007**) 7224.

(28) M. K. Nazeeruddin, A. Kay, I. Rodicio, R. Humphry-Baker, E. Mueller, P. Liska, N. Vlachopoulos, M. Graetzel , *J. Am. Chem. Soc*. 115 (**1993**) 6382.

(29) R. Kern, R. Sastrawan, J. Ferber, R. Stangl, J. Luther, *Electrochim. Acta* 47 (**2002**) 4213.

(30) N. Kopidakis, N. R. Neale, A. J. Frank, *J. Phys. Chem. B.* 110 (**2006**) 12485.

(31) H. Kusama, H. Arakawa, *J. Photochem. Photobiol. A*: Chemistry 162 (**2004**) 441.

(32) C.G. Zhang, J. Dai, Z.P. Huo, X. Pan, L.H. Hu, F. T.Kong, Y. Huang, Y.F. Sui, X.Q. Fang, K.J. Wang, S.Y. Dai, *Electrochim. Acta* 53 (**2008**) 5503.

(33) M.K.Nazeeruddin, A.Kay, I.Rodicio, R.Humphry-Baker, E.Möller, P.Liska, N. Vlachopoulos, M.Grätzel, *J.Am.Chem.Soc*, 115 (**1993**) 6382

(34) Q. Wang, J. E. Moser, M. Graetzel, *J. Phys. Chem. B* 109 (**2005**) 14945.

(35) F. Fabregat-Santiago, J. Bisquert, G. Garcia-Belmonte, G. Boschloo, A. Hagfeldt, Sol. Energy Mater. Sol. Cells 87 (2005) 117.

(36) J. Bisquert, Phys. Chem. Chem. Phys. 5 (2003) 5360.

(37) B. C. O'Regan, S. Scully, A. C. Mayer, J. Phys. Chem. B 109 (2005) 4616.

(38) M. Adachi, M. Sakamoto, J. Jiu, Y. Ogata, S. Isoda, J. Phys. Chem. B 110(28) (2006) 13872.

(39) B. van Duffel, T. Verbiest, S. Van Elshocht, A. Persoons, F. C. De Schryver, R. A. Schoonheydt, Langmuir 17 (2001) 1243.

[40] S. Fantacci, F. De Angelis, Coord. Chem. Rev. 255 (2011) 2704.

[41] N. Iguchi, , C. Cady, R. C. Snoeberger III, B. M.Hunter, E. M. Sproviero, C. A. Schmuttenmaer, R. H. Crabtree, G. W. Brudvig, V. S. Batista, Proc. SPIE 7034 (2008) 70340C.

[42] S. Carli, L. Casarin, S. Caramori, R. Boaretto, E. Busatto, R. Argazzi and C.A. Bignozzi, *Polyhedron* **2014**, 82, 173–180

3.2 A photophysical and photoelectrochemical study of innovative β–monosubstituted Zn(II) tetraarylporphirin dyes

3.2.1 Introduction

As presented in section 1.6 of this thesis, a molecular sensitizer for DSSC should be characterized by good chemical and photochemical stability, and by a broad absorption spectrum, covering up to the near-infrared region, provided with high extinction coefficients [1].

In the photosynthetic cores of bacteria and plants, solar energy is collected by chromophores based on porphyrinic structures [2], and converted into chemical energy by complex biological redox processes. Inspired by this natural process of light harvesting and conversion, numerous porphyrins have been investigated as sensitizers for DSSC [3]. The intrinsic advantages of porphyrinic dyes are their high chemical and photochemical stability and their very strong Soret (about 450 nm) and Q (550−650 nm) absorption bands. In addition their electrochemical and light harvesting properties are tunable acting on four meso and eight β pyrrolic positions, by specific chemical functionalization. The energy level of the lowest unoccupied molecular orbital (LUMO) of metal porphyrins is generally above the energy of the TiO_2 conduction band, allowing efficient electron injection; while the energy of the highest occupied molecular orbital (HOMO) usually lays below the redox potential of today's most used electrolyte (I^-/ I_3^-), allowing efficient dye regeneration [1].

In particular, meso disubstituted Zn^{II} porphyrinates, characterized by a strong and directional electron excitation process along their push−pull system, have been extensively investigated as dyes for DSSC [3]. Indeed, record solar cell efficiencies (~13%) were reached in 2014 by a well engineered meso disubstituted push−pull Zn^{II} porphyrinate, in combination with a $Co(bpy)_3^{II/III}$ based electrolyte [4].

IPCE spectra of Zn^{II} porphyrinic dyes generally show two well separated peaks corresponding to B and Q absorption bands, with a region of lower intensity between 450 and 550 nm. IPCE spectra with a significant intensity over a broad range of wavelengths may be achieved by two means: i) addition of an organic cosensitizer with significant electronic absorption (IPCE intensities between 430 and 600 nm [5]); ii) introduction of a dithienylethylene (DTE) unit in a π delocalized chain, connecting the porphyrinic ring and the anchoring group, [6] in order to produce a relevant electronic absorption between 430 and 650 nm and significant IPCE intensities in this region. The π DTE unit also induces a red shift of the electronic absorption bands, with an enhancement of their intensity, together with an increase of the excited state lifetime [6, 7].

With these premises, Di Carlo and his colleagues at Milano University have given their contribution to the topic in the last years, developing valid alternatives to the commonly available porphyrinic structures [8-12]. In fact, even though meso disubstituted push−pull Zn^{II} porphyrinic dyes

are often featured by high light conversion efficiencies [3], they often require laborious multistep synthetic procedures, characterized by very low overall yields [13-17]. In 2013 a microwave-assisted synthetic approach was successfully exploited by Di Carlo et al. to obtain β monosubstituted and disubstituted push−pull tetraaryl Zn^{II} porphyrinates in a few steps [9]. It was shown that β substituted Zn^{II} porphyrin dyes can produce comparable or even improved photovoltaic efficiencies, as sensitizers in DSSC based on the I^-/I_3^- redox mediator, if compared to the meso disubstituted structures, even if these latter feature lower HOMO−LUMO energy gap, making easier the charge transfer along the push–pull system. The good performances obtained with the β-monosubstituted porphyrins were ascribed to the higher steric hindrance provided by the four bulky tert-butyl-substituted aryl rings surrounding the porphyrinic core, which led to reduced recombination events with the oxidized mediator, while the electron injection and regeneration kinetics were found to be similar for the meso and β structures [10]. The positive effect exerted by the cyanoacrylic binding group, with respect to the carboxylic one, was also evidenced.

In particular, in these comparative studies the DC145 molecule (figure 3.12a) emerged for its good spectral and photoelectrochemical characteristics. In 2014 this promising structure was further improved by the addition of a dithienylethylene (DTE) π unit in the β-pyrrolic position of the porphyrinic ring, with the aim of introducing a panchromatic effect, thus increasing the efficiencies obtainable in iodide based DSSC featuring these β-mono sobstituted porphirinic dyes [11]. The best performing molecular structure highlighted by this investigation was DC143, reported in figure 3.12b, in which the elongation of the π-delocalized system, through a 4-ethynylstyryl bridge between the porphyrinic ring and the DTE unit, produced the expected panchromatic effect, with broadened electronic absorption spectra over a wide range of wavelengths, and IPCE spectra featuring a broad plateau in the region 430−650 nm. However a direct comparison between the DC145 and DC143 structures, in order to quantify the advantages brought by the π conjugated unit, has not been conducted yet.

Therefore, as part of this thesis work, the recently developed β-monosubstituted porphirinic dye DC143, displaying a panchromatic effect thanks to the conjugated DTE unit, was characterized for the first time by the photophysical point of view, obtaining details about its excited state characteristics in solution and its electron transfer dynamics at the interface with TiO_2. In addition a newly synthesized meso disubstituted push−pull porphyrin system, named DC194 (figure 3.12c), and containing the conjugated DTE unit as well, was involved in the study, to probe the effect of the position of the DTE conjugated arm on the fast kinetics of electron transfer and recombination.

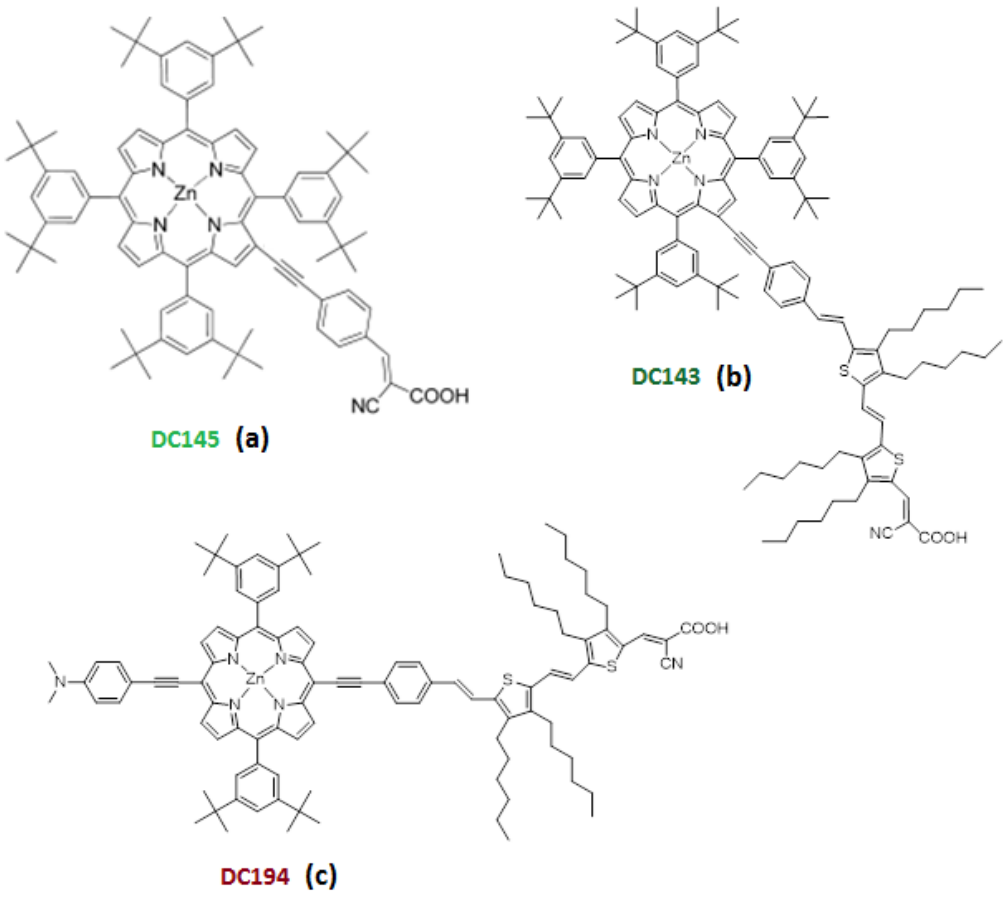

Figure 3.12 Porphyrin dyes under investigation

3.2.2 Experimental

Materials

All solvents and reactants were purchased by Sigma Aldrich and used as received. The 18NR-AO and 18NR-T TiO_2 pastes came from Dyesol, FTO glass plates from Pilkington (TEC 8, 2.3 mm thick substrates), 25 μm thick hot-melt cell sealer, Surlyn, from Dupont.

The porphyrin dyes DC145, DC143 and DC194 were synthesized by Gabriele Di Carlo et al., at Milano University, following literature procedures [17].

The PEDOT counter electrodes were prepared by electrodeposition method through cyclic voltammetry, scanning 2 times from 0 to 1,7 V vs SCE at 50 mV/s in a 10^{-2} M EDOT/0.1 M $LiClO_4$ acetonitrile solution.

Spectroscopic characterization

The apparatus used for transient absorption spectroscopy (TAS) measurements was described in section 2.3.2. Some TAS measurements were conducted in solution, employing the dye soaking solutions. Other TAS measurements were conducted on the surface: samples consisted in sensitized

TiO_2 films sintered on a microscope slide (transparent films were obtained by using 18NR-T paste; $TiCl_4$ post-treatment was applied). Decays were collected averaging 20 laser shots, at a frequency of 0.2 Hz, to reach a good S/N ratio. A 2.2 mJ/cm^2/pulse laser power was employed to excite the samples. TAS measurements in the presence of iodide-based electron donor (0.6 M poly-methylimidaziolium iodide + 0.1 M LiI + 0.05M tert-butylpyridine in CH_3CN) were performed by drawing the electrolyte by capillarity inside the chamber (ca. 6−8 μm), constituted by a glass slide pressed against the TiO_2 photoanode. Thus, the negligible optical path allowed to avoid interferences originated by excitation of I_3^-, created and accumulated at the interface during repeated measurements.

The blank electrolyte consisted in 0.1M $LiClO_4$ in ACN. The ultrafast measurements were conducted in Milan, in collaboration with Prof. Cerullo, by means of the experimental setup which was described in section 2.3.2 [18].

Photoelectrochemical characterization

Photoelectrodes were prepared following the procedure described in section 2.2.1, without blocking underlayer and using the 18NR-AO opaque paste diluted with terpineol in a 1:1,5 w/w ratio, yielding ~3μm thick films. After sintering and $TiCl_4$ post-treatment, the electrodes were immersed in a 0,2 mM solution of the dye, containing chenodeoxycholic acid 0,2 mM to prevent surface aggregation events. The following absorption conditions were optimized based on the dyes solubility and aggregation characteristics:

DC145 (ethanol/THF 9:1, immersion time 2 h)

DC194 (ethanol/THF 9:1, immersion time 5 h)

DC143 (ethanol/THF 8:2, immersion time 5 h)

Solar cells were assembled in open or closed configuration (see section 2.2.1), with a 0.25 cm^2 active area. The electrolyte composition used was: 0.6 M poly-methylimidazolium iodide, 0.02 M I_2, 0.1 M LiI, 0.05 M 4-tert-butylpyridine in acetonitrile.

Cell performances were evaluated under AM 1.5 illumination (ABET sun simulator), while details about the equipment employed for the photoelectrochemical characterization were given in Chapter 2.

IPCE measurements setup was described in section 2.2.4.

3.2.3 Results and discussion

The absorption spectra of the three porphyrins in THF are reported in figure 3.13a, with the relative spectral properties reported in Table 3.3. In figure 3.13b the normalized spectra measured for porphyrins adsorbed on transparent TiO_2 based electrodes are reported, while in figure 3.13c the

normalized diffuse reflectance spectra of the porphirins absorbed on opaque TiO_2 electrodes are presented, converted through the Kubelka-Munk transformation. In all the conditions, the panchromatic effect introduced by the DTE unit for DC143 and DC194 is evident, consisting in broad absorption in the range between 480 and 550 nm, absent in the case of the reference porphyrin DC145 [11]. In general, the three absorption spectra all display the intense B band and the weaker Q bands centered at 450 and around 600 nm, respectively (Table 3.3). It can be pointed out that the β-monosubstituted DC143 features the largest Q band red shift (ca. 30 nm) and a slightly increased extinction coefficient values for both of the absorption bands.

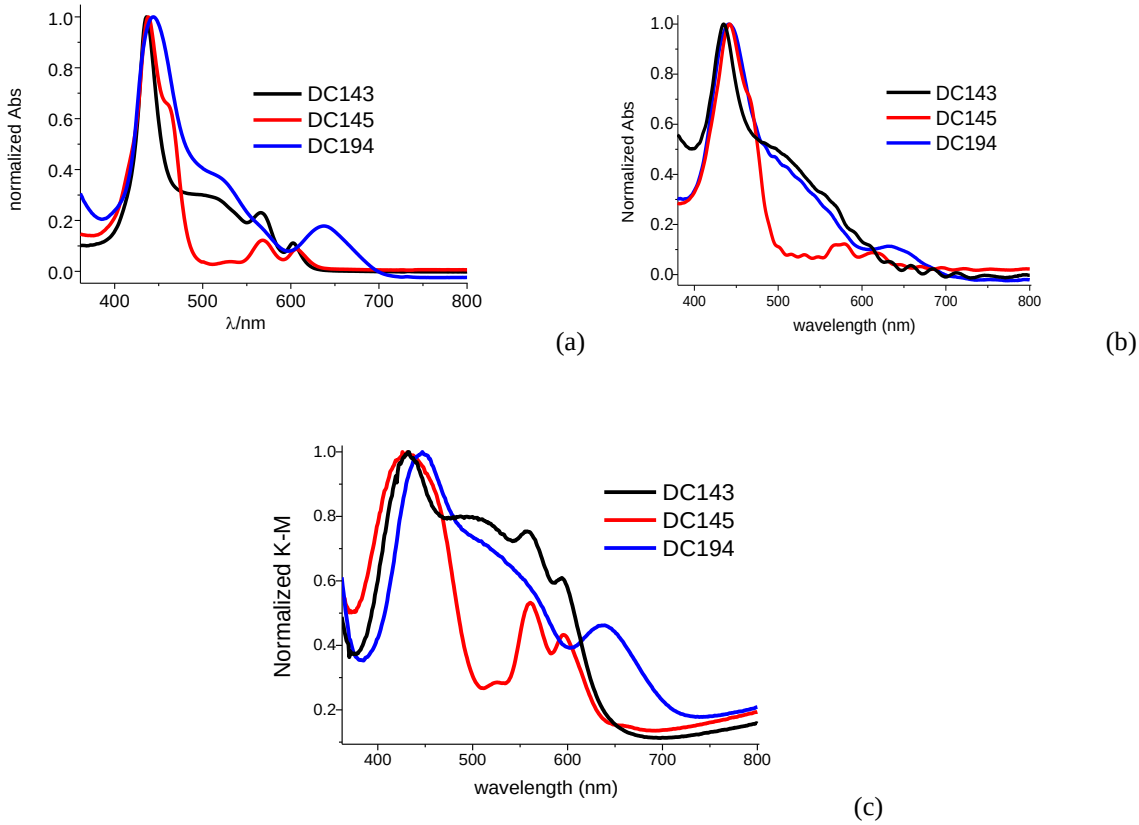

Figure 3.13 Normalized absorption spectra of the porphirin dyes in THF solution (a) and on transparent TiO_2 electrodes (b); normalized reflectance spectra for the 3 porphyrins absorbed on the opaque TiO_2 layers with the Kubelka-Munk correction (c).

Dye	**B bands λa (nm) [*logε*]**	**Q bands λa (nm) [*logε*]**
DC194	444 [*5.10*]	638 [*4.40*]
DC145	438 [*5.30*]	568 [*4.37*] 606 [*4.21*]
DC143	434 [*5.30*]	571 [*4.66*] 609 [*4.67*]

Table 3.3 Experimental Electronic Absorption Spectra in THF Solution of the Zn^{II}-Porphyrins DC194; DC145; DC143

The **photophysical properties** of DC143, DC194, and DC145 where comparatively investigated, to gain insights about the excited state dynamics relevant to TiO_2 sensitization in photoelectrochemical cells.

Transient absorption spectroscopy in the ns-μs domain

In figure 3.14 the transient absorption (TA) spectra of the dyes in solution are reported. The excited (triplet) state of DC145 in solution (figure 3.14a) is characterized by features already observed in a previous contribution [10]. In particular the bleaching of the B band and an intense absorption centred at ca. 500 nm are the predominant characteristics of its excited state. The excited state signature of the β and meso thiophene substituted dyes DC143 and DC194 are similar (figure 3.14b,c), consisting in a bleaching centered at 480-500 nm, which mirrors the absorption of the ground state due to the presence of the conjugated arm. The bleach is followed by an absorption of about the same intensity in the red part of the spectrum, with an isosbestic point at ca. 550 nm. Thus the characteristics of the triplet state are consistent with some charge transfer character to the conjugated pendant, resulting in the absorption in the red region of the spectrum.
The triplet state lifetime in aerated solution is 550 ns for DC145 and of the order of 250 ns for the other two thiophene substituted species.

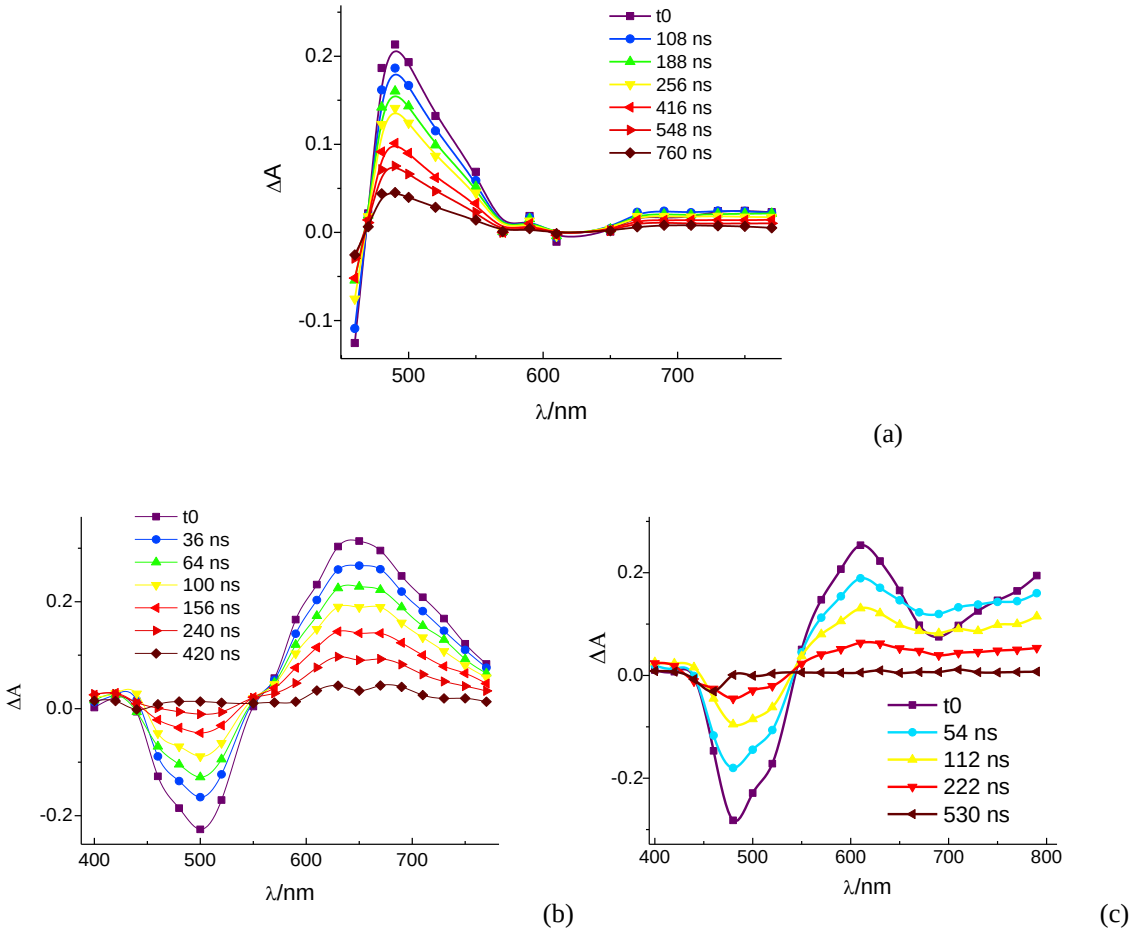

Figure 3.14 TA spectra of DC145 (a), DC143 (b), and DC194 (c) in solution following 532 nm excitation. The stimulated emission convolved with the laser excitation was eliminated by choosing appropriate delays.

The charge transfer dynamics for the three dyes were then investigated on TiO_2. Excitation of the dye molecules, anchored to TiO_2 through the cyanoacrylic group, resulted in long-lived charge separation having a lifetime (amplitude weighted) of 14 μs for DC143, 11 μs for DC194, and ca. 7 μs for DC145, clearly much longer than their respective triplets in aerated conditions. All the three dyes show similar TA spectrum on TiO_2 (see figure 3.15), displaying the bleaching of the ground state, sharp and intense in DC 145, in correspondence of its B band, and broader for DC194 and DC143, in which cases two convolved bleaching bands centered at 450 and 510 nm can be observed, extending up to 600 nm, since the ground state bleaching involves a manifold of excitations regarding both the macrocycle and the conjugated thiophene arm. In all the three cases, after an isosbestic point at about 600 nm, a large structured absorption band appears at higher wavelenghts, with two peakings at 650 nm and 750 nm, which can be assigned to the signature of the cation formed on the TiO_2 surface, probably localized onto the pyrrolic macrocycle.

For all the three dyes it was difficult to observe contributions of the excited state, indicating that the oxidized dye is the species which is predominantly formed on the titania surface.

DC143 and DC194 there is some similarity between the triplet excited state and the molecule's oxidized form, which complicates this evaluation. Nevertheless the appearance of secondary bleaching (at ca. 450 nm) and absorption bands (at ca. 750 nm) present on the TA spectra measured on TiO_2 and not evidenced in solution, are indicative, even at early delays, of the predominant formation of the oxidized dye over the triplet population.

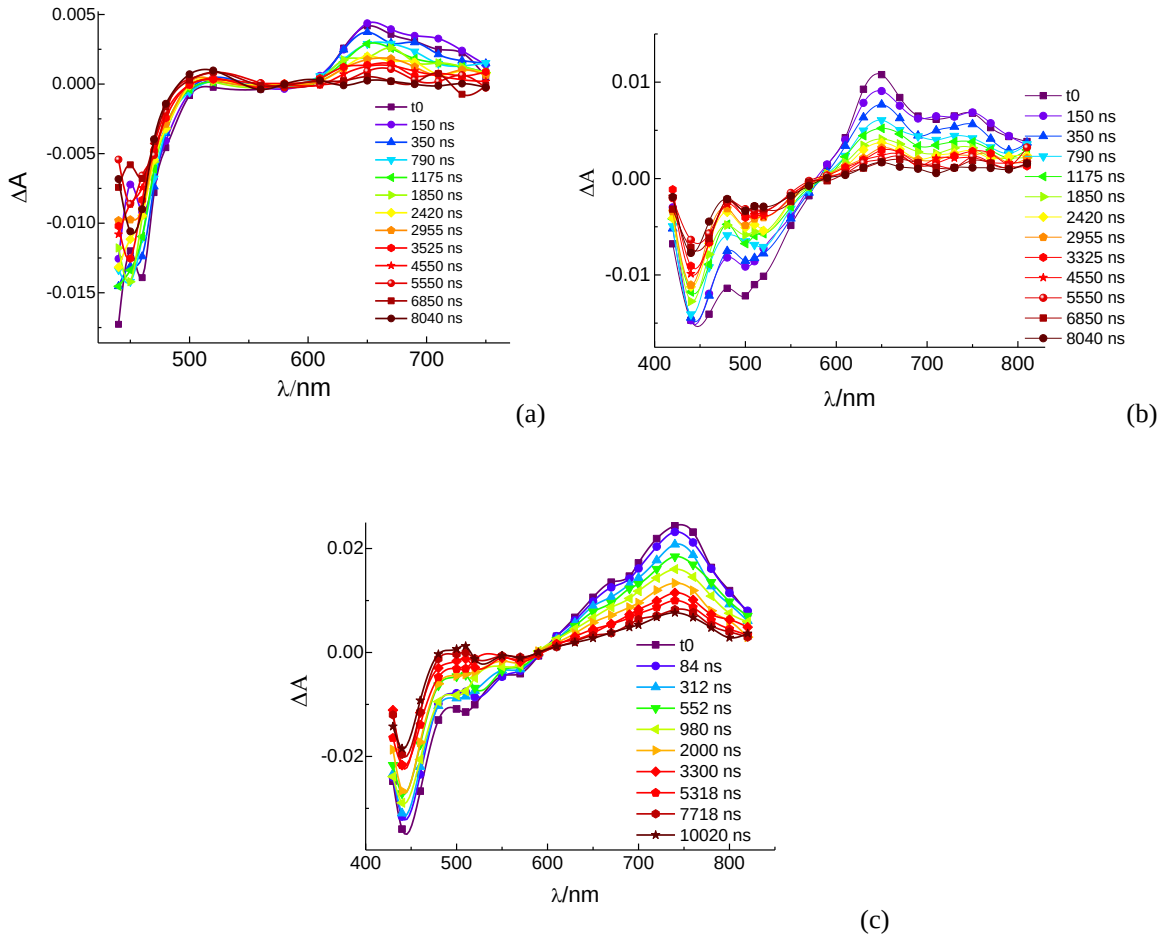

Figure 3.15 TA spectra of DC145 (a), DC143 (b), and DC194 (c), absorbed on TiO_2, in contact with ACN/Li^+, following 532 nm excitation

The lifetime of the charge separated state for the three species was substantially shortened in the presence of the electron donating electrolyte consisting of 0.6M PMII/0.1M LiI/0.05M TBP (see figure 3.16), resulting in a nearly quantitative dye regeneration efficiency (η = 96 % for DC143, 92% for DC194 and 91 % for DC145). Regeneration efficiency was calculated by using the simplified equation:

$$\eta = \frac{k'_{reg}}{k'_{rec} + k'_{reg}} \qquad \text{(Eq. 3.2)}$$

where the two pseudo first order regeneration and recombination constants, k'_{reg} and k'_{rec}, were obtained by fitting the decay curve measured in the absence of the donor species in the electrolyte,

and the one measured in the presence of the donor species at cell concentration, with a biexponential function [10, 19]. The values obtained by the fitting curves were used to obtain the average regeneration time, and the first order rate constant, by means of the following equation:

$$1/\tau_{avg} = k_{avg} = \left(\frac{(A1*t1^2+A2*t2^2)}{(A1*t1+A2*t2)}\right)^{-1} \quad \text{(Eq. 3.3)}$$

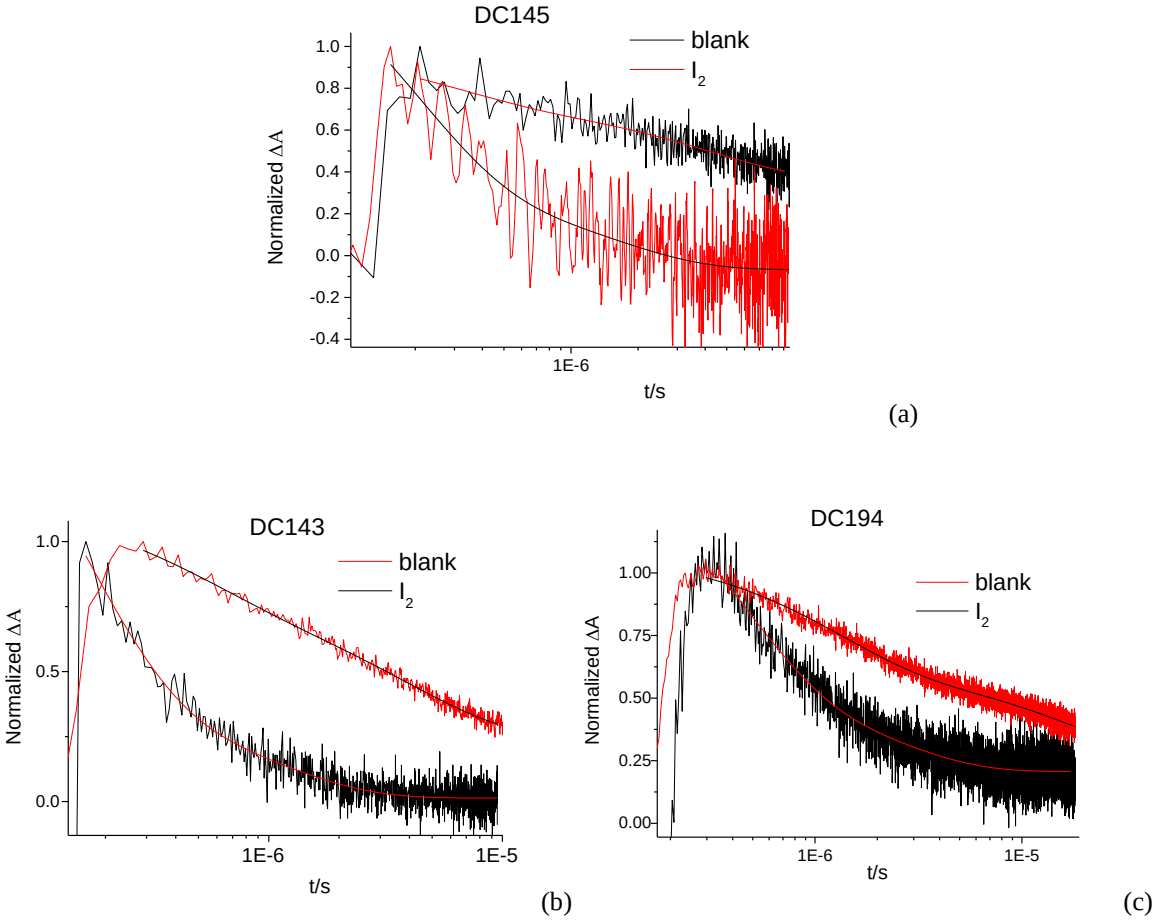

Figure 3.16 Recombination and regeneration kinetics observed on the ns-µs time scale., under 532 nm laser excitation (2.2 mJ/cm^2/pulse), of DC145 (a), at 460 nm; of DC143 (b), at 650 nm; of DC194 (c), at 720 nm, fitted with bi-exponential functions.

In addition to the nanosecond transient absorption measurement, an investigation in the sub-nanosecond timescale was conducted, in order to gain deeper insights on the porphyrin dyes excited state dynamics both in solution and when the molecules are anchored to TiO_2. Ultrafast transient absorption measurements were performed in Milan in collaboration with Prof. Cerullo, by means of the femtosecond laser instrumental setup described in section 2.3.2.

Ultrafast Excited State Dynamics in solution

The transient spectrum of DC145 following 480 nm excitation is shown in figure 3.17, where one can appreciate the formation of the singlet state, characterized by the B band bleaching (positive band in ΔT/T mode), by the appearance of a broad positive absorption band with maximum at 513 nm and of narrow absorption band at 603 nm. These spectral signatures, already present at 600 fs after the excitation (i.e 1 ps delay) (figure 3.18 a and b) decay slowly, with a monoexponential time constant, probed at both 513 and 603 nm, of ca. 130 ps (figure 3.19), to a very long lived excited state, whose lifetime is constant for the time window of the spectrometric apparatus. Beside the B band bleaching, which is scarcely informative, the population of this long lived state results in weaker characteristic features, prominently consisting in a triangular shaped broad absorption band peaking at 500 nm (figure 3.20), whereas the long wavelength (i.e.> 650 nm) region is essentially flat, in agreement with previously discussed nanosecond results, and assigned therefore to the formation of the triplet state of the dye which predominantly characterizes the excited state signature after 400 ps from the initial excitation.

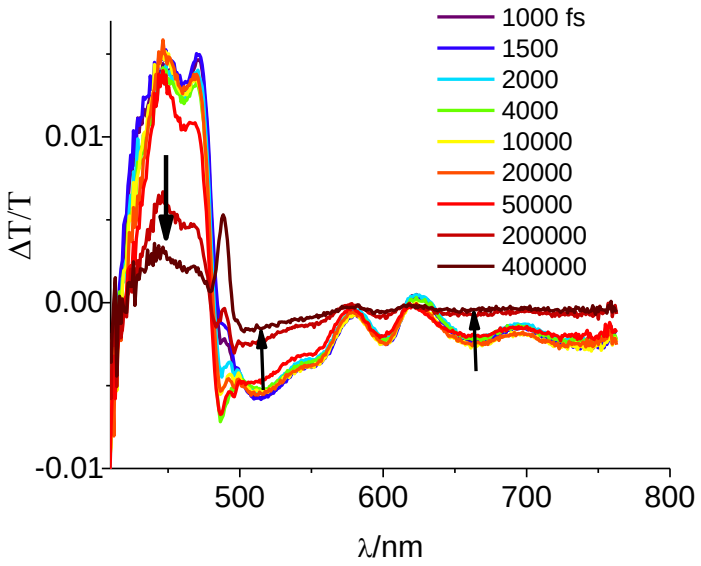

Figure 3.17 Time evolution of the transient spectrum of DC145 in ethanol, following 480 nm excitation. Significant delays sampled along the excited state decay curve are reported to illustrate the major spectral changes occurring after excitation.

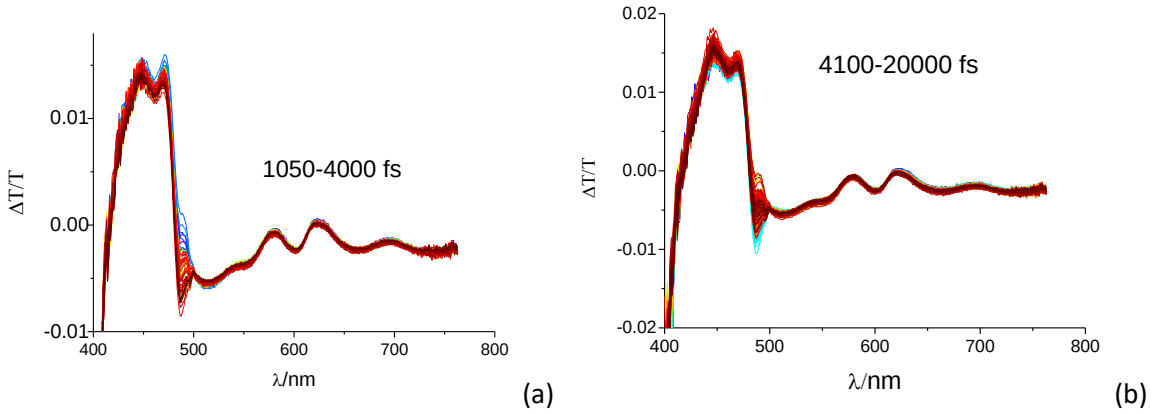

Figure 3.18 Transient spectrum of DC145 following 480 nm excitation, framed in the 1-4 ps interval (a) and in the 4.1-20 ps interval (b)

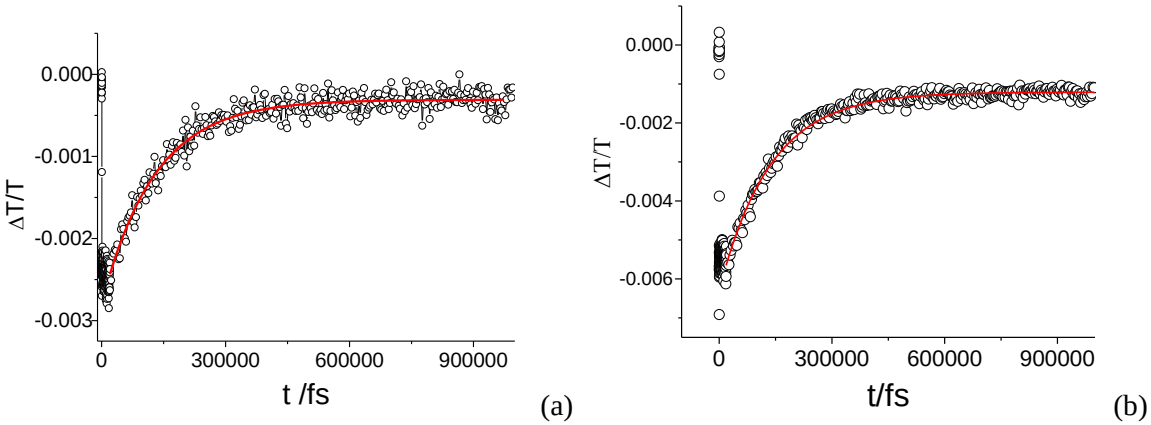

Figure 3.19 Excited state decay of DC145 observed at 603 nm (a) and at 513 nm (b), fitted by monoexponential equation

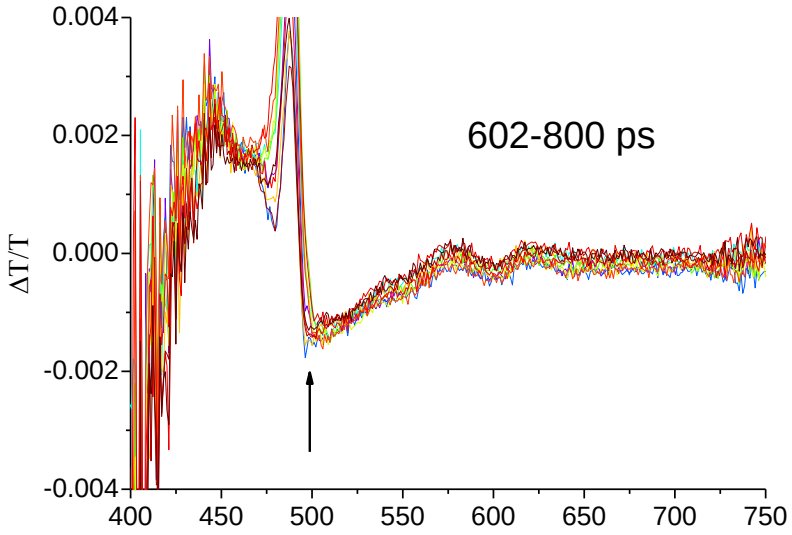

Figure 3.20 Transient spectrum of DC145 taken at 602-800 ps delay, showing the predominant features of the triplet state, i.e. the absorption band at 500 nm.

The transient spectrum of DC143 following excitation of the 510 nm absorption manifold is shown in figure 3.21. The kinetics are generally defined by a multiexponential nature, ostensibly due to the relaxation from higher lying electronic states centered on the conjugated bridge to the lowest singlet state. This process has a fast kinetics, with a major component (> 90 %) on the order of 600 fs, and a longer minor component (< 10%) with a lifetime of ca. 10 ps. This kinetics is particularly evident from the fast growth of the 500 nm absorption (figure 3.22) which then slowly decreases according to a time constant in the ns scale. This feature is particularly evident by monitoring the clean growth of the 650 nm absorption (figure 3.23). In general for longer delays (i.e. larger then 400 ps) the transient spectrum acquires strong similarities with the triplet spectrum recorded by 532 nm nanosecond excitation, suggesting that population of the lowest triplet state (T1) is the predominant dynamic on the time scale of 0.5-1 nanosecond. The major spectral features of the T1 state are the growth of the broad band at 650 nm and the increasing bleaching at 500 nm, with the presence of an isosbestic point centered around 570 nm (Figure 3.21 b).

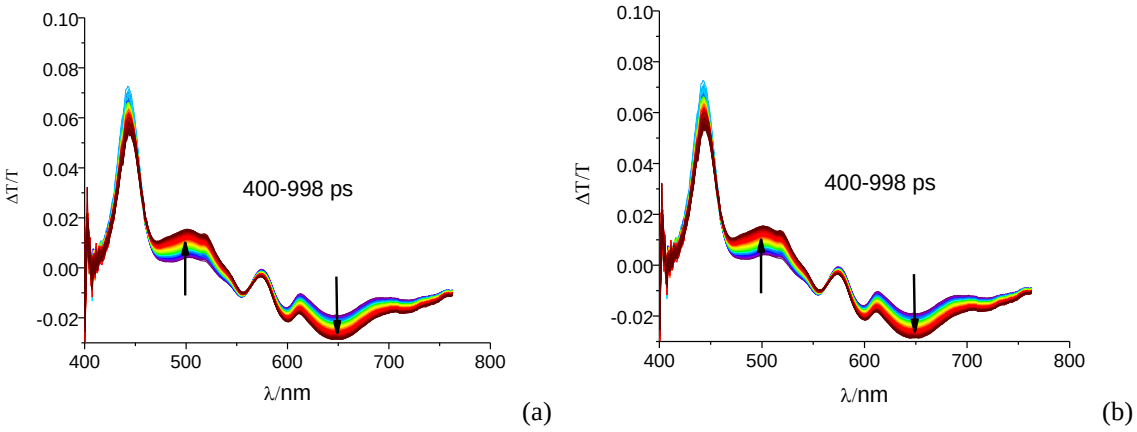

Figure 3.21 (A) Time evolution of the transient spectrum of DC143 in ethanol, following 510 nm excitation. Significant delays sampled along the excited state decay curve are reported to illustrate the major spectral changes occurring after excitation. (B) Excited state dynamics on the 400-1000 ps time scale, showing the deepening of the bleaching at 500 nm and the increase of the 650 nm band.

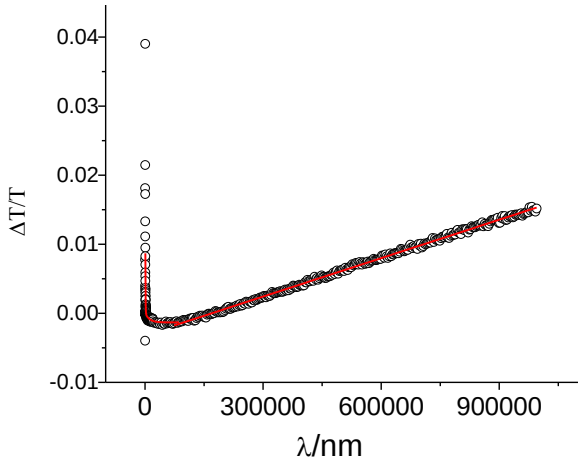

Figure 3.22 Fast growth of the 500 nm absorption, for DC143 after 510 nm excitation, followed by the slow bleaching of the band according to a ns kinetics.

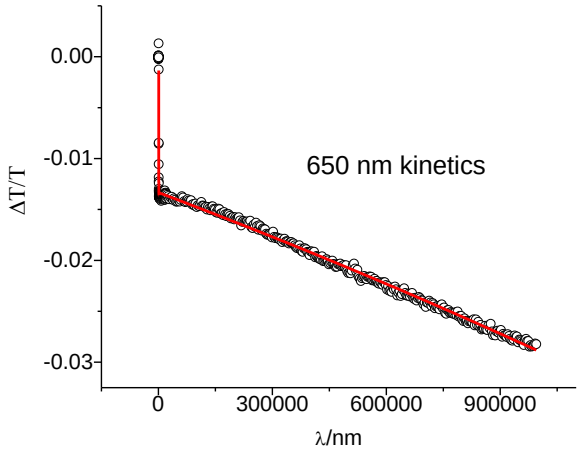

Figure 3.23 Fast growth of the 650 nm absorption, for DC143 after 510 nm excitation, followed by growth due to triplet population.

The excited state dynamics of DC194 upon 510 excitation (figure 3.24) is characterized by an initially fast decay dynamics (figure 3.25) which is ostensibly determined by the relaxation from bridge centered electronic singlet states, intercepted by 510 nm excitation. There is a red shift of the 650 nm bleaching which is achieved after ca. 1 ps after the initial pulse. The evolution of the diagnostic bleaching continues until achieving, after ca. 100 ps, a long lived state, which continues to grow with a time constant of ca. 500 ps. Such state, whose spectral features do not change appreciably in the time window 200 ps/1 ns characterized by the presence of a bleach at 700 nm, which progressively flattens, and by an absorption band centered at 600 nm, which progressively increases (figure 3.26), is reminiscent of the TA spectrum recorded under nanosecond excitation, and assigned to the lowest triplet state, suggesting that its population is already significant after 200 ps following the initial excitation.

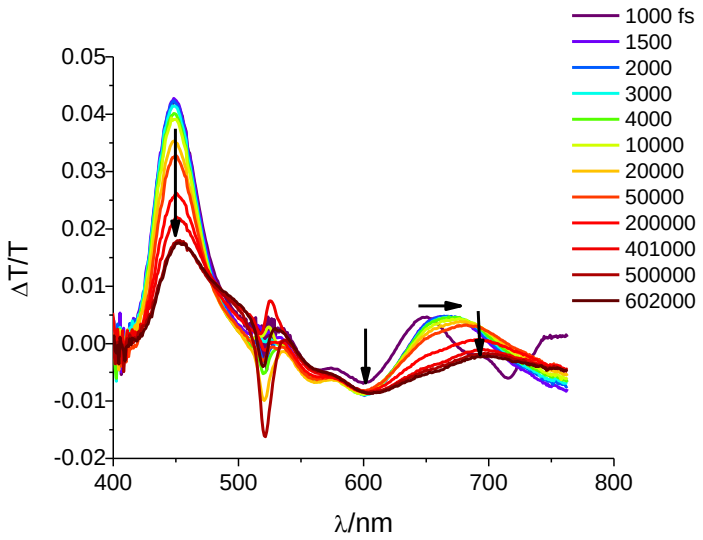

Figure 3.24 Time evolution of the transient spectrum of DC194 in ethanol, following 510 nm excitation. Significant delays sampled along the excited state decay curve are reported to illustrate the major spectral changes occurring after excitation.

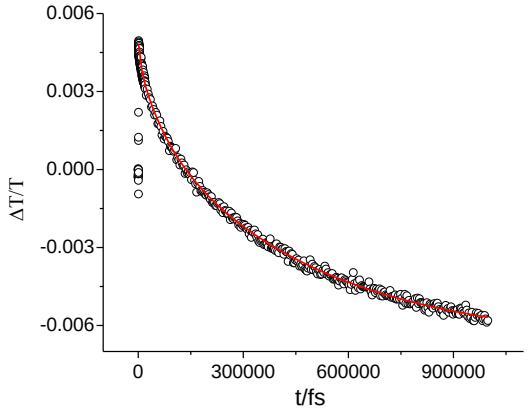

Figure 3.25 664 nm kinetics of the excited state of DC194 fitted with a triexponential function

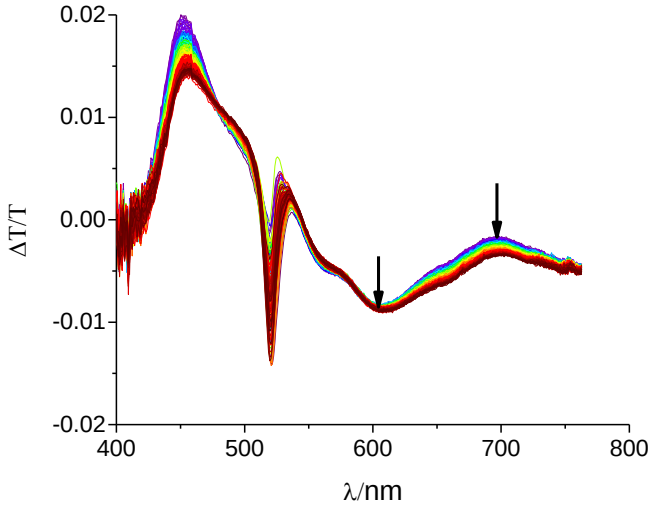

Figure 3.26 Transient spectrum of DC194 recorded in the 400-1000 ps time frame. The significant features which correlate with the nanosecond absorption, are summarized by the 700 nm bleaching which flatten out and by the increased of a 600 nm band, are indicated by arrows

Dynamics on TiO_2

Charge injection studies on TiO_2 were mainly performed at the 510 nm excitation wavelength which is similar, with regard to interception of the absorption manifold of the dye, to that (532 nm) used for nanosecond studies. In general the excitation with such wavelengths is conducted in order to excite the conjugated bridge, since it populates the absorbing states found between the B band and the lowest lying Q bands. The transient spectrum of DC145, taken in the 1-4 ps time frame, shows a signature which bears some similarities with that of the singlet state observed at comparable delays. There are, however, significant differences: at 600 nm there is a bleaching, instead of an absorption, while the long wavelength absorption in the 630-700 nm region is less structured, and increases by moving into the red (figure 3.27 a). The low energy absorption, consisting in the structureless absorption band beginning at 600 nm and increasing steadily when

moving towards lower energies, bears resemblances with that observed in the charge separated state (DC $145^{+}/e^{-}$ (TiO_2)), generated by nanosecond 532 nm excitation, suggesting that charge injection occurs on a time scale similar to the temporal width of the excitation pulse. This is also corroborated by the fact that the amplitude of the transient signal reaches its maximum intensity at very early delays, and maintains constant spectral features during the time evolution monitored up to 20 ps (figure 3.27 b), where the relative amplitudes of the diagnostic fingerprints simply evolve according to a multi-exponential kinetics without modifying their shapes. The analysis of the dynamics during the first 2000 fs at 615 nm, where the singlet excited state shows an isosbestic point, in order to avoid any interference from residual excited state (see figure 3.28 a), further confirms the occurrence of charge injection, documented by the appearance of a long lived absorption band, within the duration of the excitation pulse, irrespective of the excitation wavelength (both 480 and 510 nm excitations yield similar dynamics), attaining a long lived state (for the time scale under consideration) after ca. 250 fs from the onset of the pulse rise.

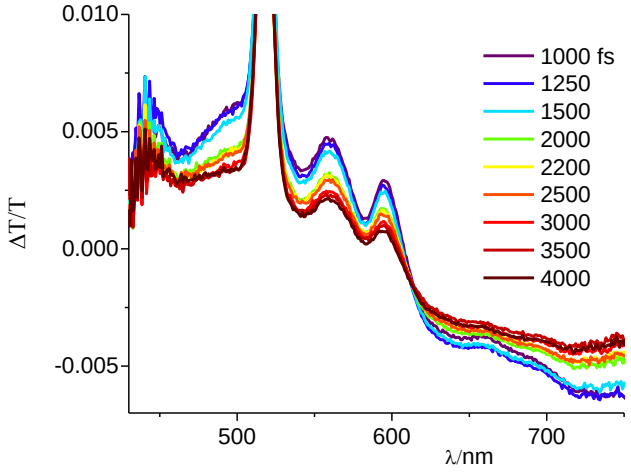

(a)

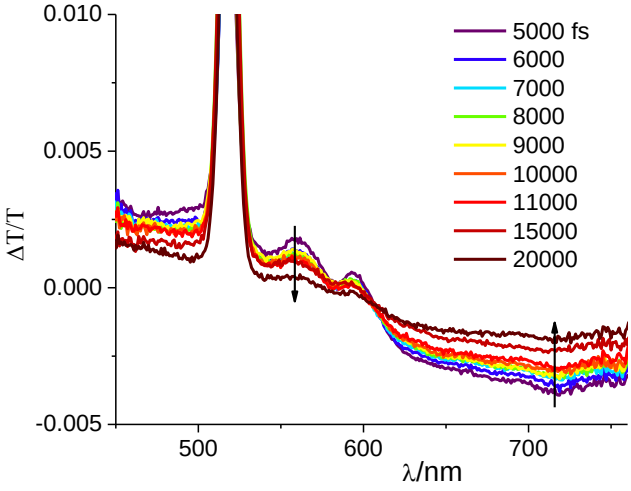

(b)

Figure 3.27 Transient spectrum of DC145 loaded on TiO_2 thin film, following 510 nm excitation, (A) early delays 1-4 ps; (B) late delays 5-20 ps. Early and late delays are reported in different figures for sake of clarity.

Similar conclusions can be drawn by observing the dynamics of the DC143 and DC194 dyes loaded on TiO_2 thin films. The formation of the charge separated state, consistent with the spectral features observed by nanosecond spectroscopy, is evident at very early delays after the fs excitation of the dye: DC143 shows the immediate appearance of a broad low energy absorption at 700 nm, preceded by the characteristic narrow 640 nm shoulder (figure 3.28 a). The bleaching bands are also structured with a narrow 450 nm shoulder followed by a broader 500 nm band, in agreement with those observed under ns excitation. The kinetic analysis at the 567 nm excited state isosbestic point of DC143 (Figure 3.29b) confirms that the injection occurs during the first 250-300 fs and is clearly convolved with the excitation pulse, showing the subsequent slow decay of the oxidized dye by electron recombination starting already within 150 fs after the maximum of the pulse width. The meso substituted dye DC194, shares spectral features quite close to those of DC143, with an intense low energy absorption reaching a maximum around 750 nm (figure 3.28 b). The main two bleaching bands at 450 and 500 nm are also similar to those of DC143. The agreement between the ultrafast spectral signature and the TA spectrum recorded under ns excitation confirms that DC194 also injects on a very fast time scale, as can be cleanly observed by monitoring the 700 nm absorption, which is very diagnostic in view of the fact that the excited state, at both early and late delays is characterized by a bleaching rather than by an absorption at such wavelength. The appearance of a long lived absorbing state (negative in ΔT/T representation) is evident from figure 3.29 C after 250 fs from the threshold of the pulse rise, essentially indicating a pulse width limited charge injection.

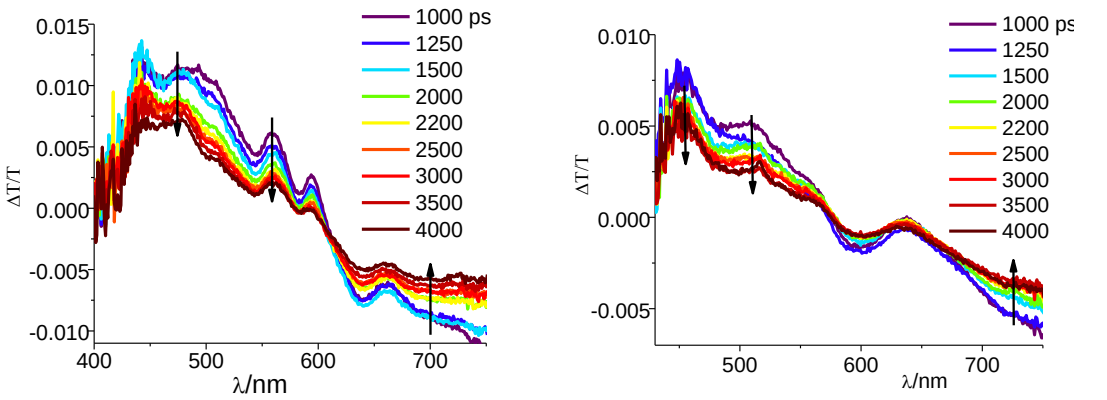

Figure 3.28 Transient spectra of DC143 (a) and DC194 (b) following 510 nm excitation observed framed up to 4 ps delay.

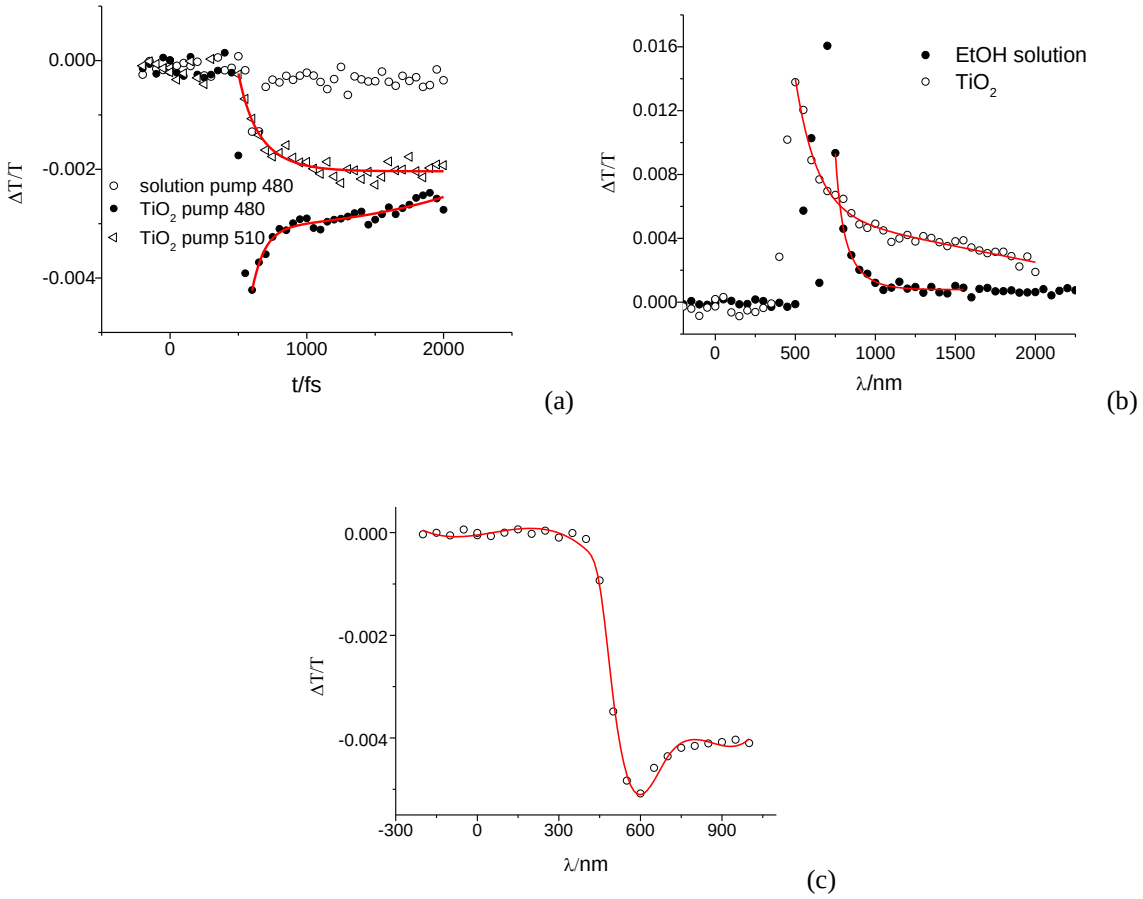

Figure 3.29 Injection kinetics into TiO_2 resulting in the formation of the oxidized dye: A) DC145 observed at the excited state isosbestic point of 615 nm; B) DC143 observed at the excited state isosbestic point of 567 nm ; C) DC194 observed at 700 nm.

The multiexponential recovery (figure 3.30) generally observed with all dyes after generation of the charge separated state is ascribed to initially fast charge recombination, which is likely due to the high power density generated by the 150 fs excitation pulse, possibly resulting in geminate recombination. In general the decay up to 20 ps, which can be well fitted by a biexponential function, reaches after ca. 5 ps a steady state having an amplitude which varies from ½ (DC145) to ca. 1/3 (DC143 and DC194) of the initial signal convolved with the excitation pulse. The smaller steady state amplitude which is found with the highly conjugated dyes bearing the bi-thiophene linker may suggest that a smaller fraction of the oxidized dye is able to survive the initial fast electron recapture, on a time scale where regeneration of the redox couple cannot occur. The amplitude weighted lifetime for recombination is consistent with this interpretation, varying in the order DC143 (1.8 ps) < DC194 (3.8 ps) < DC145 (5.3 ps). Such effect might be reasonable in view of the stronger electronic coupling between the electronic vacancy left in the conjugated dye and the electron injected into the conduction band of TiO_2. These results should be however carefully

extended to natural solar irradiation condition, given that the extremely high power densities reached in fs experiments generate much more than the average 20 electrons/particle expected in solar illumination conditions [20].

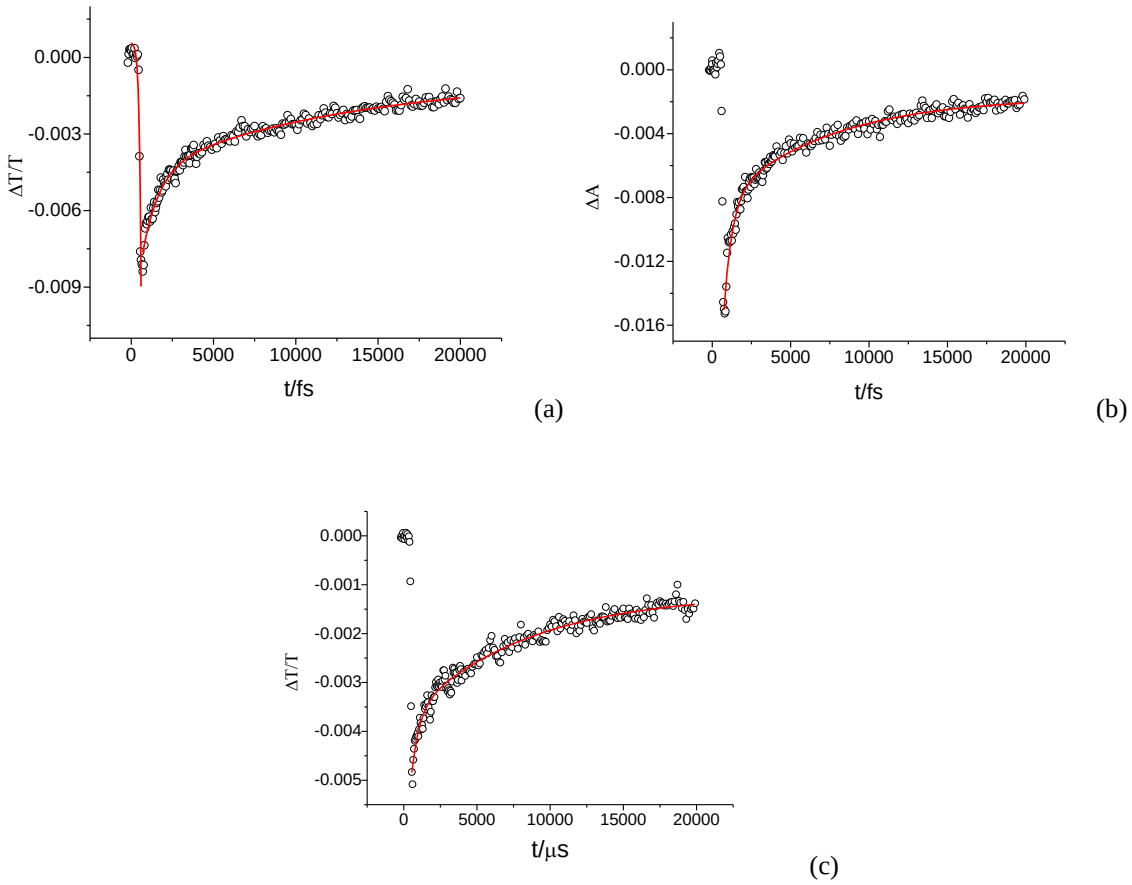

Figure 3.30 Generation and decay of the charge separated state of porphyrin dyes on TiO_2 thin films within the time frame of 20 ps fitted with bi-exponential functions. (A) DC145 observed at 750 nm; (B) DC143 observed at 750 nm (C) DC194 observed at 700 nm.

Photoelectrochemical characterization

IPCE spectra recorded on thin film TiO_2 electrodes (ca. 3 μm) in the presence of the I^-/I_2 electrolyte confirm that the thiophene bridged porphyrins are able to produce a panchromatic response (Figure 3.31 a). IPCE maximum values, close to 90 % (corrected for the FTO transmission), agree with the dye regeneration efficiency calculated by transient spectroscopy in the ns-μs time domain, and with the observation of quantitative injection on the hundred femtosecond time scale. In particular the charge transfer states originated by the delocalized bridge, responsible for the absorption between 480 and 550 nm, are highly active in the conversion of photons into electrons, resulting in the broad feature characterizing the photoaction of the DC143 and DC194 dyes. These two dyes also produce a better red responsivity than the DC145 moiety, which however displays a slightly better conversion in the UV-Vis between 400 and 450 nm.

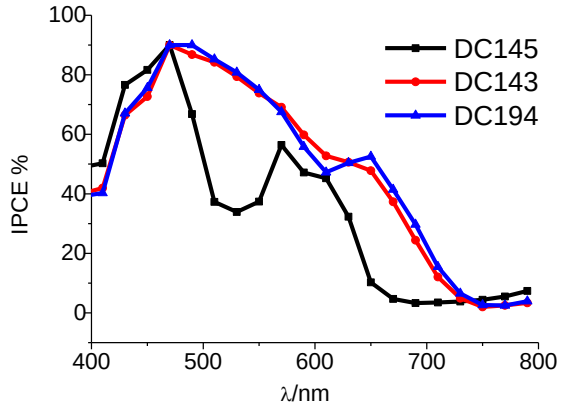

(a)

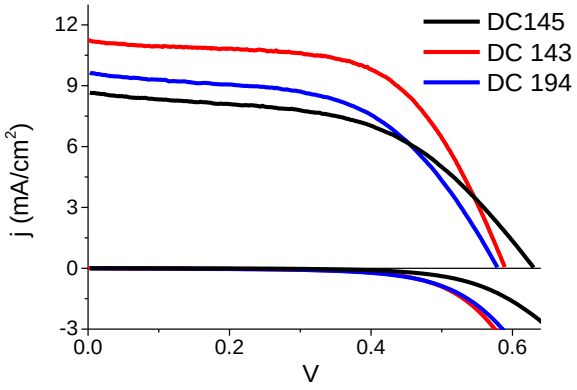

(b)

Figure 3.31 (a) IPCE spectra of DSSC based on semi-opaque TiO_2 in the presence of 0.6 M PMII/ 0.1 M LiI/ 0.02 M I_2/0.05M TBP in ACN; (b) JV curves, under illumination and under dark conditions

The JV curves recorded under simulated solar illumination (figure 3.31 b) are consistent with the IPCE, with the average photocurrents aligned around 10 mA/cm^2, with the DC194 and DC143 dyes showing, in some cases, a significantly larger photocurrent, ostensibly due to the combination of better harvesting and comparable charge injection rates with respect to the DC145 reference, as already pointed out by the transient spectroscopic analysis. However, while DC145 generally produces sets of cells having a good reproducibility, highlighted by small error bars in figure 3.32, DC194 and DC143 show a much greater dispersion, suggesting that the adsorption conditions and cell fabrication with these dyes may be more difficult to optimize. This might be due to the larger steric hindrance of these latter dyes on the TiO_2 surface, which might produce variable dye loading, and to stronger aggregation interactions, originated by the extended π delocalization, which might be more difficult to control, despite the presence of chenodeoxycholic acid in the adsorption bath. In general the β-monosubstituted DC143 produces a better response than its meso-substituted counterpart, and in hot press sealed cells, where a temperature of ca. 80 C° allows the electrolyte to achieve a better permeation of the TiO_2 film, is able to achieve photocurrents of the order of 15

mA/cm^2, (Figure 3.33) superior to those previously recorded for optimized DC145 cells (ca. 12 mA/cm^2) [9, 10].

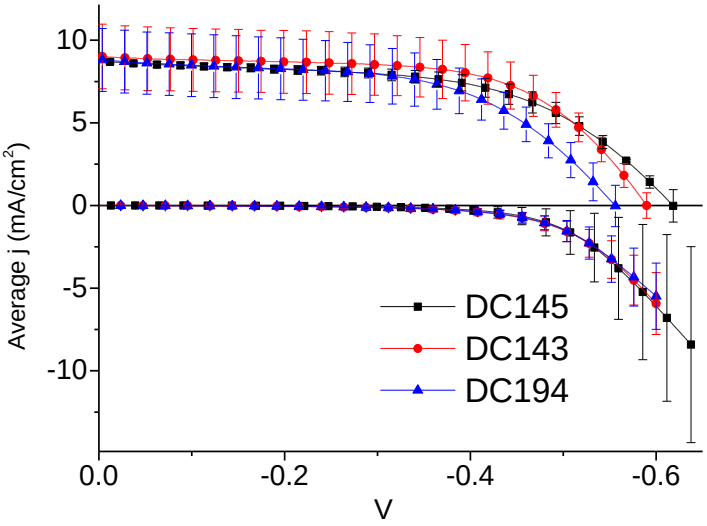

Figure 3.32 Averaged JV curves of sandwich DSSC under AM 1.5 G illumination

	Jsc	*Voc*	*FF*	*η %*
DC145	8.74	0.62	0.55	**2.98**
DC143	9.04	0.59	0.61	**3.23**
DC194	8.83	0.56	0.54	**2.69**

Table 3.4 Photovoltaic parameters calculated for the average JV curves measured under illumination

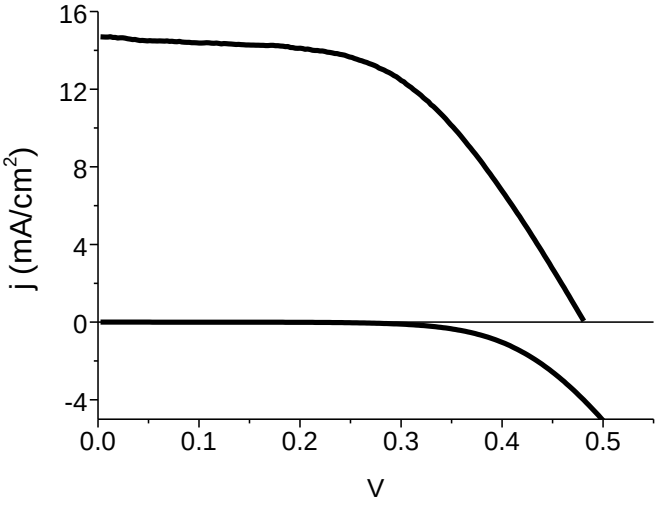

Figure 3.33 JV curves of hot press sealed DSSC based on DC143, under AM 1.5 G illumination

3.2.4 Conclusion

A new β-monosubstituted porphyrin dye (DC143) and its meso-substituted push-pull counter part (DC194) were characterized with regard to their elementary photophysical properties, relevant to sensitization and charge separation on TiO_2, followed by a photoelectrochemical study in DSSC. A comparison was made between these molecules, bearing a DTE unit in the π-conjugated arm, which is commonly employed to introduce a panchromatic effect, and a reference β-push-pull porphyrin dye previously investigated (DC145).

Transient absorption spectroscopy measurements in the ns-μs domain revealed the formation of the charge separated state when the three dye molecules are anchored to TiO_2, having a much longer lifetime than their respective triplet excited states in aerated solutions. For DC145, the evaluated charge-separated state lifetime was ~7 μs, while with DC143 and DC194 dyes it was of 14 and 11 μs respectively. It should be noted that in all cases the recovery was not complete on a time scale of 2×10^{-5} s. As a consequence, for all dyes under investigation, the slow recombination allowed for nearly quantitative regeneration efficiencies by the iodide based electron donor species, (97% for DC143, 90% for DC194 and 92% for DC145, at short circuit).

To gain deeper insights about the excited state dynamics in solution, for the three studied dyes, and the dynamics occurring on TiO_2 previous to the charge separated state formation, a series of transient absorption measurements in the sub-nanosecond timescale were performed, which confirmed the electron injection to occur during the first 250-300 fs, for all of the three dyes. A fast charge recombination process occurring just after the fs timescale injection was characterized by a lifetime which followed the order: DC143 (1.8 ps) < DC194 (3.8 ps) < DC145 (5.3 ps) suggesting that in the highly conjugated DC143 and DC194 structures with stronger electronic coupling with the surface, an initially fast Dye^+/e^- electron recapture process might reduce the fraction of oxidized dye able to be regenerated. Nonetheless, heterogeneous recombination kinetics from ultrafast spectroscopy should be carefully taken, since extremely high power densities are reached in fs experiments, generating much more than the average 20 electrons/particle expected in solar illumination conditions, accelerating thus recombination events.

Finally the photoelectrochemical study enlightened the comparable performances obtained while employing the three sensitizers, with maximum efficiencies reached by DC143. It can thus be concluded that the presence of the long conjugated arm doesn't penalize charge injection and it is beneficial from the point of view of light harvesting, introducing a panchromatic effect, leading to increased photocurrent. We can also confirm that β substituted dyes are not at a disadvantage with respect to meso-substituted structures as long as charge injection and dye regeneration is concerned. Although the best performances with the DTE modified porphyrins were superior to the reference dye DC145, notably in photocurrent, due to the above discussed panchromatic effect, the average performances obtained in a batch of three cells showed a greater variability with the new

structures than with the reference dye. This is possibly due to better defined adsorption conditions with the older and better known DC145 moiety, but also to variable dye loading resulting from the higher steric hindrance and to surface aggregation phenomena of the conjugated structures which may be more difficult to control.

References

(1) Robertson, N. Optimizing Dyes for Dye-Sensitized Solar Cells. *Angew. Chem., Int. Ed.* **2006**, 45, 2338−2345.

(2) Hasobe, T.; Imahori, H.; Kamat, P. V.; Ahn, T. K.; Kim, S. K.; Kim, D.; Fujimoto, A.; Hirakawa, T.; Fukuzumi, S. Photovoltaic Cells Using Composite Nanoclusters of Porphyrins and Fullerenes with Gold Nanoparticles. *J. Am. Chem. Soc.* **2005**, 127, 1216−1228.

(3) Li, L. L.; Diau, E. W. G. Porphyrin-Sensitized Solar Cells. *Chem. Soc. Rev.* **2013**, 42, 291−304.

(4) S. Mathew, A. Yella, P. Gao, R. Humphry-Baker, B.F. E. Curchod, N.Ashari-Astani, I. Tavernelli, U. Rothlisberger, Md. K. Nazeeruddin and M. Grätzel, **2014** *Nature Chemistry*, 6, 242–247

(5) Yella, A.; Lee, H. W.; Tsao, H. N.; Yi, C.; Chandiran, A. K.; Nazeeruddin, M. K.; Diau, E. W. G.; Yeh, C. Y.; Zakeeruddin, S. M.; Grätzel, M. *Science* **2011**, 334, 629−634.

(6) Barea, E. M.; Caballero, R.; López-Arroyo, L.; Guerrero, A.; de la Cruz, P.; Langa, F.; Bisquert, J. *ChemPhysChem* **2011**, 12, 961−965.

(7) Ziessel, R.; Bauerle, P.; Ammann, M.; Barbieri, A.; Barigelletti, F. Exciton-like Energy Collection in an Oligothiophene Wire EndCapped by Ru- and Os-Polypyridine Chromophores. *Chem. Commun*. **2005**, 802−804.

(8) Mussini, P. R.; Orbelli Biroli, A.; Tessore, F.; Pizzotti, M.; Biaggi, C.; Di Carlo, G.; Lobello, M. G.; De Angelis, F.. *Electrochim. Acta* **2012**, 85, 509−523.

(9) Di Carlo G., Orbelli Biroli A, Pizzotti M., Tessore F., Trifiletti V., Ruffo R., Abbotto A., Amat A., De Angelis F., and Mussini P.R., *Chem. Eur. J.* **2013**, 19, 10723–10740

(10) Di Carlo G., Caramori S., V.. Trifiletti, R. Giannuzzi, L. De Marco, M. Pizzotti, Orbelli Biroli A., Tessore F., Argazzi R., Bignozzi C. A. ,*ACS Appl. Mater. Interfaces* **2014**, 6, 15841−15852

(11) Di Carlo G., Orbelli Biroli A, Tessore F., Pizzotti M., Trifiletti V., Mussini, P. R.; Amat A., De Angelis F., Abbotto A., Trifiletti V., Ruffo R., *J. Phys. Chem. C* **2014**, 118, 7307−7320

(12) A. Orbelli Biroli, F. Tessore, V. Vece, G. Di Carlo, P. R. Mussini, V. Trifiletti, L. De Marco, R. Giannuzzi, M. Manca and M. Pizzotti *J. Mater. Chem. A,* **2015**,3, 2954-2959

(13) Lo, C. F.; Hsu, S. J.; Wang, C. L.; Cheng, Y. H.; Lu, H. P.; Diau, E. W. G.; Lin, C. Y. *J. Phys. Chem. C* **2010**, 114, 12018−12023.

(14) Bessho, T.; Zakeeruddin, S. M.; Yeh, C. Y.; Diau, E. W. G.; Grätzel, M. *Angew. Chem., Int. Ed.* **2010**, 49, 6646−6649.

(15) Chang, Y. C.; Wang, C. L.; Pan, T. Y.; Hong, S. H.; Lan, C. M.; Kuo, H. H.; Lo, C. F.; Hsu, H. Y.; Lin, C. Y.; Diau, E. W. G. *Chem.Commun*. **2011**, 47, 8910−8912.

(16) Wang, C. L.; Lan, C. M.; Hong, S. H.; Wang, Y. F.; Pan, T. Y.; Chang, C. W.; Kuo, H. H.; Kuo, M. Y.; Diau, E. W. G.; Lin, C. Y. *Energy Environ. Sci*. **2012,** 5, 6933−6940.

(17) Orbelli Biroli, A.; Tessore, F.; Pizzotti, M.; Biaggi, C.; Ugo, R.; Caramori, S.; Aliprandi, A.; Bignozzi, C. A.; De Angelis, F.; Giorgi, G.; Licandro, E.; Longhi, E. *J. Phys. Chem. C* **2011**, 115, 23170−23182.

(18) T. Virgili , G. Grancini , E. Molotokaite , I. Suarez-Lopez , S. K. Rajendran , A. Liscio , V. Palermo , G. Lanzani , D. Polli , and G. Cerullo *Nanoscale*, **2012**,4, 2219-2226

(19) W. Song, M. K. Brennaman, J. J. Concepcion, J. W. Jurss, P. G. Hoertz, H.Luo, C. Chen, K. Hanson, and T. J. Meyer *J.Phys.Chem. C* **2011** 115 (14), 7081-7091

(20) Helena Greijer Agrell, Gerrit Boschloo,* and Anders Hagfeldt *J. Phys. Chem. B* **2004**, 108, 12388-12396

Chapter 4: Influence of electrostatic interactions in quenching studies involving ruthenium and cobalt complexes

While developing new electronic mediators for DSSC there are many factors which have to be taken into account, in order to produce efficient devices. First of all, the potential of the chosen redox couple must be high enough to reduce the oxidized dye and to achieve high photovoltage values ($V_{OC} = E_F - E_{redox}$). Hence, in the case of cobalt complexes, which are the central point of this thesis, the ligands coordinated to the metal centre have to be carefully selected, in order to obtain, for the $Co^{II/III}$ couple, a reversible redox process provided with an opportunely tuned half-wave potential. The ligands choice must be done considering also that bulky substitutents could help preventing the recombination pathways between the oxidized cobalt center and the photoinjected electrons, but bearing in mind that this could penalize a lot the complex diffusion properties, in the cell bulk and in the TiO_2 porous structure as well. Finally the designed redox couple is required to display good kinetic properties towards the available cathodic materials, like platinum or PEDOT.
A factor that isn't frequently considered in the choice of the electronic mediator, or in the development of new ones, which hasn't been deeply analyzed so far but whose importance could be non-negligible, is that of electrostatic interactions between the species involved in the DSSC interfacial charge transfer processes. In this chapter an attempt to expand the understanding of these interactions will be presented. First, a quenching study in solution between differently charged ruthenium sensitizers and cobalt complexes was conducted, enlightening the strong influence of the charge factor on the quenching efficiencies. Later, the species showing the most interesting results in solution were considered for a photophysical and photoelectrochemical study with sensitized TiO_2 photoanodes. The obtained results proved that in specific cases the electrostatic factor has a role in the DSSC electron transfer kinetics, and hence could be exploited to induce efficient charge separation by ionic couples assembled of the semiconductor surface.

4.1 Ion-pair enhanced quenching processes between ruthenium and cobalt complexes in solution

4.1.1 Introduction

Electronic charge of molecular species involved in electron transfer processes in solution or at an interface have a dramatic effect on the magnitude and rates of these events. Studies focused on the coulombic interactions between oppositely charged donor and acceptor species find large interest in many areas of research, like catalysis, optoelectronics, and solar energy conversion [1-8].

In particular, with reference to the field of dye sensitized solar cells, systems that combine ruthenium based sensitizers and the I_3^-/I^- redox couple, characterized by a negative charge both in its reduced and oxidized form, have been extensively characterized both in solution and with the dye molecules anchored to the TiO_2 semiconductor interface [9-12]. What has emerged from the solution studies in dichloromethane and acetonitrile, was that metal-to-ligand charge transfer (MLCT) excited states of globally cationic sensitizers, like $Ru(bpy)_3(PF_6)_2$ or $Ru(bpy)_2(deeb)(PF_6)_2$, experienced reductive quenching, through electron transfer to the excited state from iodide. Moreover, the occurrence of ion-pairing between the oppositely charged donor and acceptor species was demonstrated. The formation of this encounter complex was shown to enhance the quenching process, and has been included in the accepted mechanism for the sensitizer regeneration process in DSSC [13], even if only one study has provided direct evidence for this [14].

Indeed, these observed phenomena involving charged species in solution can remarkably affect the efficiencies of the corresponding photoelectrochemical devices, where the sensitizer is anchored to the titanium dioxide semiconductor surface, influencing processes like the oxidized sensitizer regeneration at the photoanode and the oxidized electronic mediator reduction at the cathodic counterpart. However, due to the many concomitant factors controlling the overall solar cell kinetics, electronic coupling, driving force, and reorganization energy just to name a few, it is complicated to isolate and describe exhaustively a single phenomenon.

In this scenario, many efforts have been done to characterize systems containing iodide combined in solution with ruthenium based dye molecules, but, to our knowledge, little information is available regarding electron transfer processes involved in dssc based on cobalt (II) complexes [15-17], which have proved to be an important category of alternative redox mediators for dye sensitized solar cells [18-20]. Therefore in this study a cationic ruthenium compound and an anionic cobalt redox mediator were used, exploiting the coulombic attractive interaction in order to facilitate the formation of significant ion-pairing in acetonitrile solution.

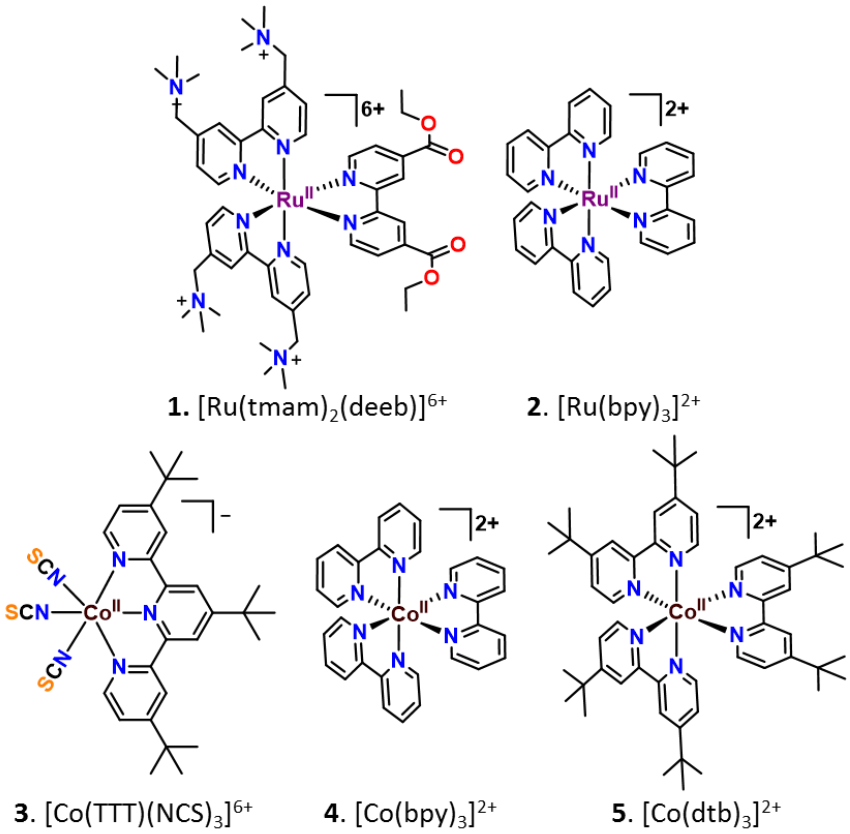

Figure 4.1 Polypyridil complexes used in this study: two ruthenium based sensitizers (**1**,**2**) and three cobalt based electronic mediators (**3**,**4**,**5**), where: *tmam* = 4,4′-bis(trimethylamino)methyl-2,2′-bipyridine, *deeb* = 4,4′-diethylester-2,2′-bipyridine, *TTT* = 4,4′,4″-tri-*tert*-butyl-2,2′:6′,2″-terpyridine, *bpy* = 2,2'-bipyridine, *dtb* = 4,4'-ditertbutyl-2,2'-bipyridine

Indeed, with the aim of deeper insights about photoelectrochemical systems utilizing cobalt and ruthenium complexes, with a focus on electrostatic interactions, a quenching study in solution was accomplished, as a basis for future characterizations on the surface.

The investigated metal complexes are depicted in figure 4.1. Two ruthenium (II) polypyridyl dyes, $[Ru(tmam)_2(deeb)](PF_6)_6$ (**1**) and $[Ru(bpy)_3](PF_6)_2$ (**2**), with different global positive charges, were examined, which had proved to display enhanced ion pairing and excited-state reactivity with iodide [9-11]. The cobalt (II) based redox mediators employed were two complexes known in dssc studies [21], $[Co(bpy)_3](PF_6)_2$ (**4**) and $[Co(DTB)_3](PF_6)_2$ (**5**), which carry a divalent positive charge, and the newly synthesized monoanionic complex $[CoTTT(NCS)_3]TBA$ (**3**).

Interesting results were obtained, all coherent with the theory of the electrostatic interactions having a determining influence on the quenching processes kinetics. Aspect that is made clear, pointing out the importance it can have in real devices.

4.1.2 Experimental

Materials

The following chemicals were purchased from Sigma-Aldrich and were used as received: cobalt(II) chloride hexahydrate (98%), cobalt(II) perchlorate hexahydrate, tetrabutylammonium thiocyanate (TBANCS, 98%), 4,4′,4″-tri-*tert*-butyl-2,2′:6′,2″-terpyridine, 2,2′-bipyridyl (TTT, 95%), 4,4′-di-tert-butyl-2,2′-bipyridyl (dtb, 98%), ammonium hexafluorophosphate (NH_4PF_6, 95%), tetrabutylammonium hexafluorophosphate ($TBAPF_6$, 98%) nitrosyl tetrafluoroborate ($NOBF_4$, 95%). Diethyl ether (Fischer, 99.0% min), Acetonitrile (for synthesis, Fischer, 99.9% min), Acetonitrile (for spectroscopy, Burdick and Jackson, 99.98%), methanol (Fischer, 99.9% min), and chloroform (Fischer, 99.8% min) were used as received.

The $[Co(bpy)_3](PF_6)_2$ and $[CoDTB)_3](PF_6)_2$ complexes were synthesized according to literature methods starting from $Co(ClO_4)_2$ [22]. The hexafluorophosphate salts were isolated by precipitation with excess NH_4PF_6 in acetonitrile, filtered and washed with diethyl ether. The $[Ru(tmam)_2(deeb)](PF_6)_6$ and $[Ru(bpy)_3](PF_6)_2$ complexes were prepared according to literature procedures [9,23].

Synthesis of [CoTTT(NCS)$_3$]TBA

TBANCS (378.79 mg, 1.26 mmol) was added to $CoCl_2 \cdot 6(H_2O)$ (51.94 mg, 0.4 mmol) dissolved in the least amount of methanol. An intense blue mixture was obtained. Then the 4,4′,4″-Tri-*tert*-Butyl-2,2′:6′,2″-terpyridine ligand (160.6 mg, 0.4 mmol) dissolved in a minimum amount of chloroform was slowly added to the stirring mixture. A green precipitate readily formed, was filtered, and washed with cold methanol and diethyl ether to yield the pure product in 73% yield.

Characterization by ^{1}H-NMR spectroscopy was afforded through the oxidation of the paramagnetic Co^{II} complex to the diamagnetic Co(III) through addition of a slight excess of $NOBF_4$ in acetonitrile. ^{1}H NMR: δ 9.05 (2H, s); 8.63 (2H, s); 7.41 (2H, d); 7.12 (2H, d); 1.97 (6H, s); 1.83 (9H, s); 1.36 (12H, s). ^{13}C NMR: δ 171.42, 168.2, 155.87, 155.83, 151.29, 127.43, 125.16, 124.8, 37.52, 35.81, 29.82, 29.18. Elem anal. Calcd for $CoC_{46}H_{60}N_7S_3$ (877.23): C, 62.98; H, 8.16; N, 11.18. Found: C, 59.58; H, 7.17; N, 11.7.

NMR. Characteristic NMR spectra were obtained in CD_3CN on Bruker Avance III 400 MHz (^{1}H) and 600 MHz (^{13}C) spectrometers. Spectra were processed with MNOVA.

Elemental Analysis. C, H, and N elemental analysis was performed by Atlantic Microlabs, Inc.

Electrochemistry. Cyclic voltammetry plots were collected in a standard three-electrode cell with an Autolab PGSTAT 302/N potentiostat at a scan rate of 100 mV/s. A glassy carbon disk electrode was used as working (Amel), a standard calomel as reference (Amel), and a Pt wire as auxiliary (Sigma-Aldrich). All measurements were conducted in nitrogen purged acetonitrile solutions,

containing 0.3 M $LiClO_4$ or 0.1M $TBAPF_6$ as supporting electrolytes.

Squarewave voltammetry was performed on a BASi Epsilon electrochemical detector. A standard three-electrode cell composed of platinum disk working and auxiliary electrodes and an $Ag^+/AgCl$ pseudo reference electrode. An external ferrocene reference was used ($Fc^{+/0}$ = 630 mV vs. NHE).

UV−vis absorption. UV-vis absorption spectra were recorded on a Varian Cary 60 UV−vis spectrophotometer in 1 cm path length spectrophotometric quartz cuvettes.

Steady-state Photoluminescence. Steady-state photoluminescence (PL) measurements were obtained with a Horiba Fluorolog 3 Fluorimeter equipped with a 450 W Xe lamp as excitation source. PL spectra were corrected for lamp intensity fluctuations and detector response. Excitation of solutions was performed at 480 nm for $[Ru(tmam)_2(deeb)]^{6+}$ and 425 nm for $[Ru(bpy)_3]^{2+}$.

Time-resolved PL. Single wavelength decays were acquired on a nitrogen dye laser system described previously [24] with a 445 nm excitation wavelength. Photoluminescence intensity decays were monitored near the steady-state emission maximum, 650 nm for $[Ru(tmam)_2(deeb)]^{6+}$ and 625 nm for $[Ru(bpy)_3]^{2+}$.

Cobalt titrations. The Ru and Co acetonitrile solutions were purged with Argon for 40 minutes prior to measurements. Samples of 6 μM $[Ru(tmam)_2(deeb)](PF_6)_6$ and $[Ru(bpy)_3](PF_6)_2$ complexes at room temperature were analyzed as increasing cobalt concentrations were titrated with the Ruthenium concentration fixed. Titrations were completed using the same sample for steady-state absorption, steady-state and time-resolved PL measurements. Data analysis for all experiments was performed using OriginLab, version 9.0 and Mathematica version 13.0.

4.1.2 Results

The synthesized $[CoTTT(NCS)_3]TBA$ was electrochemically and spectroscopically characterized. Through cyclic voltammetry measurements the $Co^{II/II}$ and $Co^{I/II}$ reduction potential values, in acetonitrile with 0.3M $LiClO_4$, were identified at 0.24 and -0.76 V vs NHE respectively, and compared to the other studied cobalt complexes in Figure 4.2A. The irreversible process whose oxidative peak is positioned at 1.04 V vs NHE was assigned to the thiocyanate ligands oxidation, figure 4.2B. $Ru(bpy)_3^{2+}$ has well established redox active properties in acetonitrile [25], while $Ru(tmam)_2(deeb)^{6+}$ has been recently characterized[9], however a first ligand reduction potential had not been acquired. Cyclic voltammetry produced irreversible chemistry. Squarewave voltammetry showed a quasi-reversible reduction when the voltage was scanned in a negative direction. However, upon a positive scan, no appreciable current was measured. The peak of the quasi-reversible wave was taken to be an approximation for the half wave potential ($E_{1/2}$) for the ligand reduction, 1.45 V vs. NHE. Electrochemical data for the compounds used are compiled in table 4.1.

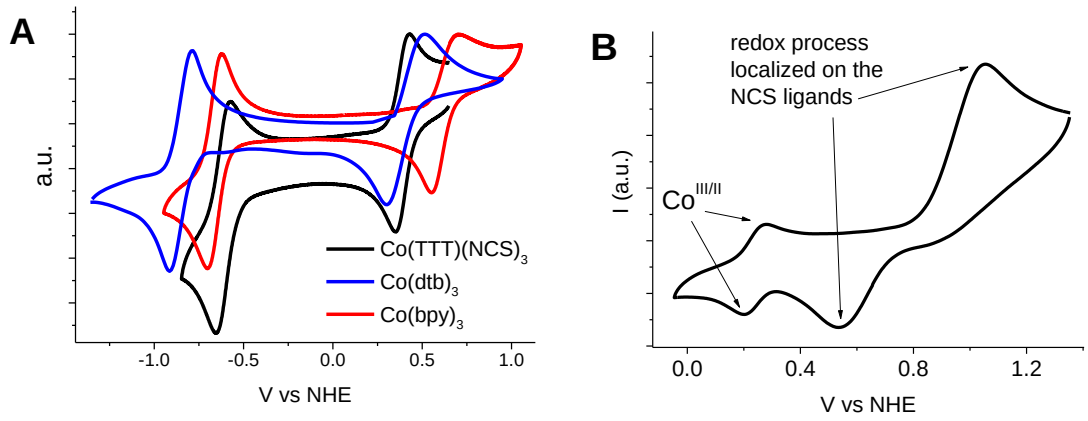

Figure 4.2 Cyclic voltammetry of (A) [CoTTT(NCS)$_3$]TBA in 0.1M TBAPF$_6$ ACN, in comparison with [Co(bpy)$_3$] and Co(dtb)$_3$ (B) [CoTTT(NCS)$_3$]TBA in 0.1M LiClO$_4$ ACN, showing the irreversible process localized on the NCS ligands

	E° (V vs NHE)						
	$Ru^{II*/+}$	**$Ru^{III/II*}$**	**$Ru^{III/II}$**	**$Ru^{II/+}$**		**$Co^{II/I}$**	**$Co^{III/II}$**
Ru(tmam)$_2$(deeb)	1.45	-0.44 [a]	1.72 [a]	-0.71	**CoTTT(NCS)$_3$**	-0.76	0.24
Ru(bpy)$_3$	1.01	-0.57	1.53	-1.10	**Co(bpy)$_3$**	-0.79	0.41
[a] values taken from reference [9]					**Co(DTB)$_3$**	-0.94	0.49

Table 4.1 Redox potentials of the cobalt and ruthenium complexes measured in 0.3 M LiClO$_4$ acetonitrile

The photophysical properties of the used ruthenium coompounds were previously described in detail [9, 26]. Figure 4.3A depicts the absorption characteristics of all five compounds at the concentrations utilized in this study. The Ru(bpy)$_3^{2+}$ and Ru(tmam)$_2$(deeb)$^{6+}$ spectra show the characteristic metal-to-ligand charge transfer absorbance with maxima at 452 nm (ε = 14,500 M^{-1} cm^{-1}) and 463 nm (ε = 16,000 M^{-1} cm^{-1}). Co(bpy)$_3$ and Co(dtb)$_3$ don't show appreciable absorbance in the visible range, while the green Co(TTT)(NCS)$_3^-$ compound displays a series of unresolved, low-intensity absorption bands which can be reasonably attributed to MLCT transitions [27-29] (Figure 4.3B). An extinction coefficient of 930 M^{-1} cm^{-1} was calculated at 625 nm. The more intense absorption peaks observed in the UV region were assigned as ligand-localized π-π* transitions. The oxidized forms of the three cobalt complexes don't have any significant absorption in the visible range.

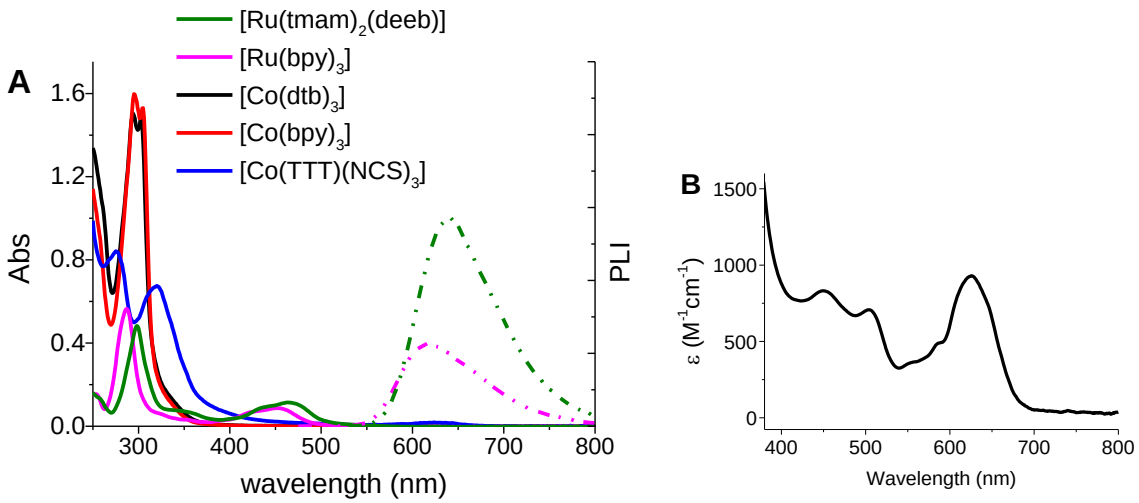

Figure 4.3 (A) UV-vis absorption spectra in acetonitrile for the three cobalt complexes, 40 μM (maximum concentration reached in the titration experiments), compared to the $[Ru(tmam)_2(deeb)]$ and $[Ru(bpy)_3]$ absorption spectra, 6 μM (concentration used in the titration experiments); PL spectra for the ruthenium compounds (dashed line). (B) Zoom on the $[CoTTT(NCS)_3]^-$ visible absorption, normalized to concentration.

Titration of an argon purged acetonitrile solution of the highly charged ruthenium complex with $[CoTTT(NCS)_3]^-$ resulted in distinct steady-state absorption changes (Figure 4.4A). A red-shift of the low energy MLCT band was observed, together wih a decrease in its intensity. Two isosbestic points were individuated at 417 and 480 nm. Absorbance increases below 400 nm and at ~ 630 nm were ascribed solely to the added cobalt compound, which fortunately has a small extinction coefficient with respect to $[Ru(tmam)_2(deeb)]^{6+}$. The $Co(TTT)(NCS)_3^-$ addition does not account for the observable decrease in the ruthenium compound absorbance as the ruthenium concentration was kept the same throughout the titration. Therefore, the observed red shift and decrease of the MLCT were attributed to ion-paired adduct formation between the hexacathionic ruthenium and the anionic cobalt complex [1].

When the $Ru(tmam)_2(deeb)^{6+}$ compound was titrated instead with either the cationic $[Co(bpy)_3]^{2+}$ or $Co(dtb)_3^{2+}$ no significant changes in the ground-state MLCT absorption were observed (Figure 4.4B,C). A titration was also performed through the addition of $[CoTTT(NCS)_3]^-$ to an acetonitrile solution of $[Ru(bpy)_3]^{2+}$ (Figure 4.4D). Observable spectral changes that could be described to a process other than absorption of the added cobalt compound were not observed for this reference case. A global absorbance increase that followed the increasing cobalt concentration was identified, which was not present in the $Ru(tmam)_2(deeb)^{6+}$ case as the MLCT decrease due to ion-pairing outcompeted the growth.

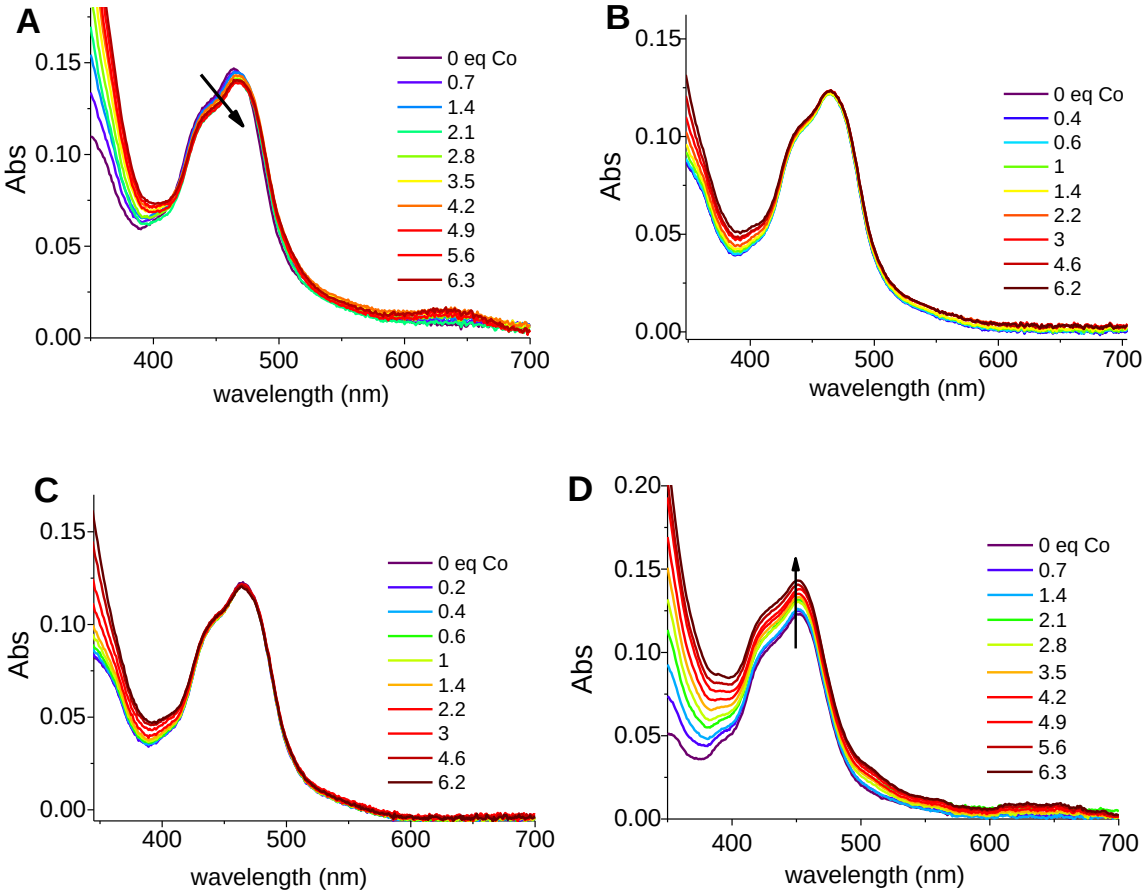

Figure 4.4 UV-vis absorption spectra of $[Ru(tmam)_2(deeb)]^{6+}$ in acetonitrile with the indicated number of cobalt equivalents with $[CoTTT(NCS)_3]^-$ (A), with $[Co(bpy)_3]^{2+}$(B); with $[Co(dtb)_3]^{2+}$(C); UV-vis absorption spectra of $[Ru(bpy)_3]^{2+}$ in acetonitrile with the indicated number of $[CoTTT(NCS)_3]^-$ (D).

Light excitation of $[Ru(tmam)_2(deeb)]^{6+}$ in acetonitrile resulted in room temperature photoluminescence, PL, which was significantly quenched upon the addition of $[CoTTT(NCS)_3]^-$. Steady-state PL excitation at 480 nm was utilized as this corresponded to an isosbestic point where ground-state absorption changes were minimal. Stern-Volmer analysis, represented by equation 4.1, of the integrated steady-state PL, produced an upward curving plot (figure 4.5A).

Time-resolved PL decay kinetics, produced by excitation at 445 nm, measured under different cobalt concentrations, were well described by a first-order kinetic model. Both the initial amplitude (I) after laser excitation and the lifetime (τ) were quenched by the addition of $[Co(TTT)(NCS)_3]^-$. The slopes from the Stern-Volmer analysis of the time-resolved data lead to the extraction of static (equation 4.2) and dynamic (equation 4.3) quenching constants, K_S = 106,200 M^{-1} and K_D = 13,600 M^{-1}, respectively, figure 4.6A. A second-order dynamic quenching rate constant, k_q, of 6 x 10^9 M^{-1} s^{-1} was obtained from equation 4.4, where τ_0 is the lifetime in absence of cobalt [1].

$$\frac{PLI_0}{PLI} = 1 + K_{SV}[Co] \qquad \text{(Eq. 4.1)}$$

$$\frac{I_0}{I} = 1 + K_S[Co] \qquad \text{(Eq. 4.2)}$$

$$\frac{\tau_0}{\tau} = 1 + K_D[Co] \qquad \text{(Eq. 4.3)}$$

$$k_q = \frac{K_D}{\tau_0} \qquad \text{(Eq. 4.4)}$$

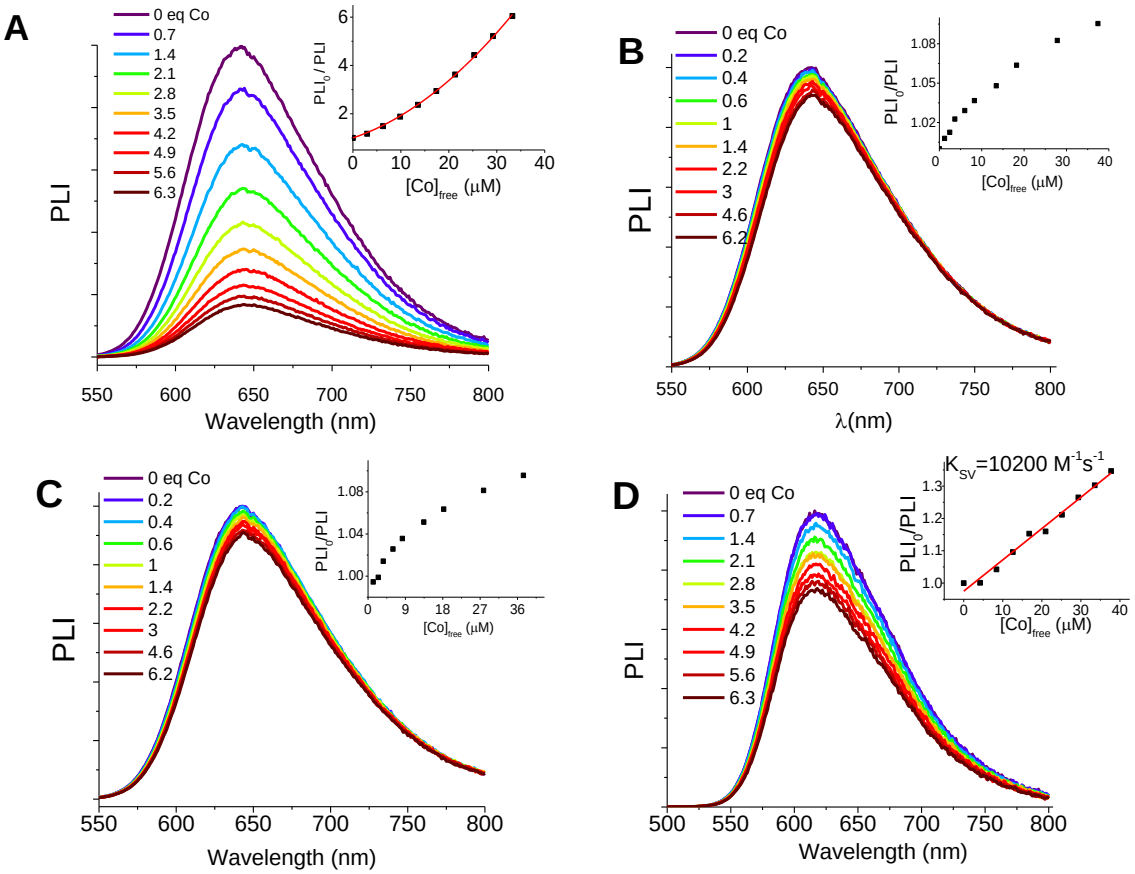

Figure 4.5 PL spectra of $[Ru(tmam)_2(deeb)]^{6+}$* in ACN with the indicated equivalent numbers of $[CoTTT(NCS)_3]^-$ (A), with $[Co(bpy)_3]^{2+}$ (B), with $[Co(dtb)_3]^{2+}$ (C); PL spectra of $[Ru(bpy)_3]^{2+}$* in ACN with the indicated equivalent numbers of $[CoTTT(NCS)_3]^-$ (D). Insets: Stern-Volmer analysis (PLI_0/PLI) of the integrated steady-state PL (equation 4.1), as a function of cobalt concentration.

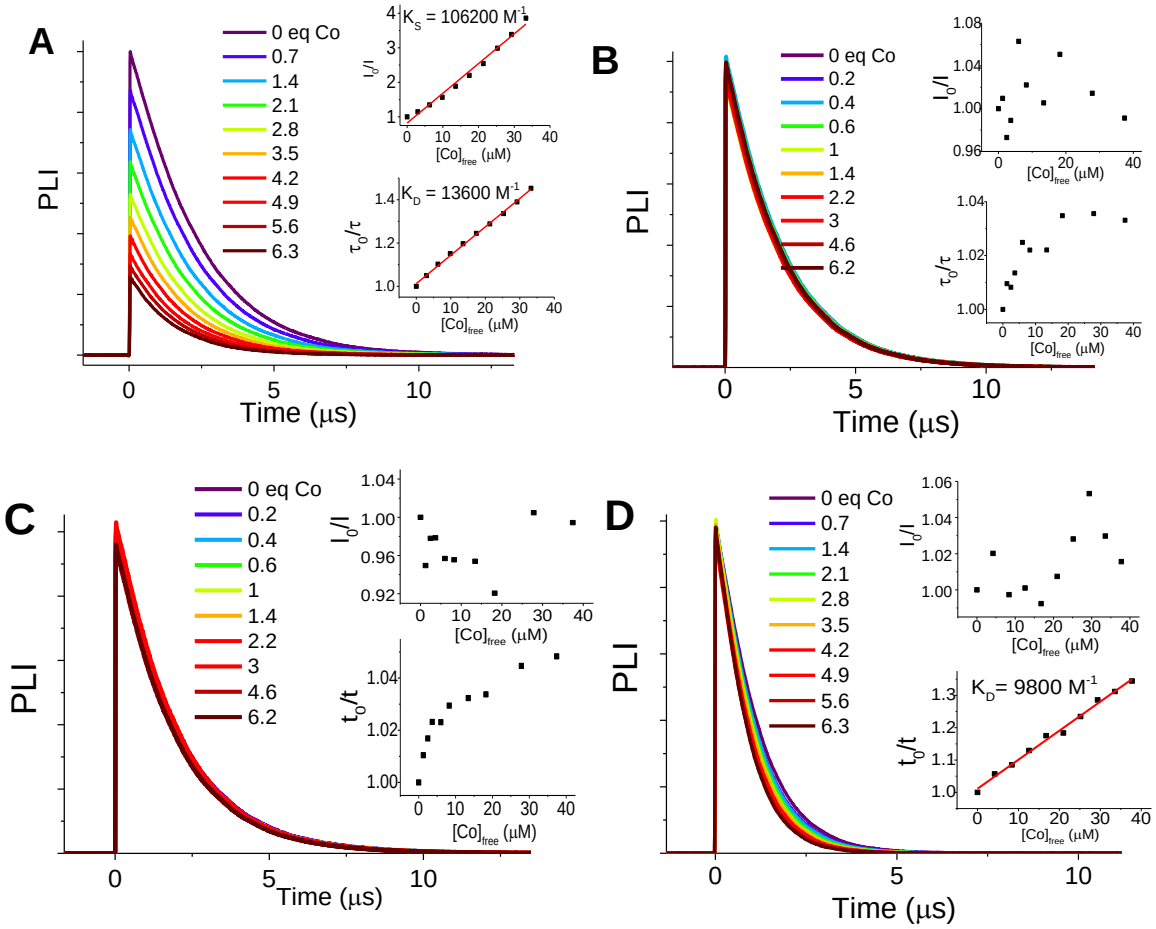

Figure 4.6 Time-resolved PL decays of $[Ru(tmam)_2(deeb)]^{6+}$* in acetonitrile with increasing concentration of $[CoTTT(NCS)_3]^-$ (A), $[Co(bpy)_3]^{2+}$ (B), $[Co(dtb)_3]^{2+}$(C); Time-resolved PL decays of $[Ru(bpy)_3]^{2+}$* in ACN with the indicated equivalent numbers of $[CoTTT(NCS)_3]^-$ (D). Insets: fractional initial amplitude and average lifetime quenching as a function of the different cobalt complexes concentration.

In titrations of $[Ru(tmam)_2(deeb)]^{6+}$ with $[Co(bpy)_3]^{2+}$ and $[Co(dtb)_3]^{2+}$ steady-state PL decreased only slightly. The Stern-Volmer analysis was non-linear and saturated at very low cobalt concentrations, figure 4.5B,C. The time-resolved PL showed no static decrease in the initial amplitude and a very small lifetime decrease that followed the steady-state one, figure 4.6B,C.

Illumination of $[Ru(bpy)_3]^{2+}$ at 425 nm led to photoluminescence that was less intense than the obtained by $[Ru(tmam)_2(deeb)]^{2+}$ excitation. This is due to the decreased quantum yield and lifetime of $[Ru(bpy)_3]^{2+}$ (τ = 0.67 μs, with respect to the τ = 1.07 μs for $[Ru(tmam)_2(deeb)]^{2+}$) . The steady-state PL excitation wavelength was chosen as the absorbance was similar to that of $[Ru(tmam)_2(deeb)]^{2+}$ and ensured a similar number of ruthenium excited states were produced. The Stern-Volmer analysis was linear with respect to the $[CoTTT(NCS)_3]^-$ concentration and indicated a purely dynamic quenching mechanism (figure 4.5D). The linear regression gave a slope corresponding to a Stern-Volmer constant value of 10,200 ± 500 M^{-1}. The time-resolved PL corroborated that only dynamic quenching was present for the $[Ru(bpy)_3]^{2+}$ system. Stern-Volmer

analysis (figure 4.6D) agreed with the steady-state PL results, showing a decrease of the lifetime and no variation in the initial amplitude. The extracted dynamic quenching constant K_D = 9,800 ± 900 M^{-1} was within the error of the value derived from the steady-state PL.

Studies were performed where the ionic strength of the $[Ru(tmam)_2(deeb)]^{6+}$ solution was increased through the addition of $TBAPF_6$. The UV-vis spectral changes induced by the $[Ru(tmam)_2(deeb)]^{6+}$–$[CoTTT(NCS)_3]^-$ ion-pair formation were progressively reduced by incrementing ionic strength. At 100 mM $TBAPF_6$, all spectral changes associated with the ion-pair formation were lost, Figure 4.7A. Increment in the $TBAPF_6$ concentration also led to decreases in both the static and dynamic photoluminescence quenching, Figures 4.7B and 4.8. In particular the static component decreased faster respect to the dynamic one. In fact, the static quenching constant (K_S) was zero at the highest concentration studied. Results obtained from Stern-Volmer analysis of time-resolved PL data are summarized in Table 4.2 and pictured in Figure 4.8, for all of the studied cases.

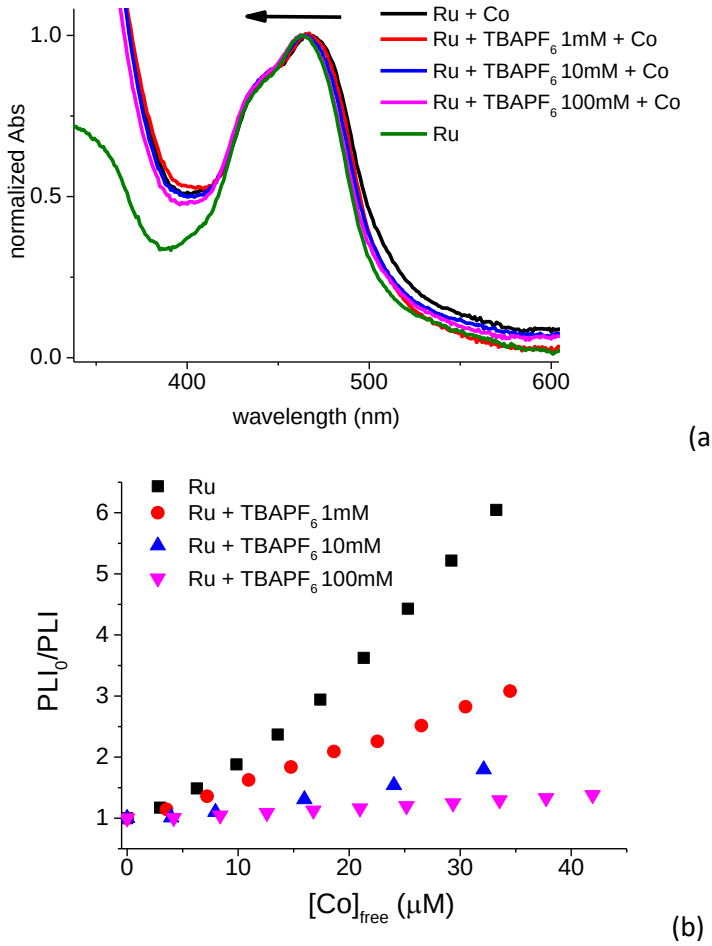

Figure 4.7 Changes in the MLCT absorption band maximum for $[Ru(tmam)_2(deeb)]^{6+}$ in acetonitrile, with 5.6 equivalents of $[CoTTT(NCS)_3]^-$ and different ionic strength values, increasing in the sense of the arrow (A); Stern-Volmer plots for $[Ru(tmam)_2(deeb)]^{6+*}$ (steady-State PL) quenched by $[CoTTT(NCS)_3]^-$ under different ionic strength values (B).

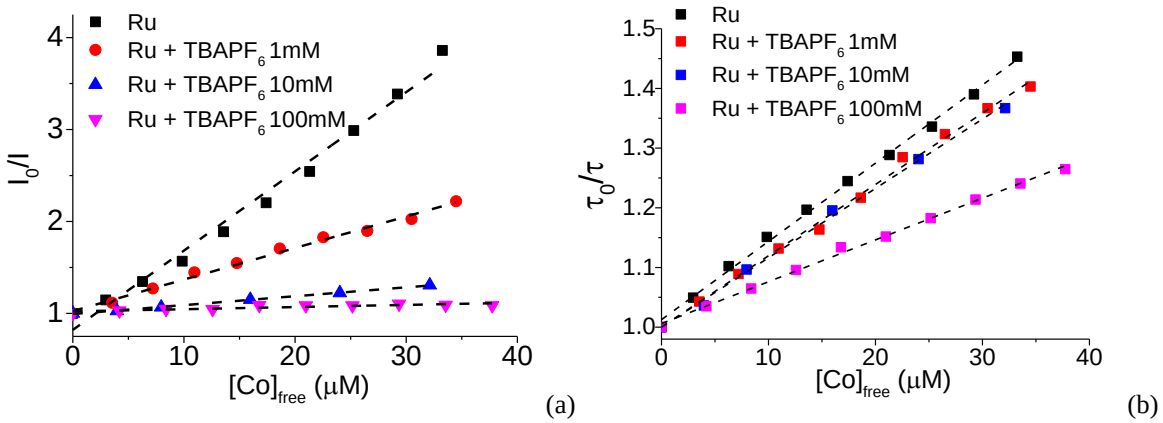

Figure 4.8 Fractional initial amplitude (a) and average lifetime (b) quenching as a function of $[CoTTT(NCS)_3]^-$ concentration for $[Ru(tmam)_2(deeb)]^{6+}$* under different ionic strength conditions.

	Co⁻	***Co⁻ + PF_6^- 1mM***	***Co⁻ + PF_6^- 10mM***	***Co⁻ + PF_6^- 100mM***	***$Co(bpy)_3$***	***$Co(dtb)_3$***	***Co⁻ + $Ru(bpy)_3$***
K_S *(*10^4 M^{-1})*	10.62	3.43	0.97	[a]	[a,b]	[a,b]	[a]
K_D *(*10^4 M^{-1})*	1.36	1.19	1.18	0.68	[b]	[b]	0.98
k_q *(*10^9 M^{-1} s^{-1})*	6.02	5.63	4.83	2.91	[b]	[b]	8.36

Table 4.2 Stern-Volmer quenching constants obtained through time-resolved PL (where Co^- is $[CoTTT(NCS)_3]^-$). [a] No static quenching was observed over the cobalt concentration studied. [b] No photoluminescence quenching due to electron or energy transfer was observed.

4.1.4 Discussion

The synthesis and study of a novel anionic, redox active cobalt compound was successful. The compound showed visible absorbance out to 700 nm, significantly more red shifted than the other cobalt compounds utilized in this study. However, the small extinction coefficient allowed optical monitoring of titrations without significant interference from the increased absorbance. Comparison studies to model complexes indicated that enhanced ion-pairing occurred between the anionic cobalt compound and the cationic $[Ru(tmam)_2(deeb)]^{6+}$. Below, the ion-pair characterization and quenching mechanism is discussed in reference to the present literature with a brief discussion on the impact of these studies to solar energy conversion.

Coulombic association enhances excited-state quenching

The addition of the anionic $[Co(TTT)(NCS)_3]^-$ to solutions of $Ru(tmam)_2(deeb)^{6+}$ led to systematic shifts in the ground-state MLCT absorption bands that have been previously ascribed to the formation of an ion-pair in solution, equation 4.5. The presence of a singular set of isosbestic points was consistent with the formation of an equilibrium between the donor, $[Co(TTT)(NCS)_3]^-$, and acceptor, $[Ru(tmam)_2(deeb)]^{6+}$, species.

$$Ru^{6+} + Co^- \overset{Keq}{\rightleftharpoons} [Ru,Co]^{5+} \quad \text{(Eq. 4.5)}$$

The steady-state and time-resolved spectroscopy data also confirmed this behaviour. In fact the upward curvature of the steady-state Stern-Volmer plot is diagnostic for the presence of ion-pairing [1]. Time-resolved Stern-Volmer analysis gave a quantification of the static Stern-Volmer constant, K_S = 86,200 M^{-1}. This static Stern-Volmer quenching arises as the quenching within the ion-pair is faster than our instrument response (k_{et} = > 10^8 s^{-1}). As such, the K_S calculated is directly the ion-pairing equilibrium (K_S = K_{eq}) in the ground state, equation 4.5. The non-ion-paired $[Ru(tmam)_2(deeb)]^{6+}$ excited states were quenched by free $[Co(TTT)(NCS)_3]^-$, through a dynamic process, which resulted in the decrease of the excited-state lifetime. As both static and dynamic quenching were observed, the upward curvature of the integrated steady-state PL Stern-Volmer analysis, deviating from equation 4.1, can be explained, since a linear Stern-Volmer plot is only accurate for the case when static quenching is not observed. For a system such as the one here, the integrated steady-state PL analysis must include the combination of the static and dynamic Stern-Volmer parameters, equation 4.6 [1].

$$\frac{PLI_0}{PLI} = (1 + K_D[Co])(1 + K_S[Co]) = 1 + (K_D + K_S)[Co] + K_D K_S[Co]^2 \qquad \text{(Eq. 4.6)}$$

It is important to note that the ion-pairing process lowers the freely diffusing concentration of cobalt ($[Co]_{free}$) through the formation of the ion-pair. This matters as the Stern-Volmer analysis must be the fractional photoluminescence decrease versus the concentration of free cobalt. To correct for the lowered concentration of cobalt equation 4.7 was utilized. Where *x* defines the concentration of the ion-paired species at equilibrium, $[Ru]_0$ and $[Co]_0$ are the initial (added) concentrations of the species. $[Co]_{free}$ was then calculated subtracting the obtained value for *x* from $[Co]_0$. It was assumed that the ion-paired species, formed within the studied $[Co(TTT)(NCS)_3]^-$ concentrations, was a 1:1 complex, and therefore the concentration of the ion-paired species was equivalent to the free cobalt loss. This process was iterated, by using the Mathematica software, until the K_S value obtained from the Stern-Volmer plot stayed steady with each iteration.

$$K_S = \frac{\boldsymbol{x}}{([\boldsymbol{Ru}]_\mathbf{0} - \boldsymbol{x})([\boldsymbol{Co}]_\mathbf{0} - \boldsymbol{x})} \qquad \text{(Eq. 4.7)}$$

The K_S and K_D values abstracted from the corrected time-resolved PL Stern-Volmer plots, table 4.2, were used to model the steady-state PL Stern-Volmer plot following equation 4.6. While not perfectly overlayed, the general upward curvature was observed and did overlay the data within reason, Figure 4.9.

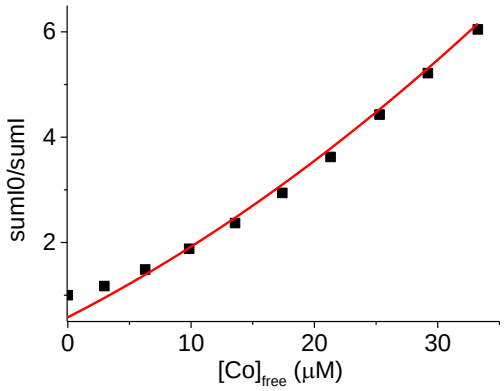

Figure 4.9 Steady-state PL Stern-Volmer plot relative to the $[Ru(tmam)_2(deeb)]^{6+}$ titration experiment with $[CoTTT(NCS)_3]^-$, modeled by equation 4.6.

As it has been said in the results, by increasing ionic strength of the dye solution through the addition of the inert salt $TBAPF_6$, quenching efficiency by $[CoTTT(NCS)_3]^-$ was progressively decreased, Figures 4.7 and 4.8. Interestingly, the static quenching component was more significantly affected by the increased ionic strength than the dynamic component. This behaviour clearly indicated the strong ion-pairing affinity that existed between the positively charged sensitizer and the negative cobalt complex. Only at high ionic strength (100 mM $TBAPF_6$) ion-pairing was completely suppressed, indicating that the attraction between the cobalt and ruthenium compounds was much greater than that with the PF_6^- anions and was only overcome by a large excess of these ions in solution.

Results obtained from the titration experiments with the cationic complexes $[Co(bpy)_3]^{2+}$ and $[Co(dtb)_3]^{2+}$ showed that not only was ion-pairing absent in these cases, but no quenching of the $[Ru(tmam)_2(deeb)]^{6+}$ excited state occurred. Indeed, Stern-Volmer analysis of the PL data collected was not possible. The observed slight decrease in the steady-state photoluminescence was associated with the incremented ionic strength, due to the addition of the cobalt compounds, rather than electron or energy transfer quenching processes. The concave Stern-Volmer plots are indicative of this assignment.

In order to further confirm the proposed results analysis based on electrostatic interactions the $[Ru(tmam)_2(deeb)]^{6+}$ quenching by $[CoTTT(NCS)_3]^-$ was compared to that of the model compound $[Ru(bpy)_3]^{2+}$ which has less positive global charge. The Stern-Volmer analysis of PL data revealed a fractional PL linear with cobalt concentration, suggesting the absence of the static quenching component but the presence of the dynamic one. Moreover, the reported similarity between the quenching constants values arising from the fractional PL and average lifetime quenching plots is characteristic of a pure dynamic quenching mechanism. What can be assumed from these results is

that with a less charged dye and less attractive interaction with the negative cobalt quencher the electronic coupling was reduced so ion pairing was absent and the dynamic quenching was slighter also, supporting the relevance that molecules charges have in quenching processes, together with the involved Gibbs free energy contributions.

Quenching mechanisms

Three quenching pathways are possible for *Ru(II) in the presence of Co(II) complexes, which are expressed in equations 4.8-4.10 [15-17]. The MLCT excited states can undergo bimolecular reactions like charge transfer by cobalt (reductive quenching, equation 4.8), to cobalt (oxidative quenching, equation 4.9), or energy transfer to cobalt (equation 4.10). The rates of the outer-sphere electron transfer reactions are a function of the redox potentials of the couples involved, while for the occurrence of energy transfer what matters is the spectral overlap between the energy donor emission and the acceptor absorption.

$$*Ru^{II}L_3^{2+} + Co(II) \underset{}{\overset{k_{red}}{\rightleftharpoons}} Ru^{II}L_3^{+} + Co(III) \quad \text{(Eq. 4.8)}$$

$$*Ru^{II}L_3^{2+} + Co(II) \underset{}{\overset{k_{ox}}{\rightleftharpoons}} Ru^{III}L_3^{3+} + Co(I) \quad \text{(Eq. 4.9)}$$

$$*Ru^{II}L_3^{2+} + Co(II) \underset{}{\overset{k_{en}}{\rightleftharpoons}} Ru^{II}L_3^{2+} + *Co(II) \quad \text{(Eq. 4.10)}$$

Analyzing the reduction potential values of the species used in this study, reported in Table 4.1, it can be assumed for all the studied species that the oxidative quenching of the $*Ru^{II}$ by Co^{II} is thermodynamically forbidden ($\Delta G > 0.1$ V), while the reductive quenching is highly thermodynamically allowed ($\Delta G < -1$ V). However, energy transfer can't be excluded, especially in the $CoTTT(NCS)_3$ case, due to the positive overlap between the cobalt ground-state absorption and the $*Ru^{II}$ emission, hence between the energetic levels involved in the energy transfer process.
In equations 4.11-4.15 the proposed electron-transfer mechanisms possible after photoexcitation of the ruthenium dye are reported [8]. The generated MLCT excited state can relax through dynamic diffusional or static associational quenching mechanisms (equations 4.11 and 4.12). According to the conventional cage escape model [30], the ion-pair formed can undergo competitive intramolecular back electron transfer (eq. 4.13) or diffusional cage escape (eq. 4.14). The redox pair in solution can be subject to electron-transfer charge recombination afterwards, regenerating the starting species in their ground-state (eq. 4.15).

$$*[Ru(II)]^{6+} + [Co(II)]^{-} \xrightarrow{dynamic\ q.} [Ru(II)]^{5+} + [Co(III)] \quad \text{(Eq. 4.11)}$$

$$*[Ru(II)]^{6+} + [Co(II)]^{-} \xrightarrow{static\ q.} [Ru(II)^{5+} \text{--- } Co(III)] \quad \text{(Eq. 4.12)}$$

$$[Ru(II)^{5+} \text{ --- } Co(III)] \xrightarrow{\textit{back electron transfer}} [Ru(II)^{6+} \text{ --- } Co(II)^{-}] \quad \text{(Eq. 4.13)}$$

$$[Ru(II)^{5+} \text{ --- } Co(III)] \xrightarrow{\textit{diffusional cage escape}} [Ru(II)]^{5+} + [Co(III)] \quad \text{(Eq. 4.14)}$$

$$[Ru(II)]^{5+} + [Co(III)] \xrightarrow{\textit{recombination}} [Ru(II)]^{6+} + [Co(II)]^{-} \quad \text{(Eq. 4.15)}$$

Nanosecond time-resolved transient absorption studies were performed to have evidence of any quenching products. Unfortunately, within the time resolution of the apparatus used no charge-transfer products were detected: in figure 4.10 the full TA spectrum of the 6 μM $[Ru(tmam)_2(deeb)]^{6+}$ dye in ACN, in the presence of 20 μM $CoTTT(NCS)_3$, is reported. It shows the $*Ru^{II}$ excited state absorption at 360 nm and the $Ru(II)^{2+}$ ground state absorption bleaching at 460 nm, while the absorption relative to the $Ru(II)^{+}$ quenching product formation, expected at 510 nm, is not observed. Neither any trace of the Co(III) formation, expected as a bleaching, can be identified.

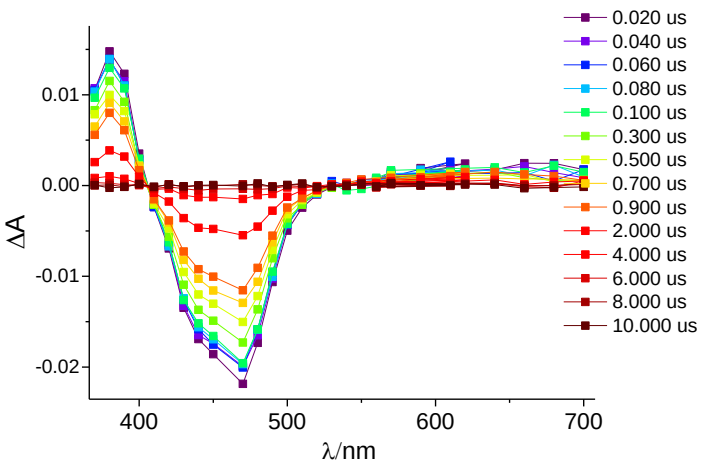

Figure 4.10 Full TA spectrum for 6 μM $[Ru(tmam)_2(deeb)]^{6+}$ in ACN, in the presence of 20 μM **[**$CoTTT(NCS)_3]^{-}$

Because of the cobalt based redox mediators nature, characterized by enhanced recombination rates in photoelectrochemical systems [31-34], it is possible that back electron transfer processes inside the ion-pairs formed, described by equation 4.13, are so fast that the solution quenching products $[Ru(II)]^{5+}$ and [Co(III)] cannot be seen through nanosecond transient absorption spectroscopy techniques or in new outer-sphere charge transfer bands in the visible absorption spectrum of the dye. Therefore it wasn't possible to have a proof of the studied quenching process taking place through electron transfer rather than energy transfer mechanism.

The results obtained with this study, with regard to the electrostatic interactions between molecules involved in solution quenching processes, could be significant in terms of solar energy conversion.

In particular the ion-pairing interaction between a sensitizer anchored to the TiO_2 surface and a redox mediator in the electrolyte in a dye sensitized solar cell could possibly facilitate electron-transfer processes at the interface, i.e. the oxidized sensitizer regeneration. As, in previous studies, ruthenium based sensitizers ion-pairing with iodide has been assumed to facilitate the regeneration process, the verified ion-pairing interaction between the anionic **[**$CoTTT(NCS)_3]^-$ and the highly cationic $[Ru(tmam)_2(deeb)]^{6+}$ could act similarly, with the enhanced attractive inteaction, thanks to the high charge of the compounds involved, improving the formation of the encounter complexes, thus improving substantially the interfacial charge-transfer processes. To demostrate these hypotesis quenching studies must be done where the hexacationic sensitizer is anchored to the surface. On the other hand, the occurring of repulsive interactions between molecules like sensitizers and redox mediators in DSSC could lower the extent to which electron transfer processes take place. This needs to be proved, simultaneously taking into account the multiple factors which regulate the kinetics in this type of devices.

Moreover, **[**$CoTTT(NCS)_3$]TBA appears as an interesting complex to be employed as redox mediator in DSSC, and will be further examined.

4.1.5 Conclusion

The highly cationic dye $[Ru(tmam)_2(deeb)](PF_6)_6$ was found to be efficiently quenched by the negative redox mediator $[CoTTT(NCS)_3]$TBA in acetonitrile. Steady-state and time-resolved photoluminescence studies together with UV-vis spectroscopy demostrated the occurrance of ion pairing to a great extent, in addition to the dynamic diffusional quenching mechanism. The presence of ion pairing was confirmed by experiments performed under different ionic strength values. On the other hand a significant quenching was not observed for $[Ru(tmam)_2(deeb)](PF_6)_6$ excited states by the cationic redox mediators $[Co(bpy)_3](PF_6)_2$ and $[Co(dtb)_3](PF_6)_2$, which clearly display a negligible electronic coupling with the positive dye. Finally a comparative experiment was conducted where the quenching by $[CoTTT(NCS)_3]$TBA of the less positively charged model compound $[Ru(bpy)_3](PF_6)_2$ was studied, showing that dynamic quenching was reduced and the static component was absent. All together these results, demonstrate the fundamental role which electrostatic interactions have between molecular species involved in excited states quenching processes in solution. Indeed, in all the studied quenching experiments the huge differences observed can only be rationalized in terms of the occurring electrostatic repulsive or attractive interactions. These outcomes bring attention to an issue that is not much considered when new molecular species to be used in solar energy conversion systems are designed, but should be thoughtfully taken into account.

References

(1) J. R. Lakowicz, Principles of Fluorescence Spectroscopy. *Springer,* **2006**, chapter 8

(2) Y. Park, Liu Z., Routh P.K., Kuo C., Park Y., Tsai H., Martinez J.S., Shreve A.P., Cotlet M., Wang H.; *Phys.Chem.Chem.Phys*. **2015**, 17, 15675

(3) A. Pal, S. Srivastava, P. Saini, S. Raina, P. P. Ingole, R. Gupta, S. Sapra; *J.Phys.Chem.C* **2015**, 119 (39), 22690-22699

(4) S. Rapino, E. Treossi, V. Palermo, M. Marcaccio, F. Paoluccia, F. Zerbetto; *Chem. Commun.*, **2014**, 50, 13117

(5) T. Kono, N. Masaki, M.Nishikawa, R. Tamura, H. Matsuzaki, M. Kimura, S. Mori;; *ACS Appl. Mater. Interfaces* **2016**, 8, 16677−16683

(6) Md. K. Nazeeruddin , S. M. Zakeeruddin , R. Humphry-Baker , M. Jirousek , P. Liska , N. Vlachopoulos , V. Shklover, C.Fischer, M.Grätzel, *Inorg. Chem.*, **1999**, 38 (26), pp 6298–6305

(7) W.Swords, S. Simon, F. Parlane, R.Dean, C.W.Kellett, K.Hu, G.J.Meyer, C.P. Berlinguette, *Angew.Chem*. **2016**, 128,6060 –6064

(8) Clark C.D., Hoffman M.Z.; *J.Phys.Chem*. **1996**, 100, 7526-7532

(9) Swords W.B., Li G., Meyer G.J *Inorg. Chem*, **2015**, 54, 4512-4519.

(10) C.C. Clark, A. Marton, R. Srinivasan, A.A. Narducci Sarjeant, G. J. Meyer; *Inorg. Chem*. **2006**, 45, 4728−4734

(11) A. Marton, C. C. Clark, R. Srinivasan, R. E. Freundlich, A.A. Narducci Sarjeant, G.J. Meyer; *Inorg. Chem*., **2006,** ,45 , 362−369

(12) C. C. Clark, A. Marton, G.J. Meyer; *Inorg. Chem*. **2005,** 44 , 3383−3385

(13) Boschloo, G.; Hagfeldt, A., *Acc. Chem. Res*. **2009**, 42, 1819

(14) Clifford, J. N., Palomares, E., Nazeeruddin, M. K., Grätzel, M., & Durrant, J. R. *J. Phys. Chem .C* **2007**, *111*(17), 6561-6567.

(15) R. Ziessel, J. Hawecker, J.M. Lehn, *Helvetica Chimica Acta* **1986,** Vol. 69, 1065-1084

(16) F. R. Keene, C. Creutz , and N. Sutin, *Coordi.Chem. Reviews*, **1985** 64, 247-260

(17) C. Creutz , N. Sutin , *Coord. Chem.Reviews*, **1985,** 64, 321-341

(18) S. Yanagida, Y.Yu, K. Manseki, *Accounts of Chemical Research* **2009**, 42 (11) 1827-1838

(19) S.M. Feldt, E. A. Gibson, E. Gabrielsson, L.Sun,G. Boschloo, A.Hagfeldt, , *J. Am. Chem. Soc.* **2010**, 132, 16714–16724

(20) S. Mathew, A.Yella, P. Gao, R. Humphry-Baker, B. F. E. Curchod, N. Ashari-Astani, I. Tavernelli, U.Rothlisberger, Md. K. Nazeeruddin, M. Gratzel *Nature Chemistry* **2014**, 6, 242-247

(21) S. A. Sapp, C. M. Elliott, C.Contado, S.Caramori, C. A. Bignozzi, *J. Am. Chem. Soc.* **2002**, 124, 11215-11222

(22) Carli S., Busatto E., Caramori S., Boaretto R., Argazzi R., Timpson C.J., C.A. Bignozzi; *J. Phys. Chem. C* **2013**, 117, 5142−5153

(23) Seddon E.A., Seddon K.R., "The Chemistry of Ruthenium" Elsevier, **1984**

(24) Argazzi, R.; Bignozzi, C. A.; Heimer, T. A.; Castellano, F. N.; Meyer, G. J. *Inorg. Chem.* **1994**, 33, 5741−5749

(25) C. R. Bock, J. A. Connor, A. R. Gutierrez, T.J. Meyer, D. G. Whitten, B. P. Sullivan, J. K. Nagle *J. Am. Chem. Soc.* **1979**, 101, pp. 4815-4824

(26) Juris A., Balzani V., Barigelletti F., Campagna S., Belser P., Von Zelewsky A., *Coord. Chem. Rev*. **1988**, 84, 85-27

(27) Enachescu C., Krivokapic I., Zerara M., Real J.A., Amstutz N., Hauser A., *Inorg. Chimica Acta* **2007,** 360, 3945–3950

(28) J.S. Judge, W.A. Baker, *Inorg. Chim. Acta* **1967**, 1, 68

(29) S. Kremer, W. Henke, D. Reinen , *Inorg. Chem.* **1982**, 21, 3013

(30) Balzani V., Scandola F., *Energy Resources Through Photochemistry and Catalysis*; **1983**, pp 1-48

(31) Klahr B.M., Hamann T.W., *J. Phys. Chem. C* **2009**, 113, 14040–14045

(32) S. Aghazada, P.Gao, A.Yella, G. Marotta, T.Moehl, J.Teuscher, J.-E. Moser, F. De Angelis, M. Grätzel, M.K. Nazeeruddin; *Inorg. Chem.* **2016**, 55, 6653−6659

(33) K.Omata, S. Kuwahara, K. Katayama, S. Qing, T. Toyoda, K..M. Leec, C.-G. Wu; *Phys.Chem.Chem.Phys.,* **2015**, 17, 10170

(34) Y. Wang, Z. Sun, H. Wang, M.Liang, S. Xuel; *J. Phys. Chem. C* **2016**, 120, 13891−13900

4.2 Effect of molecular charges on the electron transfer processes at the TiO_2/electrolyte interface

4.2.1 Introduction

As introduced in section 1.8, polypiridine cobalt complexes have emerged as one of the most interesting and promising classes of redox mediators alternative to the iodide/triiodide couple [1,2], because of the fast dye regeneration, good exchange currents at the counter electrodes and efficient mass transport provided by the unsubstituted kinetically fast redox couple $[Co(bpy)_3]^{2+/3+}$. One of the main drawbacks of fast Co(II)/(III) couples is their ability to recapture photoinjected electrons, yielding high recombination (dark) current, which limits the cell performances obtainable by employing the ample variety of cheaply available Ru(II) sensitizers, even in the presence of passivating layers, making it necessary to introduce bulky organic dyes based on push-pull structures. For example, the D35 [3], Y123 [4], and MK2 [5] sensitizers are characterized by enhanced steric hindrance and assemble on the titania surface in such a way to screen completely the surface from Co(III), making it possible to reach record efficiencies in conjuction with cobalt mediators and optimized cell configurations, but are usually expensive and synthetically laborious.

Thus, it would be interesting to define alternative strategies in order to circumvent the Co(III) recombination drawback. One is to exploit extremely efficient methods to passivate the photoelectrode surface. Another is to work on the cobalt complex coordination sphere, in order to protect the metal centre from electron recombination events with its oxidized form by means of bulky substituents. For example, in $[Co(dtb)_3]^{2+}$ [1,6,7] recombination current is efficiently suppressed thanks to the steric hindrance confered by tert-butyl substituents on the bypiridine ligand, in respect to $Co(bpy)_3$. Nonetheless bulky structures like $[Co(dtb)_3]^{2+}$ suffer of slow diffusion issues, penalizing the cell performances [8-11].

It would be interesting to follow another strategy, aiming at efficient DSSC based on cobalt complexes, that is to make more or less favoured the electron transfer processes determining the solar cells performances (i.e. electron injection, dye regeneration and charge recombination), by exploiting the electrostatic interactions which occur between the species involved in these electron transfer processes, in particular the chosen sensitizer and redox mediator [12].

First of all, the relevance that electrostatic interactions have, in the panorama of many simultaneous effects acting in DSSC operation, has to be carefully evaluated. In section 4.1 a quenching study in solution was conducted involving $[CoTTT(NCS)_3]^-$, a new potential cobalt (II) based redox mediator, characterized by a global negative charge, and the hexacationic $[Ru^{II}(tmam)_2(deeb)]^{6+}$ sensitizer [13]. The outset of strong ion pairing between the two oppositely charged species was observed, which enhanced the excited ruthenium quenching, either by electron or energy transfer

processes, if compared with the cationic $[Co(bpy)_3]^{2+}$ and $[Co(dtb)_3]^{2+}$ complexes, in which cases no significant quenching was observed.

This result demonstrated the strong influence electrostatic interactions could have on electron transfer processes between molecular species employed in DSSC, however investigations involving systems where the sensitizing species is anchored to the TiO_2 surface, while the redox mediator is in solution, are necessary to confirm these effects in conditions that are closer to those of real devices.

Thus, in this chapter the hexacationic sensitizer $[Ru^{II}(tmam)_2(dcb)]^{6+}$ (**TMAM**, where dcb= 4,4'-dicarboxy-2,2'-bipyridine) was grafted on the TiO_2 surface, and a study involving both photophysical and photoelectrochemical methods was conducted, in order to analyze the electron transfer dynamics induced by light in the presence of differently charged cobalt redox mediators, $[CoTTT(NCS)_3]^-$ (**Co-**), $[Co(bpy)_3]^{2+}$ (**bpy**) and $[Co(dtb)_3]^{2+}$ (**DTB**).

Moreover, a photoelectrochemical and photophysical study involving the same cobalt mediator species was also conducted employing a common sterically hindered ruthenium based sensitizer (Z907 [14]), in order to analyze the electron transfer dynamics with a neutral/negative species, and to gain deeper insights especially about the $[CoTTT(NCS)_3]^-$ complex properties.

4.2.2 Experimental

Materials

All chemicals were Sigma Aldrich products and were used as received. TiO_2 colloidal paste (18NR-T) was purchased from Dyesol, FTO glass plates (TEC 8, 2.3 mm thick substrates) by Pilkington. PEDOT counter electrodes were prepared by cyclic voltammetry (2 subsequent scans in the potential range 0-1.7 V at a scan rate of 50 mV s^{-1}, see chapter 5.1 for more details), in a 10^{-2}M EDOT/0.1M $LiClO_4$ acetonitrile solution. The electrodes were conditioned at 100 °C for 20 min in air immediately before use. $[Ru(dcb)_2(dnb)_2]$ (Z907) dye (*dcb* = 4,4′-dicarboxy-2,2′-bipyridine, *dnb* = 4,4′-di-nonyl-2,2′-bipyridyl) was purchased by Solaronix, while $[Ru(tmam)_2(dcb)](PF_6)_6$ (*tmam* = 4,4′-bis(trimethylamino)methyl-2,2′-bipyridine) was synthetized by W. Swords at North Carolina University (UNC) following a reported procedure [13].

$Co(L)_3(CF_3SO_3)_2$ and $Co(L)_3(PF_6)_3$ (L= bpy, 2,2'-bipyridine or L= dtb, 4,4'-di-tert-butyl-2,2'-bipyridine) complexes were prepared according to literature procedures [15].

$CoTTT(NCS)_3TBA$ was prepared as described in section 4.1.2, while its oxidized form was obtained by addition of a slight excess of $NOBF_4$ in acetonitrile.

Preparation of solar cells

Transparent TiO_2 (18NR-T paste) electrodes were prepared as described in section 2.2.1. These were immersed in an ethanolic dye solution for 24 hours. PEDOT counter electrodes were prepared by electrodeposition through cyclic voltammetry technique, scanning two times from 0 to 1.7 V vs SCE at 50 mV/s, in a 10^{-2} M EDOT/0.1 M $LiClO_4$ acetonitrile solution.

Solar cells were assembled using 25 μm thick Surlyn and closed with metallic clamps in open configuration. In the photoelectrochemical measurements involving the TMAM dye an active area of 0.2 cm^2 was used, and a blocking underlayer prepared as described in section 2.2.1 was applied.

In the DSSC and dummy cells measurements involving the Z907 dye, an active area of 0.25 cm^2 was used; no blocking underlayer was applied to the photoelectrodes surface, in order to study the intrinsic recombination characteristics of the different cobalt redox mediators.

The concentrations and solvents used in the cobalt electrolytes preparation reflected the compounds solubility properties, in particular those of $CoTTT(NCS)_3$. The formulations employed were the following:

$CoTTT(NCS)_3^{-1/0}$: 0.08M Co(II)/0.008 Co(III) $LiCF_3SO_3$ 0.1M, ACN/DMF 3:1 **(Co-)**

$Co(bpy)_3^{2+/3+}$: 0.08M Co(II)/0.008 Co(III) $LiCF_3SO_3$ 0.1M, ACN/DMF 3:1 **(bpy)**

$Co(dtb)_3^{2+/3+}$: 0.08M Co(II)/0.008 Co(III) $LiCF_3SO_3$ 0.1M, ACN/DMF 3:1 **(DTB)**

I^-/I_3^-: PMMI 0.6M, LiI 0.1M, I_2 0.02M, TBP 0.05M, ACN **(I_2)**

Symmetrical dummy cells were assembled, for a better understanding of the cathodic and anodic kinetics, based on two facing PEDOT counter electrodes or two Z907 sensitized photoelectrodes, respectively, and on the just listed cobalt based electrolytes. They were then closed with metallic clamps in open configuration.

Photoelectrochemical characterization

Current−voltage LSV measurements were performed at a scan rate of 10 $mV \cdot s^{-1}$ under light (AM 1.5 illumination) and dark conditions, to evaluate DSSC performances. CV or LSV measurements were performed to analyze dummy cells, at a 10 $mV \cdot s^{-1}$ scan rate as well, in the dark.

Electrochemical Impedance Spectroscopy (EIS) measurements in PEDOT dummy cells were performed at 0 V (short circuit condition), by applying a sinusoidal perturbation of the amplitude of 10 mV in the 10^5-10^{-2} Hz frequency range. The electric equivalent employed to fit the experimental EIS spectra is represented in figure 4.11, where the circuit elements modeling the counter electrode (CE)/electrolyte interfaces are reported (see section 2.2.4).

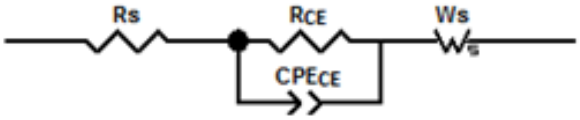

Figure 4.11 Electrical circuit model used to fit experimental EIS data at 0 V in dummy cells

IPCE measurements setup was described in section 2.2.4.

Diffusion coefficients were calculated for 10^{-2} M solutions of the Co(II) electroactive species, in 0.1 M LiOTf 1:3 DMF/ACN, by cyclic voltammetry measurements performed at 10 different scan rate values between 5 and 500 mV/s and then applying the Randles-Sevcick equation (see section 2.1.2).

Paramagnetic susceptibility measurements

The NMR Evans method [16, 17] was employed to have information about the cobalt spin state in the three studied complexes. For each of them, three ^{1}H-NMR spectra (400Hz) were collected: in the first, the tube, containing a capillary with t-butanol inside, was filled with 0.7 ml of CD_3CN. In the second, 30 μl of t-butanol were added; in the third 5 mg of the Co(II) compound were added. After collecting the spectra, the following equations were applied, based on the dependence of the t-butanol peak shift on the Co(II) species effective magnetic moment μ. The resulting values were compared to literature tables [18, 19], where values of 4.30-5.20 are reported for high spin Co(II) complexes; 1.80 for low spin.

$$\chi_M = \frac{3 \cdot MW \cdot \Delta\nu}{4\pi\nu c + \chi_0} \quad \text{(Eq. 4.16)}$$

$$\mu = 2.828\,(\chi_M T)^{1/2} \quad \text{(Eq. 4.17)}$$

(where χ_M is molar susceptibility in cm^3mol^{-1}, ν is spectrometer freq, e.g. 399.732×10^6 Hz, MW is the species molecular weight, Δν is obs freq diff in Hz, c is concentration in g/mL, χ_0 is mass susceptibility of solvent in cm^3g^{-1})

Spectroscopic characterization

The transient absorption spectroscopy (TAS) measurements presented in this section were performed in Ferrara for what concerns the initial part of the surface study with TMAM, and at North Carolina University (UNC) for the part regarding the Z907 regeneration study. The two slightly different experimental setups were described in section 2.3.2. In general, TAS measurements were conducted in solution or on sensitized slides, based on TiO_2 films sintered on a microscope slide. In this latter case, TAS measurements were performed by drawing the electrolyte by capillarity inside the chamber (ca. 6−8 μm), constituted by a glass slide pressed against the TiO_2 photoanode, in order to avoid interferences originated by excitation of I_3^- or by cobalt absorption, thanks to a negligible optical path. Decays were collected averaging between 20 and 30 laser shots, to reach a good S/N ratio.

For what concerns the surface study with TMAM, measurements were conducted first with a laser power of 1.5 mJ/cm^2/pulse, using a white analysis light attenuated by a 420 nm cut-off and a 50%

T neutral filter. Subsequently, some measurements were conducted at 2.25 mJ/cm^2/pulse, using a monochromatic analysis light and removing the 420 cut-off and the neutral 50% filter, in order to improve the signal to noise ratio with the aim of detecting the Co(III) species.
The electrolytes formulation used were:
BLANK: 0.1M $LiCF_3SO_3$, 3:1 ACN/DMF
CoTTT(NCS)$_3$: 0.08M Co(II), 0.1M $LiCF_3SO_3$, 3:1 ACN/DMF **(Co-)**
Co(DTB)$_3$: 0.08M Co(II), 0.1M $LiCF_3SO_3$, 3:1 ACN/DMF **(DTB)**

Regarding the Z907 regeneration study performed at UNC, measurements were conducted at slightly different laser power values (0.4 mJ/pulse/cm^2 for bpy, 1 for DTB, 0.5 for Co-), which were obtained by varying the polarizer and slits opening or the Q-switch value, in order to have an initial signal intensity around 10 mOD. A 475 cutoff and a BP505 band pass (485-550 nm) filters were employed to select the analysis light wavelengths. The experiments were repeated twice in order to confirm the obtained results.
The electrolytes employed were three series of solutions based on 0.1M $LiCF_3SO_3$ in a 3:1 ACN/DMF mixture, containing different concentrations of the bpy, DTB and Co- complexes (0, 10, 28, 46, 64, 82, 100 mM).

Spectroelectrochemistry

A nude TiO_2 slide was used as working electrode in a three electrodes electrochemical cell (1cm cuvette), containing the blank (0.1M $LiCF_3SO_3$ in 1:3 DMF/ACN) solution. The sample was purged in an Argon atmosphere for 30 minutes before the experiment. Then the absorbance changes under increasingly negative applied potential were monitored as it was explained in section 2.3.1.

4.2.3 Results and discussion

Photoelectrochemical characterization with Ru(dcb)(tmam)$_2$

The JV curves obtained for DSSC based on TMAM sensitized photoanodes and PEDOT counter electrodes, in combination with the three studied cobalt electrolytes, are reported in figure 4.12, where the iodide based electrolyte was used as a comparison, since this ruthenium sensitizer has not been studied before. In table 4.3 the photovoltaic parameters relative to the current-voltage measurements are reported. Low power conversion efficiency values are obtained by these devices, even with the reference iodide/triiodide redox couple. The PCE trend follows the order: **Co-** (0.21%) > **DTB** (0.15%) > **bpy** (0.02%), where the higher efficiency for Co- is given by a higher

generated photocurrent (Jsc: **Co-** > **DTB** > **bpy**). This trend is consistent with high attractive electrostatic interaction between the cationic dye and the Co- mediator, resulting into the formation of ion-pairs, which should promote the regeneration process by electron transfer between them. On the other hand, the photovoltage is higher for DTB, due to its higher redox potential in respect to Co-, and to lower recombination current when using this mediator (Voc: **DTB** > **Co-** > **bpy)**. Indeed, the dark currents follow the order: **bpy** > **Co-** > **DTB** , where the bulky structure of DTB if effective in protecting the oxidized cobalt center by recombination processes with the TiO_2 injected electrons, whereas the unsubstituted structure of bpy makes it particularly subjected to such loss processes. Co- is in an intermediate situation, as it can be reasonably expected based on the fact that a fraction of the Co- molecules in the electrolyte are strongly coupled to the dye molecules, while, for the remaining free molecules, the tri-tert-butyl functionalities on the terpyridine ligand partially protect the Co- metal center from the interactions with TiO_2 and uncovered FTO areas.

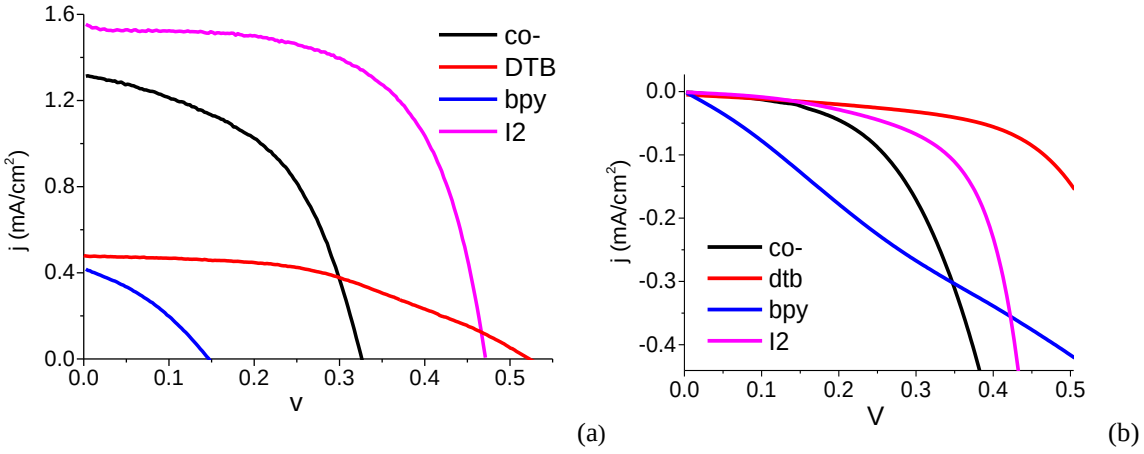

Figure 4.12 JV curves under illumination (a) and under dark (b), for DSSC based on TMAM sensitizer and various electrolytes

	Jsc	***Voc***	***FF***	***η %***
Co-	1.31	0.33	0.49	**0.21**
DTB	0.48	0.52	0.44	**0.11**
bpy	0.42	0.15	0.32	**0.02**
I_2	1.55	0.47	0.62	**0.45**

Table 4.3 Photovoltaic parameters extracted from the JV curves of figure 4.12 a.

The Co- ion-pairing with TMAM on the surface was confirmed by UV-vis spectroscopy (figure 4.13), in fact recording an absorption spectrum of the sensitized photoanode before and after the measurement with Co-, a slight absorbance decrease was observed, together with a 7 nm red-shift of the Ru MLCT maximum, and the appearance of cobalt absorption at 620 nm (figure 4.13 a). Indeed, the resulting difference spectrum features two isosbestic points at 398 and 481 nm (figure

4.13 b). Even after rinsing carefully the photoanode and letting it soak for two hours in neat acetonitrile, the obtained spectrum did not return to its initial aspect, suggesting the occurrence of strong ion-pairing on the surface between the cationic sensitizer and the negative cobalt complex, similarly to what had been previously observed in solution.

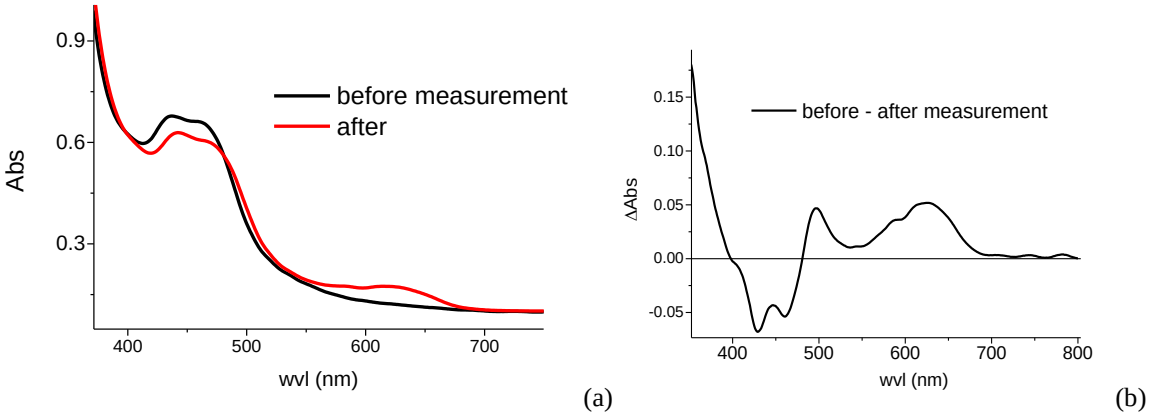

Figure 4.13 (a) Abs spectra of a TMAM sensitized photoelectrode before (red) and after (black) its employment in measurements with the co- electrolyte, (corrected for the absorption of a non sensitized electrode). (b) Difference spectrum (ΔA) relative to figure 2a, showing two isosbestic points (398 and 481 nm) corresponding to the red shift related to ion-pairing on the surface, and the Co- absorption appearance (max at 620 nm)

In figure 4.14 photoaction spectra are reported, which provide IPCE values (see table 4.4) in agreement with the JV curves of figure 4.12, measured on the same devices. Generally, low IPCE is observed, also with the I_2 electrolyte, consistent with low LHE and injection yield characterizing the TMAM dye. Interestingly, a 60% higher maximum IPCE is obtained in the presence of Co- (25.5%), comparably to iodide, with respect to those observed with the positive cobalt couples (16.3% for DTB and 15.4% for bpy). This is consistent with the idea that the surface ion pair formation between TMAM and Co- leads to improved dye regeneration, since the recombination component observed in JV curves collected under dark, involving the photoinjected electrons and the oxidized cobalt species, which also affects the IPCE, would be in favour of DTB. Due to the low LHE which characterizes the TMAM dye, the APCE values were calculated, and they are also reported in table 4.4. The low APCE values (ca. 40 % with the best electron mediators I_2 and Co-) are also a proof of low injection yield for TMAM.

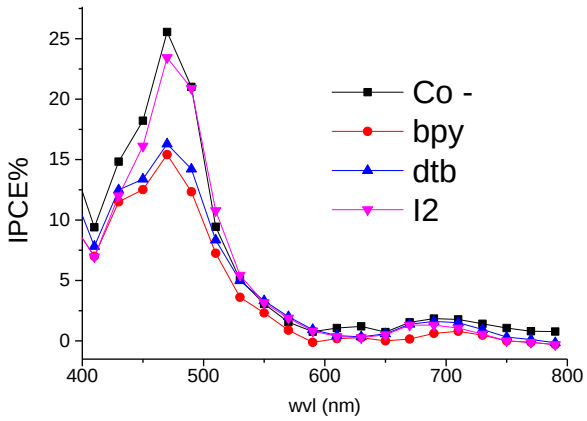

Figure 4.14 IPCE spectra relative to the devices whose JV curves are reported in figure 4.12.

(λ = 470nm, Abs = 0.42)	IPCE%	APCE% = IPCE/LHE (LHE = 1-10 $^{-Abs(\lambda)}$)
Co-	25.5	41.1
DTB	16.3	26.3
Bpy	15.4	24.8
I2	23.4	37.7

Table 4.4 IPCE and calculated APCE values at 470 nm relative to figure 4.14 data.

Despite the low efficiencies obtained in DSSC with the TMAM sensitizer, it is impressive that the results obtained by this photoelectrochemical study are consistent with the observations drawn from the spectroscopic study in solution, presented in section 4.1. This had shown effective quenching of the ruthenium photoexcited state by $[CoTTT(NCS)_3]^-$, through both static and dynamic mechanisms, favoured by strong ion pairing between the two oppositely charged species, which had been demonstrated. In the present case, the ion pairing on the surface was evidenced by UV-vis spectroscopy, and can reasonably explain the higher IPCE and photovoltaic parameters obtained by devices employing the negative cobalt complex. On the other hand, negligible quenching had been observed in the solution study by the bicationic $[Co(bpy)_3]^{2+}$ and $[Co(dtb)_3]^{2+}$ complexes, imputing this to the repulsive electrostatic interactions with the hexacationic ruthenium complex, which would reduce the electronic coupling between them. An analogous behaviour was observed in the surface study, where the 60% lower IPCE, measured for DSSC based on the bicationic species as redox mediators, can be definitely ascribed to a lower regeneration efficiency deriving from the reduced electron coupling.

Spectroscopic Ru(dcb)(tmam)$_2$ characterization

TAS experiments were conducted on TMAM sensitized slides in a blank acetonitrile based solution and in the presence of the two best performing cobalt electrolytes of the photoelectrochemical DSSC study, $[CoTTT(NCS)_3]^-$ (Co^-) and $[Co(dtb)_3]^{2+}$ (DTB).

In figure 4.15 the TA spectra of TMAM in the blank solution and in the DTB and Co- electrolytes are reported.

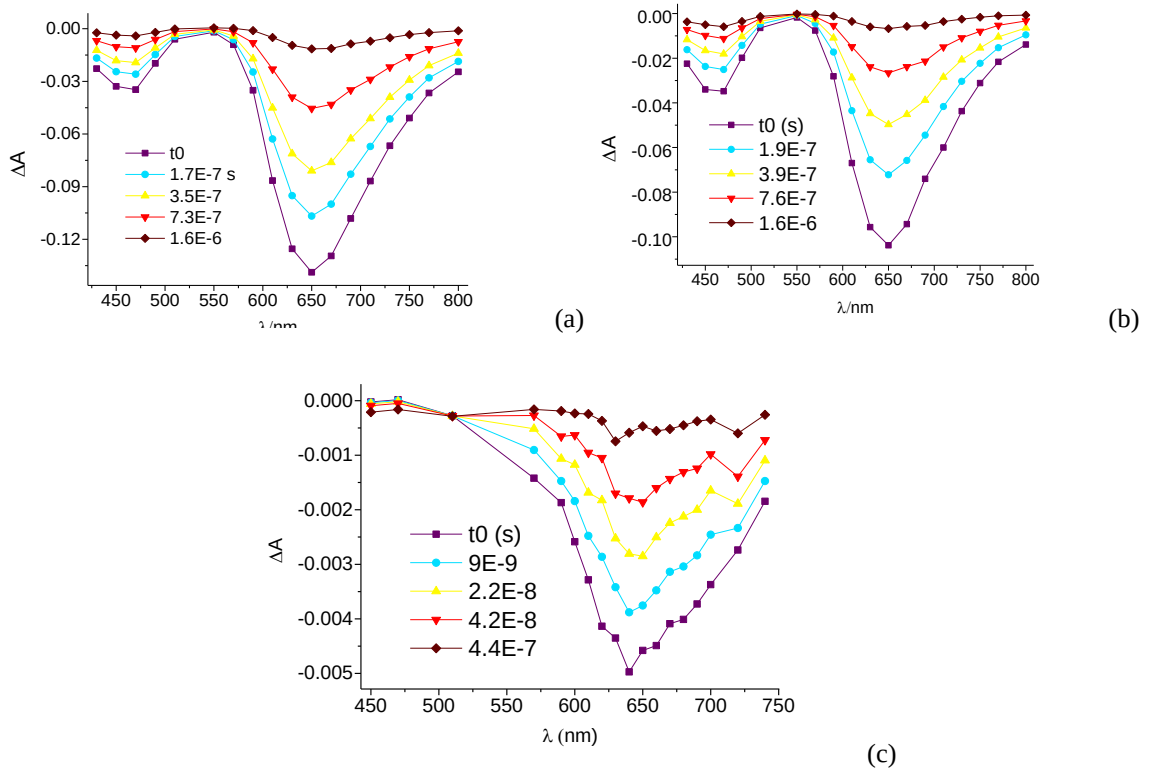

Figure 4.15 Full TA spectra of Ru6+ in the blank (a), in the DTB (b), and in the co- electrolyte (c) (532 nm excitation, 1.5mJ/cm^2/p, 420 nm cut-off and 50% neutral filter, white analysis light). Please note the much shorter delays of the TA spectrum in figure c.

The TMAM full transient absorption spectrum (figure 4.15a) in the presence of the blank electrolyte shows a first bleaching with maximum at 470 nm. This can be assigned to the formation of both the charge separated state (Ru^{3+}) and the $*Ru^{2+}$ MLCT excited state, which cannot be easily distinguished in this spectral region. From the IPCE data, suggesting a low injection yield (around 40%), a prevalence of the excited state is expected. This explains the second bleaching, peaking at 650 nm [13], identified with the $*Ru^{2+}$ photoluminescence, which is indeed remarkably intense due to the low injection efficiency of this sensitizer.

Running the TA experiment in the presence of the DTB electrolyte (figure 4.15 b), the $*Ru^{2+}$ photoluminescence appears slightly reduced, probably due to some marginal energy transfer

involving cobalt. Indeed the relative intensity of the Ru bleaching at 470 nm, with respect to the 650 nm emission, is slightly increased.

On the other hand, in the presence of the negative cobalt mediator (figure 4.15 c), it can be observed that the $*Ru^{2+}$ photoluminescence at 650 nm is substantially quenched, in agreement with the solution study results. Furthermore, the first bleaching with maximum at 470 nm disappears, which is ascribable to both the absence of Ru(III) and the complete quenching of the $*Ru^{2+}$ excited state, within the pulse duration.

This suggests that, after photoinduced electron injection, Ru(III) is immediately brought back to its reduced Ru(II) form by the ion-paired Co(II), in the sub-nanosecond timescale, coherently with the IPCE spectra which indicate an increased quantum yield of charge injection in the presence of the Co- mediator, with respect to the others under investigation.

The just described injection and regeneration processes are assumed to take place in the laser pulse time, so in the sub-nanosecond timescale, consistently with the results previously obtained in solution, where the quenching product $Ru(II)^{+}$ was not observed even running the experiment under high concentrations (see section 4.1). Alternatively, another pathway could be possible, in the case that the reductive quenching of the excited state $*Ru(II)^{2+}$ by ion-paired Co(II) was faster than the electron injection into TiO_2. This latter could then occur afterwards, from the reduced species $Ru(II)^{+}$, which happens to be even more reductive that the excited state itself. In either case, being these processes too fast to be seen in the ns timescale, the only response from the ns TA apparatus would be the observed absence of the spectral fingerprints of the Ru(III) species.

Because the bleaching centered at 470 nm sums both the Ru^{3+} and excited state absorption contributions, the ultimate proof of the reductive quenching by ion-paired Co(II) would be the detection of Co(III). Unfortunately the Co(II) absorption has a maximum at 620 nm, which is located in the same wavelength range of the *Ru(II) photoluminescence. An attempt was made to separate these two contributions, by adopting experimental strategies to increase the cobalt response. As described in the experimental section, the laser power was increased from 1.5 to 2.25 mJ/cm^2/pulse, monochromatic analysis light was used at each wavelength instead of the white light attenuated by a 420 nm cut-off and a 50% T neutral filter. These expedients were followed in order to improve the signal to noise ratio, with the aim of detecting the weak Co(III) signal.

Thus, on the same sample both the transient absorption and emission spectra were measured, in the range of wavelengths where the Co- absorption takes place, at a series of time delays after the laser pulse (figure 4.16). A further improvement of the signal/noise ratio was accomplished by conducting the measurements on a sensitized slide which had been previously immersed in the Co-electrolyte, in the presence of the blank solution. In fact, the ion-paired cobalt had been proved, by UV-vis spectroscopy, to be stuck on the surface even after hours soaking in the neat solvent. Hence, conducting the experiment in these conditions makes sure that only the paired cobalt species have a role in the electron transfer processes induced by light. This allows to exclude the

interferences carried by the light absorbing cobalt solution, which could also fasten the Co(III) signal disappearance due to electron transfer processes by the reduced cobalt species in solution.
The resulting spectra are reported in figure 4.17, where the improvements reached with respect to figure 4.16 are visible. The TA and emission spectra (figure 4.17 a and b, respectively) at the various time delays were then normalized and subtracted, giving a profile that is only ascribable to the contribution of Co(III) absorption, which appears as a bleaching signal mirroring the Co(II) absorption spectrum, with a minimum at 620 nm (figure 4.18). This corroborates the evidence for the instrument response limited (ns-sub ns) electron transfer within the ion paired adduct, generating Co(III) and improving dye regeneration. The transient bleaching in the 590-660 nm region agrees well with the difference spectrum recorded on the TMAM sensitized film before and after Co- adsorption.

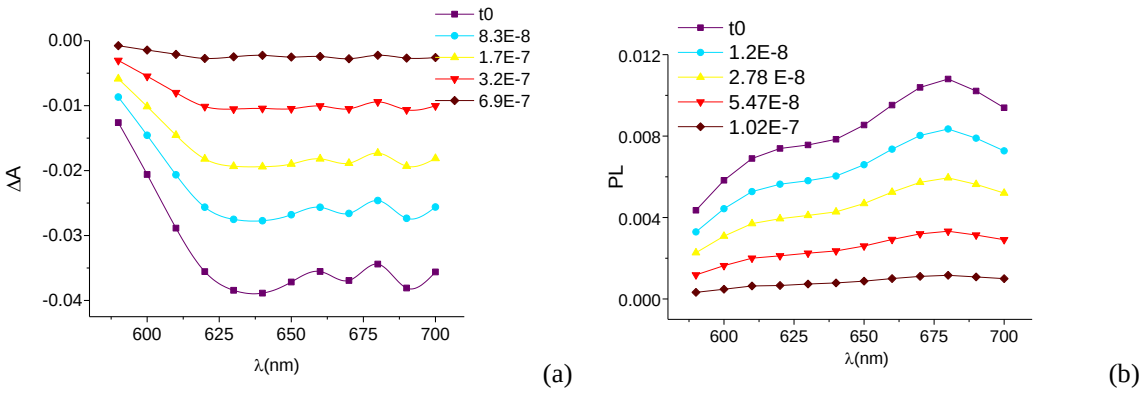

Figure 4.16 TA (a) and emission (b) spectra in the range 590-700 nm, where the bleaching due to Co(III) formation is expected, at various time delays (532 nm excitation, laser power 2.25 mJ/cm^2/p; under monocromatic probe sampling), for a TMAM sensitized slide in the presence of the Co- liquid electrolyte.

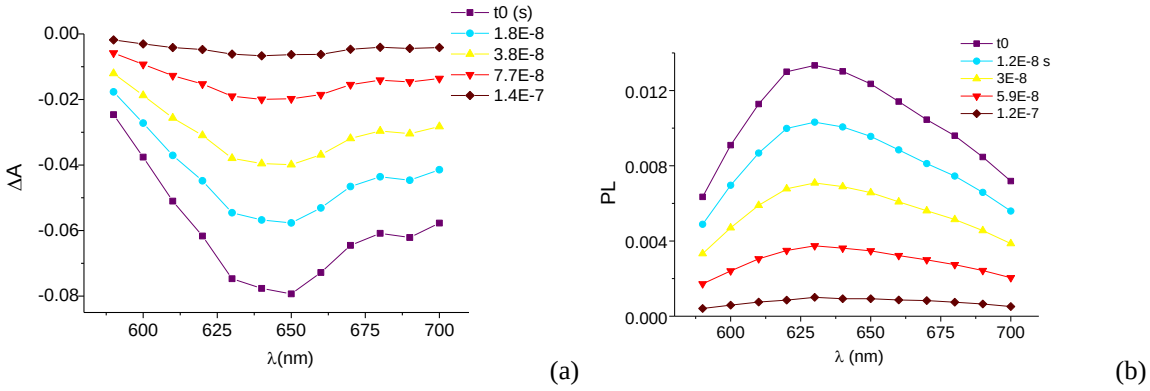

Figure 4.17 TA (a) and emission (b) spectra in the range 590-700 nm, where the bleaching due to Co(III) formation is expected, at various time delays (532 nm excitation, laser power 2.25 mJ/cm^2/p; under monocromatic probe sampling), for a TMAM sensitized slide in the presence of the ion-paired Co-, in the blank liquid electrolyte.

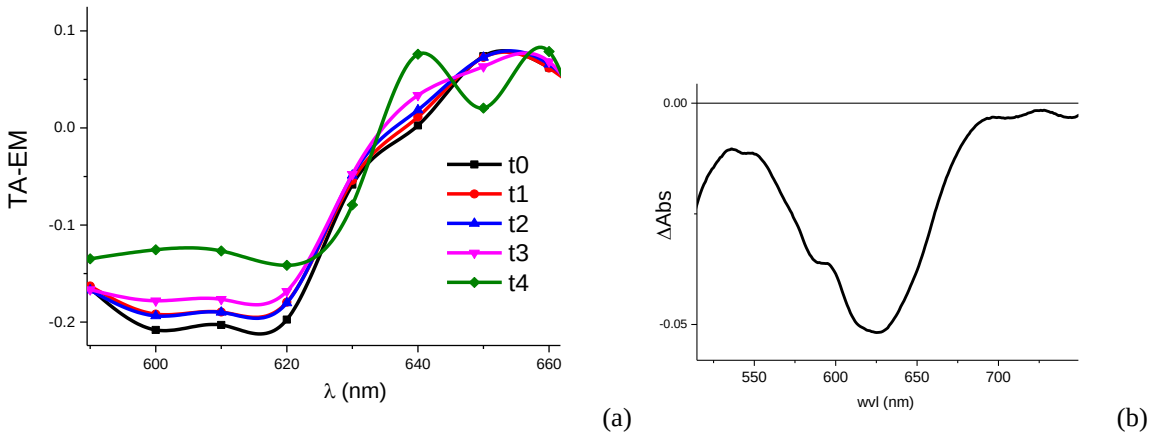

Figure 4.18 Difference spectra, at various delays, between the normalized TA and emission spectra (a); Co-absorption around 620 nm (zoom of picture 4.13b), pictured in negative (b)

Beside the identification of a transient spectral profile assigned to Co(III), a difference in the normalized transient decay and emission lifetimes can be appreciated due to the convolution of the residual Ru MLCT emission with the Co(III) bleaching of the charge separated state which is longer lived. Such difference reaches a maximum (19%) in correspondence with the Co- maximum absorption bleaching (see figure 4.19 and table 4.5) where it should be expected on the basis of its the higher relative weight to the overall transient signal. As we move further to the red, where the spectral contribution of the Co(III) decreases, the lifetimes of the transient emission and absorption become increasingly aligned consistent with the increasingly prevailing contribution of the stimulated emission to the transient signal measured in absorption mode.

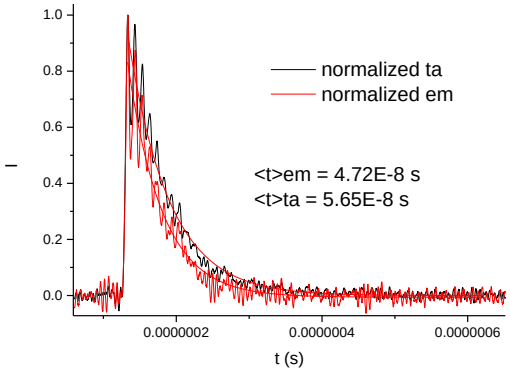

Figure 4.19 Emission and transient decays of TMAM ion-paired to cobalt, at 630 nm

wvl (nm)	$\langle\tau\rangle_{em}$ (ns)	$\langle\tau\rangle_{TA}$ (ns)
610	46.7	55.1
630	47.2	56.5
660	48.1	55.4
700	42.9	47.9

Table 4.5 Average emission and transient lifetimes at various wavelengths

Photoelectrochemical characterization with Z907 dye

In order to have a term of comparison, with respect to the measurements performed with the new TMAM sensitizer, a regeneration study and a characterization in DSSC were conducted using a common ruthenium dye, $[Ru(dcb)_2(dnb)_2]$ (Z907, figure 4.20), characterized by long alkyl chains providing a sterical hindrance to suppress charge recombination processes occurring on the TiO_2 surface [14], adding an analysis in symmetrical dummy cells to gain details about the investigated redox mediators kinetic properties.

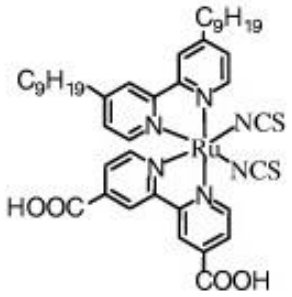

Figure 4.20 Z907 dye ($E_0(A^+/A)$ = 0.93 V vs NHE)

Z907 is globally neutral but bears partial negative charges localized on the thiocyanate groups [20], and could have an increased negative charge in the case that the dissociated carboxylic groups were not both bonded to the TiO_2 surface.

Focusing on the electrostatic interactions occurring in the presence of this sensitizer and the differently charged cobalt species under investigation, it can be observed that a more favourable interaction is to be expected with the cationic DTB and bpy, whereas the presence of NCS^- groups both on the dye and on the Co- complex would reduce the interactions with this latter. Anyway it can be pointed out that other factors, rather than the electrostatic one, could have a bigger influence in this case. Indeed, comparing the three considered cobalt complexes is not easy and immediate, because of the multiple circumstances acting simultaneously in determining the final cell performances.

The *driving force for dye regeneration* for the three cobalt complexes combined with Z907 was initially estimated: based on their redox potential values (see table 4.1), it follows the order Co- > DTB > bpy, (0.43 eV for Co-, 0.33 for DTB, 0.14 for bpy in the case of Z907; while it is higher in the case of the highly cationic TMAM sensitizer, 1.48 eV for Co-, 1.31 for DTB, 1.23 for bpy). Clearly, a lower redox potential for the $Co^{II/III}$ species will also mean lower photovoltage extractable from the solar device.

The *spin configuration* for the Co(II) compounds was calculated by paramagnetic susceptibility (χ_M) measurements, yielding a high spin configuration for bpy (μ = 4.72), confirming the data found in literature [17, 18], and a mixed ~ 1:1 high/low spin configuration for Co- (μ = 3.5) and DTB

(μ = 3.14), which should then be favoured in electron transfer processes involving oxidation and reduction of the cobalt center.

The *diffusion coefficient* was measured for the three complexes in solution by cyclic voltammetry measurements at different scan rates, employing the Randles-Sevcik relation, as explained in section 4.2.2. The confirmed trend was: bpy > DTB > Co- (see table 4.6). $Co(bpy)_3$, thanks to its smaller size, turned out to be the fastest diffusing species, while $Co(DTB)_3$ is slightly penalized by its bulky structure. Co- appeared to be extremely slow diffusing, and to exclude that this was due to its large TBA counter ion, the diffusion coefficient of the Co- ammonium salt was calculated as well, revealing a slightly faster but still slow coefficient.

D (cm^2/s)	**by CV (10^{-2}M solutions)**
$Co(bpy)_3(OTf)_2$	1,47 E^{-6}
$Co(DTB)_3(OTf)_2$	1,01 E^{-6}
$CoTTT(NCS)_3TBA$	4,28 E^{-7}
$CoTTT(NCS)_3NH_4$	4,99 E^{-7}

Table 4.6 Diffusion coefficient determined by CV for the studied cobalt complexes.

With these premises, a photoelectrochemical study was first conducted in *symmetrical dummy cells*, in order to separately analyze the anodic and cathodic components of the final solar device.

Measurements run on symmetrical cells built using two facing Z907 sensitized TiO_2 electrodes gave information about the recombination current occurring between the injected TiO_2 electrons and the redox mediator, principally. The current-voltage measurements, reported in figure 4.21a, show that for $Co(DTB)_3$ and $CoTTT(NCS)_3$ charge recombination at the photoanodic surface is effectively suppressed if compared to $Co(bpy)_3$. This could be ascribed to the steric effect brought by the presence of bulky tert-butyl groups in $Co(DTB)_3$, and also in Co-, in which also the partial negative charges, localized on the NCS^- groups, could play a role, opposing an electrostatic barrier to recombination [12]. In particular, figure 4.21 b reveals the effect of the Z907 dye presence on recombination currents, in fact a comparison between dummy cells based on nude or sensitized TiO_2 electrodes and the Co- and bpy mediators makes clear that the bulky sensitizer decreases the interfacial electron recapture occurrence.

CV measurements run on symmetrical cells based on two facing PEDOT electrodes were useful to get information about the cathodic kinetics regarding the three cobalt mediators. As it is clear from figure 4.22, the simple $Co(bpy)_3$ turned out to have the fastest cathodic kinetics, based on steeper slope of the linear JV trait, and on a higher plateau limit current reached, which means higher photocurrent extractable by the final device based on this mediator-cathodic material combination. The bpy kinetics is followed by that of DTB, while Co- emerged as the kinetically slowest redox couple. This was further investigated by means of EIS measurements conducted on the same

dummy cells: in figure 4.23, wher both the Nyquist and Bode phase plots are presented, it's clearly visible that $CoTTT(NCS)_3$ displays very high charge transfer and diffusion resistances, if compared to the bpy and DTB complexes. The values extracted by the data fitting are reported in table 4.7.
In the case of DTB, the higher resistance values can be explained by the bigger size of the complex, in respect to bpy, provided by its hindered structure, which affects bulk diffusion and reduces electronic coupling. In the case of $CoTTT(NCS)_3$ both the resistances to charge transfer and to mass diffusion are considerably higher respect to the other two complexes, revealing an intrinsically low kinetics which is probably ascribable to high internal reorganization energy relative to the $Co^{II/III}$ self-exchange reaction, due to the presence of three monodentate ligands in $CoTTT(NCS)_3$.

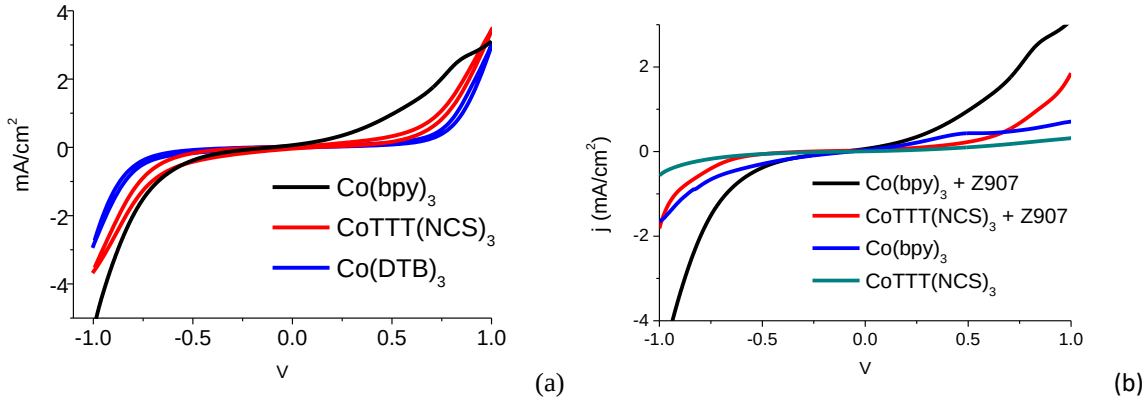

Figure 4.21 CV curves for the anodic dummy cells (a), enlightening the recombination suppression effect introduced by the Z907 dye, in the case of bpy and Co- (b)

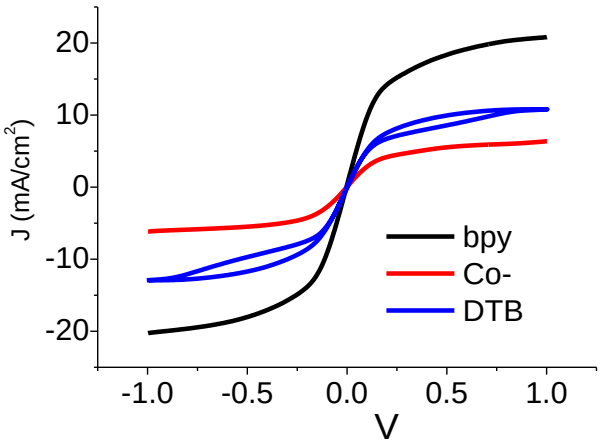

Figure 4.22 CV curves for the cathodic dummy cells

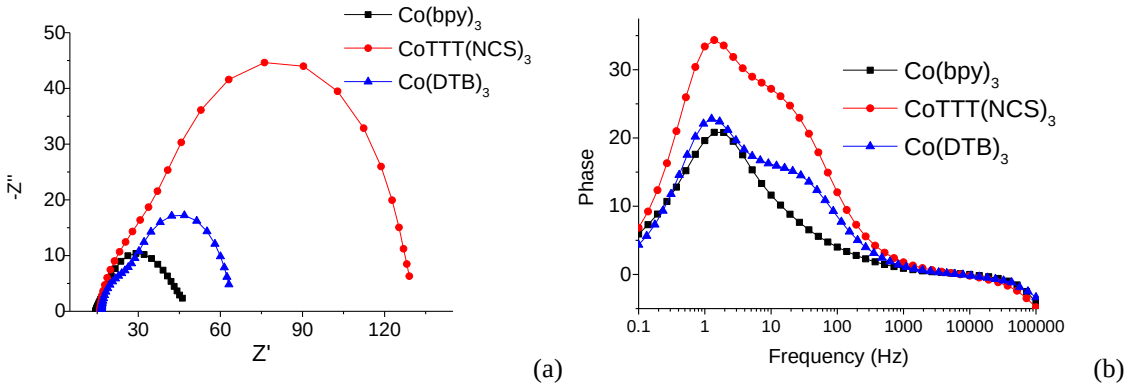

Figure 4.23 EIS spectra, Nyquist (a) and Bode phase (b) plots, for the cathodic dummy cells at 0 V applied potential.

	$CoTTT(NCS)_3$	**$Co(DTB)_3$**	**$Co(bpy)_3$**
R_{CT}	15,8	8,7	4,4
R_{DIFF}	96,63	37,6	24,8

Table 4.7 EIS fitting parameters

The current-voltage curves, measured for DSSC based on Z907 and the investigate cobalt mediators, are reported in figure 4.24 No blocking underlayer was adopted to passivate the photoanode surface, with the aim of analyzing the intrinsic properties of the mediators with respect to the electron transfer processes ruling the DSSC functioning. Observing the photovoltaic values reported in table 4.8, the overall efficiencies follow the order: DTB > Co- > bpy. Bpy is, as expected, penalized by enhanced dark current, due to recombination processes at the TiO_2 and FTO surface. Moreover, the driving force for dye regeneration, the spin properties aren't in favour of this species, which is however characterized by the highest diffusion coefficient and by the smallest charge transfer resistance characteristics. The DTB is favoured by its bulky structure in effectively suppressing recombination, thus producing the best performance, despite its slower diffusion in respect to bpy, having an intermediate driving force, between the three cobalt species, and a spin situation that is favorable, in respect to bpy, and comparable to that of Co-. Finally Co- yields intermediate efficiency between the three redox couples, since it's favoured for what concerns the spin properties, the driving force for dye regeneration and the recombination current, which is slightly superior than that of DTB, but it's highly penalized by very slow diffusion coefficient and very high cathodic charge transfer resistance, probably due to internal reorganization energy issues. The observed performances are in accord with the predictable effects of electrostatic interactions in this study. Indeed, given the partial negative charges positioned on the Z907 NCS^- ligands, the cationic mediators are expected to be more attracted, thus leading to an increase of the electronic

coupling and of the charge transfer kinetics. On the other hand, this leads to enhanced recombination currents in the case of the unsubstituted bpy couple. On the contrary, the anionic Co- species is supposed to be electrostatically repelled by the sensitized TiO_2 surface, reasonably leading to reduced electronic coupling so to reduced recombination currents but also to low charge transfer kinetics. To validate this idea, an accurate regeneration study was conducted.

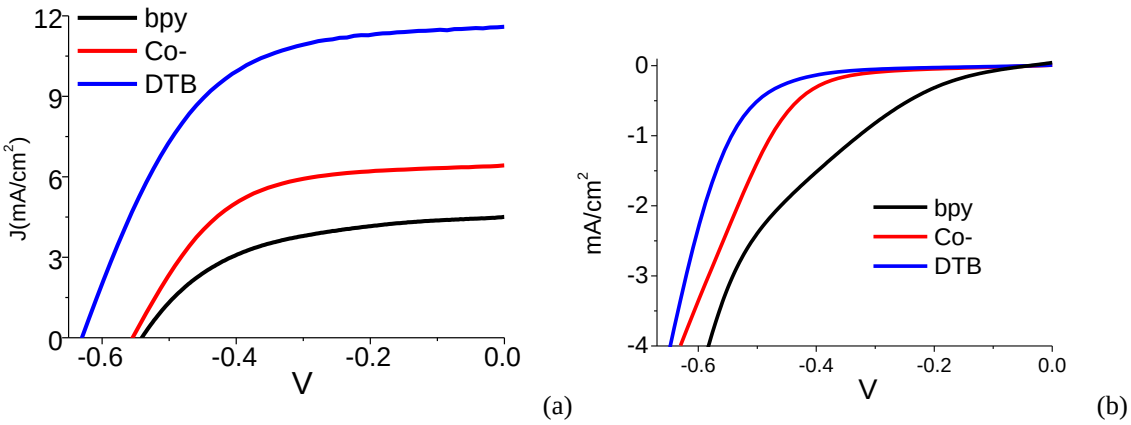

Figure 4.24 JV curves under 1 sun illumination (a) and in the dark (b) for DSSC based on Z907 and the studied cobalt mediators

	$[Co(DTB)_3]^{2+/3+}$	**$[Co(TTT)(NCS)_3]^{-1/0}$**	**$[Co(bpy)_3]^{2+/3+}$**
Voc (V)	-0,63	-0,55	-0,54
Jsc (mA/cm²)	11,59	6,42	4,5
FF	0,55	0,57	0,51
η %	**4,03**	**2,02**	**1,25**

Table 4.8 Photovoltaic parameters extracted from the JV curves of figure 4.24a

Z907 regeneration study

A thorough regeneration study of Z907 was conducted at UNC, with an experimental equipment which was described in section 2.3.2, using a 532 nm laser pulse to generate the interfacial charge separated state $Dye^+/TiO_2(e^-)$ on sensitized TiO_2 slides, in a 0.1 M $LiCF_3SO_3$ 1:3 DMF:ACN electrolyte containing different concentrations of the $[Co(bpy)_3]^{2+}$, $[Co(DTB)_3]^{2+}$ and $[CoTTT(NCS)_3]^{-1}$ cobalt donors.

Absorption changes after laser excitation were recorded at an observation wavelength of 486 nm, in order to take account of the slight Stark effect contribution [21] occurring in the presence of the LiOTf electrolyte, in respect to the neat solvent situation. As it is represented in figure 4.25, the difference spectrum between that of the sensitized slide in neat solvent and that in 0.1M LiOTf 1:3 DMF:ACN, identified two isosbestic points: the second was too close to the laser excitation wavelength so the first, corresponding to 486 nm, was chosen.

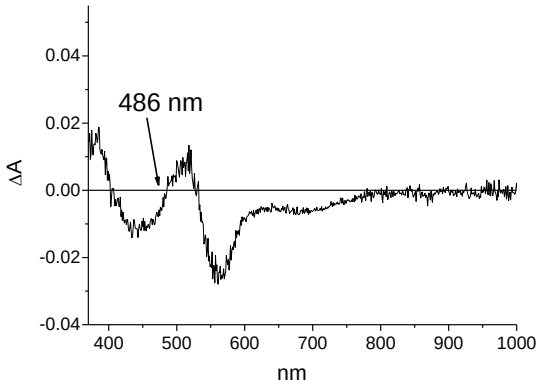

Figure 4.25 Difference spectrum of the Z907 sensitized slide in neat solvent and in solvent + LiOTf 0.1 M, where one of the two isosbestic poins was individuated as observation wavelength

Transient absorption decays after laser excitation were recorded under different cobalt mediators concentrations and fitted by the Kohlrausch−Williams−Watts (KWW) function (equation 4.18) [22, 23]. The pseudo-first order rate constants k'_{reg} ($1/\tau_{avg}$) were calculated by equation 4.19, where τ_{avg} is the average regeneration time, between the different electrons arrival times, β is the stretching parameter ($0< \beta <1$), Γ is the gamma function [24].

$$\Delta Abs = A \exp[-(t/\tau)^{\beta}] \qquad \text{(Eq. 4.18)}$$

$$k'_{reg} = [\tau/\beta \times \Gamma(1/\beta)]^{-1} \qquad \text{(Eq. 4.19)}$$

The k'_{reg} values were linear in the cobalt concentration. Slopes from the linear fittings provided the second-order rate constants for dye regeneration, k_{reg} .

The pseudo-first order recombination rate constants under no voltage application, k'_{rec} , were obtained by fitting the decay curves in the blank electrolyte (Co 0M), for each of the three sets of measurements. The regeneration efficiency, η_{reg}, was then quantified on the basis of the obtained charge recombination first order and regeneration second order rate constants, following the equation:

$$\eta_{reg} = \frac{k_{reg}[Co]}{(k'_{rec} + k_{reg}[Co])} \qquad \text{(Eq. 4.20)}$$

The three series of fitted decays at the various cobalt concentrations, with the relative linear plot providing the k_{reg} value, are reported in figure 4.26, and the derivated constant values are listed in table 4.9. It turned out that, in the short circuit condition, the most efficient cobalt complex in regenerating the oxidized dye is $Co(dtb)_3$, which is characterized by higher driving force if compared to $Co(bpy)_3$. Despite the highest driving force for $CoTTT(NCS)_3$, unfortunately this complex turned out to be the slowest in regenerating by electron transfer the oxidized Z907 dye, which is in agreement with the observations previously made about i

ts expected low electronic coupling caused by unfavourable electrostatic interactions between the redox mediator and the sensitizer.

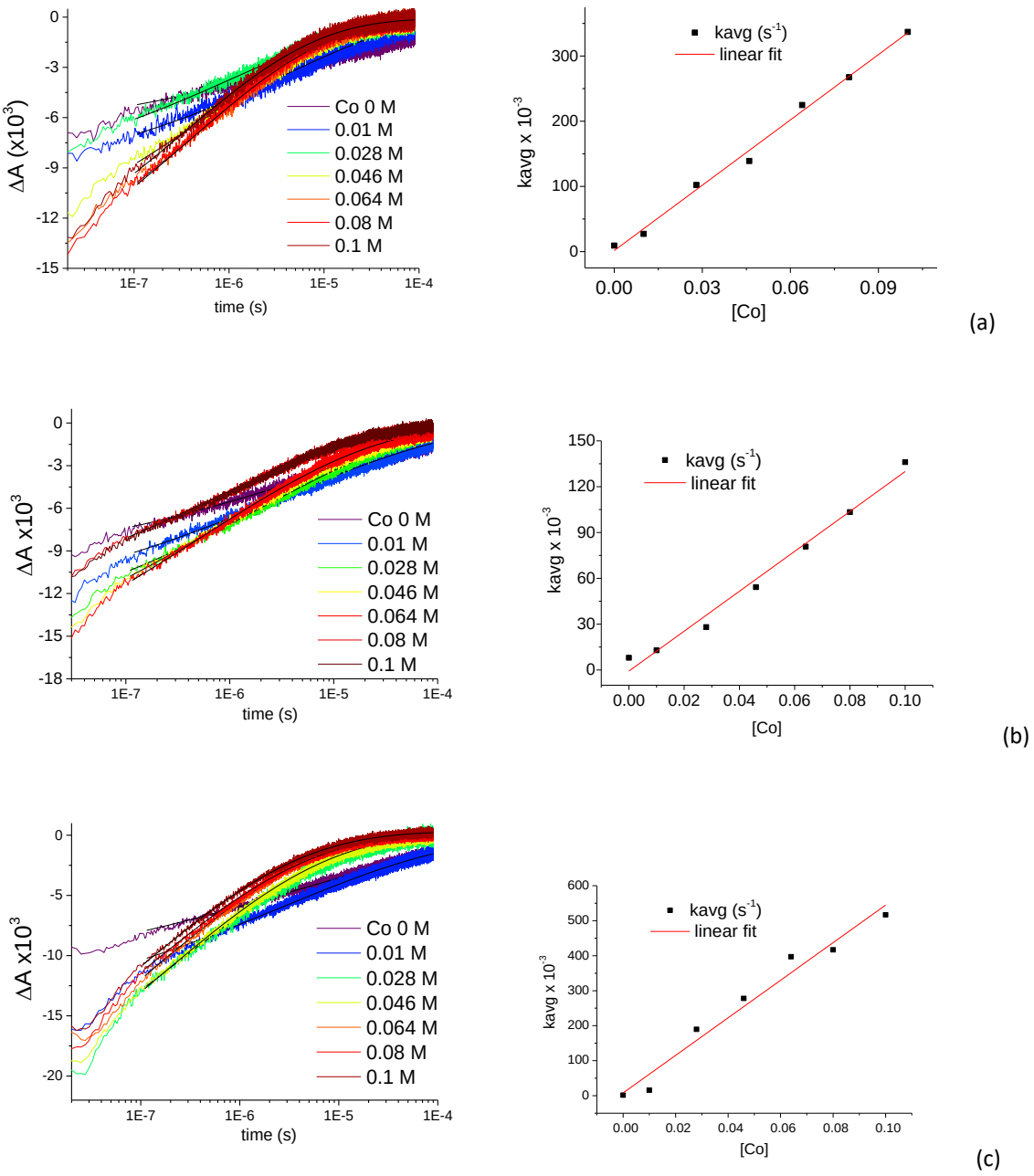

Figure 4.26 Absorption changes after laser excitation (a) for $Co(DTB)_3(OTf)_2$, (b) for $CoTTT(NCS)_3TBA$, (c) for $Co(DTB)_3(OTf)_2$, under various mediator concentrations in the 0.1M LiTf DMF:ACN 1:3 electrolyte; and relative linear trends obtained by extrapolating the k'_{reg} values from the decays' fittings and plotting them respect to the cobalt concentration.

It must be pointed out that when no voltage is applied to the photoelectrode, the estimated regeneration efficiencies are far from the values that would be obtained when the cell is operative, in which case electrons are injected in TiO_2 thus increasing notably the recombination events. As a consequence, to evaluate the regeneration efficiencies in a situation that is closer to the real

operative cell conditions, the potential to be applied in order to get closer to the cell maximum power point (MPP), corresponding to the situation of 20 electrons per TiO_2 nanoparticle [25], was derivated by spectroelectrochemistry [22]. Absorbance changes were monitored under the application of increasingly negative potential values, in order to examine the progressive reduction of TiO_2, as pictured in figure 4.27 a. The increase of the number of electrons in TiO_2, obtained by increasing the negative potential applied, was calculated by applying equation 4.21 to the measured absorbance values at the 700 nm electrons absorption wavelength:

$$n°electrons/TiO_2\ nanoparticle = A\cdot (4/3\ \pi r^3 \cdot N_A \cdot 1000) / (\varepsilon_e \cdot 5 \cdot 1.414 \cdot 10^{-4} \cdot 0.5) \qquad \text{(Eq. 4.21)}$$

where A = Abs; r = TiO_2 nanoparticles radius = $7.5E^{-9}$ m; $N_A = 6.022\ 10^{23}$; $\varepsilon_e = 930\ M^{-1}cm^{-1}$; 5 µm = TiO_2 layer thickness; $1.414 \cdot 10^{-4}$ = term taking account of the 45° slide position to the probe light; 0.5 = porosity.

According to these results, the condition of 20 electrons in TiO_2, corresponding to the cell MPP, is reached with an applied voltage of -631 mV vs NHE.

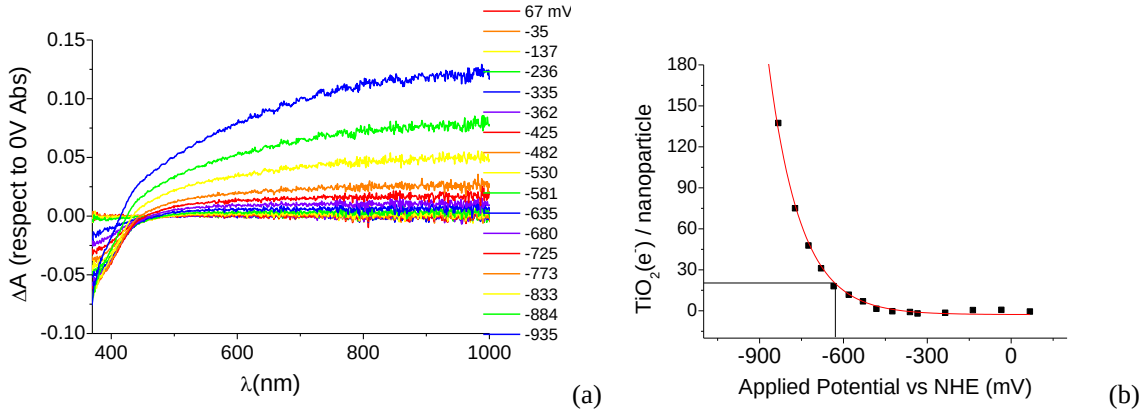

Figure 4.27 (a) Abs changes due to electrons absorption under different applied potentials, for non dyed TiO_2 slide in a 0.1M LiTf ACN/DMF 3:1 solution; (b) Calculated number of electrons per TiO_2 nanoparticle plotted versus the applied potential, fitted with monoexponential function

Hence, the obtained - 631 mV potential was applied to the sensitized TiO_2 slide during the TA experiment in the blank electrolyte, then the transient absorpion spectrum was fitted with the KWW function (equations 4.18, 4.19), yielding the first order recombination rate constant value at the cell MPP, $k'_{rec} = 656{,}732\ s^{-1}$. This was then inserted in equation 4.20 to yield the regeneration efficiency at MPP. The k'_{rec} and η_{reg} (V_{MPP}) values are also reported in table 4.9. While the same trend is observed, it emerges that efficiency values are considerably lower in respect to the short circuit condition, pointing out how much the recombination kinetics is accelerated by an increase in concentration of electrons in TiO_2, induced by applying a negative potential to the photoelectrode. In figure 4.28 a comparison is made between the 486 nm TA decay registered with no bias (blue

trace) and under -631 mV (black trace): the faster recombination kinetics occurring when a potential is applied can be appreciated, so this effect can't be neglected if realistic DSSC regeneration efficiencies have to be estimated.

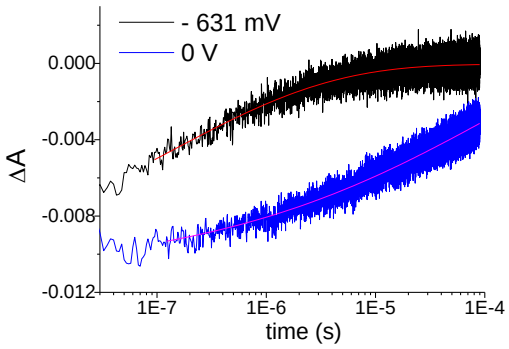

Figure 4.28 Absorption changes after laser excitation at 486 nm under a - 631 mV vs NHE applied potential, put in comparison with the no bias condition, for non dyed TiO_2 in a ACN/DMF 3:1 LiTf 0.1M solution.

	k_{reg} ($s^{-1}M^{-1}$)	k'_{rec} (s^{-1}) no bias (=$1/\tau_{avg}$ for [Co]=0M)	k'_{rec} (s^{-1}) at MPP	η_{reg}, no bias	η_{reg} at MPP
$Co(bpy)_3$	$3.34 \cdot 10^6$	$9.13 \cdot 10^3$	$6{,}57 \cdot 10^5$	**96.7%**	**28.9%**
$CoTTT(NCS)_3$	$1.3 \cdot 10^6$	$7.98 \cdot 10^3$		**92.9%**	**13.7%**
$Co(DTB)_3$	$5.37 \cdot 10^6$	$1.66 \cdot 10^3$		**99.6 %**	**47.9%**

Table 4.2.9 Rate constants and η values obtained by the measurements conducted without voltage application (no bias), or with - 631 mV vs NHE applied (at MPP) to the photoelectrode

4.2.4 Conclusion

In this chapter the properties of the negative cobalt (II) complex $[CoTTT(NCS)_3]^-$, which had shown interesting results in a quenching study previously conducted, where it had been combined with a highly charged ruthenium sensitizer in solution, have been further analyzed.

First, an analogous quenching study was conducted on the surface, with the $[Ru^{II}(tmam)_2(dcb)]^{6+}$ sensitizer grafted on TiO_2, confirming the outset of strong ion pairing between the oppositely charged species, which binds the cobalt species irreversibly to the sensitized slide.

Transient absorption spectroscopy gave evidence for sub-nanosecond dye regeneration induced by ion pairing, consistent with a maximum IPCE (25%), despite the low injection yield which characterizes the employed dye. On the contrary, the positive $[Co(dtb)_3]^{2+}$ complex didn't seem to regenerate efficiently the oxidized ruthenium, yielding a 60% reduced IPCE (15%) despite its

minor recombination current detected by photoelectrochemistry. Unfortunately the charge separated state was difficult to detect, since its fingerprint, consisting in a bleaching around 470 nm in the $[Ru^{II}(tmam)_2(dcb)]$ TA spectrum, lays at the same wavelength of the residual dye's excited state absorption, impeding to separate the two contributions. Nonetheless, the noteworthy photocurrent, flowing in DSSC under illumination, and IPCE values undoubtedly suggest the occurring of a significant electron injection thus the formation of the charge separated state. This was, however, not visible in the (TMAM+Co^-) TA, showing a flat ΔA profile in the 470 nm region, since the photogenerated Ru(III) is rapidly regenerated by the ion-paired Co-, in a sub-nanosecond timescale. A more convincing proof of the electron transfer occurring to Ru^{III} by ion-paired Co^{II} was the detection of a bleaching ascribable to Co^{II} oxidation, signal which was accurately deconvolved by the residual excited dye emission at 630 nm. An analysis based on sub-nanosecond timescale resolution spectroscopy would be the next step in order to gain deeper insights about the ultrafast electron transfer processes occurring in the investigated system.

A comparative photoelectrochemical and phophysical regeneration study was conducted, involving the $[CoTTT(NCS)_3]^-$, $[Co(bpy)_3]^{2+}$ and $[Co(dtb)_3]^{2+}$ redox mediators and a common sterically hindered ruthenium based sensitizer (Z907), characterized by localized partial negative charges. The results of this investigation were coherent with the hypothesis made based on the occurring electrostatic interactions, in particular the regeneration by Co- was noticeably low, in respect to that achieved with bpy and DTB.

Despite the DSSC efficiencies obtained combining the TMAM dye and the Co- redox mediator were not high, given the low injection yield of this particular sensitizer, and the diffusion issues encountered with the $[CoTTT(NCS)_3]^-$ complex, this study should serve as the basis for the design of opportunely charged cobalt based mediators, exploiting the easy adjustability of the cobalt coordination sphere, with the aim of favourably exploiting the electrostatic interaction in facilitating the regeneration process while suppressing at the same time electron recombination, without the need to reduce the electron coupling thus penalizing the charge transfer kinetics. Appropriate combinations of sensitizers and mediator systems could lead to the development of enhanced performing DSSC devices, based on the electrostatic factor.

References

(1) Sapp, S.A.; Elliott, C.M.; Contado, C.; Caramori, S.; Bignozzi, C.A.. *J. Am. Chem. Soc.* **2002**, 124, 11215–11222.

(2) Bella F., Galliano S., Gerbaldi C. and Viscardi G. *Energies* **2016**, 9, 384,

(3) S. M. Feldt, E. A. Gibson, E. Gabrielsson, L. Sun, G. Boschloo, A. Hagfedlt, *J. Am. Chem. Soc.* 132 (**2010**) 16714.

(4) H.N. Tsao, C. Yi , T. Moehl, J. H. Yum, S.M. Zakeeruddin, M.K. Nazeeruddin, M. Graetzel , *ChemSusChem* 4 (**2011**) 591.

(5) M.K. Kashif, J.C. Axelson, N.W. Duffy, C.M. Forsyth, C.J. Chang, J.R. Long, L. Spiccia, U. Bach, *J. Am. Chem. Soc.* 134 (**2012**) 16646.

(6) Gaddie R.S., Moss C.B., Elliott C.M., *Langmuir* **2013**, 29, 825−831

(7) T.W. Hamann, *Dalton Trans.*, **2012**, 41, 3111

(8) J.J. Nelson, T.J. Amick, C. M. Elliott, *J. Phys. Chem. C* **2008**, 112, 18255–18263

(9) B. M. Klahr, T.W. Hamann, *J. Phys. Chem. C* **2009**, 113, 14040–1404514040

(10) Ohta M., Koumura N., Hara K., Mori S., *Electrochem. Comm*. **2011**, 13, 778-780

(11) Liberatore M., Petrocco A., Caprioli F., la Mesa C., Decker F., Bignozzi C.A., *Electrochim. Acta* **2010**, 55, 4025-4029

(12) T. Kono, N. Masaki, M.Nishikawa, R. Tamura, H. Matsuzaki, M. Kimura, S. Mori; *ACS Appl. Mater. Interfaces* **2016**, 8, 16677−16683

(13) Swords W.B., Li G., Meyer G.J *Inorg. Chem*, **2015**, 54, 4512-4519.

(14) P.Wang, S.M.Zakeeruddin, J.E.Moser, M.K..Nazeeruddin, T.Sekiguchi, M. Grätzel, *Nature Materials* **2003**, 2 ,402–407.

(15) Carli S., Busatto E., Caramori S., Boaretto R., Argazzi R., Timpson C.J., C.A. Bignozzi; *J. Phys. Chem. C* **2013**, 117, 5142−5153

(16) Piguet C., *Journal of Chemical Education* **1997**, Vol. 74, No. 7

(17) Bain G.A., Berry J. F., *Journal of Chemical Education* **2008**, Vol. 85 No. 4

(18) Sacconi L., "Conformational and spin state interconversions in transition metal complexes", *Iupac publications*

(19) Burger K., "Coordination chemistry: experimental methods", **1973**, Butterworth, London

(20) Mosconi E., Yum J.H., Kessler F., Gomez Garcia C.J., Zuccaccia C., Nazeeruddin M.K., Graetzel M., De Angelis F., *J. Am.Che.Soc*. **2012**, 134, 19438-53

(21) U.B. Cappel, S. M. Feldt, J. Schoneboom, A. Hagfeldt, G. Boschloo *J.Am.Chem.Soc*. **2010**, 132, 9096–9101

(22) K. C. D. Robson, K. Hu, G. J. Meyer, C. P. Berlinguette, *J. Am. Chem. Soc*. **2013**, 135, 1961−1971

(23) Williams, G.; Watts, D. C. *Trans. Faraday Soc*. **1970**, 66, 3348− 3358.

(24) Lindsey, C. P.; Patterson, G. D. *J. Chem. Phys.* **1980**, 73, 3348− 3357.

(25) H. G. Agrell, G.Boschloo, A.Hagfeldt, *J. Phys. Chem. B* **2004**, 108, 12388-12396

Chapter 5: Promising cathodic materials for DSSC

The counter electrode is a DSSC fundamental component, from which good catalytic properties towards the redox mediator are required, in order to have low charge transfer resistance at the counter electrode/electrolyte interface thus improving the obtainable cell performances.

Besides the commonly used platinum based counter electrodes, which are quite expensive and don't show good catalytic properties towards cobalt based mediators, other promising categories have emerged. Conductive polymers have been intensively investigated, in particular PEDOT (polyethylenedioxythiophene) turned out to be a very efficient and stable cathodic material, especially combined with cobalt redox mediators, with whom it displays better kinetic properties than platinum itself [1]. Over the years many methods have been developed to produce PEDOT electrodes, depositing the polymer by physical methods on the FTO substrates, or growing the polymer in situ by chemical and electrochemical polymerization methods. The contribution given by this thesis work consists in a strategy to improve the adhesion of the polymer to the FTO surface through the formation of chemical interactions between them, reducing further the interfacial resistance to charge transfer. This was accomplished by synthetically modifying the 3,4-ethylenedioxythiophene (EDOT) monomer with a silane unit prior to its electrodeposition, treating at the same time the FTO surface with silanes, so that chemical bonds are created between the catalytic material and the substrate, enhancing the electronic coupling.

Another class of materials that has been highly exploited in the last decades, in many research fields and finally also in DSSC, is that of carbon nanomaterials. In particular, graphene and graphene oxide have been employed to prepare efficient and stable counter electrodes, requiring a partial graphene oxidation to produce a catalytic material that is both conductive and mechanically stable on the FTO surface [2]. The same philosophy was applied in this thesis work to prepare electrodes made of *carbon nanohorns* [3]. This innovative nanomaterial, discovered in 1999 [4], can be easily and cheaply synthesized, yielding a product that displays some advantages with respect to graphene and carbon nanotubes. By an easy spray-coating deposition method, *carbon nanohorns* based counter electrodes were prepared, and their cathodic behaviour was studied in DSSC based on cobalt redox mediators. High performances were obtained, comparable to those achieved with PEDOT, which is known for its excellent kinetic properties towards the $Co^{II/III}$ redox couple. Long time stability was also found, revealing carbon nanohorns to be a very promising and easy to produce cathodic material.

5.1 Conductive PEDOT covalently bound to transparent FTO electrodes

5.1.1 Introduction

Poly(3,4-ethylenedioxythiophene) (PEDOT) was first synthesized by Jonas et al, from Bayer AG Laboratories, in the late 1980s [5]. Since then the intrinsically conductive polymer PEDOT has been intensively studied due to its high conductivity (up to 300 $S \cdot cm^{-1}$) and good stability [6], PEDOT has found many applications in organic light-emitting diodes [7], electrochromic windows [8], sensors [9] and organic solar cells [10]. When it's present in its oxidized doped state PEDOT has good transparency in the UV-visible region, helping its adoption as counter electrode material in DSSC, in alternative to the most widely used Platinum [11, 12].

Recently we examined the cathodic activity of various types of PEDOT coated FTO electrodes in DSSC, containing cobalt complexes as electronic mediators, trying to clarify the key factors affecting cell performances [13]. It was concluded that the use of PEDOT electrodes produced by potentiostatic electropolymerization of 3,4-ethylenedioxythiophene (EDOT), generates enhanced photocurrents in solar devices based on the Co(III)/(II) redox couple, with respect to platinum and gold counter electrodes. The main reason for this is the lower mass transport resistance arising from the increased electroactive area of the polymeric material.

One of the main drawbacks for the practical application of PEDOT as counter electrode is, however, its weak adhesion to the conductive glass base, which can result in the loss of catalytic material from the electrode, affecting the long term operation of the solar device. In order to circumvent this problem, which may become crucial in the dimensional scaling up of the counter electrodes for large area (> 10 cm^2) solar devices, a new alkoxysilane substituted EDOT monomer was developed in this thesis work (figure 5.1), which can be firmly grafted to the FTO conductive glass. The silane used in this project was aminopropyl-triethoxysilane (APTES). It was found that the irreversible electro-oxidation of the surface bound EDOT-APTES, in the presence of unsubstituted EDOT monomers in solution, triggered the cationic polymerization of EDOT, resulting in the nucleation and growth of PEDOT on the modified FTO surface, finally leading to a strongly adherent conducting film with good electrocatalytic properties in respect to the Co(II)/(III) redox couple.

Hereinafter it will be reported on the preparation of the new EDOT monomer and on the morphological and electrochemical characterization of PEDOT films electrochemically grown on EDOT-APTES modified FTO surfaces. Testing the so obtained cathodic material in DSSC in conjunction with cobalt based redox mediators, an increased efficiency of about 10% was achieved in respect to devices built with either platinum or conventional PEDOT counter electrodes.

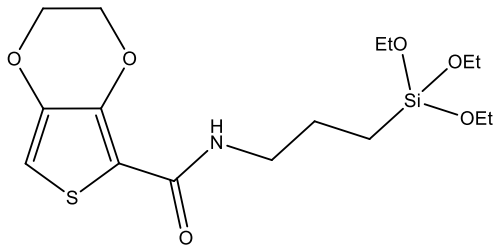

(**1**)

Figure 5.1 Structure of the silanized monomer EDOT-APTES (**1**).

5.1.2 Experimental

Materials

All chemicals, including the MK2 dye, were Sigma Aldrich products and were used as received, except for 2,3-Dihydrothieno[3,4-b][1,4]dioxine-5-carboxylic acid (carboxy-EDOT **1a**) by ABCR-Gelest, and TiO_2 colloidal paste (18NR-T) that was purchased from Dyesol. FTO glass plates (TEC 8, 2.3 mm thick substrates, by Pilkington) were carefully cleaned by several washings in ethanol, acetone, and Alconox followed by annealing at 400 °C in air before use. Platinized FTO counter electrodes were annealed at 400 °C for 10 min in air immediately before use.

$Co(L)_3(CF_3SO_3)_2$ and $Co(L)_3(PF_6)_3$ (L= bpy, 2,2'-bipyridine or L= dtb, 4,4'-di-tert-butyl-2,2'-bipyridine) complexes were prepared according to literature procedures [14].

*Synthesis of the EDOT-APTES monomer (**1**)*

A solution of 2,3-dihydrothieno[3,4-b][1,4]dioxine-5-carboxylic acid (**1a**) (200 mg, 1.08 mmol) in dichloromethane (20 mL) was treated with oxalyl chloride (0.66 g, 5.18 mmol) and a catalytic amount of N,N-dimethylformamide (DMF, ca. 8 drops). The solution was stirred and heated to reflux for four hours. The solvent was removed and the crude mixture was dissolved in dichloromethane. Triethylamine (TEA, 0.22 g, 4 mmol) and aminopropyl-triethoxysilane (239 mg, 1.08 mmol) were added in sequence and stirring was continued for 24 hours at room temperature until the reaction was completed. The solvent was evaporated to dryness of the reaction mixture and the crude product was purified by flash chromatography, through a silica gel plug (Silica gel 60) to give (**1**) as a white hygroscopic solid (80%).

^{1}H-NMR (CD_2Cl_2, δ/ppm): 6.81 (1H, broad, NH), 6.55 (1H, s, aromatic), 4.36 (2H, m, CH_2), 4.24 (2H, m, CH_2), 3.81 (6H, q J=7 Hz, CH_2), 3.37 (2H, m, CH_2), 1.65 (2H, m, CH_2), 1.2 (9H, t J=7 Hz, CH_3), 0.65 (2H, m, CH_2). ^{13}C NMR (CD_2Cl_2, δ/ppm) 161.20 (C_q, CONH), 144.05 (C_q, aromatic), 141.55 (C_q, aromatic), 104.05 (C_q, aromatic), 104.38 (CH, aromatic), 65.96 (CH_2), 64.59 (CH_2),

58.68 (APTES, CH_2), 42.21 (APTES, CH_2), 23.66 (APTES, CH_2), 18.47 (APTES, CH_3), 7.98 (APTES, CH_2).

FTO functionalization

Previously cleaned FTO electrodes were soaked for 24 hours in a 10 mM solution of (**1**) in toluene. The electrodes were then rinsed with toluene and acetonitrile, and dried in air.

PEDOT electrodeposition

Either unmodified or EDOT-APTES derivatized FTO electrodes were used as working electrodes in a three-electrodes electrochemical cell with a titanium foil as counter electrode and a saturated calomel electrode (SCE, by Amel) as reference. The distance between cofacially assembled FTO and titanium electrodes was ca. 2.5mm. PEDOT deposition was carried out by either potentiostatic (chronoamperometry: step potential program 0 V, 5 s; 0.2 V, 5 s; 0.5 V, 5 s; 1.6 V, 30 s) or potentiodynamic (cyclic voltammetry: 2 subsequent scans in the potential range 0-1.7 V at a scan rate of 50 mV s^{-1}) techniques, in a 10^{-2}M EDOT/0.1M $LiClO_4$ acetonitrile solution. The freshly deposited PEDOT electrodes were carefully washed with acetonitrile to remove residual oligomers weakly interacting with the surface.

AFM and SEM imaging

AFM imaging was performed using a Nanoscope Multimode 8 (Bruker, Santa Barbara, USA) equipped with a 15 um piezoelectric scanner. The AFM was operated in tapping mode and in peak-force tapping mode. SEM imaging was performed with a Zeiss EVO 40 electronic microscope with a maximum acceleration voltage of 30 KV.

Solar Cells Fabrication

Mesoporous titania films (ca. 6 μm thick) were prepared following the procedure reported in section 2.2.1, without blocking underlayer, and immersed in a 0.2 mM solution of MK2 in a 1:1 toluene/acetonitrile mixture for 24 hours. Solar cells were assembled in open configuration by holding the two electrodes together with metallic clamps and by using a 25 μm thick Surlyn frame as sealer. The active cell area was 0.25 cm^2. A similar configuration was used for symmetrical dummy cells consisting of two identical PEDOT electrodes working, respectively, as anode and cathode, separated by a ca. 100μm thick parafilm frame.
The electrolytes used in symmetrical cells consisted either of 0.05 M $Co(bpy)_3^{2+/3+}$ or of the less soluble 0.03 M $Co(dtb)_3^{2+/3+}$, in the presence of 0.1 M $LiClO_4$ in acetonitrile.

Two different types of acetonitrile based electrolytes (type A and B) were evaluated in DSSC. Type A electrolyte consisted of $Co(bpy)_3^{2+/3+}$: 0.18M, Co(II) / 0.028M,Co(III) / 0.1M $Li(CF_3SO_3)$ / 0.2 TBP (TBP = 4-Tert-butyl-pyridine), in acetonitrile. Type B electrolyte was based on $Co(dtb)_3^{2+/3+}$: 0.18 M, Co(II) / saturated Co(III) / 0.1M $Li(CF_3SO_3)$ / 0.2 TBP, in acetonitrile.

Solar cells characterization

Current−voltage measurements were performed at a scan rate of 20 $mV \cdot s^{-1}$. Cell performances were evaluated under AM 1.5 illumination (ABET sun simulator).

Counter electrode characterization in dummy cells

The counter electrodes catalytic properties were investigated in thin layer (100 μm) symmetrical cells, with a geometric active area of 0.25 cm^2. The electrochemical techniques used were linear sweep voltammetry (LSV), at a 5 $mV \cdot s^{-1}$ scan rate, and Electrochemical Impedance Spectroscopy (EIS), consisting in superimposing a sinusoidal 10 mV perturbation at a fixed DC potential (0 mV, or where specified, 0.05 V and 0.1 V). Impedance data were analyzed using the commercially available ZSimpWin 3.21 software and were fitted in terms of the equivalent electric circuits shown in Scheme 3, with relative errors <5%.
The heterogeneous electron transfer rate constant k^0 was evaluated according to the equation:

$$k^0 = [(RT)/(nFTR_{CT}A)](FC_{OX}{}^{\beta}C_{RED}{}^{1-\beta})^{-1} \quad \text{(Eq. 5.1)}$$

where R, T, and F are the ideal gas constant, the absolute temperature, and the Faraday constant, respectively. C_{OX} and C_{RED} are the concentrations of Co(III) and Co(II) in $mol \cdot cm^{-3}$, A is the electrode area (cm^2), β is the transfer coefficient and R_{CT} is the charge-transfer resistance evaluated by EIS near equilibrium. Equation 5.1 is conveniently reduced to:

$$k_0 = (RT)/(nF^2R_{CT}CA) \quad \text{(Eq. 5.2)}$$

when $C_{OX} = C_{RED} = C$, thus avoiding the evaluation of the transfer coefficient β which reflects the shape of the activation barrier at the interface, and may therefore be dependent on both the electrode material and the structure of the redox couple [15,16].

5.1.3 Results and discussion

PEDOT deposition on EDOT-APTES modified FTO

The silanized monomer *EDOT-APTES* (**1**) was prepared via a two steps reaction as indicated in scheme 5.1: carboxy-EDOT (**1a**) was first converted into the acyl chloride, that was treated without further purification with APTES/TEA in dichlorometane to give the monomer (**1**) with an 80% yield.

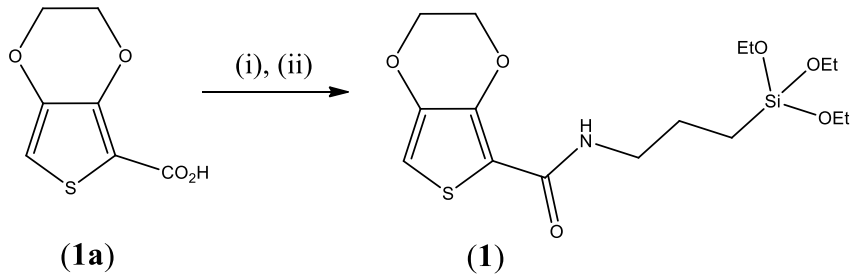

(**1a**) (**1**)

Scheme 5.1: (*i*) oxalyl chloride, CH_2Cl_2, DMF_{cat} ; (*ii*) APTES/TEA 2 eq., CH_2Cl_2

The functionalization of hydrophilic inorganic surfaces with silanes of general formula $RSi(X)_3$ (R= aminopropyl, or other alkyl chain and X= methoxy or ethoxy) occurs by substitution of the X groups with surface hydroxyl groups, resulting in a very robust covalent bridge between the organic moiety and the surface [17-19]. The anchoring of the silane to an hydroxilated surface is often described as tripodal, however it has been suggested that this particular configuration is not the most probable, and that trioxysilanes rather tend to form only two covalent bonds with the surface, leaving an unreacted alkoxy group [20-22] which may undergo cross-linking reactions. Due to the possibility of having hydrolytic cross-linking between adjacent silanes, surface silanization can also result in a more complex multilayered structure containing both horizontally and vertically arranged siloxanes. Nevertheless, highly ordered and well-packed monolayers can be obtained by making alkylmethyldichlorosilanes and alkyltrichlorosilanes react in toluene with basic catalysis at elevated temperatures [23].

The irreversible electro-oxidation of surface bound EDOT-APTES, in the presence of unsubstituted EDOT monomers in solution, can trigger the cationic polymerization of EDOT, resulting in the nucleation and growth of PEDOT chains directly linked via an α-coupling to EDOT-APTES groups, as represented in figure 5.2. A similar principle was exploited by Simon et al., who prepared a polypyrrole based anodic material by anodic electropolymerization of N-(3-(trimethoxysilyI)-propyl)pyrrole pre-anchored to n-type silicon and platinum electrodes in a pyrrole solution [24].

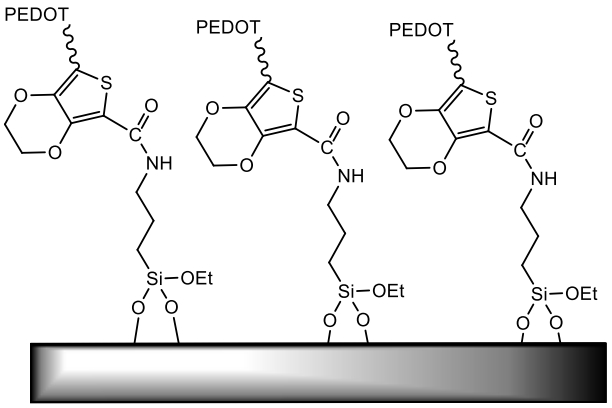

Figure 5.2 Schematic representation of PEDOT grown at EDOT-APTES modified FTO surfaces.

FTO electrodes were functionalized by immersion in a 10 mM toluene solution of the monomer (**1**) for 24 hours at room temperature. Cyclic voltammetry in acetonitrile/$LiClO_4$ (figure 5.3 b) confirmed the presence of the chemisorbed monomer**,** showing an irreversible wave with an oxidation peak at 1.5V vs SCE, in good agreement with the oxidation wave observed for the free monomer in solution using a glassy carbon electrode (figure 5.3 a). Most of the surface attached monomer is consumed during the first scan, as indicated by the almost complete disappearance of the irreversible wave in the second scan.

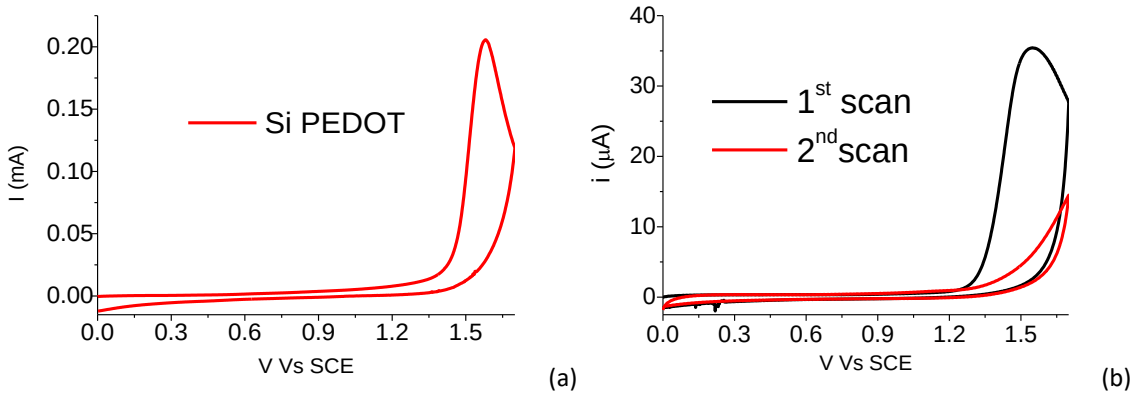

Figure 5.3 CV of APTES-EDOT in solution in ACN/$LiClO_4$ at a glassy carbon electrode (a); CV of APTES-EDOT modified FTO in ACN/$LiClO_4$ (b)

The PEDOT electrodeposition was probed on APTES-EDOT modified FTO electrodes as well as on bare FTO electrodes by cyclic voltammetry (CV). As will be later discussed, the potentiodynamic method was selected because it provided the best performing electrodes, thanks to their higher active area with respect to that obtained through the potentiostatic procedure.

From the deposition CVs reported in figure 5.4 a, a sharp threshold of the anodic current at 1.3 V vs SCE can be observed in the case of the APTES-EDOT modified FTO substrate, which is anodically shifted by about 100 mV in respect to that found for the unmodified FTO (ca. +1.2 V vs

SCE). The trace crossing on the reverse sweep (Figure 5.4 and 5.5 a) is typical of the first cycle in voltammograms registered for PEDOT deposition, and is ascribed to the initial stages of the polymer nucleation and growth on the surface [25]. Such feature disappears in the second scan, where the irreversible process assigned to the free EDOT oxidation in solution is still clearly evident but with the onset shifted of about 300 mV at lower overpotentials (figures 5.5 a and b).

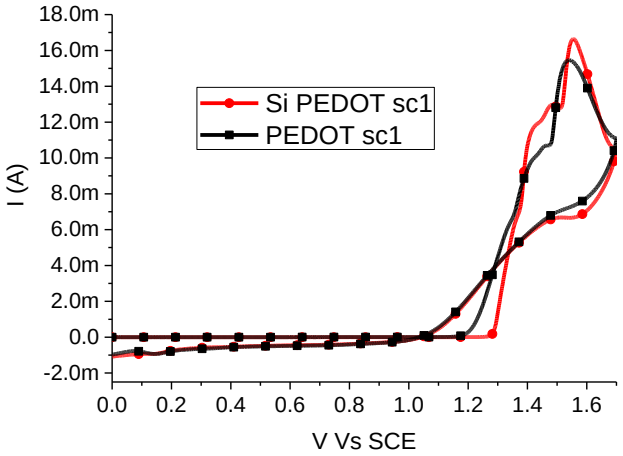

Figure 5.4 Overlay of the first cycle of the PEDOT potentiodynamic deposition on APTES-EDOT modified FTO (red) and bare FTO (black)

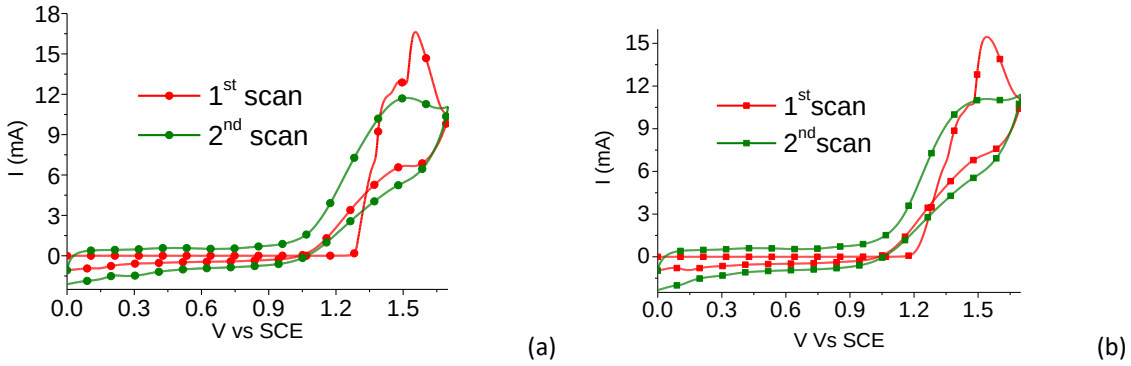

Figure 5.5 Deposition of PEDOT on APTES-EDOT modified FTO, first and second cycle (a); deposition of PEDOT on unmodified FTO, first cycle (red), and second cycle (green).

The onset potential in the case of functionalized surface (figure 5.4) agrees with that observed in figures 5.3a (APTES-EDOT in solution at a glassy carbon electrode) and 5.3b (APTES-EDOT modified FTO in inert electrolyte), suggesting that the primary event for PEDOT deposition at the modified FTO surface is the oxidation of the surface bound APTES-EDOT, followed by electron transfer from EDOT moieties in solution, leading to propagation of the cationic polymerization and finally resulting in the incorporation of APTES-EDOT into the PEDOT chains, which are then covalently bound to the FTO surface.

The exoergonicity of the electron transfer step from EDOT to APTES-EDOT^{+}, estimated from the difference of about 100 mV in the anodic thresholds, reported in figure 5.4, was corroborated by ab-initio calculations at the DFT-B3LYP- 6-31G* level, showing a stronger stabilization (240 meV) of the HOMO (highest occupied molecular orbital) in APTES-EDOT (-6.04 eV) in respect to the simple EDOT monomer (-5.8 eV). As expected, in both cases (Figure 5.6) the HOMOs have large lobes localized on the sulfur atom and on the 2,5 carbon atoms of the thiophene ring, but in the case of APTES-EDOT a substantial contribution by the electron withdrawing carbonyl group is observed, justifying its lower HOMO energy.

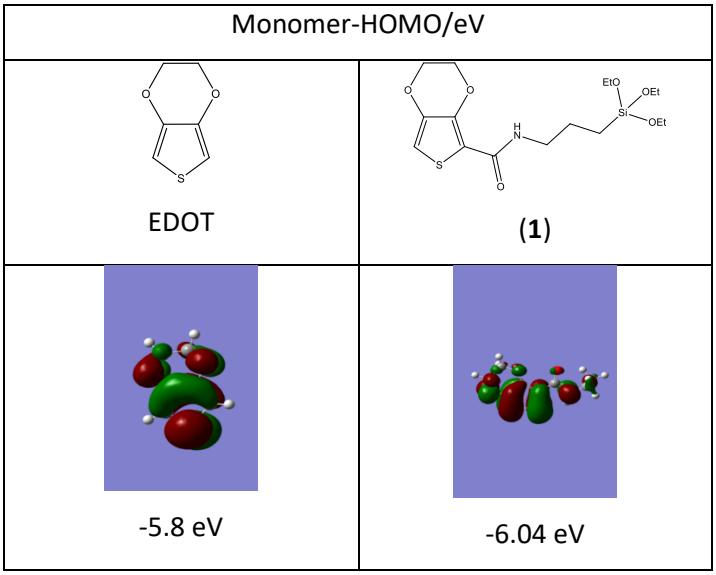

Figure 5.6. Optimized ground state geometries, HOMO isodensity plots and energies calculated for EDOT and APTES-EDOT in vacuo. DFT-B3LYP-631G*

From now on, for sake of brevity, the term *Si-PEDOT* will be used for referring to the PEDOT films grown on APTES-EDOT modified FTO.

The freshly deposited PEDOT films were uniform, with no visible unhomogeneities, had a good transparency and the typical sky blue color arising from the broad absorption peaking at 900 nm (figure 5.7), that has been ascribed to the polaron type carrier in oxidized p-type PEDOT polymer [26, 27]. No noticeable differences in the electronic spectra of Si-PEDOT and PEDOT were observed. The deposition, carried out by either potentiostatic or potentiodynamic method, was reasonably reproducible, with the 800 nm absorption, obviously related to the film thickness, varying slightly from 1.4 to 1.7 absorbance units.

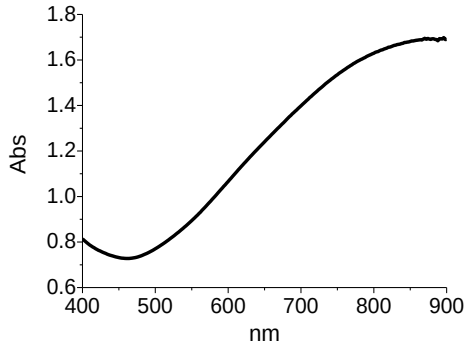

Figure 5.7 UV/Vis spectrum of freshly prepared Si-PEDOT

Films of *Si-PEDOT* display strong adhesion to the FTO surface compared to conventional PEDOT films, and this was pointed out by simple mechanical stress tests consisting in scotch tape peeling experiments and ultrasonic treatments (electrodes immersed in water and sonicated for 1 minute at maximum power, using an Ultrasonic Cleaner CP104 300W-39KHz).

In figure 5.8 the Si-PEDOT films stronger anchoring to the FTO surface is clearly demonstrated, together with an increased capability of withstanding stresses that are critical for the stability of regular PEDOT films electrodeposited on unmodified FTO. These latter are easily peeled off by the scotch tape, and quickly damaged (< 1 minute) by the mechanical shocks induced by ultrasonic waves.

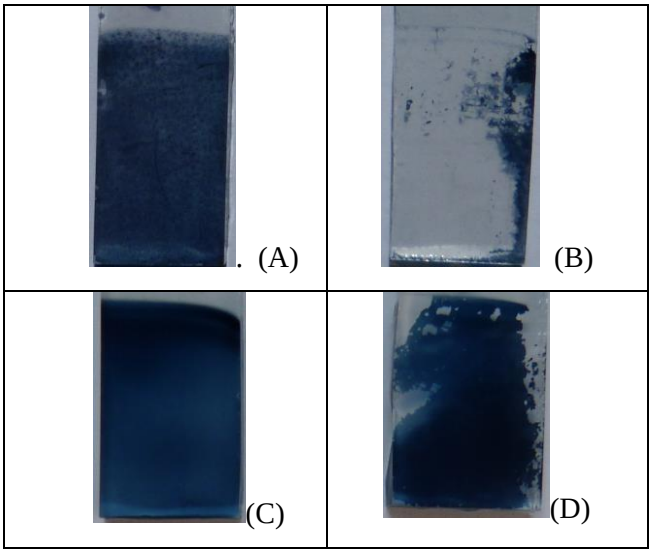

Figure 5.8 Mechanical stress tests carried out on PEDOT films. Top: **"***Scotch tape test"*on A) Si-PEDOT and B) PEDOT. Bottom: ultrasonic stress test on C) Si-PEDOT and D) PEDOT.

To the best of our knowledge the only other example of a strongly adhered PEDOT film onto an oxide surface was reported by Pang et al [28]. In that case PEDOT was obtained by vapor phase

deposition on a previously $FeCl_3$ coated aminosilane, bound to SiO_2 surface. The authors claimed that EDOT monomers can polymerize, leading to PEDOT growth, only on the $FeCl_3$ coated aminosilane SAM patterns. The stronger adhesion of the PEDOT/aminosilane adduct was probably due to a combination of factors, including stronger Van Der Waals forces between the polymer and the organic substrate and interactions of the aminosilanes nitrogen atoms lone pair with the positively charged polymer matrix of the oxidized PEDOT film. It is known that the use of $FeCl_3$ as oxidizing agent yields iron contaminated PEDOT films [11], therefore it must be pointed out that this antecedent multi-step procedure, besides being carried out on a different non conductive substrate, may not be suitable for DSSC applications and, in general, for all the other applications requiring electrochemically pure substrates. For example, the introduction of fast unspecific Fe(III)/(II) couples in DSSC may be detrimental to the cell efficiency, leading to increased recombination.

Morphology of the Si-PEDOT films

The Si-PEDOT electrodes morphology was studied by SEM and AFM microscopy and compared to that of conventional PEDOT films electrodeposited on unmodified FTO. Two different electrodeposition procedures were tested: potentiostatic deposition at 1.6 V vs SCE for 30 s and potentiodynamic deposition consisting of two sequential CV cycles in the interval 0-1.7 V vs SCE at a sweep rate of 50 mV s^{-1}. Figure 5.9 reports the surface morphology of both Si-PEDOT and PEDOT films obtained according to the two different deposition processes, imaged at different magnifications (ca. 40000 and 20000 x). In general, regardless of their nature, all the PEDOT films considered in this study reveal a considerably porous sponge-like three-dimensional network. In particular, the discontinuous polymer growth during multicycle potentiodynamic deposition leads to layer by layer polymer formation, yielding a fibrous and reticular morphology [29] which should be ideal to have an enhanced electrochemically active area. By contrast, the potentiostatic deposition procedure leads to a smoother, more compact surface with smaller pores (figure 5.9 e-f).

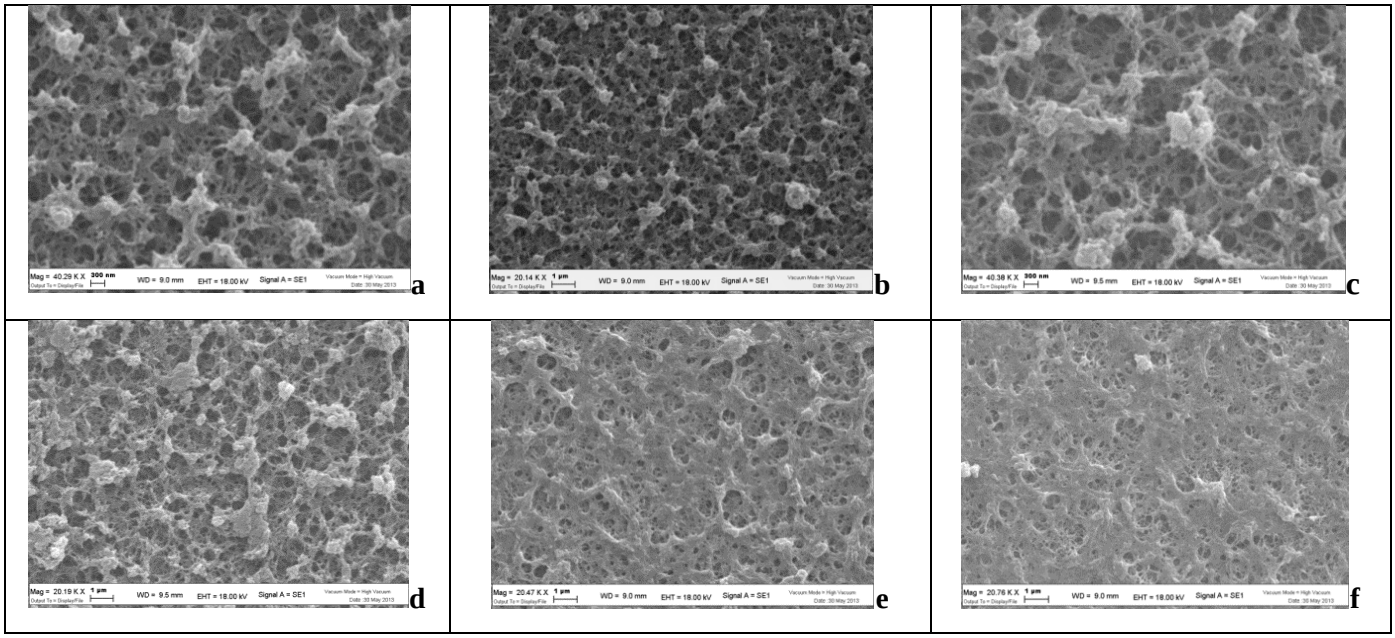

Figure 5.9: SEM micrographs of: potentiodynamic PEDOT imaged at 40290 x (a) and at 20140 x (b); potentiodynamic Si-PEDOT imaged at 40380 x (c) and at 20190 x (d) ; potentiostatic PEDOT imaged at 20470 x (e); potentiostatic Si-PEDOT imaged at 20760 x (f).

AFM analysis (table 1 and figure 5.10) substantially corroborated the qualitative observations carried out by SEM microscopy: considering the potentiodynamic deposition, it was observed that the thickness (700 nm) of the Si-PEDOT film was only marginally lower (by ca. 12%) than that of regular PEDOT films (800 nm), but the former exhibited a slightly higher surface roughness (R_q = 238 vs 200 for PEDOT). In general, both Si-PEDOT and PEDOT films deposited by the potentiodynamic procedure were confirmed to be thicker, at least by a ca. x2 factor, and substantially more porous (R_q = 238 and 200) than their potentiostatic counterparts (R_q = 111 and 58). It was also noted that the potentiostatic procedure left some exposed bare FTO surface, evident as dark cavities in the polymeric matrix (figure 5.10 d), reducing thus the catalytically active area of the counter electrode. Therefore, in view of their superior morphological characteristics, only the polymer films obtained in potentiodynamic mode were comparatively evaluated as catalytic counter electrodes for two different Co(III)/(II) couples having distinct electrochemical properties.

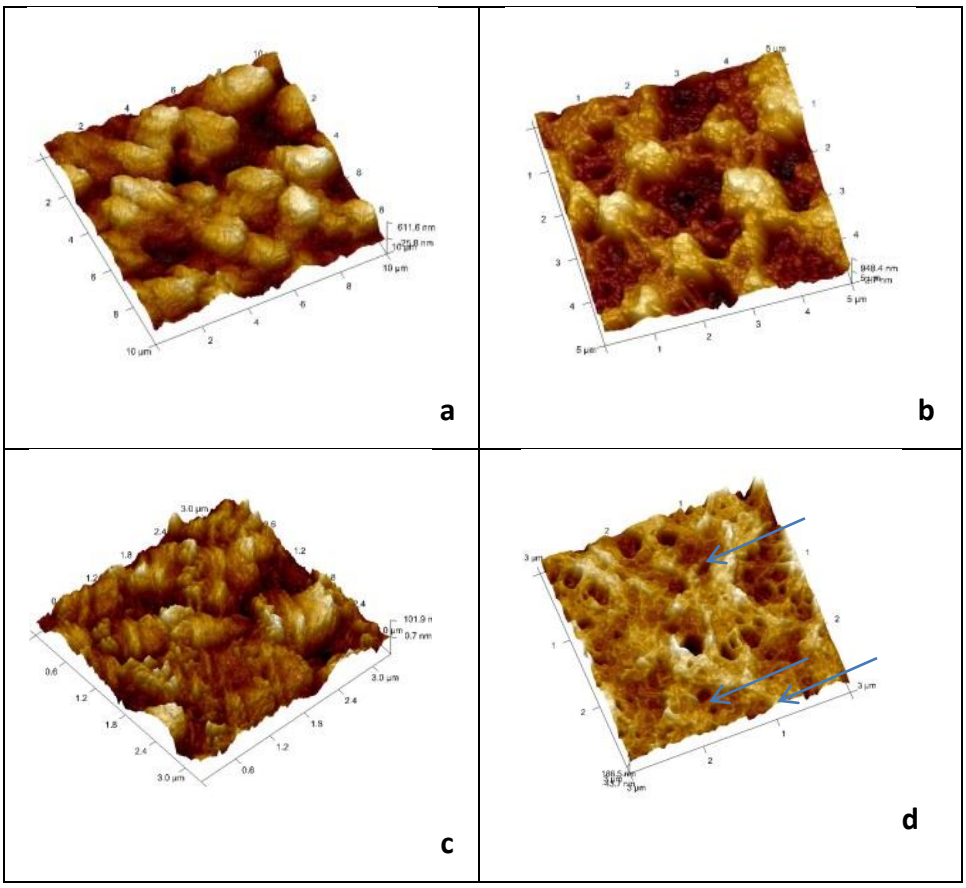

Figure 5.10 AFM images of a) Potentiodynamic PEDOT; b) Potentiodynamic Si-PEDOT; c) Potentiostatic PEDOT d) Potentiostatic Si-PEDOT: note the dark cavities in the polymeric matrix indicating some exposed FTO surface.

	R_q (nm)	R_a (nm)	R_{max} (nm)	Thickness (nm)
Si PEDOT	238	191	1570	700
PEDOT	200	170	1432	800
Si PEDOT	111	86.2	900	400
PEDOT	58.1	45	456	250-280

Table 5.1 Surface morphology parameters from AFM analysis. (R_q, root mean square: average of height deviations taken from the mean image data plane; R_a: arithmetic average of the absolute values of the surface height deviations measured from the mean plane; R_{max}: maximum vertical distance between the highest and lowest data points in the image following the planefit)

The electrocatalytic properties of silanized PEDOT counter electrodes have been investigated in thin layer symmetrical dummy cells by linear sweep voltammetry (LSV) and electrochemical impedance spectroscopy (EIS) with two Co(II)/(III) electrolytes based on the complexes $Co(bpy)_3$ (bpy = 2,2'-bipyridine) and $Co(dtb)_3$ (dtb = 4,4'-di-*tert*-butyl-2,2'-bipyridine) [13,16].

The LSV conducted at a 5 mV s^{-1} scan rate, reported in figure 5.11, shows that the electrochemical response of the PEDOT electrodes, comprising both Si-PEDOT and PEDOT, is either comparable or superior to platinum counter electrodes, fabricated with screen printable platinum paste. In all cases the purely diffusion controlled current (J_L) is achieved at overpotentials ≤ 200 mV, yielding a diffusion coefficient of 6.4 $\times 10^{-6}$ cm^2 s^{-1} and 4.6 $\times$ 10^{-6} cm^2 s^{-1} for $Co(bpy)_3$ and $Co(dtb)_3$ respectively, in agreement with our previous data [13].

A closer inspection of the linear trait of the JV characteristic reported in figure 5.11a ($Co(bpy)_3$), reveals that Si-PEDOT generates the steepest slope, indicating the realization, within the explored series, of the most favorable combination of mass transport and electron transfer kinetics. Previous studies [13] indicated that, even under very small overpotentials, it was difficult to access a purely kinetically controlled regime with such types of cobalt couples and cell configuration, therefore LSV cannot lead to more precise information about the current determining processes in dummy cells. In the case of $Co(dtb)_3$ (figure 5.11b) the catalytic electrodes produced nearly superimposable results, with the limiting current being only marginally higher in the case of Si-PEDOT. Table 2 summarizes the relevant parameters obtainable from this type of LSV measurements.

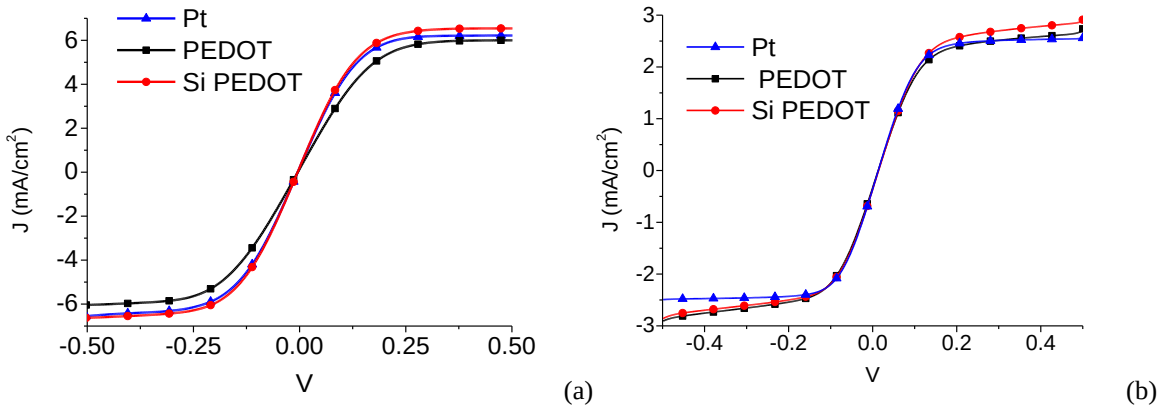

Figure 5.11 Linear sweep voltammetry on symmetric dummy cells fabricated with Pt (blue), PEDOT (black), and *Si-PEDOT* (red) counter electrodes, and containing a) 0.05M $Co(bpy)_3^{2+}$ / 0.05M $Co(bpy)_3^{3+}$, 0.1M $LiClO_4$, ACN and b) 0.03M $Co(dtb)_3^{2+}$ / 0.03M $Co(dtb)_3^{3+}$, 0.1M $LiClO_4$, ACN (scan rate 5 mV s^{-1}).

	Electrode	J_L (mA cm^{-2})	Slope (mA V^{-1})	$(\partial i/\partial V)^{-1}$ (Ω)
$Co(bpy)_3$	*Si PEDOT*	6.5	11.4	87.7
	PEDOT	6	8.58	116
	Pt	6.2	11	90.9
$Co(dtb)_3$	*Si PEDOT*	2.85	6.50	154
	PEDOT	2.59	6.20	161
	Pt	2.51	6.66	150.1

Table 2 Significant parameters from LSV in thin layer dummy cells: limiting current (J_L), slope and reciprocal of the slope near equilibrium ($(\partial i/\partial V)^{-1}$, differential resistance)

More precise information about the nature of the electrodic processes involving the Co (II)/(III) couple can be obtained by EIS at open circuit voltage (0 V), which allows the resolution, in the frequency domain, of the individual resistive contributions, arising from both charge transfer and mass transport. The dummy cell impedance response was satisfactorily fitted to the equivalent electric circuit shown in Scheme 3, where Rs is the ohmic serial resistance, R_{CT} is the charge transfer resistance, in parallel respect to the constant phase element CPE, describing the non ideal interfacial capacitance of the porous electrodes; W_S is the short Warburg term, also known as Nernst impedance [30].

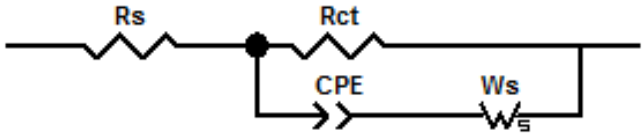

Scheme 3 Electric equivalent used to fit EIS data. According to Kirchoff's law, in symmetrical cells R_{CT} = $1/2R_{ct}$ of the single interfaces and C is twice the capacitance of the single electrodes

The fitted Nyquist plots, obtained from the impedance analysis of dummy cells containing the $Co(bpy)_3^{3+/2+}$ and $Co(dtb)_3^{3+/2+}$ electrolytes, are reported in figure 5.12, where it is clear that the electrodic impedance is dominated by the diffusional contribution, appearing as a large low frequency loop, having an amplitude of 60-70 Ω in the case of $Co(bpy)_3^{3+/2+}$ and > 100 Ω for $Co(dtb)_3^{3+/2+}$. By contrast, the heterogeneous charge transfer resistance was at least 30 times smaller than the diffusional resistance, and also significantly smaller than the ohmic contribution, mainly arising from the contact resistance of the FTO. This was essentially constant, of the order of 20±1 Ω. Table 3 summarizes the relevant parameters obtained by the fitting of experimental data with the equivalent circuit reported in scheme 3. The consistency of EIS data with the figures extracted from LSV can be appreciated, as shown by the good agreement between $(\partial i/\partial V)^{-1}$ and the zero frequency resistance R_0.

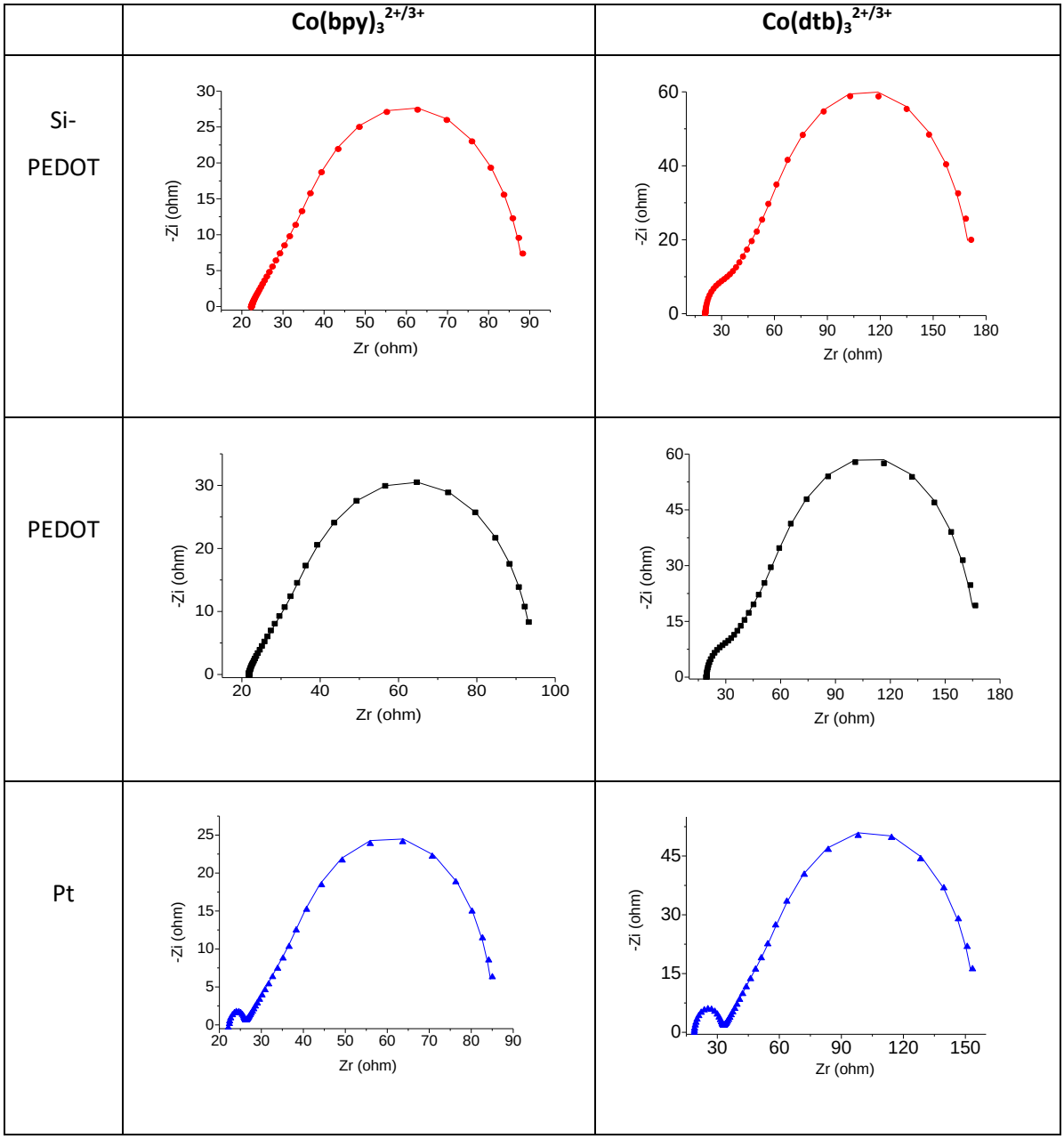

Figure 5.12 EIS of dummy cells (solid lines are the corresponding fits of experimental data) with 0.05M $Co(bpy)_3^{2+/3+}$ and 0.03M $Co(dtb)_3^{2+/3+}$ in $LiClO_4$ 0.1M/ACN, freq. range $10^4 \div 10^{-2}$Hz ($10^5 \div 10^{-2}$Hz for Pt), active area A_{cell} 25mm^2, layer thickness ca 100 μm

	Co(bpy)$_3$					**Co(dtb)$_3$**				
CEs	Rs Ω	Rct Ω	Rd Ω	R_0 Ω	k_0 ($\times 10^3$ cm/s)	Rs Ω	Rct Ω	Rd Ω	R_0 Ω	k_0 ($\times 10^3$ cm/s)
Si PEDOT	22,3	0.8	65	88	2.7	20.8	5.4	141	172	0.39
PEDOT	21.7	0.9	71	94	2.3	19.4	5.3	138	166	0.40
Pt	22.5	1.8	59	85	1.2	18.9	6.6	125	154	0.32

Table 3 Relevant Parameters extracted from the EIS Study in dummy cells: ohmic resistance (R_S), charge transfer resistance (Rct), diffusional resistance (Rd), total resistance in the zero frequency limit (R_0) and heterogeneous electron transfer rate constant (k_0), calculated from Rct according to equation 5.1

In general PEDOT electrodes exhibit a superior heterogenous rate constant with respect to platinum, which is an important requirement for a good DSSC cathode, which should be ideally capable of reducing the oxidized electrolyte species, generated at the illuminated photoanode, at least at a comparable rate.

It is clear that the electrolyte used for the first electrochemical characterization in dummy cells differs both qualitatively (i.e. lack of basic additives to control recombination with TiO_2) and quantitatively (higher concentration of Co(III)) from the typical electrolytes used in solar devices. A different composition electrolyte may result in a substantial alteration of the electrodic behavior of the redox couple at the catalytic interface: for instance, the decreased concentration of Co(III) may lead to an increased overpotential, while the presence of additives like 4-tert-butylpyridine, may alter the heterogeneous rate constant, for example by adsorbing on the organic PEDOT surface. To clarify this point EIS measurements (figure 5.13) were performed in dummy cells filled with the same electrolyte commonly used to assemble the DSSC devices (typically $Co(bpy)_3^{2+/3+}$ 0.18/0.028M, 0.1M $Li(CF_3SO_3)$, 0.2 M TBP in acetonitrile) and polarized from 0 to 100 mV, up to the threshold of the dummy cells limiting current.

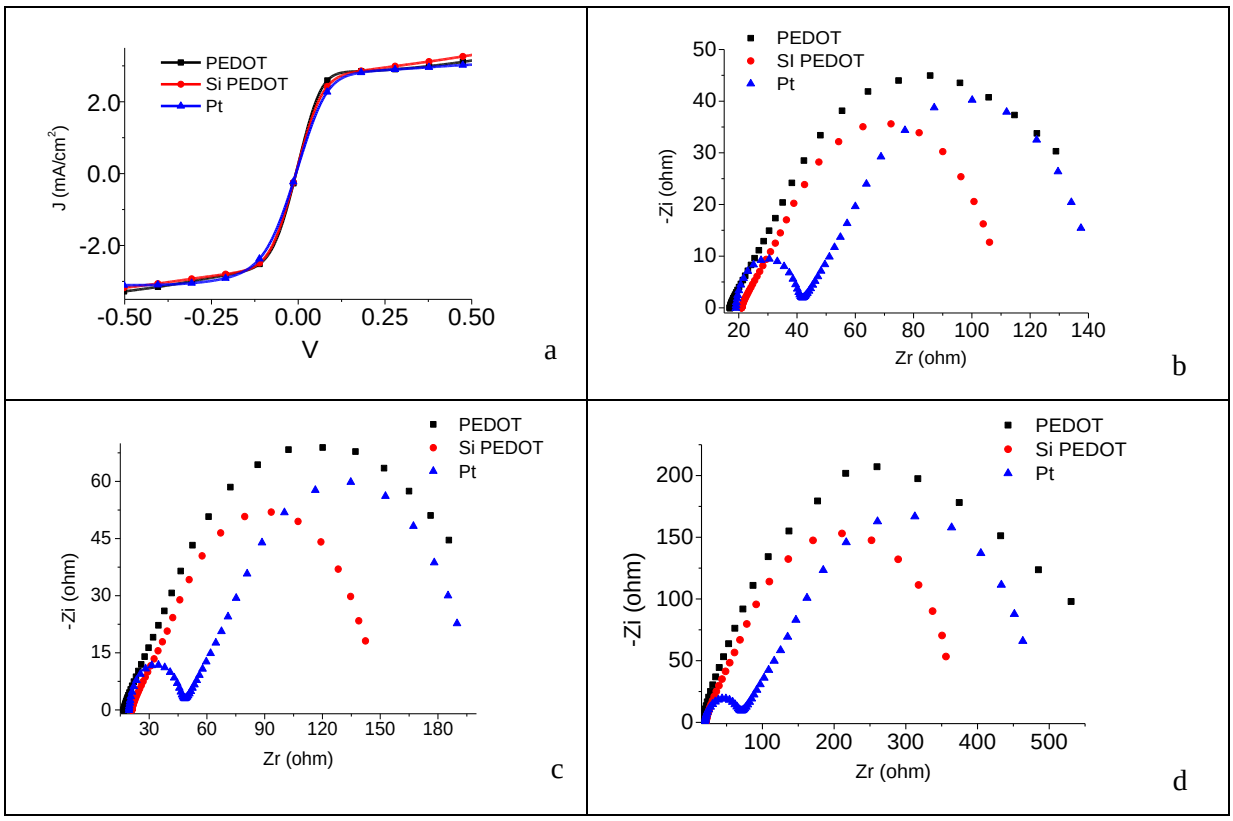

Figure 5.13 Electrochemical response of dummy cells (0.25 cm^2 active area) based on PEDOT (black), Si-PEDOT (red), and Pt (blue), in the presence of $Co(bpy)_3^{2+/3+}$ 0.18/0.028M, 0.1M $Li(CF_3SO_3)$, 0.2 TBP in acetonitrile. A) LSV recorded at 5 mV s^{-1} B) EIS at 0V; C) EIS at 0.05 V; D) EIS at 0.1 V

When the potential is increased from 0 V to 0.05 V and finally to 0.1 V, the progressive increase of the total cell resistance can be observed (figure 5.13), which can be readily appreciated by the projection of the arcs on the real axis of the Nyquist plots. The mass transport resistance exhibits the most significant increase when the symmetric cell is polarized close to its diffusional limit, undergoing a ca. four fold increase when biasing from 0 to 100 mV. In the case of platinum electrodes the charge transfer resistance is the highest and shows a more moderate increase than the diffusional resistance (a ca. x 1.5 factor), when passing from 0 to 100 mV. It is also evident that *Si-PEDOT* show in every condition both the lowest charge transfer resistance and diffusional resistance, making it a very promising candidate as stable counter electrode in cobalt mediated DSSC.

The electrochemical response of Si-PEDOT was finally evaluated in **MK2** sensitized solar cells sealed with a 25 μm spacer, in order to minimize the diffusional resistance which had previously demonstrated to be one of the major contributions to the overall cell resistance. **MK2** (figure 1.14, chapter 1) is a commercially available sterically hindered alkyl-substituted-oligothiophene organic dye with a high molar extinction coefficient (35800 $M^{-1}cm^{-1}$), which provides excellent performances in cobalt based DSSCs [31], thanks to the lateral alkyl chains that can reduce both the

recombination current and the intermolecular pi-pi stacking responsible for the deactivation of its excited state.

The current-voltage curves obtained with the cobalt based mediators $Co(bpy)_3$ and $Co(dtb)_3$, in transparent cells equipped with Si-PEDOT, Pt and PEDOT counter electrodes, are reported in figure 5.14, with the relative photovoltaic parameters summarized in table 4. It can be appreciated that in the case of both mediators the use of Si-PEDOT counter electrodes allows for a relative cell efficiency improvement of on the order of 10 % (12 % for $Co(bpy)_3$ and 9.6 % for $Co(dtb)_3$), thanks to superior Jsc and Fill Factor (FF). This behavior is consistent with the decreased serial resistance of the Si-PEDOT equipped solar cells. In fact the use of a porous catalytic substrate, displaying superior electron transfer kinetics, reduces both the activation and the concentration overpotentials at the cell counter electrode.

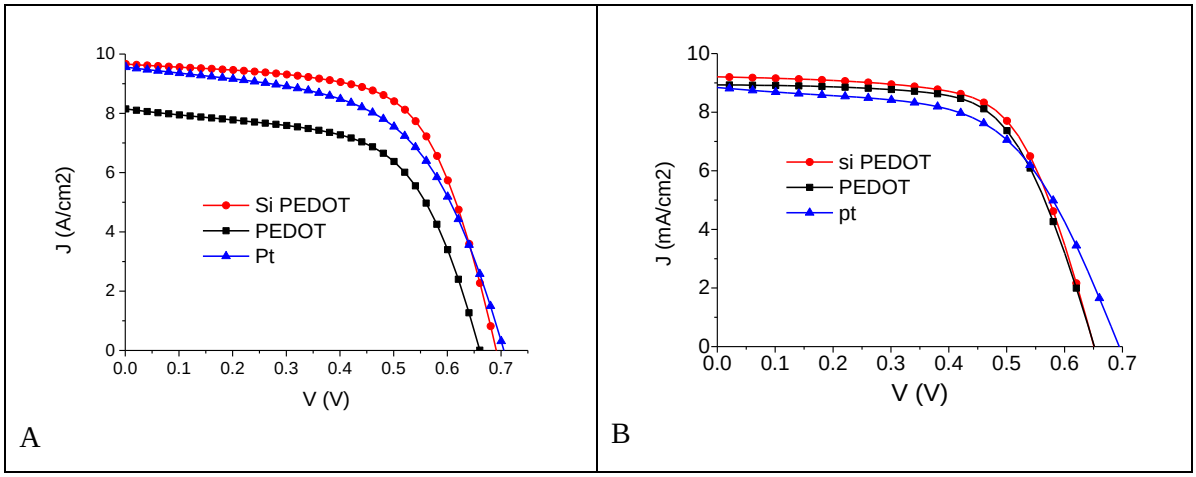

Figure 5.14 *JV* curves of DSSCs (0.25 cm^2 active area) sensitized by MK2 dye and equipped with different counter electrodes: PEDOT (black); Si-PEDOT (red); platinum (blue). A) $Co(bpy)_3^{2+/3+}$ 0.18/0.028M, 0.1M $Li(CF_3SO_3)$, 0.2 TBP in acetonitrile B) $Co(dtb)_3^{2+/3+}$ 0.18 M /sat., 0.1M $Li(CF_3SO_3)$, 0.2 TBP in acetonitrile. AM 1.5 G illumination, sweep rate 20 mV/s

electrolyte	CE	Voc	Jsc	FF	η (%)
$Co(bpy)_3$	**Si-PEDOT**	0,69	9,65	0,64	4,23
	PEDOT	0,66	8,15	0,58	3,12
	Pt	0,7	9,5	0,57	3,78
$Co(dtb)_3$	**Si-PEDOT**	0,65	9,21	0,65	3,88
	PEDOT	0,65	8,94	0,64	3,74
	Pt	0,69	8,83	0,58	3,54

Table 4 Relevant parameters from JV curves reported in figure 5.14

5.1.4 Conclusion

A new silanized EDOT derivative (APTES-EDOT) was prepared via a simple two step reaction in high yield. The new monomer can be firmly grafted to a FTO conductive glass, where the irreversible electro-oxidation of surface bound EDOT-APTES, in the presence of unsubstituted EDOT monomers in solution, triggers the cationic polymerization of EDOT, resulting in the incorporation of PEDOT chains onto the APTES-EDOT, covalently bound to the FTO surface. As a consequence, Si-PEDOT films are strongly anchored to the FTO surface and capable of withstanding mechanical stresses that are critical for the adhesion of regular PEDOT films electrodeposited on unmodified FTO [32].

The polymerization conducted by potentiodynamic method resulted in layer by layer polymer formation, yielding a fibrous and reticular morphology which is ideal for maximizing the permeation and the interaction with the redox electrolyte. Consequently, when tested in solar cells in association with Co(II)/(III) redox couples, Si-PEDOT based counter electrodes displayed decreased charge transfer and mass transport resistances, with respect to both platinum and conventional PEDOT films, leading to enhanced cell efficiencies.

Si-PEDOT counter electrodes are thus very stable and promising candidates for substituting noble metals in cobalt mediated DSSC. In addition, the applications of a covalently surface bound conductive polymer with a good and clean electrochemical response may not be limited to solar energy conversion, but become significant also in other branches of applied electrochemistry, including electrocatalysis and the field of electrochemical sensors for environmental and biological applications.

References

(1) A.Elschner, S. Kirchmeyer, W. Lovenich, U. Merker, K. Reutelschner, **2011**, CRC Press: Boca Raton, FL

(2) Kavan L., Yum J.H., and Graetzel M. *ACS Appl. Mater. Interfaces*, **2012**, 4 (12), pp 6999–7006

(3) Z. Zhang, S.Han , C. Wang, J. Li , G. Xu *Nanomaterials* **2015**, *5*, 1732-1755

(4) Iijima, S; Yudasaka M; Yamada R; Bandow S; Suenaga K; Kokai F; Takahashi K., *Chem. Phys. Lett.*, **1999**, 309 (3–4): 165–170.

(5) Jonas, F.; Heywang, G.; Schmidtenberg, W.; Heinze, J. Eur. Patent 339340, **1988**

(6) Groenendaal, L.B.; Jonas, F.; Freitag, D.; Pielartzik, H.; Reynolds, J.R., *Adv. Mater.*, **2000**, *12*, 481-494.

(7) Kim, Y. H.; Lee, J.; Hofmann, S.; Gather, M. C.; Meskamp, L. M.; Leo, K. *Adv. Funct. Mater.* **2013**, *23*, 3763–3769.

(8) Ma, L.; Li, Y.; Yu, X.; Yang, Q.; Noh, C. H. *Sol. Energy Mat. Sol. Cells* **2008**, *92*, 1253– 1259.

(9) Mathiyarasu, J.; Senthilkumar, S.; Phani, K. L. N.; Yegnaraman, V. *Mat. Lett.*, **2008**, *62*, 571–573.

(10) Girotto, C.; Moia, D.; Rand, B. P.; Heremans, P.*Adv. Funct. Mater.* **2011**, *21*, 64–72.

(11) Xia, J.; Masaki, N.; Jiang, K.; Yanagida, S. *J. Mater. Chem.*, **2007**, *17*, 2845–2850.

(12) Saito, Y.; Kitamura, T.; Wulia, Y.; Yanagida, S. *Chem. Lett.*, **2002**, *10*, 1060-1061.

(13) Carli, S.; Busatto, E.; Caramori, S.; Boaretto, R.; Argazzi, R.; Timpson, C. J.; Bignozzi C. A., *J. Phys. Chem. C*, **2013**, *117*, 5142−5153.

(14) Cazzanti, S.; Caramori, S.; Argazzi, R. ; Elliott, C. M.; Bignozzi, C. A., *J. Am. Chem. Soc.*, **2006**, *128*, 9996−9997.

(15) Bard, A. J.; Faulkner, L. R. Electrochemical Methods, Fundamentals and Applications; J. Wiley & Sons: Hoboken, NJ, 2001.

(16) Sapp, S. A.; Elliott, C. M.; Contado, C.; Caramori, S.; Bignozzi, C. A. *J. Am. Chem. Soc.*, **2002**, *124*, 11215−11222.

(17) Haensch, C.;Hoeppener, S.; Schubert, U.S. *Chem. Soc. Rev.*, **2010**, *39*, 2323–2334,

(18) Ulman, A. *Chem. Rev.*, **1996,** *96*, 1533-1554.

(19) Arkles, B. *CHEMTECH*, **1977**, *7*, 766-778.

(20) Iguchi, N.; Cady, C.; Snoeberger, R. C.; Hunter, B. M.; Sproviero, E. M.; Schmuttenmaer, C. A., Crabtree, R. H.; Brudvig, G. W.; Batista, V. S. *Proc. SPIE*, **2008**, *7034*, 70340C-8.

(21) Cerneaux, S.; Zakeeruddin, S. M.; Pringle, J. M.; Cheng, Y.B.; Grätzel, M.; Spiccia, L. *Adv. Funct. Mater.* **2007**, *17*, 3200–3206.

(22) Pasternack, R. M.; Amy, S. R.; Chabal, Y. J. *Langmuir*, **2008,** *24*, 12963-12971.

(23) Fadeev, A. Y.; McCarthy, T. J. *Langmuir*, **2000,** *16*, 7268-7274.

(24) Simon, R. A.; Ricco, A. J.; Wrighton, M. S *J. Am. Chem.* Soc., **1982**,*104* , 2031-2034.

(25) Randriamahazaka, H. ; Noël, V.; Chevrot, C. *J. Electroanal. Chem.*, **1999**, *472*, 103–111.

(26) Ahonen, H. J.; Lukkari, J.; Kankare, J. *Macromolecules* **2000**, *33*, 6787-6793.

(27) Chen, X.; Inganas, O.. *J. Phys. Chem.* **1996,** *100*, 15202-15206.

(28) Pang, L.; Kim, S.; Lee, J. *J. Nanosci. Nanotechnol.* **2007**, *7*, 3792-3794.

(29) Patra, S.; Barai, K.; Munichandraiah, N. *Synth. Met.* **2008,** *158*, 430–435.

(30) Wang,Q.; Moser, J.-E.; Grätzel,M. *J.Phys.Chem.B* **2005**, *109*, 14945-14953.

(31) Kashif, M. K.; Axelson, J. C.; Duffy, N. W.; Forsyth, C. M.; Chang, C. J.; Long, J. R.; Spiccia, L.; Bach, U. *J. Am. Chem. Soc.*, **2012**, *134*, 16646−16653.

(32) S. Carli, L. Casarin, G.Bergamini, S. Caramori, C. A. Bignozzi; *J. Phys. Chem. C* **2014**, 118, 16782−16790.

5.2 Single Walled Carbon Nanohorns as catalytic counter electrodes for cobalt based DSSCs

5.2.1 Introduction

DSSC functioning is based on the cooperative interplay of subsystems such as the sensitized photoanode, the electron mediator and the catalytic counter electrode [1]. Since the initial reports considerable effort has been directed towards the optimization of sensitizers [2-4], redox mediators [5-8] ,photoanode surface passivation [9,10] and counter electrodes [11,12]. The development of stable catalytic counter electrode materials characterized by high abundance, high electrochemical activity, tunable transparency and simple and scalable deposition routes is relevant for the large scale applications of dye sensitized solar cells and of other emerging photoelectrochemical technologies[13-15].

For the sake of low-cost, good stability, scalable deposition routes, morphological tunability, the p-type conducting polymer, poly(3,4-ethylenedioxythiophene) (PEDOT) has been successfully employed as organic counter electrode material, demonstrating promising electrocatalytic properties when investigated in conjunction with cobalt based redox mediators [16-18].

Carbon based Nanomaterials have also been used to replace Pt counter electrodes [19-25]. Among them, Single Walled Carbon Nanohorns (SWCNHS) represents a very promising class of materials [26]. They are produced with a metal free synthesis and typically possess conical-shaped structures having diameter between 2 and 5 nm and length ranging around 80 nm (see figure 5.15). These cones are associated in dahlia-type spherical structures with an average diameter of 100 nm [27].

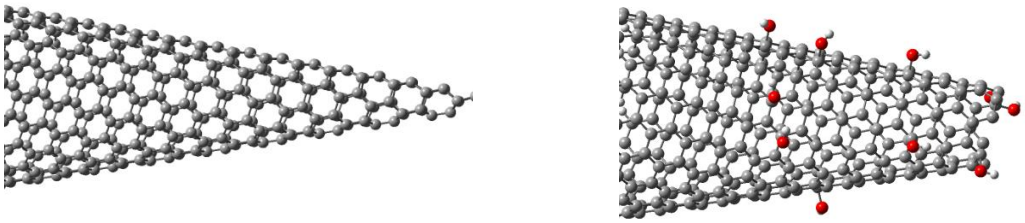

SWCNHS **ox-SWCNHS**

Figure 5.15 Typical 3D structure of pristine and oxidized Single Walled Carbon Nanohorns

SWCNHS based materials have a number of characteristics which make them attractive for energy applications and photoelectrochemical cells [26]. They have large surface area (~400 $m^2 g^{-1}$ for the pristine materials), present semiconducting character and display magnetic properties [28]. In comparison with the other carbon nanomaterials SWCNHS are easier to disperse in organic

solvents, allowing for their facile functionalization, furthermore they can form porous films with high surface area [29]. SWCNHS have been recently implemented into ionic liquid based electrolytes [30] and used in composite materials mixed with cellulose and Pt clusters for the assembly of counter electrodes in iodide/triiodide based dye sensitized solar cells [31]. The surface area of SWCNHS can be tuned by chemical oxidation in acidic environments that promotes the opening of the horn tip preserving the conductivity and electrochemical properties (figure 5.15) [32]. Herein we report, for the first time, the use of FTO-supported SWCNHS as catalytic counter electrodes in dye sensitized solar cells assembled with $Co(bpy)_3^{+2/+3}$ redox mediator (bpy = 2,2' bipyridine) [8]. Since it has been recently observed that carbon based nanomaterials tend to weakly adhere to FTO, leading to unstable devices [8,19-21], oxidized Single Walled Carbon Nanohorns (ox-SWCNHS) were also employed. In fact, it has been described that chemical oxidation of carbon nanomaterials, using mineral acids such as HNO_3 produces a higher amount of carboxylic functional groups [33,34] that might be helpful to improve the adhesion to transparent conductive glass (FTO or ITO), thanks to a stronger interaction with the surface hydroxyl groups. PEDOT has been selected as reference material for counter electrodes due to its well-established superior activity towards cobalt based redox mediators, thanks to the enhanced electroactive surface area and the reduced charge transfer resistance [16]. This work is devoted to both the evaluation of the electrocatalytic properties of these nanocarbon materials and to the assessment of their electrocatalytic stability in association with cobalt based electrolytes in DSSC.

5.2.2 Experimental

Materials

All the solvents and reactants were purchased by Sigma-Aldrich. Single Walled Carbon Nanohorns (SWCNHs) were produced by Carbonium s.r.l., Padova (Italy) by direct graphite evaporation in Ar flow, according to a patented method, and used as received [35]. Conductive FTO (TEC8, 2.3 mm thick substrates) was from Pilkington, and the slides were carefully cleaned by several washings in ethanol, acetone, and Alconox followed by annealing at 400 °C in air before use. Platinized FTO counter electrodes were loaned by the Dyepower Consortium and were prepared by screen-printing a conductive colloidal platinum paste Chimet (Pt-10−004F-05, batch 5738). TiO_2 colloidal paste (DSC 18NR-T) was purchased from Dyesol. The organic dye LEG4 was from Dyenamo.
$[Co(bpy)_3](CF_3SO_3)_2$ and $[Co(bpy)_3](PF_6)_3$ complexes were prepared according to literature procedures [8]

Equipment

Absorption spectra were collected with a JASCO V 570 UV–Vis spectrophotometer. **Thermogravimetric analyses (TGA)** were performed using a TA Instruments TGA Q500 and recorded under N_2, upon equilibration at 100 °C, followed by a ramp of 10 °C/min up to 750 °C. **Raman spectra** were acquired with a Renishaw instrument, model Invia reflex equipped with 532, 633, and 785 nm lasers. After acquisition, the spectra were normalized with respect to the G band. **Transmission electron microscopy (TEM)** experiments were performed using a Philips EM 208, accelerating voltage of 100 kV. Samples were prepared by sonication for 10 min and dropwise addition (8 μL) of the sample onto a carbon coated 200 mesh Ni grid (EM Sciences, Gibbstown, NJ), followed by solvent evaporation under vacuum. The surface morphology was investigated by **Atomic force microscopy (AFM)** measurements, conducted with a Digital Instruments Nanoscope III Scanning Probe Microscope, Digital Instruments, CA, USA. The instrument was equipped with silicon tip (model RTESP-BRUKER resonant frequency 300 kHz) and operated in tapping mode. The scanning parameters were as follows: scan rate 1 Hz, resolution 512, and scan size 5 × 5 μm. Surface topographical analysis of raw AFM images was carried out with the NanoScope Analysis 1.5 program.
SEM imaging was performed with a Zeiss EVO 40 electronic microscope with a maximum acceleration voltage of 30 KV.

ox-SWCNHS synthesis

A 100 mg amount of pristine SWCNHS was dissolved in 100 ml HNO_3 4 M and the solution was stirred under reflux for 8 hours. The mixture was cooled to room temperature, 200 mL of water were added and the solution was filtered with Millipore apparatus. The material was repeatedly washed with water until the filtrate pH changed from acidic to neutral. The material was collected, re-dispersed in 200 mL of acetone with the aid of sonic bath irradiation for 10 minutes, filtered again with the Millipore apparatus and washed with 400 mL of acetone. The material was collected and dried under vacuum.
The pristine SWCNHS (without any treatment) and the oxidized ox-SWCNHS were characterized by means of Thermogravimetric Analysis (TGA), Raman and IR spectroscopy.

Preparation of SWCNHS and ox-SWCNHS counter electrodes

A suspension of the pristine SWCNHS or the oxidized ox-SWCNHS (1 mg ml^{-1}) in ethanol was sonicated for 30 minutes at room temperature. This suspension was sprayed over masked FTO

electrodes (area 2×2.5 cm^2) placed on a hot plate at 120°C with an air-brush (FENGDA 0.33mm) placed at distance of 15 cm from the plate, using N_2 as carrier (0.5 Pa). Electrodes were subsequently annealed at 400°C for 15 minutes [31]. The deposition procedure is summarized in table 5.

	Volume of suspension (mL)	**Number of electrodes (area 2×2.5 cm^2)**
SWCNHS60	1	7
SWCNHS20	3	
SWCNHS5	5	
ox-SWCNHS55	2	5
ox-SWCNHS20	5	
ox-SWCNHS10	7	

Table 5 Typical operative conditions for the deposition of SWCNHS and ox-SWCNHS (a suspension of the pristine SWCNHS or the oxidized ox-SWCNHS (1mg/ml) in ethanol sonicated or 30' at room temperature)

Solar cells fabrication

A compact TiO_2 blocking underlayer was prepared by spin-coating a 0,3 M titanium tetraisopropoxide solution in 1-butanol (1000 rpm for 10 s, 2000 rpm for 20 s). The resulting substrates were heated at 500 °C for 15 min and cooled to room temperature. Subsequently a mesoporous TiO_2 layer was prepared by doctor blading a commercial TiO_2 paste (Dyesol 18NR-T). The coated films were gradually heated to 500 °C according to the following programmed temperature ramping: room temperature - 120°C (10 min), 120°C - 450°C (30 min), 450°C (20 min), 450°C - 500°C (10 min), 500°C (10 min). After cooling, the electrodes were treated with 0.4 M $TiCl_4$ overnight, washed with water and heated again at 450° for 30 minutes.

PEDOT based counter electrodes were prepared by potentiodynamic anodic electropolymerization of 3,4-ethylenedioxythiophene (EDOT) on FTO glass slides, following our previously reported method [36]. Platinized FTO counter electrodes, prepared by screen-printing a conductive colloidal platinum paste, were sonicated in isopropanol, dried and annealed at 400 °C for 10 min in air immediately before use.

Solar cells and symmetrical cells were assembled by sealing the electrodes with 25 μm thick hot-melt film (Surlyn, Solaronix). The redox mediator was introduced through a small channel on the Surlyn frame. The active area was 0.20 cm^2 and 0.25 cm^2 for solar cells and symmetrical cells respectively. Finally the channel was sealed with epoxy resin.

Electrolyte formulation

The electrolyte composition consisted of $[Co(bpy)_3]^{2+/3+}$: 0.18 M Co(II), 0.028 M Co(III), 0.1 M $LiCF_3SO_3$ and 0.2 M 4-tert-butylpyridine (TBP) in acetonitrile (ACN) for solar cell

characterization. The same electrolyte formulation in Methoxypropionitrile (MPN) was used for stability tests in dummy cells.

Solar cell characterization

Current−voltage measurements were performed at a scan rate of 10 mV s^{-1}. Cell performances were evaluated under AM 1.5 illumination (ABET sun simulator).

Counter electrode characterization in symmetric cells

Simmetric cells were investigated by slow scan rate cyclic voltammetry (SSCV) at 10 mV/s and by electrochemical impedance spectroscopy (EIS) by superimposing a sinusoidal 10 mV perturbation at the equilibrium potential (0 mV) of the assembled cell. Impedance data were analysed using commercially available Z-View software and were fitted in terms of equivalent electric circuits with relative errors < 5%.

5.2.3 Results and discussion

Among solution-processable deposition methods, such as spin coating, drop casting, dip coating etc., the spray coating technique, recently used to prepare graphene [37] based electrodes, has demonstrated to be a viable method for large-area fabrication of counter electrodes for DSSCs modules.

SWCNHS and ox-SWCNHS based counter electrodes were prepared by spray coating the nanocarbon suspension onto cleaned FTO kept at 120°C on an hot plate: this technique was found to be the optimal solution in terms of deposition homogeneity and reproducibility. The resulting electrodes were subsequently treated at 400° for 15 minutes to consolidate the coating. Carbon loading on the counter electrodes was evaluated through optical transmittance (*T%)* measurements at a fixed wavelength (550 nm), as previously reported [19-21]. Since the thickness of SWCNHS or ox-SWCNHS layers is a function of the number of cycles used during the spray coating deposition, for convenience we will label SWCNHS or ox-SWCNHS according to their 550 nm transmission: for example SWCNHS50 indicates a sample with T_{550} = 50%. PEDOT was chosen as the reference organic catalytic material due to its well demonstrated activity with respect to cobalt redox mediators [16].

The amount of carboxyl groups created by oxidation of pristine SWCNHS with HNO_3 can be estimated by TGA. As shown in Figure 5.16, the weight loss at 300°C, that has been related to CO_2 emission by the decomposition of carboxylic groups [38], is of the order of 1.7%, corresponding to a carbon loss of 0.46%. This means that the fraction of carbon atoms in the form of carboxylic

functions in ox-SWCNHS is about 1% (0.4 mmol g^{-1}) [39], as confirmed also by acid-base titration experiments [40].

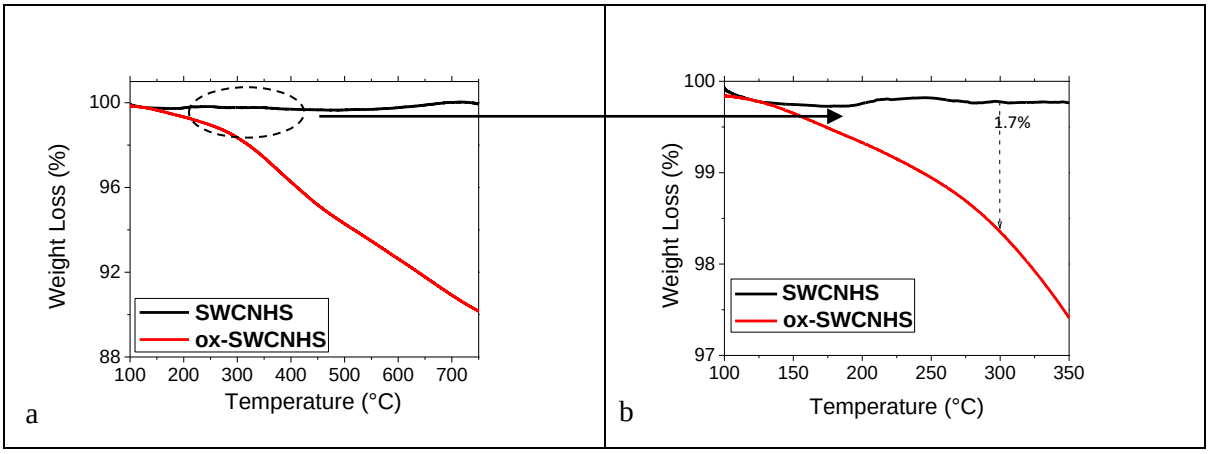

Figure 5.16 a) Thermogravimetric analysis of SWCNHS and ox-SWCNHS under N_2; b) magnification of the analysis plot in the temperature interval 100°C - 350°C

These results are supported by Raman spectroscopy, where the covalent attachment of functionalizing groups on the SWCNHS, in the form of sp^3 carbon centers, can be detected from the normalized relative area ratio of the D-band, with respect to the G-band (A_D/A_G) (Figure 5.17) [27,41-43]. The normalized A_D/A_G ratio for the ox-SWCNHS is 1.22 with respect to the pristine material, showing a significant increase of the carboxylic groups surface concentration on the ox-SWCNHS sidewalls after the HNO_3 treatment [44].

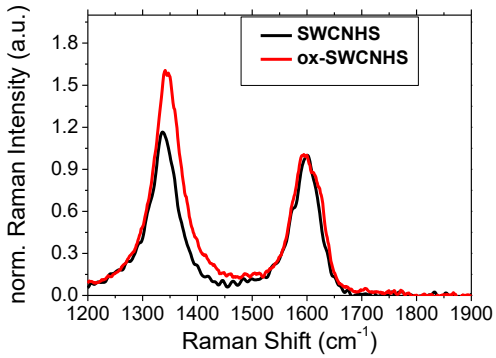

Figure 5.17 Raman spectra (with a 532 nm excitation wavelength) of SWCNHS and ox-SWCNHS, showing D (1350 cm^{-1}) and G bands (1600 cm^{-1}) [27].

The catalytic properties of the counter electrodes were investigated in thin layer (ca. 25 μm) symmetrical dummy cells by slow scan rate cyclic voltammetry (SSCV) and by electrochemical impedance spectroscopy (EIS). SSCV led to the evaluation of the limiting current J_L, expressed as $J_L = (2nFCD)/L$ (where L is the thickness of the spacer, C is the concentration of the redox couple, D is the diffusion coefficient) and of the differential resistance $(\partial\eta)/(\partial i)$ of the cell, calculated from

the reciprocal slope of the linear trait of the i-V characteristic at low overpotentials. EIS provided deeper insights into the overall electrochemical process, by resolving charge transfer and mass transfer processes in the frequency domain. Impedance spectra of dummy cells, generally showing two depressed arcs in the complex plain representation, were fitted with the electric equivalent reported in figure 5.18, where R_S is the serial ohmic resistance, R_{CT} is the charge transfer resistance, CPE is the constant phase element and Z_W is the Nernst diffusion impedance of the thin layer cell [45] . While other authors added an additional pore diffusional impedance $Z_{W,pore}$ in series to R_{CT}, in the mesh representing the counter electrode/electrolyte interface [25], in order to describe the nature of a third high frequency semicircle observed at modified graphene/(I_3^-/I^-) interfaces, we did not observe such a feature and both a satisfactory fit and interpretation of EIS results was achieved with the simplified model of figure 5.18.

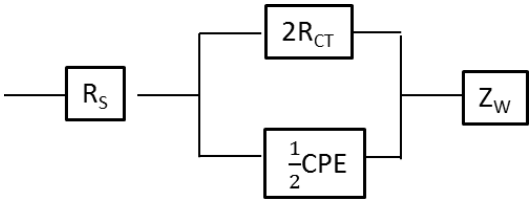

Figure 5.18 Electrical equivalent of dummy cells, used to fit EIS data.

An optimization of the spray deposition method was performed in order to yield a good compromise between electrochemical response and optical transmissivity of the counter electrodes, required for building-integrated applications where transparency is an issue. So, counter electrodes characterized by a T_{550} (trasmittance at 550 nm) of 5, 20 and 60 % were prepared, following the procedure described in section 5.2.2 and table 5. In figure 5.19 the SSCV (5.19a) and EIS plots (5.19b) of the dummy cells assembled with SWCNHS5-20-60 counter electrodes are reported, with their *T%* spectra (5.19c).

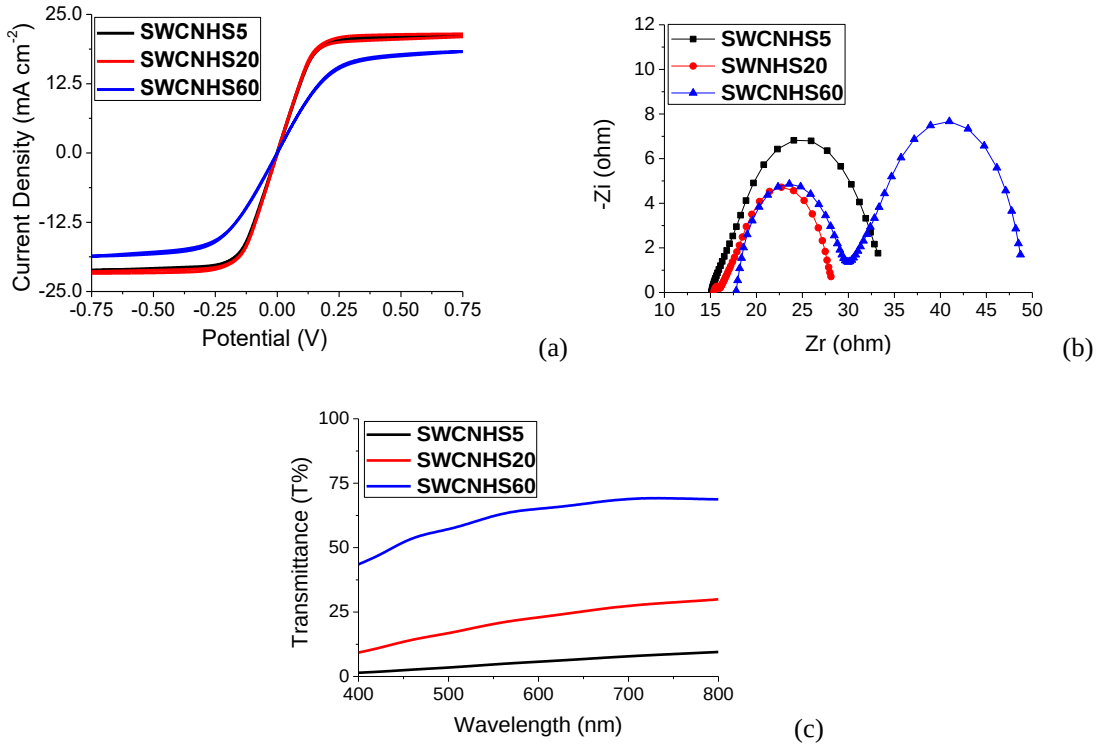

Figure 5.19 Thin layer cell characterization of SWCNHS5-20-60 counter electrodes: a) SSCV recorder at 10 mV s^{-1} b) Nyquist plot recorded at 0 V, electrolyte composition 0.18 M Co(II), 0.028 M Co(III) of $[Co(bpy)_3]^{2+/3+}$, 0.1 M $LiCF_3SO_3$ and 0.2 TBP in ACN. c) electrodes *T%* spectra.

It's made clear by figure 5.19a that the lowest limiting current and the highest overall resistance $(\partial\eta)/(\partial i)$ of the cell, are ascribed to SWCNHS60. These results are consistent with those obtained by EIS at 0 V (figure 5.19b), which shows, compared to SWCNHS5 and SWCNHS20, larger charge transfer and diffusional arcs and lower film conductivity, evident from the high frequency intercept with the real axis. This indicates that, as expected, the tuning of the electroactive area, as a function of the SWCNH loading, is critical for optimizing the counter electrode response.

Although the current-voltage (JV) response of SWCNHS20 and SWCNHS5 in dummy cell resulted nearly superimposable, SWCNHS20 was preferred to SWCNHS5 since the former showed the lowest total impedance (figure 5.19b), resulting the best compromise between transparency, conductivity, charge transfer and mass transfer resistance. Similar results were obtained at comparable loadings for the oxidized ox-SWCNHS (figure 5.20).

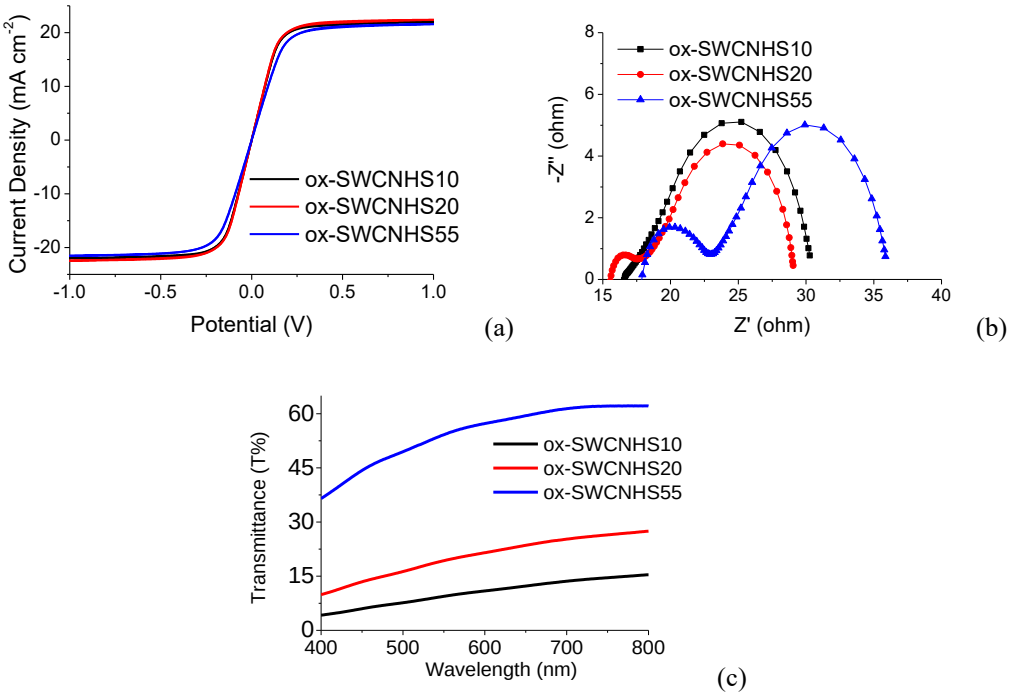

Figure 5.20 a) Thin layer cell characterization of ox-SWCNHS10-20-55 counter electrodes: a) SSCV recorder at 10 mV s^{-1} b) Nyquist plot recorded at 0 V, electrolyte composition 0.18 M Co(II), 0.028 M Co(III) of $[Co(bpy)_3]^{2+/3+}$, 0.1 M $LiCF_3SO_3$ and 0.2 TBP in ACN. c) electrodes *T%* spectra

The electrocatalytic behavior of SWCNHS20 and ox-SWCNHS20 was compared to that of electrodeposited PEDOT [36], taken as a reference organic catalytic material, (figure 5.30 and table 6). SWCNHS20, ox-SWCNHS20 and PEDOT exhibit JV curves having similar slope as well as limiting currents, ranging between 21 mA·cm^{-2} for ox-SWCNHS20 and 23 mA·cm^{-2} for PEDOT, consistently with the resistive contributions extracted from the EIS analysis. It can be pointed out that SWCNHS electrodes are generally better suited than PEDOT for transparent applications, providing comparable electrochemical response but with a significantly superior transmittance, particularly in the NIR region (figure 5.30c).

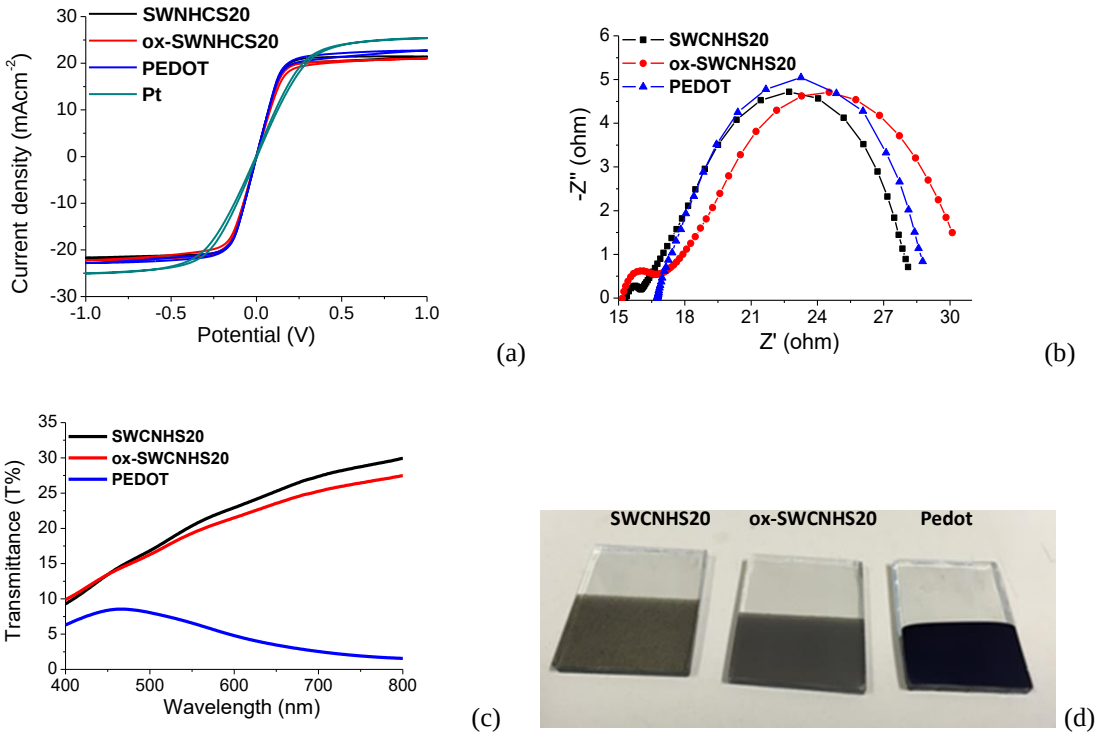

Figure 5.30 a) SSCV (10 $mV \cdot s^{-1}$) in thin layer cell: SWCNHS20 (black), ox-SWCNHS20 (red), PEDOT (blue) and Pt (dark cyan) b) Nyquist plots recorded at 0 V: SWCNHS20 (black), ox-SWCNHS20 (red) and PEDOT (blue), electrolyte composition 0.18 M Co(II), 0.028 M Co(III) of $[Co(bpy)_3]^{2+/3+}$, 0.1 M $LiCF_3SO_3$ and 0.2 TBP in ACN; c) electrodes T% spectra of and d) electrodes picture

	J_L **(mA·cm^{-2})**	Slope **(mA·V^{-1})**	$(slope)^{-1}$ **(Ω)**	R_s **(Ω)**	R_{CT} **(Ω)**	R_D **(Ω)**	R_{tot} **(Ω)**
SWCNHS20	21.4	35.6	28.1	15.5	0.21	12.0	27.9
ox-SWCNHS20	21.0	32.2	31.0	15.2	0.75	13.6	30.3
PEDOT	22.7	35.8	27.9	16.7	0.18	11.5	28.7
Pt	25.4	17.4	57.3	15.1	16.1	18.1	65.4

Table 6 Relevant parameters extracted from the EIS study in dummy cells (0.25 cm^2 active area) at 0 V

Dummy cells constituted of platinum electrodes filled with $Co(bpy)_3^{3+/2+}$ based electrolyte exhibit a certain variability in their electrochemical response, consistent with other reports concerning the electrochemical behavior of cobalt polypyridine couples at noble metal electrodes [46]. In general the platinum charge transfer resistance (R_{CT}) values are higher than those found for NH20 and PEDOT (Figure 5.30a and 5.31), whereas the cell diffusional resistance (R_D) is in all cases essentially comparable, particularly at low overvoltage (< 100 mV). As a consequence, the carbon based materials explored in this study display a lower total resistance ($R_{TOT}=(R_\Omega+R_{CT}+R_D)$ than

platinum, at least up to an overpotential of 150 mV, at which their JV curves, having a steeper slope than platinum (figure 5.30a), approach the diffusional limit. It should be noted that at 150 mV overpotential both NH and PEDOT generate a current of the order of 20 mA/cm^2, which is about the maximum that can be expected from the best dyes employed in conventional cobalt mediated DSSC. Thus, these electrodes can sustain, under a smaller overpotential than platinum, the limiting currents of the best cells reported so far. In addition, the slower charge transfer kinetics on platinum electrodes can be exacerbated by adsorption of electrolyte components like 4-tert-butylpyridine on the noble metal surface, resulting in rapid (with respect to time) decrease of the heterogeneous rate constant of the Co(II)/(III) couple [46]. Indeed electrochemical stability tests in sealed dummy cells containing Co(II)/(III) in MPN revealed, during the arc of a few days, a significant decrease of the JV curves slope, paralleled by a drop in limiting current (figure 5.32a). This effect was consistent with the increased charge transfer resistance revealed by impedance spectroscopy (figure 5.32b).

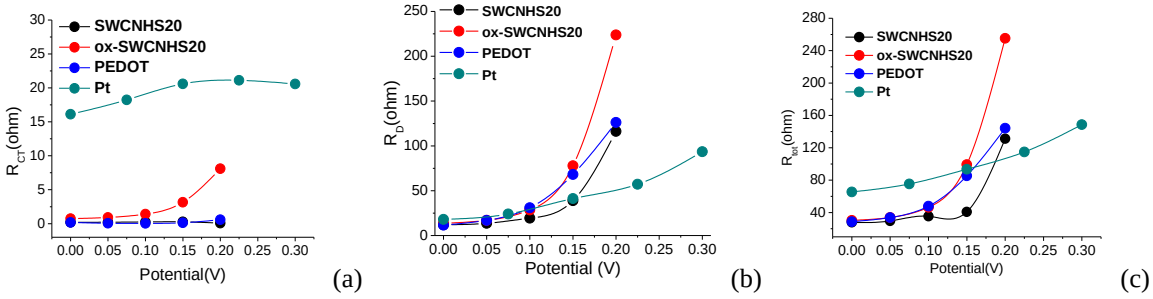

Figure 5.31 Potential dependance of charge transfer (R_{CT}) (a) diffusional (R_D) (b) and total resistance (R_{TOT}) (c) extracted from fits of impedance data in symmetric thin layer cells (electrolyte composition 0.18 M Co(II), 0.028 M Co(III) of $[Co(bpy)_3]^{2+/3+}$, 0.1 M $LiCF_3SO_3$ and 0.2 tert-butyilpyridine in ACN). Please note the difference in the scales of R_D and R_{CT} showing that diffusion is the major component of the cell resistance. The charge transfer resistance is essentially constant, while the diffusonal resistance undergoes a steep increase as the limiting current is approached.

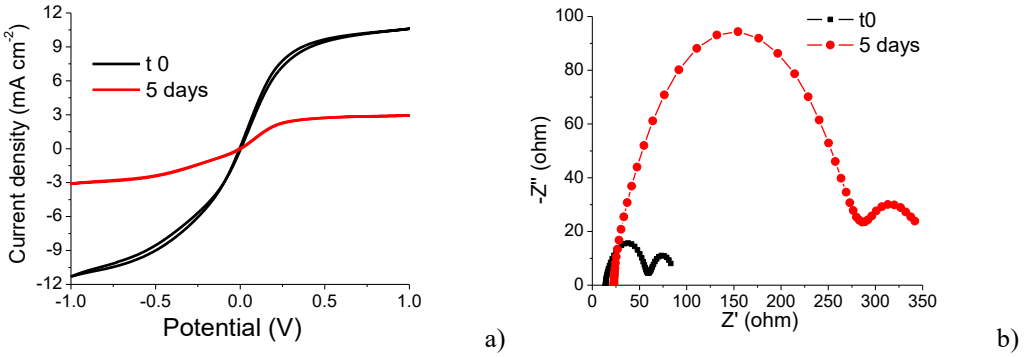

Figure 5.32 Long term electrochemical response evaluated in sealed Pt-Pt dummy cell at room temperature: a) cell was first cycled to attain a steady electrochemical response (superimposable curves), and b) subsequently analyzed by EIS at 0V after 10 s relaxation (at 0 V). Electrolyte composition 0.18 M Co(II), 0.028 M Co(III) of $[Co(bpy)_3]^{2+/3+}$, 0.1 M $LiCF_3SO_3$ and 0.2 TBP in MPN

While SWCNHS20 and PEDOT exhibit very similar R_{CT} and R_D, of the order of 0.2 Ω and 12 Ω respectively it can be observed that ox-SWCNHS20 is characterized by higher R_{CT} and R_D. The surface morphology of the electroactive material is usually the determinant factor in explaining such differences. Scanning electron microscopy (SEM), atomic force microscopy (AFM), and Transmission Electron Microscopy (TEM) analysis were used to explore the morphological properties of the two different types of carbon nanohorns based substrates.

SEM imaging (figure 5.33) showed, that SWCNHS20 exhibits a very homogeneous and porous "sponge-like" surface with cavities of the order of 100-250 nm, whereas the morphology of ox-SWCNHS20 is clearly less porous, presenting larger aggregates with diameters up to ca. 1μm, irregularly distributed on the surface.

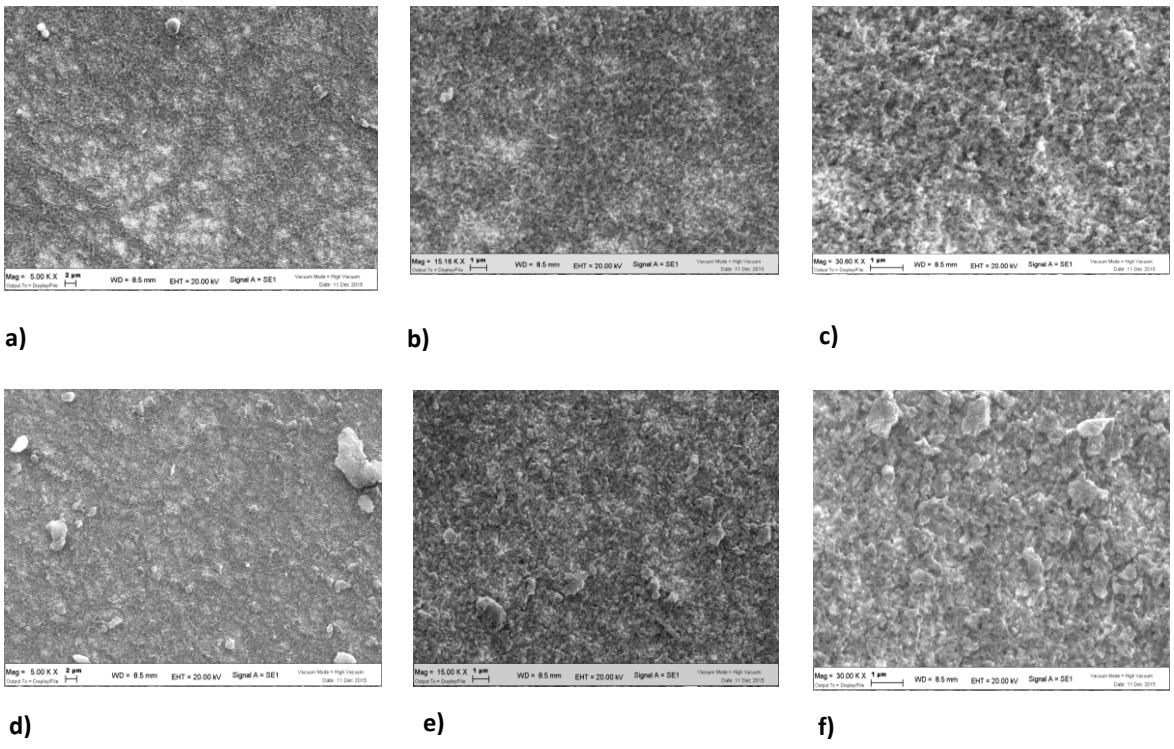

Figure 5.33 SEM micrographs of (a), (b), (c) SWCNHS20 and of (d), (e), (f) ox-SWCNHS20 at 5, 15 and 30 kX

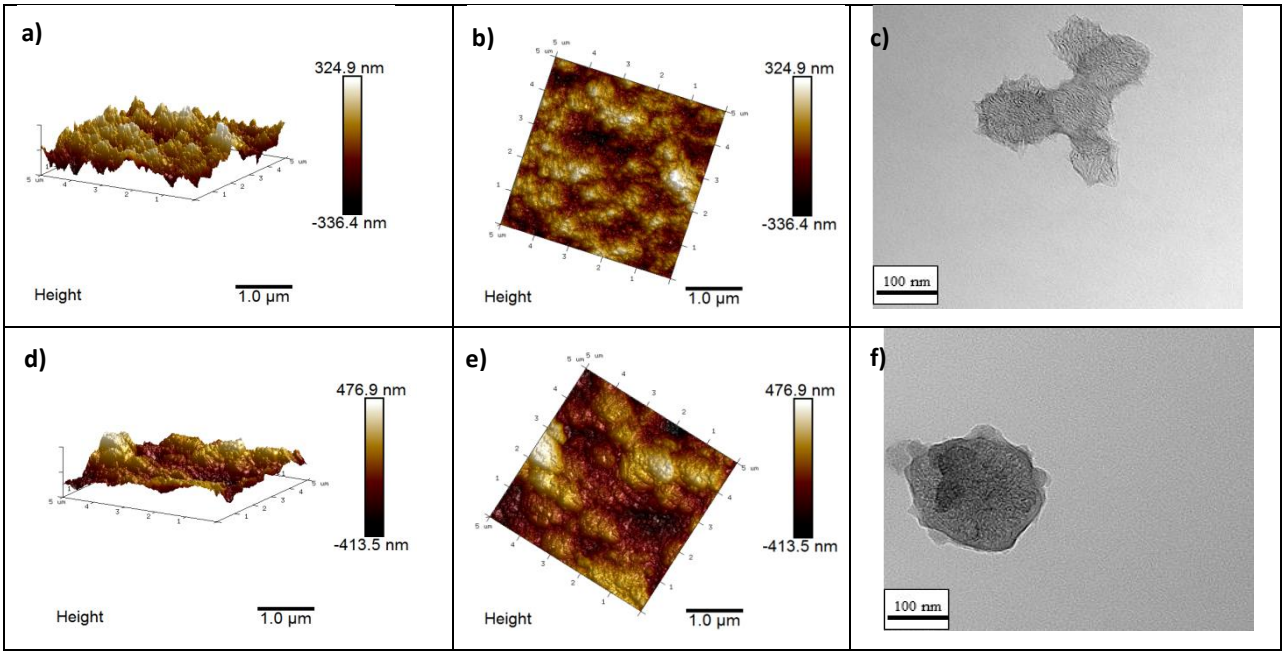

Figure 5.34 AFM imaging of (a), (b) SWCNH20 and (d), (e) ox-SWCNH20.
TEM micrograph of (c) SWCNH20 and (f) SWCNH20.

	R_q **(nm)**	R_a **(nm)**	R_{max} **(nm)**
SWCNHS20	96.1	77.4	693
ox-SWCNHS20	127	101	810

Table 7 Surface Morphology Parameters for SWCNHS20 and ox-SWCNHS20 films obtained from AFM Analysis. *(R_q*: root mean square, average of height deviations taken from the mean image data plane; R_a: arithmetic average of the absolute values of the surface height deviations, measured from the mean plane; R_{max}: maximum vertical distance between the highest and lowest data points in the image following the plane fit).

AFM analysis (Figure 5.34 and Table 7) substantially corroborated the qualitative observations carried out by SEM, showing a slightly higher surface roughness in ox-SWCNHS20 compared to SWCNHS20 (R_q = 101 nm Vs 77 nm for SWCNHS20), indicating a less regular surface coverage. This is particularly evident in the 3D AFM view: the higher R_{max} (i.e. the average vertical distance between the deepest valley and highest peak) observed for ox-SWCNHS20 is indeed affected by the presence of big carbon lumps irregularly distributed on the surface. This observation is consistent with TEM imaging showing, in ox-SWCNHS20, the formation of spherical aggregates with diameter in the order of 500 nm. On the contrary, pristine SWCNHS20 preserve a more homogeneous distribution with smaller interconnected aggregates (ca. 100 nm), exhibiting a higher content of excrescences on the borders, contributing to enhance the electroactive area of the catalyst.

The stability of SWCNHS20, ox-SWCNHS20 and PEDOT based counter electrodes was evaluated in sealed dummy cells using an electrolyte constituted by the $Co(bpy)_3^{+2/+3}$ redox mediator in methoxypropionitrile (MPN), solvent that has a better long term stability, due to its lower volatility, with respect to ACN, commonly used in record cells (Figure 5.35 and 5.36) [47]. The higher viscosity of MPN explains the lower limiting current (10-15 $mA \cdot cm^2$) observed with the nanohorns based electrodes.

The assembled cells were monitored by both SSCV and EIS at room temperature, finding a progressive increase in the electrochemical performance of the nanocarbons coated electrodes during the first 10 days, until attaining a stable response which was subsequently stably maintained. The EIS analysis showed a progressive decrease of the resistance associated to the diffusional arc, which is consistent with a progressive and more intimate permeation of the nanohorns film by the redox mediator, leading to the consequent enhancement in limiting current. Similar results had been observed for graphene based counter electrodes during ageing tests [21]. By contrast, although freshly prepared PEDOT films had shown excellent performance, a progressive decay of their electrochemical response was observed over the first 10 days, both due to an increase of the diffusional resistance and of the series ohmic resistance, which can be appreciated from the shift of the high frequency intercept of the arc on the real axis.

These results could be motivated by a loss of adhesion of the conducting polymer to the underlying FTO contact, and by adsorption of the redox mediator or of other electrolyte additives on the polymer surface, constituting local blocking layers for both the electron transfer and mass transfer processes. The increase of the PEDOT interfacial charge transfer resistance, from ca. 7 Ω in the freshly sealed cell to ca. 12 Ω, also corroborates this latter effect.

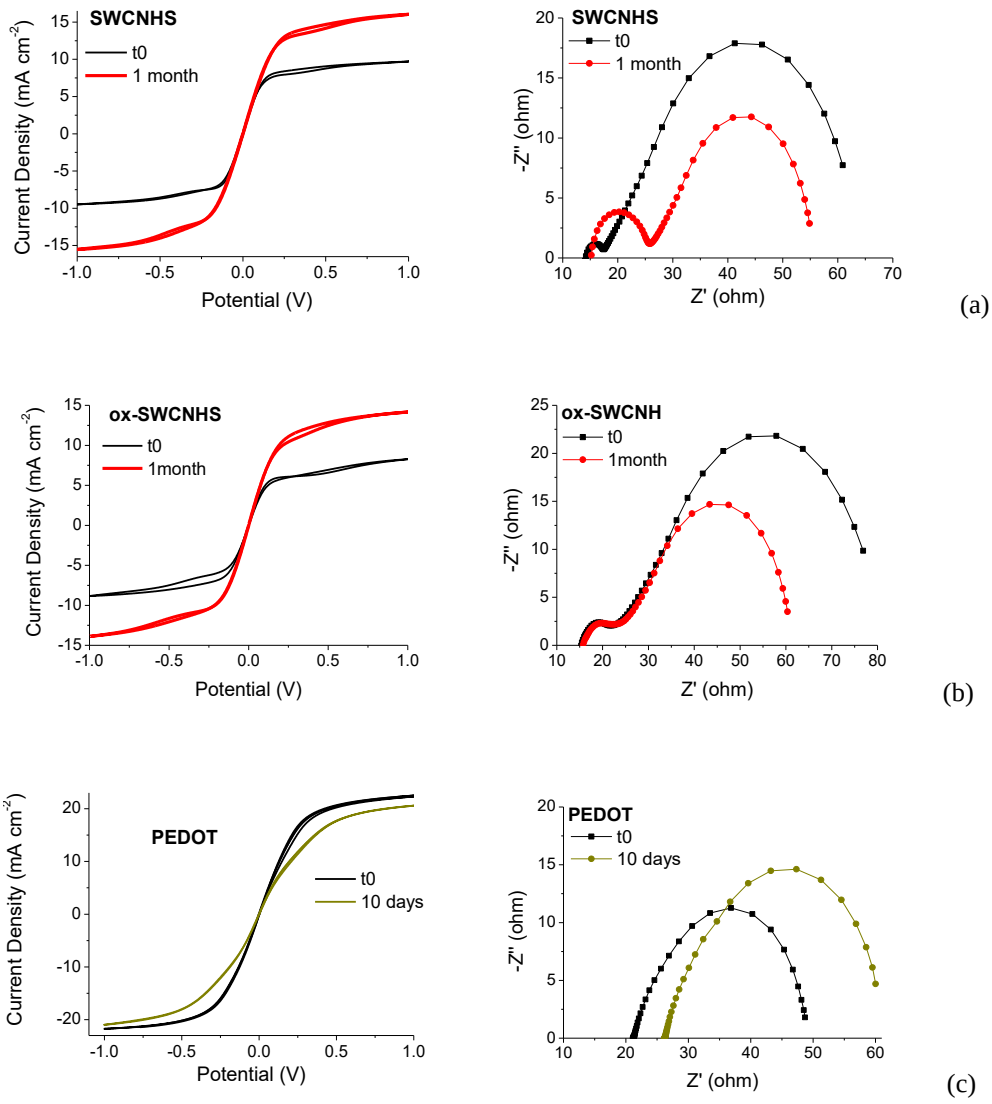

Figure 5.35 Long term electrochemical response evaluated in sealed dummy cells at room temperature for SWCHNs (a), ox—SWCNHs (b), PEDOT (c) :: cells were first cycled to attain a steady electrochemical response (superimposable curves), and subsequently analyzed by EIS at 0V after 10 s relaxation (at 0 V).

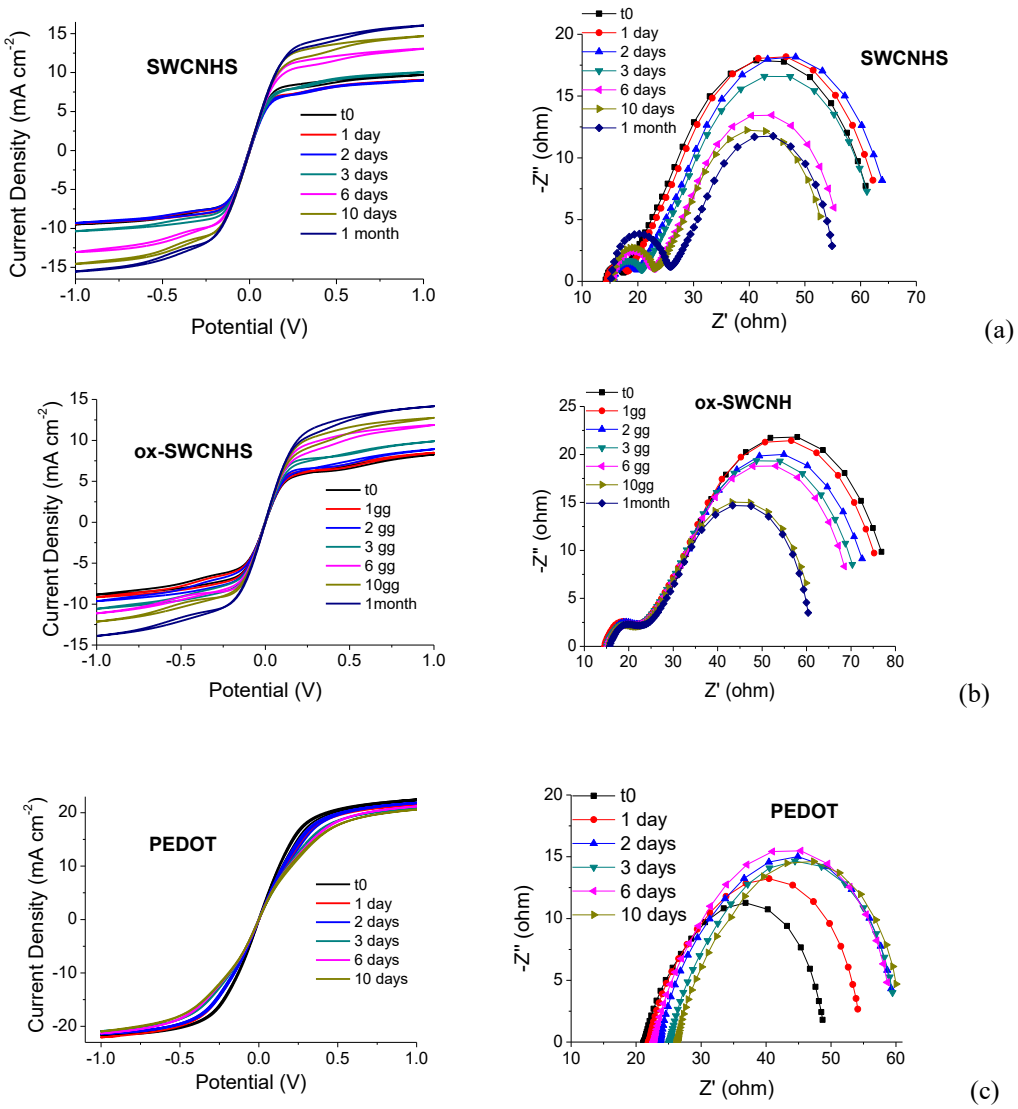

Figure 5.36 Long term electrochemical response evaluated in sealed dummy cell at room temperature for SWCHNs (a), ox—SWCNHs (b), PEDOT (c) : cells were first cycled to attain a steady electrochemical response (superimposable curves), and subsequently analyzed by EIS at 0V after 10 s relaxation. Electrolyte composition 0.18 M Co(II), 0.028 M Co(III) of $[Co(bpy)_3]^{2+/3+}$, 0.1 M $LiCF_3SO_3$ and 0.2 TBP in MPN.

The nanohorns counter electrodes were tested in solar devices employing the carbazole based organic dye LEG4, whose sterically hindered structure efficiently blocks recombination processes involving conduction band electrons and $Co(bpy)_3^{3+}$ [3]. Consistent with the dummy cell results, the nanohorns counter electrodes exhibited comparable efficiency values with respect to PEDOT, > 6.7 % in all cases (figure 5.37 and table 8), offering, at the same time, the additional benefit of a higher reproducibility of solar cell performance (Figure 5.38). In addition SWCNHs electrodes can be prepared through spray coating, which represents the ideal method for the fabrication of large-area DSSC. Among the counter electrode materials selected for this study, platinum provided the lowest performances, ascribable to the highest charge transfer resistance, as discussed before.

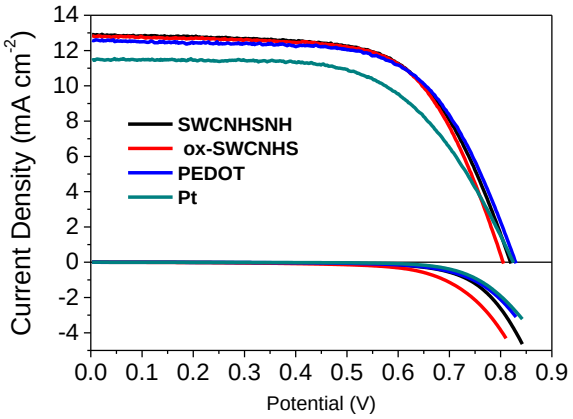

Figure 5.37 Current-voltage characteristics of DSSC with LEG4 sensitized TiO_2 photoanodes under AM 1.5G.

CEs	J_{sc} (mA cm^{-2})	V_{oc} (V)	FF	η %
SWCNH	12.91	0.82	0.64	**6.76**
ox-SWCNH	12.84	0.80	0.66	**6.75**
PEDOT	12.58	0.83	0.64	**6.73**
Pt	11.46	0.82	0.61	**5.74**

Table 8 Efficiency parameters obtained from the JV curves reported in figure 5.30

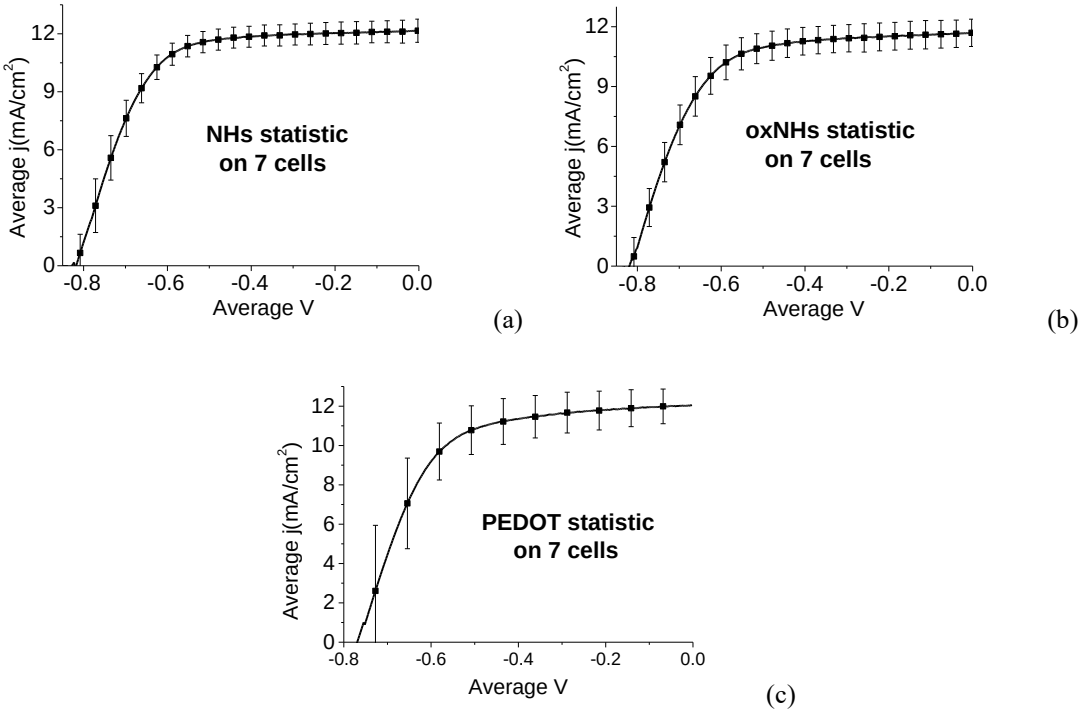

Figure 5.38 Statistic on cell performances. Current-voltage characteristics of DSSC with LEG4 sensitized TiO_2 photoanodes. Each curve representes the average of 7 cells, with the standard deviation represented by vertical bars. Light intensity: 1 sun. Electrolyte composition: $Co(bpy)_3^{+2/+3}$ 0.18M/0.028M, $LiCF_3SO_3$ 0.1M, TBP 0.2M in ACN.

5.2.4 Conclusion

In summary, counter electrodes built by spraying Single Walled Carbon Nanohorns on FTO electrodes were prepared and their electrocatalytic properties were for the first time investigated in conjunction with the $Co(bpy)_3^{+2/+3}$ redox mediator [48]. These new substrates, coupling excellent electrocatalytic properties, ease of fabrication and very promising stability, might constitute a viable replacement to noble metals and conductive polymers based counter electrodes materials for new generation photoelectrochemical devices.

References

(1) O'Regan, B.; Grätzel, M. *Nature* **1991**, *353*, 737-740.

(2) Urbani, M.; Grätzel, M.; Nazeeruddin, M. K.; Torres, T. *Chem. Rev*. **2014**, *114*, 12330−12396.

(3) Gabrielsson, E.; Ellis, H.; Feldt , S.; Tian, H.; Boschloo, G.; Hagfeldt, A.; Sun, L. *Adv. Energy Mater*. **2013**, *3*, 1647–1656.

(4) Tsao , H. N.; Yi , C.; Moehl, T.; Yum, J. H.; Zakeeruddin, S. M.; Nazeeruddin, M. K.; Grätzel, M. *ChemSusChem* **2011**, *4*, 591 - 594.

(5) Wu, J.; Lan, Z.; Lin, J.; Huang, M.; Huang, Y.; Fan, L.; Luo, G. *Chem. Rev.* **2015**, *115*, 2136−2173.

(6) Bella, F.; Vlachopoulos, N.; Nonomura, K.; Zakeeruddin, S. M.; Grätzel, M.; Gerbaldia, C.; Hagfeldt, A. *Chem. Commun.* **2015**, *51*, 16308-16311.

(7) Carli, S.; Benazzi, E.; Casarin, L.; Bernardi, T.; Bertolasi, V.; Argazzi, R.; Caramori, S.; Bignozzi, C. A. *Phys. Chem. Chem. Phys.* **2016**, *18*, 5949-5956.

(8) Sapp, S. A.; Elliot, M.; Contado, C.; Caramori, S.; Bignozzi, C. A. *J. Am. Chem. Soc.* **2002**, *124*, 11215−11222.

(9) Carli, S.; Casarin, L.; Caramori, S.; Boaretto, R.; Busatto, E.; Argazzi, R.; Bignozzi, C. A. *Polyhedron* **2014**, *82*, 173-180.

(10) Kakiage, K.; Aoyama, Y.; Yano, T.; Oya, K.; Fujisawa, J. I.; Hanay, M. *Chem. Commun.* **2015**, *51*, 15894-15897.

(11) Wu, M.; Ma, T. *J. Phys. Chem. C* **2014**, *118*, 16727−16742.

(12) Yun, S.; Hagfeldt , A.; Ma, T. *Adv. Mater.* **2014**, *26*, 6210-6237.

(13) Li, Z.; Kulkarni, S. A.; Boix, P. P.; Shi, E.; Cao, A.; Fu, K.; Batabyal, S. K.; Zhang, J.; Xiong, Q.; Wong, L. H.; Mathews, N.; Mhaisalkar, S. G. *ACS Nano* **2014**, *8*, 6797-6804.

(14) Zhang, F.; Yang, X.; Wang, H.; Cheng, M.; Zhao, J.; Sun, L. *ACS Appl. Mater. Interfaces* **2014**, *6*, 16140-16146.

(15) Zhang, F.; Yanga, X.; Cheng, M.; Wang, W.; Sun, L. *Nano Energy* **2016**, *20*, 108-116.

(16) Carli, S.; Busatto, E.; Caramori, S.; Boaretto, R.; Argazzi, R.; Timpson, C. J.; Bignozzi, C. A. *J. Phys. Chem. C* **2013**, *117*, 5142−5153.

(17) Park, B. W.; Pazoki, M.; Aitola, K.; Jeong, S.; Johansson, E. M. J.; Hagfeldt, A.; Boschloo, G. *ACS Appl. Mater. Interfaces* **2014**, *6*, 2074−2079.

(18) Ellis, H.; Vlachopoulos, N.; Häggman, L.; Perruchot, C.; Jouini, M.; Boschloo, G.; Hagfeldt, A. *Electrochim. Acta* **2013**, *107*, 45-51.

(19) Kavan, L.; Yum, J. H.; Nazeeruddin, M. K.; Grätzel, M. *ACS Nano* **2011**, *5*, 9171−9178.

(20) Kavan, L.; Yum, J. H.; Grätzel, M. *ACS Nano* **2011**, *5*, 165−172.

(21) Kavan, L.; Yum, J. H.; Grätzel, M. *Nano Lett.* **2011**, *11*, 5501-5506.

(22) Poudel, P.; Qiao, Q. Carbon *Nano Energy* **2014**, *4*, 157-175.

(23) Kavan, L.; Yum, J. H.; Grätzel, M. *ACS Appl. Mater. Interfaces* **2012**, *4*, 6999–7006.

(24) Roy-Mayhew, J. D.; Boschloo, G.; Hagfeldt, A.; Aksay, I. A. *ACS Appl. Mater. Interfaces* **2012**, *4*, 2794−2800.

(25) Roy-Mayhew, J. D.; Bozym, D. J.; Punckt, C.; Aksay, I. A. *ACS Nano* **2010**, *4*, 6203−6211.

(26) Z. Zhang; S. Han; C. Wang; J. Li; G. Xu. *Nanomaterials* **2015**, *5*, 1732.

(27) Yudasaka, M.; Iijima, S.; Crespi, V. H., *Top. Appl. Phys.* **2008**, *111*, 605-629.

(28) Zhu, S.; Xu, G. *Nanoscale* **2010**, *2*, 2538-2549.

(29) Urita, K.; Seki, S.; Utsumi, S.; Noguchi, D.; Kanoh, H.; Tanaka, H.; Hattori, Y.; Ochiai, Y.; Aoki, N.; Yudasaka, M.; Iijima, S.; Kaneko, K. *Nano Lett.* **2006**, *6*, 1325-1328.

(30) Lodermeyer, F.; Costa, R. D.; Casillas, R.; Kohler, F. T. U.; Wasserscheid, P.; Prato, M.; Guldi, D. M. *Energy Environ. Sci.* **2015**, *8*, 241-246.

(31) Cruz, R.; Brandão, L.; Mendes, A. *Int. J. Energy Res.* **2013**, *37*, 1498-1508.

(32) Brandão, L.; Boaventura, M.; Passeira, C.; Gattia, D. M.; Marazzi, R.; Antisari, M. V.; Mendes, A. *J. Nanosci. Nanotechnol.* **2011**, *11*, 9016-9024.

(33) Wepasnick, K. A.; Smith, B. A.; Schrote , K. E.; Wilson , H. K.; Diegelmann, S. R.; Fairbrother, D. H. *Carbon* **2011**, *49*, 24-36.

(34) Jung, J.; Graupner, R.; Ley, L.; Hirsch, A. *Phys. Status Solidi B* **2006**, *243*, 3217–3220.

(35) Schiavon, M. Device and method for production of carbon nanotubes, fullerene and their derivatives *EP1428794 (A2)*, **2006**.

(36) Carli, S.; Casarin, L.; Bergamini, G.; Caramori, S.; Bignozzi, C. A. *J. Phys. Chem. C* **2014**, *118*, 16782-16790.

(37) Casaluci, S.; Gemmi, M.; Pellegrini, V.; Di Carlo, A.; Bonaccorso, F. Graphene-Based Large Area Dye-Sensitized Solar Cell Module *Nanoscale* **2016**, *8*, 5368-5378.

(38) Figueiredo, J. L.; Pereira, M. F. R.; Freitas, M. M. A.; Òrfão, J. J. M. Modification of the Surface Chemistry of Activated Carbons *Carbon* **1999**, *37*, 1379-1389.

(39) Nakamura, M.; Irie, M.; Yuge, R.; Ichihashi, T.; Iijima, S.; Yudasaka, M. *Phys. Chem. Chem. Phys.* **2013**, *15*, 16672-16675.

(40) Eschemann, T. O.; Lamme, W. S.; Manchester, R. L.; Parmentier, T. E.; Cognigni, A.; Rønning, M.; de Jong, K. P. *J. Catal.* **2015**, *328*, 130-138.

(41) Rotas, G.; Sandanayaka, A. S. D.; Tagmatarchis, N.; Ichihashi, T.; Yudasaka, M.; Iijima, S.; Ito, O. *J. Am. Chem. Soc.* **2008**, *130*, 4725-4731.

(42) Sandanayaka, A. S. D.; Pagona, G.; Fan, J.; Tagmatarchis, N.; Yudasaka, M.; Iijima, S.; Araki, Y.; Ito, O. *J. Mater. Chem.* **2007**, *17*, 2540-2546.

(43) Cioffi, C.; Campidelli, S.; Sooambar, C.; Marcaccio, M.; Marcolongo, G.; Meneghetti, M.; Paolucci, D.; Paolucci, F.; Ehli, C.; Rahman, G. M. A.; Sgobba, V.; Guldi, D. M.; Prato, M. *J. Am. Chem. Soc.* **2007**, *129*, 3938-3945.

(44) Yuge, R.; Bandow, S.; Nakahara, K.; Yudasaka, M.; Toyama, K.; Yamaguchi, T.; Iijima, S.; Manako, T. *Carbon* **2014**, *75*, 322-326.

(45) Hauch, A.; Georg, A. *Electrochim. Acta* **2001**, *46*, 3457-3466.

(46) Ashbrook, L. N.; Eliott, C. M., *J. Phys. Chem. C* **2014**, *118*, 16643-16650.

(47) Hagfeldt, A.; Boschloo, G.; Sun, L.; Kloo, L.; Pettersson, H. *Chem. Rev.* **2010**, *110*, 6595-6663.

(48) Carli, S.; Casarin, L.; Benazzi, E.; Syrgiannis Z., Boaretto R., Caramori, S.; Prato M., Bignozzi C.A., *ACS Applied Materials & Interfaces* **2016**, 8, 14604−14612.

Acknowledgements

I would like to thank my supervisor, Prof. Carlo Alberto Bignozzi, for giving me the opportunity to be here and for always encouraging me, and my co-supervisor, Prof. Stefano Caramori, for patiently helping me in my scientific activity. I would also like to thank Dr. Stefano Carli for the great support and the many collaborations, and Prof. Jerry Meyer for letting me join his wonderful group for a six month period.

I would also like to thank Prof. Maddalena Pizzotti's group, in particular Dr. Gabriele Di Carlo, for giving me the chance to collaborate with them, and my colleagues from Ferrara and from Chapel Hill.